Frontier Materials & Technologies

Founded in 2008
№ 2
2024
16+
Quarterly
Scientific Journal

The Founder is
Togliatti State University

Until December 2021,
the journal was published under
the title
**"Science Vector
of Togliatti State University".**

Indexed in Scopus.
Included in the List of HAC,
RSCI core, DOAJ,
"White List".
Available in Crossref,
Google Scholar.

Registered by the Federal
Service for Supervision
of Communications,
Information Technology
and Mass Media
(Registration Certificate
ПИ No. ФС77-83040
dated March 31, 2022).

Subscription index
in the Russian Press catalogue:
13088.

Desktop publishing:
Natalya A. Nikitenko

*Responsible/technical
editor:*
Natalya A. Nikitenko

Mailing Address:
14, Belorusskaya St.,
Togliatti,
Russia, 445020
Phone: **(8482) 44-91-74**
E-mail:
vektornaukitgu@yandex.ru

Website:
https://vektornaukitech.ru

Passed for printing
28.06.2024.
Published 16.09.2024.
Format 60×84 1/8.
Digital printing.
Conventional printed sheets 14.8.
Circulation is 30 copies.
Order 3-135-24.
The price is free.

Publisher, printing house address:
Togliatti State University, 445020,
Russia, Samara Region, Togliatti,
Belorusskaya Street, 14.

EDITORIAL BOARD INFORMATION

СВЕДЕНИЯ О ЧЛЕНАХ РЕДКОЛЛЕГИИ

Кацман Александр Владимирович, кандидат физико-математических наук, PhD, старший научный сотрудник (Технион – Израильский технологический институт, Хайфа, Израиль).
Scopus AuthorID: 7004225554
Кудря Александр Викторович, доктор технических наук, профессор, заместитель заведующего кафедрой металловедения и физики прочности (Национальный исследовательский технологический университет «МИСиС», Москва, Россия).
Scopus AuthorID: 6603628218
Кузьмин Сергей Викторович, член-корреспондент РАН, доктор технических наук, профессор, первый проректор, профессор кафедры «Оборудование и технология сварочного производства» (Волгоградский государственный технический университет, Волгоград, Россия).
Scopus AuthorID: 57217278342
ResearcherID: I-7424-2012
ORCID: https://orcid.org/0000-0003-2802-8497
Макаров Алексей Викторович, член-корреспондент РАН, доктор технических наук, главный научный сотрудник, заведующий отделом материаловедения и лабораторией механических свойств (Институт физики металлов имени М.Н. Михеева Уральского отделения Российской академии наук, Екатеринбург, Россия).
Scopus AuthorID: 36889178900
Scopus AuthorID: 57195590138
ResearcherID: D-5663-2016
ORCID: https://orcid.org/0000-0002-2228-0643
Мулюков Радик Рафикович, член-корреспондент РАН, доктор физико-математических наук, профессор, директор (Институт проблем сверхпластичности металлов Российской академии наук, Уфа, Россия).
Scopus AuthorID: 7003520439
ResearcherID: B-3800-2016
ORCID: https://orcid.org/0000-0002-0452-3816
Наймарк Олег Борисович, доктор физико-математических наук, профессор, заведующий лабораторией «Физические основы прочности» (Институт механики сплошных сред Уральского отделения Российской академии наук, Пермь, Россия).
Scopus AuthorID: 6701720806
Носов Николай Васильевич, доктор технических наук, профессор, профессор кафедры «Технология машиностроения, станки и инструменты» (Самарский государственный технический университет, Самара, Россия).
Scopus AuthorID: 6602506825
Пилинский Александр Вениаминович, кандидат технических наук, доцент, MSME (Master of Science in Mechanical Engineering), Лос-Анджелес, США).
ORCID: https://orcid.org/0009-0009-8933-195X
Романов Алексей Евгеньевич, доктор физико-математических наук, профессор Института перспективных систем передачи данных, руководитель научно-исследовательского центра перспективных функциональных материалов и лазерных коммуникационных систем (Национальный исследовательский университет ИТМО, Санкт-Петербург, Россия).
Scopus AuthorID: 7202768874
Рубаник Василий Васильевич, член-корреспондент Национальной академии наук Беларуси, доктор технических наук, заведующий лабораторией физики металлов (Институт технической акустики Национальной академии наук Беларуси, Витебск, Республика Беларусь).
Scopus AuthorID: 57215218253
Сонар Тушар Мадхукар, кандидат технических наук, старший научный сотрудник кафедры «Оборудование и технология сварочного производства» (Южно-Уральский государственный университет, Челябинск, Россия)
Scopus AuthorID: 57200800257
ResearcherID: AAS-6037-2021
ORCID: https://orcid.org/0000-0002-3997-5337
Старобинский Рудольф Натанович, доктор технических наук, профессор, научный консультант (консалтинг-бюро “Prof. Starobinski. Silencers. Consulting and Engineering”, Гамбург, Германия).
Scopus AuthorID: 6602638504
Сундер Рамасуббу, член Индийской академии наук, кандидат технических наук, директор (“BISS (P) Ltd”, Бангалор, Индия).
Scopus AuthorID: 7003530245
ResearcherID: H-6740-2016
ORCID: https://orcid.org/0000-0001-6143-0723
Табаков Владимир Петрович, доктор технических наук, профессор, заведующий кафедрой «Инновационные технологии в машиностроении» (Ульяновский государственный технический университет, Ульяновск, Россия).
Scopus AuthorID: 6701501345
ResearcherID: E-1832-2017
ORCID: https://orcid.org/0000-0002-2568-9401
Шишков Владимир Александрович, доктор технических наук, начальник технического отдела (ООО «Палладио», Тольятти, Россия).
AuthorID РИНЦ: 596086
SPIN-код: 9504-4454
Эстрин Юрий Захарович, доктор физико-математических наук, профессор, профессор кафедры инженерных материалов (Университет им. Монаша, Мельбурн, Австралия).
Scopus AuthorID: 7005031984

CONTENT

СОДЕРЖАНИЕ

doi: 10.18323/2782-4039-2024-2-68-1

Influence of high-pressure torsion on the structure and mechanical properties of Zn–1%Fe–5%Mg zinc alloy

Elmira D. Abdrakhmanova[1], student
Elvira D. Khafizova*[2], PhD (Engineering),
assistant professor of Chair of Materials Science and Physics of Metals,
senior researcher of Scientific Research Laboratory "Metals and Alloys under Extreme Impacts"
Milena V. Polenok[3], student
Ruslan K. Nafikov[4], junior researcher of Scientific Research Laboratory "Metals and Alloys under Extreme Impacts"
Elena A. Korznikova[5], Doctor of Sciences (Physics and Mathematics), Professor,
professor of Chair of Materials Science and Physics of Metals,
Head of Scientific Research Laboratory "Metals and Alloys under Extreme Impacts"
Ufa University of Science and Technology, Ufa (Russia)

***E-mail:** KhafizovaED@uust.ru, ela.90@mail.ru

[1]ORCID: https://orcid.org/0009-0009-2775-7488
[2]ORCID: https://orcid.org/0000-0002-4618-412X
[3]ORCID: https://orcid.org/0000-0001-9774-1689
[4]ORCID: https://orcid.org/0000-0003-1280-6258
[5]ORCID: https://orcid.org/0000-0002-5975-4849

Received 27.06.2023 *Accepted 06.03.2024*

Abstract: Currently, scientists search for new materials for temporary implants that can dissolve in the body, which leads to the fact that there is no need for repeated surgery. In the last decade, scientific interest has focused on zinc-based materials because, unlike other metals, it has suitable corrosion rates and good biocompatibility. The paper describes an experiment for the study of the influence of deformation on the microstructure, strength and corrosion properties of an alloy of the Zn–Fe–Mg system. The authors carried out energy dispersive analysis and calculation of the volume fraction of the second phase of the Zn–Fe–Mg zinc alloy. The corrosion properties of the Zn–Fe–Mg zinc alloy with different microstructures (before and after high-pressure torsion) were studied using the gravimetric method under conditions simulating conditions inside a living organism (temperature, corrosive environment composition). During the tests, the corrosion mechanism was determined, its rate and mass loss of the samples were calculated. The relief of the corrosion surface was studied using scanning electron microscopy. It has been found that the destruction of the material in a corrosive environment occurs through a matrix containing the active Mg metal. The results of calculations of the corrosion rate for the original sample and samples subjected to high-pressure torsion differed due to a more even distribution of second phase particles during severe plastic deformation. In this work, by alloying zinc with iron and magnesium, as well as using high-pressure torsion, it was possible to increase the microhardness of the samples to 239.6±8 HV, which is a high indicator for zinc alloys.

Keywords: zinc alloys; Zn–Fe–Mg; biodegradable implants; high-pressure torsion; biocompatible materials.

Acknowledgments: The research was financially supported by a grant in the field of science from the budget of the Republic of Bashkortostan for state support of young scientists (Scientific and Educational Center – Grant for Young Scientists – 2022, Agreement No. 1 of 13.12.2022).

The work of Korznikova E.A., Nafikov R.K. was carried out under financial support of the Ministry of Science and Higher Education of the Russian Federation within the state assignment for public service delivery given to Ufa University of Science and Technology (Agreement No. 075-03-2024-123/1) "Youth Science and Research Laboratory of Scientific and Educational Center "Metals and Alloys under Extreme Impacts".

The research part of the work was carried out using the equipment of the Core Facility Centre "Nanotech" of Ufa University of Science and Technology.

The paper was written on the reports of the participants of the XI International School of Physical Materials Science (SPM-2023), Togliatti, September 11–15, 2023.

For citation: Abdrakhmanova E.D., Khafizova E.D., Polenok M.V., Nafikov R.K., Korznikova E.A. Influence of high-pressure torsion on the structure and mechanical properties of Zn–1%Fe–5%Mg zinc alloy. *Frontier Materials & Technologies*, 2024, no. 2, pp. 9–22. DOI: 10.18323/2782-4039-2024-2-68-1.

INTRODUCTION

Currently, biodegradable materials are considered as temporary implants for osteosynthesis and vascular stenting. Biodegradable materials have certain advantages over implant materials traditionally used in medicine due to theirability to dissolve in the body. During research, it has been found that zinc alloys have better mechanical and corrosion properties than previously studied magnesium- and iron-based materials.

Zinc is an essential ion in many cellular and biochemical processes, and promotes accelerated wound healing [1], thereby reducing the body recovery time in the post-surgery period. Pure zinc is a rather brittle material with low hardness (38.24±1.06 HV), and it is impossible to consider it in its pure form as a material for the production of implants. Alloying is one of the main effective methods for improving the complex properties of pure Zn. A mandatory requirement for alloying elements of a material for the production of medical implants is their non-toxicity. An interesting combination is the alloying with Fe and Mg, since they are biodegradable metals and at the same time strengthen the alloy [2]. In vitro studies of magnesium alloys showed that Mg corrosion products are not harmful to cells [2], and in Zn–Mg alloys [3], the survival rate of MC3T3-E1 mouse cells is higher, but Zn–Fe turned out to be cytotoxic, although human umbilical vein endothelial cells (HUVECs) turned out to be biocompatible with it [3].

Iron in the solid state has insignificant solubility in the Zn matrix, which leads to the formation of large particles of the second phase and has a strengthening effect on the alloy [4]. This is why in this work, Fe was chosen as one of the alloying metals. In the Zn–Fe state diagram, the equilibrium phase composition at room temperature consists of Zn and $FeZn_{13}$ due to the negligible solubility of Fe in Zn in the solid state [5]. The Zn–0.4Fe zinc alloy demonstrates good mechanical properties and biocompatibility, however, it is reported that when the iron content in the alloy increases to 2.5 %, the ductility values sharply decrease due to an increase in the volume fraction of the intermetallic phase [6]. The Zn–Mg–Fe zinc alloy showed good compatibility in in vivo studies on beagle dogs [7]. Osteosynthesis plates were placed in the frontal bone, mandible, and astragalus. The Zn–Mg–Fe alloy degraded uniformly, without significant differences in the rate of degradation of the frontal, mandibular, and astragalus implants. The corrosion rate reached approximately 0.183 mm/year in the first 3 months and then decreased to approximately 0.065 mm/year after 12 months [7].

Magnesium is also an important cation playing a crucial role in many physiological functions, so it was chosen as one of the alloying metals. Previously, an alloy with magnesium concentrations from 0.15 to 3.0 wt. % was developed [8]. Increasing the Mg content increased the microhardness values and tensile strength of Zn–Mg alloys, as the volume fraction of the solid intermetallic Mg_2Zn_{11} phase increased. Zn–Mg system alloys have a structure consisting of primary zinc and an interdendritic eutectic mixture. This structure provides mechanical strength comparable to that of a human bone [9]. In fine-grained alloys, a change in the corrosion mechanism from pitted to more uniform due to the second phase refinement was observed. With an increase in the Mg amount in the Zn–Mg alloy composition, its cytocompatibility increases and more uniform corrosion is observed, while localized corrosion was observed in the alloy with iron [3].

Through alloying and severe plastic deformation, it is possible to increase the strength properties of the alloy and regulate the corrosion rate by changing the structure parameters. Controlling the material destruction rate is one of the important tasks, since corrosion products should not exceed the maximum permissible concentration in the human body. The implant should not be destroyed until the bone tissue is completely restored, and the stent should not be destroyed until the vessel is restored. It is known that a fine-grained structure is formed in a metal after treatment by high-pressure torsion (HPT), and grain refinement leads to improved mechanical properties [10].

Currently, the alloy of the Zn–Fe–Mg system is understudied. This work studies the Zn–1%Fe–5%Mg alloy subjected to high-pressure torsion.

The purpose of the work is to study the influence of high-pressure torsion on the structure and mechanical properties of the Zn–1%Fe–5%Mg zinc alloy.

METHODS

The research material is the Zn–1%Fe–5%Mg alloy (Table 1). The chemical composition was determined on a Thermo Scientific ARL Optim'X X-ray fluorescence spectrometer. Melting was carried out in a chamber furnace in a graphite crucible with a diameter of 20 mm with a lid at a temperature of 580 °C. After that, the samples were subjected to homogenizing annealing at a temperature of 350 °C for 12 h.

Disks with a diameter of 20 mm and a thickness of 1.8 mm were cut on an ARTA 120 CNC electrical discharge machine. The disks were sanded using waterproof sanding paper of various grits. After that, the samples were subjected to high-pressure torsion in a SKRUDZH-200 machine at room temperature with an upper striker pressure of 6 GPa. The number of torsion revolutions is 0.5–10. When deformed by torsion, the original and resulting samples had the shape of disks. Samples were examined in the initial state and after deformation.

Table 1. *Chemical composition of the Zn–1%Fe–5%Mg alloy, wt. %*
Таблица 1. *Химический состав сплава Zn–1%Fe–5%Mg, вес. %*

Content of chemical elements, wt. %			
Zn	**Fe**	**Mg**	**The rest**
92.72±0.13	0.911±0.045	5.32±0.11	1.049±0.030

Static tensile tests were carried out on small samples (Fig. 1) on an Instron 5982 electromechanical measuring system at room temperature and a speed of 0.24 mm/min. The length of the test specimens was 10 mm, thickness – 0.8 mm, and neck thickness – 1 mm.

The microhardness of deformed samples was determined using an EMCO-Test DuraJet 10 hardness tester using the Vickers method (GOST 9450–76) under a load of 0.1 kg. The values were studied at 20 points with a step of 1 mm along the entire diameter of the sample.

Studies of the structure, the corrosion surface relief and analysis using energy dispersive X-ray spectroscopy (EDS) were carried out using a JEOL JSM-6490LV scanning electron microscope.

To study the structure, the samples were preliminarily etched in a 15 % sulfuric acid solution for 10 s. Calculations of the volume fraction of the second phase in zinc alloys were performed using the ImageJ program.

Corrosion tests were carried out for 60 days using the gravimetric method in accordance with the ASTM G1-03-E standard. Samples were studied in the initial state and after high-pressure torsion for 10 revolutions. At least 3 samples were taken for each state. The tests included exposing the samples to a corrosive environment – Ringer's solution (composition: 8.6 g/l of NaCl; 0.3 g/l of KCl; 0.25 g/l of $CaCl_2$, saline solution pH 7). The tests were carried out at a constant temperature of 38±1 °C.

The samples were weighed and photographed before and after cleaning from corrosion products every 2 days. Cleaning from corrosion products was carried out in a VI chromium oxide solution (200 g of reagent per 1000 ml of distilled water), then in distilled water using a KAISI-105 ultrasonic bath. After cleaning, the samples were dried and weighed on an EJ-123 electronic balance providing measurement accuracy of up to 0.01 mg. After cleaning from corrosion products and weighing, the samples were again kept in a corrosive environment. The surface of the samples was examined more closely by scanning electron microscopy every 14 days.

The corrosion rate *CR* mm/year was calculated according to the ASTM G3–63592 standard using the formula:

$$CR = \frac{87.6\,(M_0 - M_1)}{S\,t\,\rho},$$

where *CR* is the corrosion rate, mm/year;
S is the sample surface area, cm^2;
M_0 is the initial mass, mg;
M_1 is the mass after immersion, mg;
t is the holding time, h;
ρ is the metal density, g/cm^3.

Mass loss in % was calculated using the formula:

$$ML = \frac{(M_0 - M_1)}{M_0} \cdot 100\,\%,$$

where *ML* is the mass loss, %.

X-ray diffraction analysis (XRD) was carried out on a D2 Phaser desktop X-ray diffractometer with CuKα radiation at 30 kV and 10 mA with a shooting step of 0.02° and a scan rate of 1 °/min. X-ray phase analysis (XPA) of the obtained x-ray patterns was carried out in the Diffrac.Eva software package.

RESULTS

Structure and microhardness studies

The resulting alloy in the initial state had high microhardness values (210±4.6 HV). Samples after high-pressure torsion showed an uneven microhardness distribution over the entire diameter. The average microhardness values after high-pressure torsion are presented in Fig. 2, where after 2 torsion revolutions, a slight increase in microhardness to 239.6±8 HV is observed.

Studies of the structure have shown that in the initial state (Fig. 3 a) the alloy consists of a eutectic matrix with a fine-plate α-Zn and Mg_2Zn_{11} structure (Fig. 3 b), large

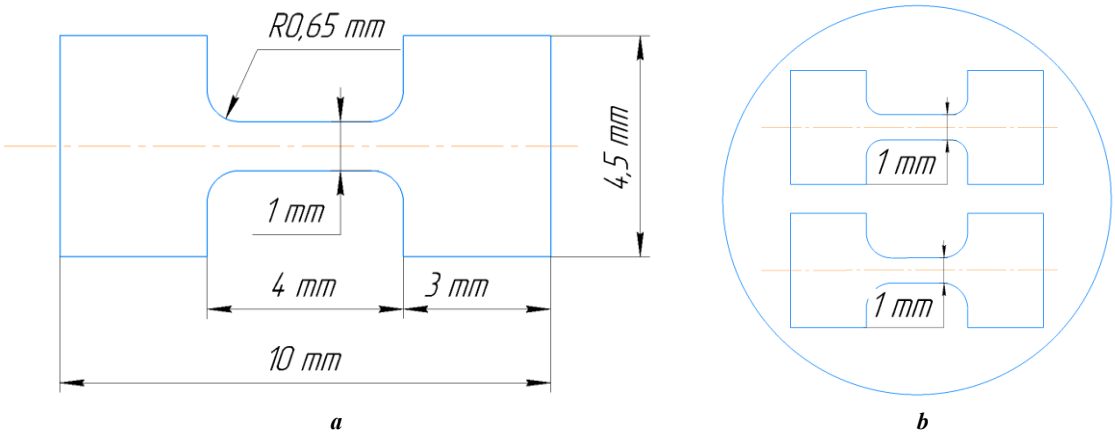

Fig. 1. *Shape of small samples for static tension tests:*
a *– drawing;* ***b*** *– layout of samples on the disk*
Рис. 1. *Форма малых образцов для испытаний на статическое растяжение:*
а *– чертеж;* ***b*** *– схема расположения образцов на диске*

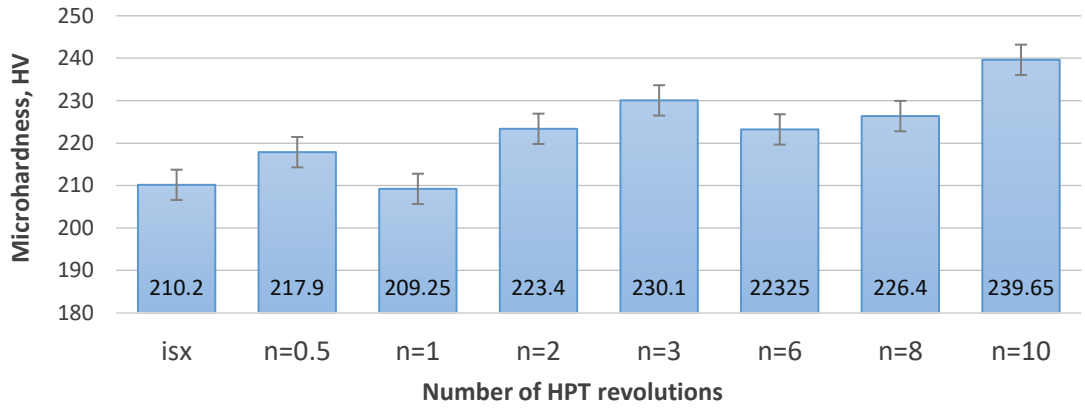

Fig. 2. *Microhardness of Zn–1%Fe–5%Mg samples after HPT with different number of revolutions*
Рис. 2. *Микротвердость образцов Zn–1%Fe–5%Mg после ИПДК с различным количеством оборотов*

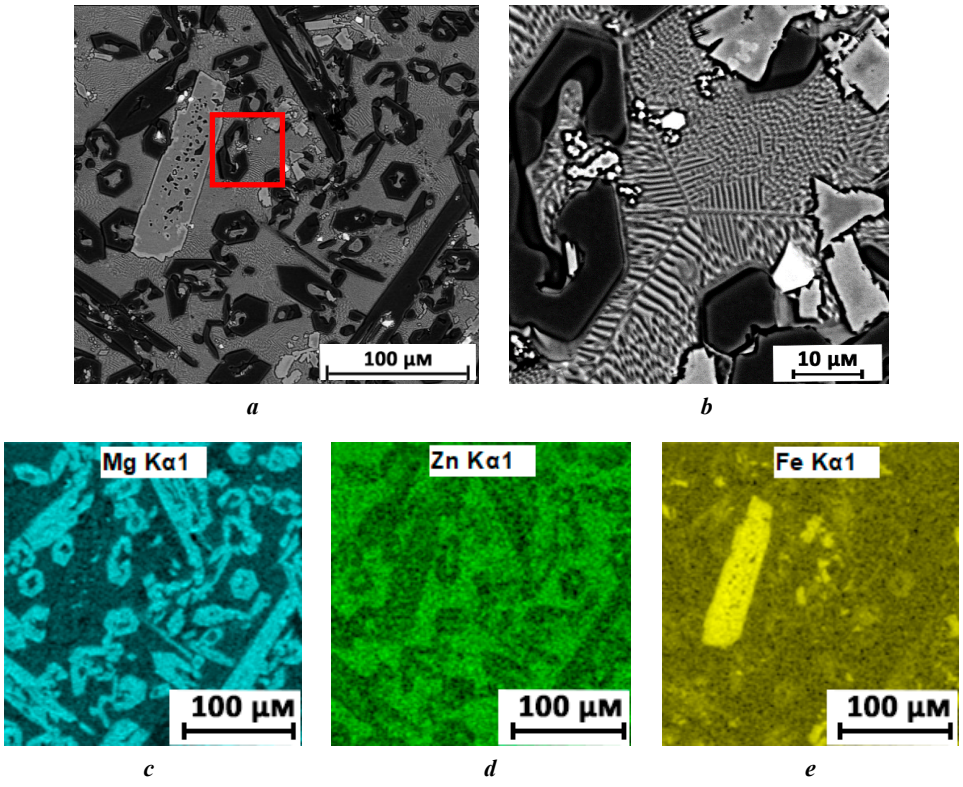

Fig. 3. *Structure of the Zn–1%Fe–5%Mg zinc alloy in the initial state (**a**, **b**) and EDS analysis of the Zn–1%Fe–5%Mg alloy (**c**–**e**)*
Рис. 3. *Структура цинкового сплава Zn–1%Fe–5%Mg в исходном состоянии (**a**, **b**) и EDS-анализ сплава Zn–1%Fe–5%Mg (**c**–**e**)*

$FeZn_{11}$ and $FeZn_{13}$ phases (light elements of irregular shape, hereinafter $FeZn_y$) and Fe and Mg content (dark elements of irregular shape), which is confirmed by EDS analysis (Fig. 3 c–e).

The structure after high-pressure torsion has undergone changes. The matrix is completely crushed; the fine-plate structure is transformed into ultra-fine-grained Mg_2Zn_{11}. The grain size is about 1 µm after 2 revolutions (Fig. 4 a). The solid phases Fe–Mg and $FeZn_y$ are crushed (Fig. 4 b). The results of EDS analysis (Fig. 4 c) showed that the dark-gray areas are the Fe–Mg phase, and the light-gray areas are pure zinc. After 8 revolutions, further refinement of the solid phases and their distribution throughout the entire sample volume are observed (Fig. 5). The volume fraction of the second phase did not change during deformation. Analysis of diffraction patterns showed (Fig. 6 a) that all X-ray spectra are characterized by the same set of intense peaks, and that the identified reflections belong to the Zn, $FeZn_{11}$ and $FeZn_{13}$, $MgZn_2$ and Mg_2Zn_{11} phases. There is a quantitative change in the ratio of peak intensities (Fig. 6 a), the profile shape, and the positions of the gravity centers of the X-ray peaks compared to the X-ray patterns of the corresponding initial state (Fig. 6 b). An increased integral

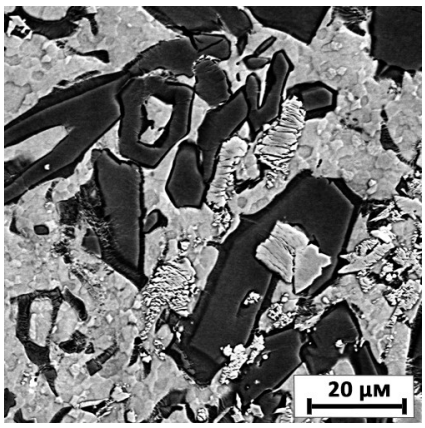

a

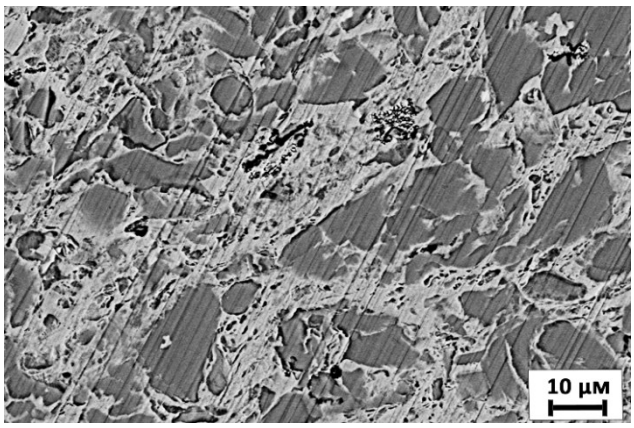

b

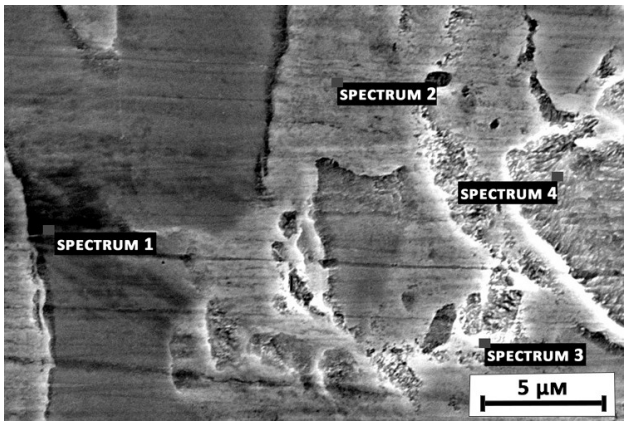

c

Spectrum	Mg	Fe	Zn	Total
Spectrum 1	15.19	0,47	84.33	100.00
Spectrum 2	0.00	0.00	100.00	100.00
Spectrum 3	1.06	0.00	98.94	100.00
Spectrum 4	13.92	0.42	85.67	100.00

Fig. 4. *Structure of the Zn–1%Fe–5%Mg zinc alloy after HPT for 2 revolutions:*
a *– SEM image at ×3000 magnification;* ***b*** *– SEM image at ×1000 magnification;* ***c*** *– EDS analysis of the Zn–1%Fe–5%Mg alloy*
Рис. 4. *Структура цинкового сплава Zn–1%Fe–5%Mg после ИПДК на 2 оборота:*
a *– РЭМ-изображение при увеличении ×3000;* ***b*** *– РЭМ-изображение при увеличении ×1000;* ***c*** *– EDS-анализ сплава Zn–1%Fe–5%Mg*

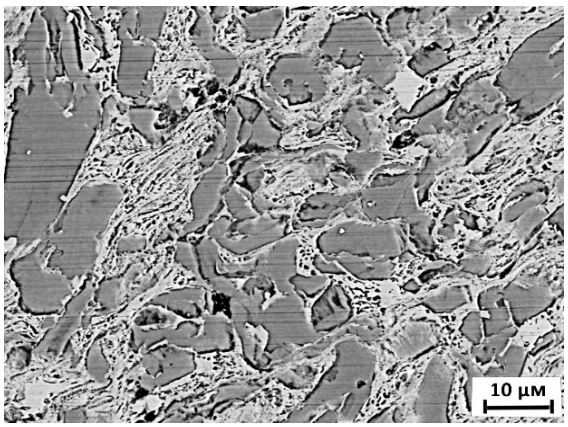

a

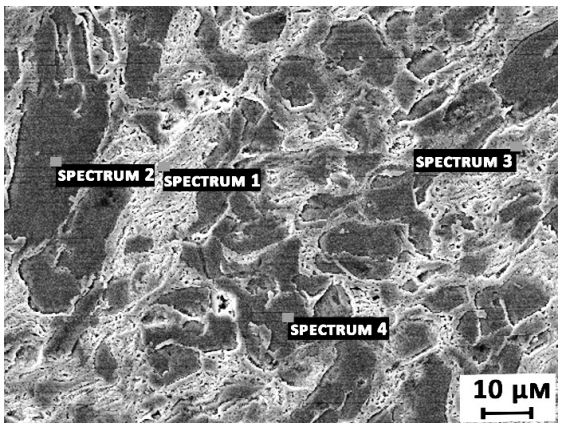

b

Spectrum	Mg	Fe	Zn	Total
Spectrum 1	1.51	0.89	97.60	100.00
Spectrum 2	15.09	2.41	82.50	100.00
Spectrum 3	0.00	0.00	100.00	100.00
Spectrum 4	13.54	2.04	84.42	100.00

Fig. 5. *Structure of the Zn–1%Fe–5%Mg zinc alloy after HPT for 8 revolutions:*
a *– SEM image;* ***b*** *– EDS analysis of the Zn–1%Fe–5%Mg alloy*
Рис. 5. *Структура цинкового сплава Zn–1%Fe–5%Mg после ИПДК на 8 оборотов:*
a *– РЭМ-изображение;* ***b*** *– EDS-анализ сплава Zn–1%Fe–5%Mg*

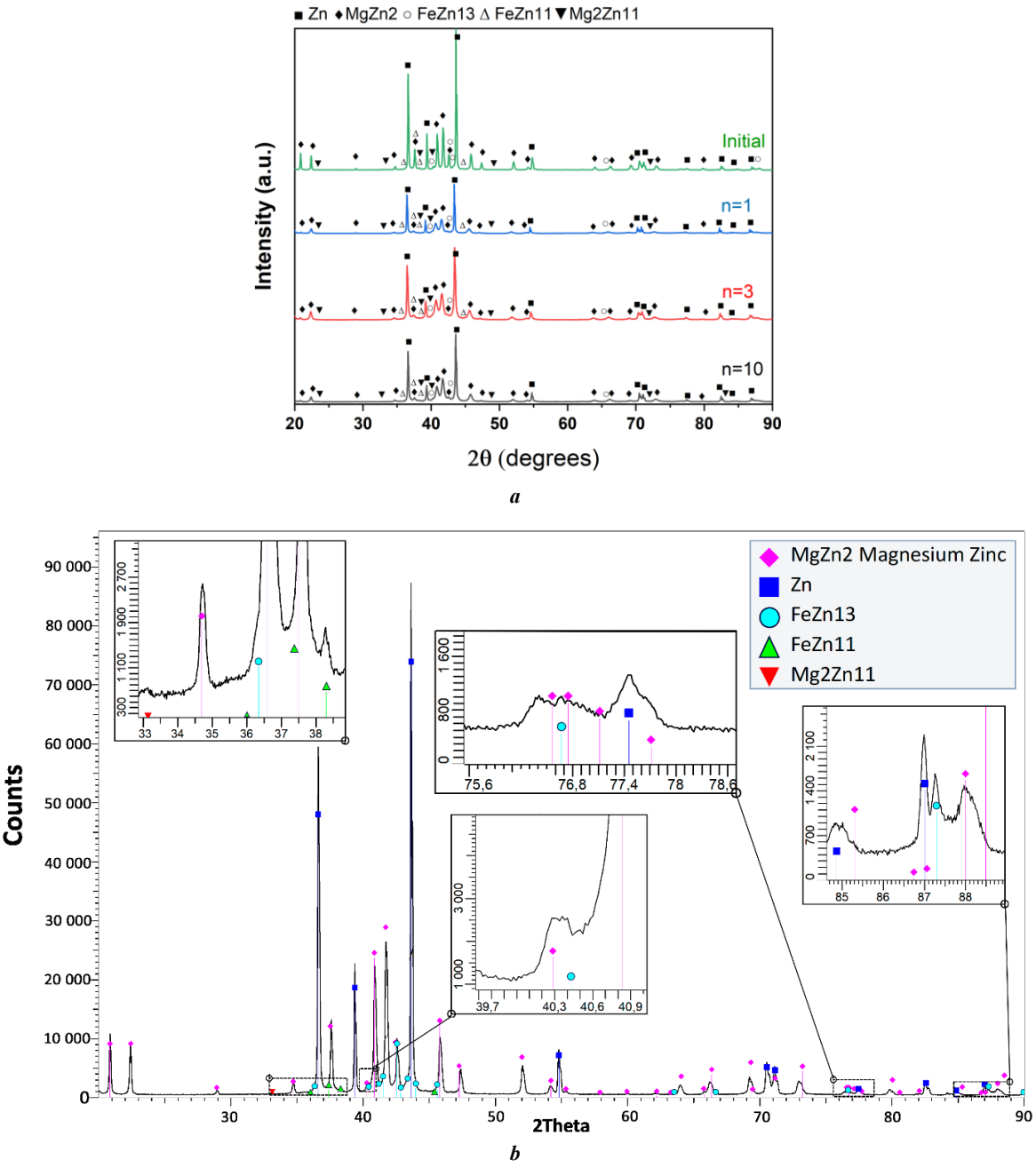

Fig. 6. *X-ray diffraction patterns of the Zn–1%Fe–5%Mg zinc alloy:* ***a*** *– before and after HPT;* ***b*** *– initial*
Рис. 6. *Рентгенограммы цинкового сплава Zn–1%Fe–5%Mg:* ***a*** *– до и после ИПДК;* ***b*** *– исходный*

intensity of the diffuse scattering background was detected (Fig. 6–8), which indicates changes in the identified phases and the occurrence of phase transitions in the alloy under study after high-pressure torsion treatment.

After 0.5 revolutions of high-pressure torsion, large particles with a size of approximately 40 μm are observed, most of them have an oblong shape and are elongated along one direction. After 3 revolutions, the structure begins to change significantly. The second phase particles are crushed and distributed throughout the entire volume. In the sample that underwent 8 revolutions of torsional deformation, the second phase particles were crushed to an average of 20 μm (Fig. 5 a), and after 10 revolutions – to 10 μm.

Corrosive characteristics

Corrosion destruction of a zinc alloy is determined by its heterogeneity in chemical and phase composition. Table 2 shows the influence of Ringer's solution during 60 days on the structure of the initial sample and the sample after high-pressure torsion for 10 revolutions. An increase in the corroded surface area is observed with increasing duration of the solution's influence on the samples, as well as a corrosion penetration deeper into the material, which correlates with the mass loss of the samples presented in Table 3. On the 10^{th} day, visible pores began to form in the original sample, which over time became larger. Fig. 9 presents photographs of the structure after 56 days of corrosion tests, where solid

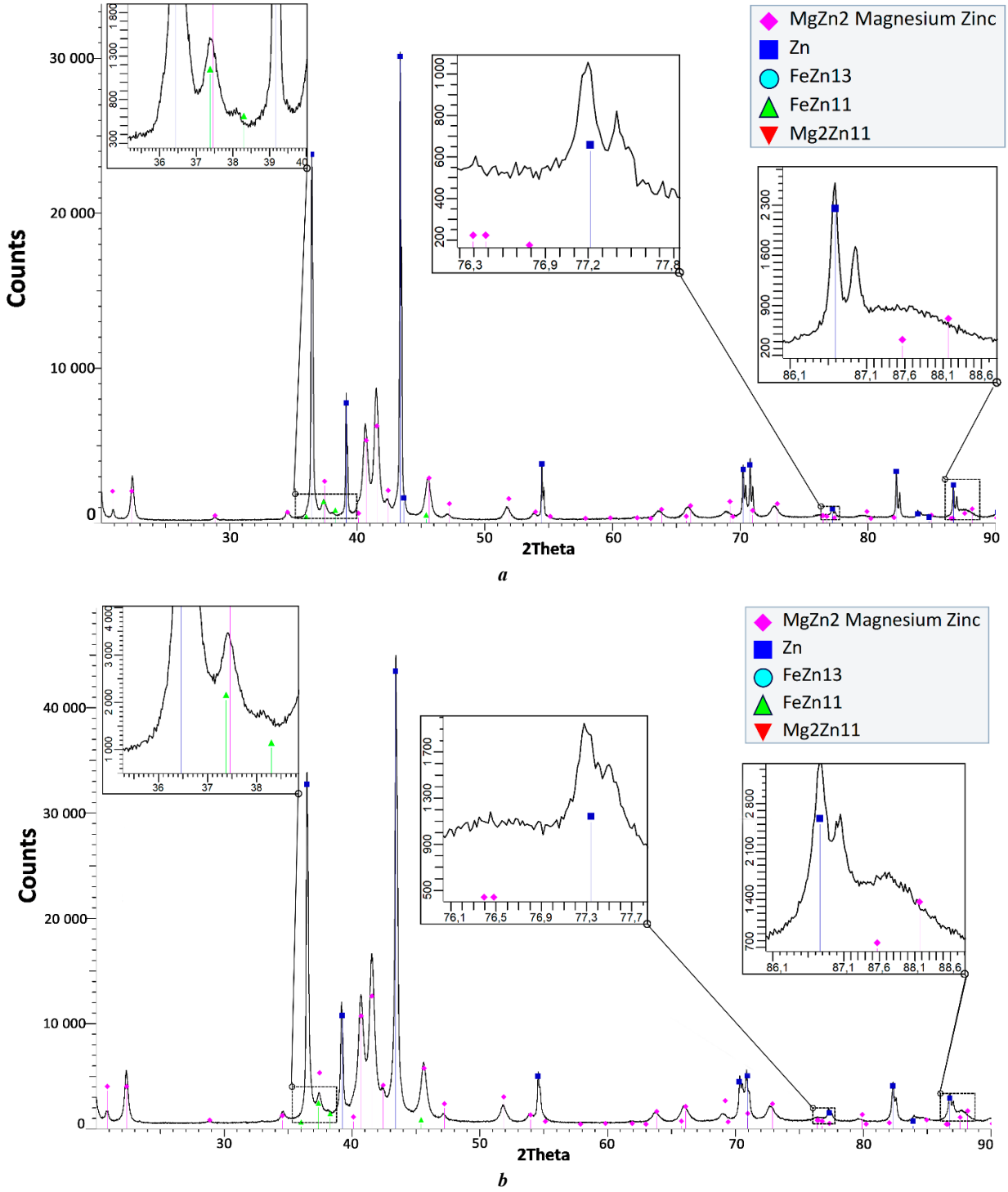

Fig. 7. *X-ray diffraction patterns of the Zn–1%Fe–5%Mg zinc alloy:* ***a*** *– after HPT for 1 revolution;* ***b*** *– after HPT for 3 revolutions*
Рис. 7. *Рентгенограммы цинкового сплава Zn–1%Fe–5%Mg:* ***а*** *– после ИПДК 1 на оборот;* ***b*** *– после ИПДК на 3 оборота*

particles in the initial state (Fig. 9 a) do not react with the solution; intercrystalline corrosion occurs when the active metal, in our case Mg, is a part of the matrix separating the metal crystalline grains. Corrosion in the original sample occurs in places where Mg is concentrated.

In a sample subjected to high-pressure torsion, similar cavities are observed after 28 days. In the deformed sample, corrosion proceeds visually more uniformly (Table 2 and Fig. 9 b), and mass loss occurs slightly faster than in the original (Table 3). Due to severe plastic deformation, the second phase containing Fe–Mg is refined and distributed throughout the entire volume of the sample. Refinement of structural elements using the method of severe plastic deformation promotes more uniform corrosion. The corrosion rate of the original sample on the 40th day of testing was 0.08 mm/year, on the 70th and 90th days – 0.13 mm/year. The corrosion rate of samples after HPT on the 40th day – 0.09 mm/year, on the 70th and 90th days – 0.15 mm/year.

On all HPT samples, pits are observed in the center that go deeper (Fig. 10 a), corrosion proceeds uniformly over

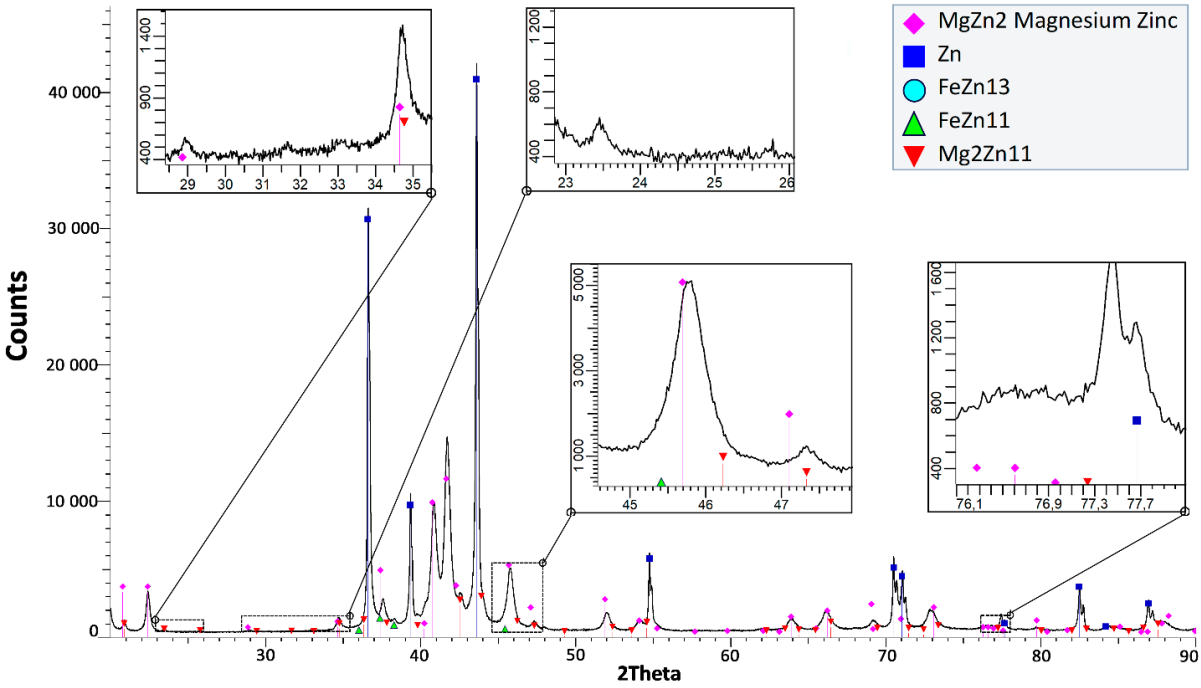

Fig. 8. *X-ray diffraction patterns of the Zn–1%Fe–5%Mg zinc alloy after HPT for 10 revolutions*
Рис. 8. *Рентгенограммы цинкового сплава Zn–1%Fe–5%Mg после ИПДК на 10 оборотов*

Table 2. *Photographs of the surface of samples after cleaning during corrosion tests*
Таблица 2. *Фотографии поверхности образцов после очистки в ходе коррозионных испытаний*

State	Test duration				
	2 days	10 days	25 days	40 days	60 days
Initial					
After HPT for 10 revolutions					

a larger area of the sample (Fig. 10 b). During HPT, a non-uniform structure is formed along the sample diameter. The grains take an elongated shape in the direction of torsion, since the angular rotation rate of the striker becomes greater with distance from the sample center, which affects the degree of material deformation, respectively, as well as the size of the structural elements and their orientations.

There were no gas emissions while the samples were in Ringer's solution.

Table 3. *Mass loss of samples during corrosion tests*
Таблица 3. *Потеря массы образцов во время коррозионных испытаний*

State	Test duration				
	1 day	10 days	25 days	40 days	60 days
Initial	0.55 %	1.55 %	2.21 %	2.88 %	4.31 %
After HPT for 10 revolutions	0.50 %	1.63 %	2.50 %	3.50 %	5.00 %

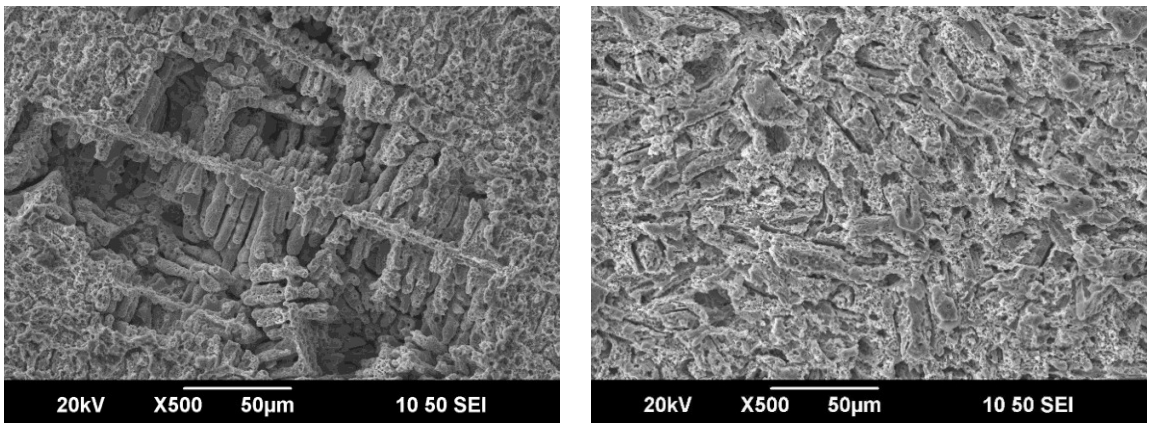

a ***b***

Fig. 9. *SEM images of the surface of samples of the Zn–1%Fe–5%Mg zinc alloy after 56 days of corrosion tests:* ***a*** *– initial;* ***b*** *– sample after 10 revolutions of HPT*
Рис. 9. *РЭМ-изображения поверхности образцов сплава Zn–1%Fe–5%Mg спустя 56 дней коррозионных испытаний:* ***a*** *– исходный;* ***b*** *– образец после 10 оборотов ИПДК*

DISCUSSION

In the initial state, the alloy consists of a eutectic matrix with a fine-plate α-Zn and Mg_2Zn_{11} structure (Fig. 3 b), which is also confirmed by X-ray diffraction analysis (Fig. 6 a). According to the Zn–Mg phase diagram [11], when Zn–Mg is cooled with a liquid containing 1 wt. % of Mg up to approximately 410 °C, the Zn phase first separates from the liquid. Next, at 364 °C the Mg_2Zn_{11} intermetallic compound appears. Thus, eutectics containing Zn and Mg_2Zn_{11} were formed along the boundaries of Zn grains. This is consistent with the results obtained in [12; 13]. Some small $MgZn_2$ peaks were detected (Fig. 6 b), which is likely related to the nonequilibrium solidification of Zn–Mg alloys during casting. Supercooling of the interdendritic liquid and deviation from the equilibrium diagram can lead to the $MgZn_2$ intermetallic compound precipitation in this alloy. A similar structure was observed in [14], where the Zn+Mg_2Zn_{11} eutectic, the needle $FeZn_{13}$ phase and the dendritic matrix Zn phase were present.

In the Zn–1%Fe–5%Mg alloy we studied, bright large $FeZn_{11}$ and $FeZn_{13}$ particles of irregular shape were also observed. X-ray spectral analysis detected two phases, but we could not separate them in the structure, so we left the designation $FeZn_y$. This elemental composition is also confirmed by EDS analysis. Except for this large phase, the structure contains dark-colored phases containing Fe and Mg (Fig. 3 c–e), but there are no cards with such content in the database of the program installed on the diffractometer.

In the Zn–Fe phase diagram, the temperature range of $FeZn_{13}$ formation by peritectic reaction is very wide and extends from 530 °C to room temperature, which may be the reason for the growth of $FeZn_{13}$ particles [14].

After severe plastic deformation, the solid Fe–Mg and $FeZn_y$ phases are crushed, and the matrix is completely refined. The fine-lamellar structure transforms into an ultrafine-grained structure with a grain size of about 1 μm after 2 revolutions (Fig. 4 a). A quantitative change in the ratio of the intensities of the Zn, $FeZn_{11}$ and $FeZn_{13}$, $MgZn_2$ and Mg_2Zn_{11} phase peaks (Fig. 6 a), the profile shape, the positions of the gravity centers of X-ray peaks, as well as the increased integral intensity of the diffuse scattering background (Fig. 7, 8) in comparison with radiographs of the corresponding initial state (Fig. 6 b) are observed. This indicates changes in the identified phases and the occurrence of phase transitions in the alloy under study as a result of high-pressure torsion.

There is no noticeable increase in microhardness after high-pressure torsion of a zinc alloy, but, unlike pure zinc [15] and other zinc alloys [16], the hardness of the considered Zn–1%Fe–5%Mg is the highest and reaches

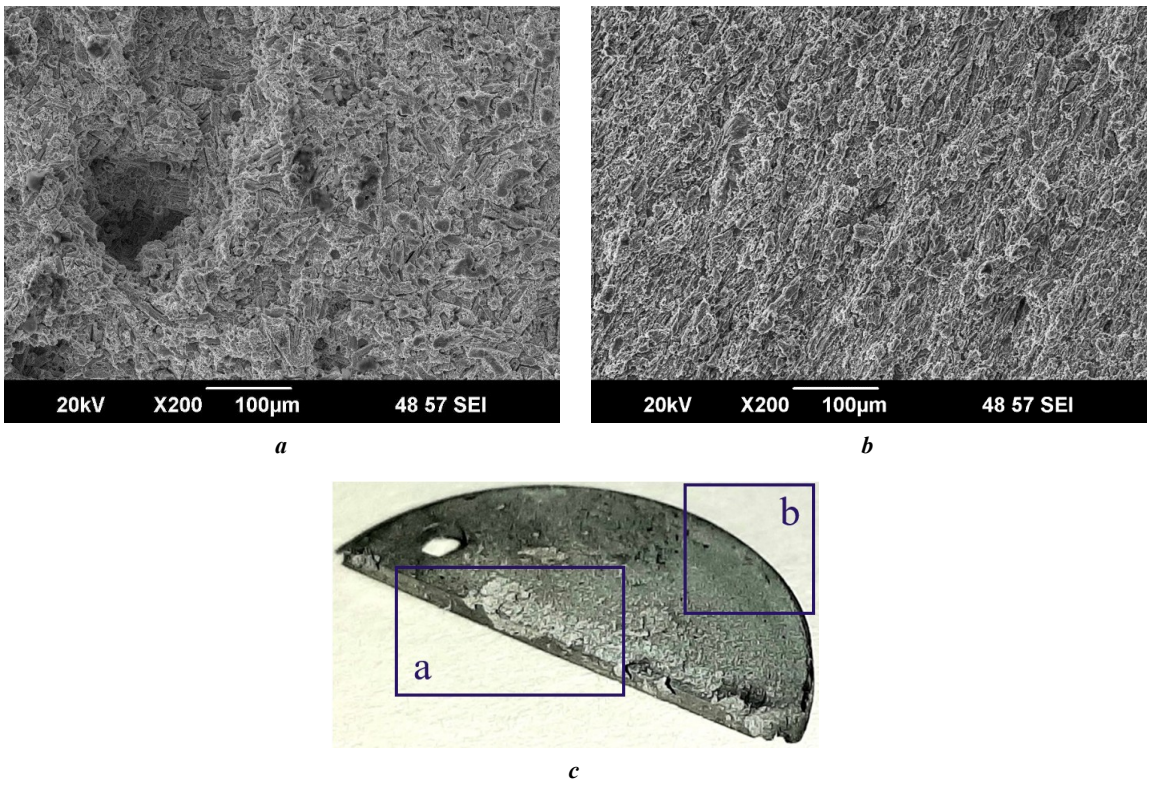

Fig. 10. *The structure of the sample subjected to 10 revolutions of HPT after 90 days of corrosion tests:* ***a*** *– central part of the sample;* ***b*** *– edge with changed texture;* ***c*** *– macroscopic image of the sample*
Рис. 10. *Структура образца, прошедшего 10 оборотов ИПДК, после 90 дней коррозионных испытаний:* ***a*** *– центральная часть образца;* ***b*** *– край с измененной текстурой;* ***c*** *– макроскопическое изображение образца*

210–240 HV due to alloying with Mg and Fe. The research in this work confirms that the Mg and Fe addition to a zinc alloy contributes to a significant increase in hardness values. In this case, the samples become very brittle.

The main deformation mechanism is glide of dislocations. In [14], measurements of the microhardness of the $FeZn_{13}$ and Mg_2Zn_{11} phases were made, which are 243±8 HV and 110±5 HV, respectively, with the Zn microhardness of 76.1 HV±2 HV, which leads to deformation incompatibility at the phase interface. Near the phase interface, a concentration of stresses and energy occurs, which causes dislocation glide and anomalous transformation determined by diffusion on moving defects (dislocations, grain boundaries) [17], and subsequently – dynamic Mg_2Zn_{11} phase recrystallization. Part of the stored energy was also released during $FeZn_{13}$ phase fragmentation.

The absence of gas emissions on the surface of the samples during corrosion tests is consistent with [14; 18]. When the samples were in the Ringer's solution, the pH of the corrosive environment gradually increased over time, which indicates the absorption of hydrogen ions in the solution, so the solution was often replenished during the experiment – every 48 h. A similar method of immersion test, where samples are cleaned every 24–48 h followed by repeated placement in a corrosive environment, was also used in works [19; 20]. This method allows estimating the rate of mass loss and corrosion rate for any time interval within 90 days. However, this method does not take into account the formation of a protective film and the change in corrosion rate due to passivation, so we plan to conduct continuous immersion tests.

The corrosion of zinc alloy is significantly higher than that of pure zinc, which is caused by the high potential difference between Mg_2Zn_{11} and $FeZn_{13}$. Corrosive destructions of a material depend on the metal activity; they easily react because they easily part with electrons at the external energy level. The degree of metal activity is characterized by the corresponding electrochemical series of metal stresses. Among the zinc alloy elements Zn (−0.76), Fe (−0.440), Mg (−2.363), Mg is the most active. Corrosion occurs in places where Mg is concentrated, since it has a more electronegative potential, therefore it acts as anodic centers and dissolves faster [21; 22]. $FeZn_{13}$ particles are cathodic and accelerate the dissolution of Zn and Mg-containing phases [23]. As in the study [24], an acceleration of corrosion processes in samples after high-pressure torsion is observed. The formation of a heterogeneous structure in the sample is consistent with [25]. The formation of visible corrosion pits in the center of HPT samples is determined by different crystallographic grain orientations in the HCP-lattice metal. A similar dependence was also reported in [26; 27].

The study of the mechanical properties and microstructure of the zinc alloy allows evaluating the prospects for its further research in vitro and in vivo for application as a material for the production of medical implants.

CONCLUSIONS

As a result of processing the Zn–1%Fe–5%Mg alloy by high-pressure torsion, samples with high hardness values (up to 239 MPa), but very brittle, were obtained.

The structure of the zinc alloy is multiphase; it contains $FeZn_{11}$, $FeZn_{13}$ and Mg–Fe solid particles, which are destroyed and partially dissolved during high-pressure torsion. The solid phases are located in a matrix of Zn and Mg_2Zn_{11}, which is transformed during the high-pressure torsion process into equiaxial grains of 1 μm in size.

The use of high-pressure torsion does not lead to significant changes in the corrosion rate, but leads to more uniform corrosion throughout the volume of the sample. The exception is the center with a less developed structure, where an intense penetration is observed.

REFERENCES

1. Kogan S., Sood A., Granick M.S. Zinc and Wound Healing: A Review of Zinc Physiology and Clinical Applications. *Wounds*, 2017, vol. 29, no. 4, pp. 102–106.
2. Lin Mao, Li Shen, Jiahui Chen et al. A promising biodegradable magnesium alloy suitable for clinical vascular stent application. *Scientific Reports*, 2017, vol. 7, article number 46343. DOI: 10.1038/srep46343.
3. Yang Hongtao, Jia Bo, Zhang Zechuan, Qu Xinhua, Li Guannan, Lin Wenjiao, Zhu Donghui, Dai Kerong, Zheng Yufeng. Alloying design of biodegradable zinc as promising bone implants for load-bearing applications. *Nature Communications*, 2020, vol. 11, article number 401. DOI: 10.1038/s41467-019-14153-7.
4. Shi Zhangzhi, Li Changheng, Li Meng, Li Xiangmin, Wang Luning. Second phase refining induced optimization of Fe alloying in Zn: Significantly enhanced strengthening effect and corrosion uniformity. *International Journal Minerals, Metallurgy and Materials*, 2022, vol. 29, pp. 796–806. DOI: 10.1007/s12613-022-2468-6.
5. Mita K., Ikeda T., Maeda M. Phase diagram study of Fe–Zn intermetallics. *Journal of Phase Equilibria*, 2001, vol. 22, pp. 122–125. DOI: 10.1361/105497101770338978.
6. Su Yingchao, Fu Jiayin, Lee Wonsae, Du Shaokang, Qin Yi-Xian, Zheng Yufeng, Wang Yadong, Zhu Donghui. Improved mechanical, degradation, and biological perfomaces of Zn–Fe alloys as bioresorbable implants. *Bioactive Materials*, 2022, vol. 17, pp. 334–343. DOI: 10.1016/j.bioactmat.2021.12.030.
7. Shao Xiaoxi, Wang Xiang, Xu Fangfang et al. In vivo biocompatibility and degradability of a Zn–Mg–Fe alloy osteosynthesis system // Bioactive Materials. 2022. Vol. 7. P. 154–166. DOI: 10.1016/j.bioactmat.2021.05.012.
8. Mostaed E., Sikora-Jasinska M., Mostaed A., Loffredo S., Demir A.G., Previtali B., Mantovani D., Beanland R., Vedani M. Novel Zn-based alloys for biodegradable stent applications: Design, development and in vitro degradation // Journal of the Mechanical Behavior of Biomedical Materials. 2016. Vol. 60. P. 581–602. DOI: 10.1016/j.jmbbm.2016.03.018.
9. Vojtěch D., Kubásek J., Šerák J., Novák P. Mechanical and corrosion properties of newly developed biodegradable Zn-based alloys for bone fixation. *Acta Biomaterialia*, 2011, vol. 7, no. 9, pp. 3515–3522. DOI: 10.1016/j.actbio.2011.05.008.
10. Valiev R.Z., Islamgaliev R.K., Alexandrov I.V. Bulk nanostructured materials from severe plastic deformation. *Progress in Materials Science*, 2000, vol. 45, no. 2, pp. 103–189. DOI: 10.1016/S0079-6425(99)00007-9.
11. Li Baoping, Dong Anping, Zhu Guoliang, Chu Shuangjie, Qian Hongwei, Hu Chengjie, Sun Baode, Wang Jun. Investigation of the corrosion behaviors of continuously hot-dip galvanizing Zn–Mg coating. *Surface and Coatings Technology*, 2012, vol. 206, no. 19-20, pp. 3989–3999. DOI: 10.1016/j.surfcoat.2012.03.079.
12. Prosek T., Nazarov A., Bexell U., Thierry D., Serak J. Corrosion mechanism of model zinc–magnesium alloys in atmospheric conditions. *Corrosion Science*, 2008, vol. 50, no. 8, pp. 2216–2231. DOI: 10.1016/j.corsci.2008.06.008.
13. Xue Penghao, Ma Minglong, Li Yongjun, Li Xinggang, Yuan Jiawei, Shi Guoliang, Wang Kaikun, Zhang Kui. Microstructure, Hot Deformation Behavior, and Recrystallization Behavior of Zn–1Fe–1Mg Alloy under Isothermal Compression. *Materials*, 2021, vol. 14, no. 7, article number 1735. DOI: 10.3390/ma14071735.
14. Xue Penghao, Ma Minglong, Li Yongjun, Li Xinggang, Yuan Jiawei, Shi Guoliang, Wang Kaikun, Zhang Kui. Microstructure, Mechanical Properties, and In Vitro Corrosion Behavior of Biodegradable Zn–1Fe–xMg Alloy. *Materials*, 2020, vol. 13, no. 21, article number 4835. DOI: 10.3390/ma13214835.
15. Polenok M.V., Khafizova E.D., Islamgaliev R.K. The influence of severe plastic deformation on mechanical properties of pure zinc. *Frontier Materials & Technologies*, 2022, no. 3-2, pp. 25–31. DOI: 10.18323/2782-4039-2022-3-2-25-31.
16. Mostaed E., Sikora-Jasinska M., Drelich J.W., Vedani M. Zinc-based alloys for degradable vascular stent application. *Acta Biomaterialia*, 2018, vol. 71, pp. 1–23. DOI: 10.1016/j.actbio.2018.03.005.
17. Razumov I.K., Ermakov A.Y., Gornostyrev Yu.N., Straumal B.B. Nonequilibrium phase transformations in alloys under severe plastic deformation. *Physics-Uspekhi*, 2020, vol. 63, no. 8, pp. 733–757. DOI: DOI: 10.3367/UFNe.2019.10.038671.
18. Zhang Xiaoge Gregory. Corrosion potential and corrosion current. *Corrosion and Electrochemistry of Zinc*. Boston, Springer Publ., 1996, pp. 125–156. DOI: 10.1007/978-1-4757-9877-7_5.
19. Khudododova G.D., Kulyasova O.B., Islamgaliev R.K. Strength and corrosion resistance of the UFG Mg-Zn-Ca alloy. *Nanoindustriya*, 2022, vol. 15, no. 7-8, pp. 426–433. DOI: 10.22184/1993-8578.2022.15.7-8.426.433.
20. Byun Jong Min, Yu Jin Min, Kim Dae Kyung, Kim Tae Yeob, Jun Woo Sung, Kim Young Do. Corrosion Behavior of Mg_2Zn_{11} and $MgZn_2$ Single Phases. *Korean Journal of Metals and Materials*, 2013, vol. 51, no. 6, pp. 413–419. DOI: 10.3365/KJMM.2013.51.6.413.
21. Wątroba M., Mech K., Bednarczyk W., Kawałko J., Marciszko-Wiąckowska M., Marzec M., Shepherd D.E.T., Bała P. Long-term in vitro corrosion behavior of Zn–3Ag and Zn–3Ag–0.5Mg alloys considered for biodegradable implant applications. *Materials & Design*, 2022, vol. 213, article number 110289. DOI: 10.1016/j.matdes.2021.110289.

22. Bowen P.K., Shearier E.R., Shan Zhao, Guillory R.J., Feng Zhao, Goldman J., Drelich J.W. Biodegradable Metals for Cardiovascular Stents: from Clinical Concerns to Recent Zn-Alloys. *Advanced Healthcare Materials*, 2016, vol. 5, no. 10, pp. 1121–1140. DOI: 10.1002/adhm.201501019.
23. Shi Zhang-Zhi, Gao Xi-Xian, Chen Hong-Ting, Liu Xue-Feng, Li Ang, Zhang Hai-Jun, Wang Lu-Ning. Enhancement in mechanical and corrosion resistance properties of a biodegradable Zn–Fe alloy through second phase refinement. *Materials Science and Engineering: C*, 2020, vol. 116, article number 111197. DOI: 10.1016/j.msec.2020.111197.
24. Yan Zhaoming, Zhu Jiaxuan, Zhang Zhimin, Wang Qiang, Xue Yong. The microstructural, textural, and mechanical effects of high-pressure torsion processing on Mg alloys: A review. *Frontiers in Materials*, 2022, vol. 9, article number 964992. DOI: 10.3389/fmats.2022.964992.
25. Myagkikh P.N., Merson E.D., Poluyanov V.A., Merson D.L. The dependence of the biodegradable ZX10 alloy corrosion process on the structural factors and local pH level. *Frontier Materials & Technologies*, 2023, no. 2, pp. 59–76. DOI: 10.18323/2782-4039-2023-2-64-3.
26. Vinogradov A., Merson E., Myagkikh P., Linderov M., Brilevsky A., Merson D. Attaining High Functional Performance in Biodegradable Mg-Alloys: An Overview of Challenges and Prospects for the Mg–Zn–Ca System. *Materials*, 2023, vol. 16, no. 3, article number 1324. DOI: 10.3390/ma16031324.
27. Yao Caizhen, Wang Zichao, Tay See Leng, Zhu Tianping, Gao Wei. Effects of Mg on microstructure and corrosion properties of Zn–Mg alloy. *Journal of Alloys and Compounds*, 2014, vol. 602, pp. 101–107. DOI: 10.1016/j.jallcom.2014.03.025.

СПИСОК ЛИТЕРАТУРЫ

1. Kogan S., Sood A., Granick M.S. Zinc and Wound Healing: A Review of Zinc Physiology and Clinical Applications // Wounds. 2017. Vol. 29. № 4. P. 102–106.
2. Lin Mao, Li Shen, Jiahui Chen et al. A promising biodegradable magnesium alloy suitable for clinical vascular stent application // Scientific Reports. 2017. Vol. 7. Article number 46343. DOI: 10.1038/srep46343.
3. Yang Hongtao, Jia Bo, Zhang Zechuan, Qu Xinhua, Li Guannan, Lin Wenjiao, Zhu Donghui, Dai Kerong, Zheng Yufeng. Alloying design of biodegradable zinc as promising bone implants for load-bearing applications // Nature Communications. 2020. Vol. 11. Article number 401. DOI: 10.1038/s41467-019-14153-7.
4. Shi Zhangzhi, Li Changheng, Li Meng, Li Xiangmin, Wang Luning. Second phase refining induced optimization of Fe alloying in Zn: Significantly enhanced strengthening effect and corrosion uniformity // International Journal Minerals, Metallurgy and Materials. 2022. Vol. 29. P. 796–806. DOI: 10.1007/s12613-022-2468-6.
5. Mita K., Ikeda T., Maeda M. Phase diagram study of Fe–Zn intermetallics // Journal of Phase Equilibria. 2001. Vol. 22. P. 122–125. DOI: 10.1361/105497101770338978.
6. Su Yingchao, Fu Jiayin, Lee Wonsae, Du Shaokang, Qin Yi-Xian, Zheng Yufeng, Wang Yadong, Zhu Donghui. Improved mechanical, degradation, and biological perfomaces of Zn–Fe alloys as bioresorbable implants // Bioactive Materials. 2022. Vol. 17. P. 334–343. DOI: 10.1016/j.bioactmat.2021.12.030.
7. Shao Xiaoxi, Wang Xiang, Xu Fangfang et al. In vivo biocompatibility and degradability of a Zn–Mg–Fe alloy osteosynthesis system // Bioactive Materials. 2022. Vol. 7. P. 154–166. DOI: 10.1016/j.bioactmat.2021.05.012.
8. Mostaed E., Sikora-Jasinska M., Mostaed A., Loffredo S., Demir A.G., Previtali B., Mantovani D., Beanland R., Vedani M. Novel Zn-based alloys for biodegradable stent applications: Design, development and in vitro degradation // Journal of the Mechanical Behavior of Biomedical Materials. 2016. Vol. 60. P. 581–602. DOI: 10.1016/j.jmbbm.2016.03.018.
9. Vojtěch D., Kubásek J., Šerák J., Novák P. Mechanical and corrosion properties of newly developed biodegradable Zn-based alloys for bone fixation // Acta Biomaterialia. 2011. Vol. 7. № 9. P. 3515–3522. DOI: 10.1016/j.actbio.2011.05.008.
10. Valiev R.Z., Islamgaliev R.K., Alexandrov I.V. Bulk nanostructured materials from severe plastic deformation // Progress in Materials Science. 2000. Vol. 45. № 2. P. 103–189. DOI: 10.1016/S0079-6425(99)00007-9.
11. Li Baoping, Dong Anping, Zhu Guoliang, Chu Shuangjie, Qian Hongwei, Hu Chengjie, Sun Baode, Wang Jun. Investigation of the corrosion behaviors of continuously hot-dip galvanizing Zn–Mg coating // Surface and Coatings Technology. 2012. Vol. 206. № 19-20. P. 3989–3999. DOI: 10.1016/j.surfcoat.2012.03.079.
12. Prosek T., Nazarov A., Bexell U., Thierry D., Serak J. Corrosion mechanism of model zinc–magnesium alloys in atmospheric conditions // Corrosion Science. 2008. Vol. 50. № 8. P. 2216–2231. DOI: 10.1016/j.corsci.2008.06.008.
13. Xue Penghao, Ma Minglong, Li Yongjun, Li Xinggang, Yuan Jiawei, Shi Guoliang, Wang Kaikun, Zhang Kui. Microstructure, Hot Deformation Behavior, and Recrystallization Behavior of Zn–1Fe–1Mg Alloy under Isothermal Compression // Materials. 2021. Vol. 14. № 7. Article number 1735. DOI: 10.3390/ma14071735.
14. Xue Penghao, Ma Minglong, Li Yongjun, Li Xinggang, Yuan Jiawei, Shi Guoliang, Wang Kaikun, Zhang Kui. Microstructure, Mechanical Properties, and In Vitro Corrosion Behavior of Biodegradable Zn–1Fe–xMg Alloy // Materials. 2020. Vol. 13. № 21. Article number 4835. DOI: 10.3390/ma13214835.
15. Поленок М.В., Хафизова Э.Д., Исламгалиев Р.К. Влияние интенсивной пластической деформации на механические свойства чистого цинка // Frontier Materials & Technologies. 2022. № 3-2. С. 25–31. DOI: 10.18323/2782-4039-2022-3-2-25-31.
16. Mostaed E., Sikora-Jasinska M., Drelich J.W., Vedani M. Zinc-based alloys for degradable vascular stent application // Acta Biomaterialia. 2018. Vol. 71. P. 1–23. DOI: 10.1016/j.actbio.2018.03.005.
17. Разумов И.К., Ермаков А.Е., Горностырев Ю.Н., Страумал Б.Б. Неравновесные фазовые превращения в сплавах // Успехи физических наук. 2019. Т. 190. № 8. С. 785–810. DOI: 10.3367/UFNr.2019.10.038671.
18. Zhang Xiaoge Gregory. Corrosion potential and corrosion current // Corrosion and Electrochemistry of Zinc. Boston: Springer, 1996. P. 125–156. DOI: 10.1007/978-1-4757-9877-7_5.

19. Худододова Г.Д., Кулясова О.Б., Исламгалиев Р.К. Прочностные и коррозионные свойства УМЗ-сплава Mg–Zn–Ca // Наноиндустрия. 2022. Т. 15. № 7-8. С. 426–433. DOI: 10.22184/1993-8578.2022.15.7-8.426.433.
20. Byun Jong Min, Yu Jin Min, Kim Dae Kyung, Kim Tae Yeob, Jun Woo Sung, Kim Young Do. Corrosion Behavior of Mg_2Zn_{11} and $MgZn_2$ Single Phases // Korean Journal of Metals and Materials. 2013. Vol. 51. № 6. P. 413–419. DOI: 10.3365/KJMM.2013.51.6.413.
21. Wątroba M., Mech K., Bednarczyk W., Kawałko J., Marciszko-Wiąckowska M., Marzec M., Shepherd D.E.T., Bała P. Long-term in vitro corrosion behavior of Zn–3Ag and Zn–3Ag–0.5Mg alloys considered for biodegradable implant applications // Materials & Design. 2022. Vol. 213. Article number 110289. DOI: 10.1016/j.matdes.2021.110289.
22. Bowen P.K., Shearier E.R., Shan Zhao, Guillory R.J., Feng Zhao, Goldman J., Drelich J.W. Biodegradable Metals for Cardiovascular Stents: from Clinical Concerns to Recent Zn-Alloys // Advanced Healthcare Materials. 2016. Vol. 5. № 10. P. 1121–1140. DOI: 10.1002/adhm.201501019.
23. Shi Zhang-Zhi, Gao Xi-Xian, Chen Hong-Ting, Liu Xue-Feng, Li Ang, Zhang Hai-Jun, Wang Lu-Ning. Enhancement in mechanical and corrosion resistance properties of a biodegradable Zn–Fe alloy through second phase refinement // Materials Science and Engineering: C. 2020. Vol. 116. Article number 111197. DOI: 10.1016/j.msec.2020.111197.
24. Yan Zhaoming, Zhu Jiaxuan, Zhang Zhimin, Wang Qiang, Xue Yong. The microstructural, textural, and mechanical effects of high-pressure torsion processing on Mg alloys: A review // Frontiers in Materials. 2022. Vol. 9. Article number 964992. DOI: 10.3389/fmats.2022.964992.
25. Мягких П.Н., Мерсон Е.Д., Полуянов В.А., Мерсон Д.Л. Зависимость процесса коррозии биорезорбируемого сплава ZX10 от структурных факторов и локального уровня pH // Frontier Materials & Technologies. 2023. № 2. С. 59–76. DOI: 10.18323/2782-4039-2023-2-64-3.
26. Vinogradov A., Merson E., Myagkikh P., Linderov M., Brilevsky A., Merson D. Attaining High Functional Performance in Biodegradable Mg-Alloys: An Overview of Challenges and Prospects for the Mg–Zn–Ca System // Materials. 2023. Vol. 16. № 3. Article number 1324. DOI: 10.3390/ma16031324.
27. Yao Caizhen, Wang Zichao, Tay See Leng, Zhu Tianping, Gao Wei. Effects of Mg on microstructure and corrosion properties of Zn–Mg alloy // Journal of Alloys and Compounds. 2014. Vol. 602. P. 101–107. DOI: 10.1016/j.jallcom.2014.03.025.

Влияние интенсивной пластической деформации кручением на структуру и механические свойства цинкового сплава Zn–1%Fe–5%Mg

Абдрахманова Эльмира Дамировна[1], студент
Хафизова Эльвира Динифовна*[2], кандидат технических наук,
доцент кафедры материаловедения и физики металлов, старший научный сотрудник
научно-исследовательской лаборатории «Металлы и сплавы при экстремальных воздействиях»
Поленок Милена Владиславовна[3], студент
Нафиков Руслан Камилович[4], младший научный сотрудник
научно-исследовательской лаборатории «Металлы и сплавы при экстремальных воздействиях»
Корзникова Елена Александровна[5], доктор физико-математических наук, профессор,
профессор кафедры материаловедения и физики металлов,
заведующий научно-исследовательской лабораторией «Металлы и сплавы при экстремальных воздействиях»
Уфимский университет науки и технологий, Уфа (Россия)

***E-mail:** KhafizovaED@uust.ru,
ela.90@mail.ru

[1]ORCID: https://orcid.org/0009-0009-2775-7488
[2]ORCID: https://orcid.org/0000-0002-4618-412X
[3]ORCID: https://orcid.org/0000-0001-9774-1689
[4]ORCID: https://orcid.org/0000-0003-1280-6258
[5]ORCID: https://orcid.org/0000-0002-5975-4849

Поступила в редакцию 27.06.2023 *Принята к публикации 06.03.2024*

Аннотация: В настоящее время ведутся поиски новых материалов для временных имплантатов, способных растворяться в организме, что приводит к исчезновению потребности в повторной операции. В последнее десятилетие интерес ученых был сосредоточен на материалах на основе цинка, так как он, в отличие от других металлов, имеет подходящую скорость коррозии и хорошую биосовместимость. В работе описан эксперимент по изучению влияния деформации на микроструктуру, прочностные и коррозионные свойства сплава системы Zn–Fe–Mg. Проведен энергодисперсионный анализ и расчет объемной доли второй фазы цинкового сплава Zn–Fe–Mg. Гравиметрическим методом исследованы коррозионные свойства цинкового сплава Zn–Fe–Mg с разной микроструктурой (до и после интенсивной пластической деформации кручением) в условиях, имитирующих условия внутри живого организма (температура, состав коррозионной среды). В ходе испытаний определен механизм протекания коррозии, рассчитаны ее скорость и потеря массы образцов. Проведены исследования рельефа коррозионной поверхности методом растровой электронной микроскопии. Установлено, что разрушение материала в коррозионной среде происходит по матрице, содержащей активный металл Mg. Результаты расчетов скорости коррозии у исходного

и ИПДК-образцов отличались из-за более равномерного распределения частиц второй фазы во время интенсивной пластической деформации. В данной работе методом легирования цинка железом и магнием, а также применением интенсивной пластической деформации кручением получилось повысить микротвердость образцов до 239,6±8 HV, что является высоким показателем для цинковых сплавов.

Ключевые слова: цинковые сплавы; Zn–Fe–Mg; биодеградируемые имплантаты; интенсивная пластическая деформация кручением; биосовместимые материалы.

Благодарности: Исследования выполнены за счет средств гранта в области науки из бюджета Республики Башкортостан для государственной поддержки молодых ученых (НОЦ-ГМУ-2022, Соглашение № 1 от 13.12.2022).

Работа Корзниковой Е.А., Нафикова Р.К. выполнена при финансовой поддержке Министерства науки и высшего образования РФ в рамках государственного задания на оказание государственных услуг ФГБОУ ВО УУНиТ (соглашение № 075-03-2024-123/1) «Молодежная научно-исследовательская лаборатория НОЦ "Металлы и сплавы при экстремальных воздействиях"».

Исследовательская часть работы выполнена с использованием оборудования ЦКП «Нанотех» ФГБОУ ВО УУНиТ.

Статья подготовлена по материалам докладов участников XI Международной школы «Физическое материаловедение» (ШФМ-2023), Тольятти, 11–15 сентября 2023 года.

Для цитирования: Абдрахманова Э.Д., Хафизова Э.Д., Поленок М.В., Нафиков Р.К., Корзникова Е.А. Влияние интенсивной пластической деформации кручением на структуру и механические свойства цинкового сплава Zn–1%Fe–5%Mg // Frontier Materials & Technologies. 2024. № 2. С. 9–22. DOI: 10.18323/2782-4039-2024-2-68-1.

doi: 10.18323/2782-4039-2024-2-68-2

The influence of preliminary plasma treatment of the 09G2S steel surface on the formation of a coating as a result of hot galvanizing

***Olga S. Bondareva**[1], PhD (Engineering),
assistant professor of Chair of Metal Technology and Aviation Materials Science
Olga S. Dobychina, postgraduate student of Chair of Metal Technology and Aviation Materials Science
Leonid S. Kukankov, student
Yuliya N. Korotkova, student
Vitaly A. Tretyakov, student
Academician S.P. Korolev Samara National Research University, Samara (Russia)

***E-mail:** osbondareva@ssau.ru, osbond@yandex.ru

[1]ORCID: https://orcid.org/0000-0002-4273-2483

Received 27.06.2023 *Accepted 22.11.2023*

Abstract: In recent years, the range of silicon-containing steels subjected to hot galvanizing has been expanding. Alloying of steel with 0.5–1 % of silicon leads to the formation of a zinc coating of great thickness with a matte or multi-colored surface. This is associated with the changes in phase reactions between iron and zinc in the Fe–Zn–Si system. The development of ways to neutralize the negative influence of silicon on the formation of zinc coating is an urgent task. The purpose of the work is to study the influence of preliminary plasma cutting and plasma surface hardening of 09G2S (S355J2) steel on the thickness and structure of zinc coating formed on treated surfaces. It was found that after plasma cutting, the structure of the surface layer of steel is martensite, and after plasma surface hardening, it is martensite and ferrite. Analysis of the change in microhardness from the steel surface to the middle showed that the hardened layer depth is 400 μm. A zinc coating consisting of a δ-phase and a ζ-phase is formed on the surface of the steel without pretreatment. On the surface of the steel after plasma treatment, a zinc coating is formed characteristic of low-silicon steels and consisting of the δ-phase, ζ-phase, and η-phase. It was found that the thickness of the zinc coating on the surface after plasma cutting is two times less than on the untreated surface, and the reduction in the coating thickness occurs due to a decrease in the ζ-phase thickness. A hypothesis was suggested that the martensite formation on the steel surface leads to the disappearance of the ordered FeSi phase and changes the phase equilibrium in the Fe–Zn–Si system. Consequently, preliminary plasma treatment of the steel surface allows controlling the structure and thickness of the resulting zinc coating and is therefore recommended for introduction into the hot galvanizing process of silicon-containing steels.

Keywords: hot galvanizing; zinc coating; silicon-containing steels; Fe–Zn–Si; plasma treatment; surface hardening.

For citation: Bondareva O.S., Dobychina O.S., Kukankov L.S., Korotkova Yu.N., Tretyakov V.A. The influence of preliminary plasma treatment of the 09G2S steel surface on the formation of a coating as a result of hot galvanizing. *Frontier Materials & Technologies*, 2024, no. 2, pp. 23–31. DOI: 10.18323/2782-4039-2024-2-68-2.

INTRODUCTION

For the last two decades, an expansion in the range of steels subjected to hot galvanizing have been seen. It is associated with the need in the construction, and automotive industries for modern advanced high-strength steels (AHSS), including press hardening steel (PHS), austenitic plastic steels (Transformation Induced Plasticity, TRIP steels), dual-phase steels (DP steels), complex phase steels (CP steels), martensitic steels (MS), cold-deformable steels, etc. The unique complex of properties of these steels is high structural strength, low weight, and the ability to self-adapt to extreme external influences, which are ensured by thermomechanical processing, and an alloying system. Silicon is one of the main alloying elements that stabilize austenite [1; 2]. Silicon is also a cheap reinforcer of structural steels widely used for welded building structures, including 09G2S (S355J2) steel [3]. However, a high silicon content (more than 0.4 %) promotes the formation of a zinc coating of large thickness, 200–500 μm, on steel [4]. Such a thickness of the zinc coating leads to excessive consumption of zinc raw materials, and in some cases, to coating peeling, which is unacceptable. It has been found that this is associated with the influence of silicon on the processes of mutual diffusion of iron and zinc, during the coating formation [5–7].

It is known that zinc coatings produced by immersing steel in a melt, have in their structure, layers of intermetallic phases of the Fe–Zn system: δ, ζ, and η. These phases are well studied; they differ in structure, chemical composition and crystal lattice. The δ-phase layer is adjacent to the steel substrate, its thickness is uniform, and its structure is relatively compact. The next layer of the ζ-phase has a branched dendritic structure; the crystallites are elongated in the direction of heat removal from the base to the coating surface. When removing the product from the bath, almost pure zinc is formed on the surface – the η-phase [8].

When galvanizing steels with a silicon content of more than 0.4 %, the η-phase is absent, and the morphology of the ζ-phase changes, it becomes coarse-crystalline, and makes up about 90 % of the total coating thickness. In this case, the ζ-phase reaches the surface of the coating, giving it a matte appearance [9].

One of the options for controlling the growth of the zinc coating thickness is to control the galvanizing temperature, since it has a decisive influence on the coating thickness, structure, and phase composition [10]. The technology of high-temperature galvanizing (530–590 °C) is known, which makes it possible to produce coatings consisting mainly of the δ-phase – the densest phase providing a minimum coating thickness, including on silicon steels [11]. However, this technology requires the use of ceramic baths, since the steel ones have a shorter service life, and energy costs increase.

Another way to neutralize the negative influence of silicon on the galvanizing process, is to remove it from the steel surface by a special chemical pre-treatment, before hot galvanizing. It includes etching steel in complex solutions containing hydrofluoric and hydrochloric acids or ammonium, and sodium fluorides in various concentrations [12]. The disadvantage of this technology is the difficulty of recycling etching solutions.

Systems for alloying zinc melt with nickel, aluminum, bismuth, and tin have been developed, and implemented to control the structure, thickness and properties of coatings on silicon-containing steels [13]. For steels with a silicon content of up to 0.3 %, the application of zinc melt with nickel microadditives (0.05 %) has proven to be successful [14]. However, with a silicon content of more than 0.3 %, it was not possible to achieve a significant reduction in the coating thickness.

Before hot galvanizing, it is possible to apply preliminary metal coatings, such as iron, nickel, copper and/or their alloys, which form a diffusion barrier and prevent the formation of coating defects [15; 16].

The authors of this work found, that on the surfaces of steel parts after plasma and laser cutting, the coating thickness is significantly less than on other surfaces. Preliminary studies have shown that the insufficient thickness of the zinc coating on surfaces after plasma and laser cutting, depends not on surface defects, and the presence of scale, but on structural changes in the heat-affected zone. As a result of the impact of the torch during plasma cutting, the metal melts and quickly cools due to heat removal deep into the metal, therefore the near-surface structure is characterized by the presence of a martensitic component [17]. By plasma surface hardening, it is possible to obtain a surface martensitic layer both in the cut zone and on any machined surface [18]. The essence of the surface plasma hardening method is the rapid heating of the surface, by plasma jet exposure, and subsequent rapid cooling by removing heat into the bulk metal, which remains cold. Therefore, it is important to study in detail the influence of structural changes during plasma treatment of steel, on the formation of a zinc coating in order to develop new methods for controlling the zinc coating thickness.

The purpose of this research is to study the influence of preliminary plasma cutting and plasma surface hardening of 09G2S (S355J2) steel, on the zinc coating thickness and structure.

METHODS

For the study, samples of industrial hot-rolled 09G2S (S355J2) steel sheet in accordance with GOST 5520-79 with dimensions of 100×100×25 mm were selected. The chemical composition of the samples is determined on a Foundry-Master XPR optical emission analyzer and is shown in Table 1.

Samples were cut using a HyPerfomance 400 XD plasma cutter. Surface hardening of the samples was carried out using a UDGZ-200 manual plasma-hardening machine. The principle of its operation, is that the plasma flow heats the surface of the product very quickly, and due to heat removal from the surface into the depth of the product, the surface layer with a thickness of 1–2 mm is hardened. Hardening occurs in air without forced cooling with water or oil. The distance from the plasmatron to the surface of the product was 20 mm, the hardening current was 200 A, and the productivity was 110 cm/min.

Sections for studying the microstructure were made on a Remet LS 2 grinding and polishing machine. After hardening, the hardness of the samples was measured on a NOVOTEST TS-BRV stationary hardness tester using the Rockwell scale; measurements were taken from the machined side, and from the ends. The microstructure of the samples was studied using a Carl Zeiss Axio Vert 40 MAT digital trinocular inverted microscope. Then the samples were subjected to hot galvanizing, which included the following stages: degreasing in 20 % NaOH, etching in 10 % HCl, fluxing in $ZnCl_2$–NH_4Cl, drying, and immersion in zinc melt at a temperature of 450±3 °C; the time of holding in the melt is 2 min.

Microstructure studies and thickness measurements of the coating phase layers were carried out using a TESCAN VEGA SB scanning electron microscope. The microhardness of the subsurface layer of the samples was measured using a PMT-3 microhardness tester with a load of 20 g. It is important to note that the key factor in the formation of the structure, and properties of the heat-affected zone is the cooling rate. In our study, cooling occurred in air, which influenced the nature of the change in the microstructure. Air was chosen as a coolant, considering that the heating depth during surface hardening is small, so the heat is transferred into the sample thickness.

RESULTS

As a result of the analysis of the cross section of the sample after plasma hardening and the sample after plasma cutting, images of the microstructure were obtained, which are shown in Fig. 1 and 2.

In the microstructure of the sample after surface hardening (Fig. 1 a), a clear boundary between the surface structure, and the middle is visible – this is the depth of thermal influence, it amounts to about 950 μm. The near-surface layer is heterogeneous and has an incompletely hardened structure – martensite and ferrite (Fig. 1 b). The depth of the hardened layer is about 300 microns. The transition layer is represented in the form of a ferrite-pearlite structure (Fig. 1 c).

Table 1. *Chemical composition of 09G2S steel, %*
Таблица 1. *Химический состав стали 09Г2С, %*

Fe	C	Si	Mn	Ni	Cr	V	Cu
Base	0.137	0.608	1.670	0.015	0.038	0.012	0.009

In the microstructure of the sample, after plasma cutting (Fig. 2 a), there is a clear boundary between the surface structure, and the middle, the depth of thermal influence is about 600 μm. The near-surface layer is acicular martensite (Fig. 2 b). The hardened layer thickness is about 200 μm.

The depth of the hardened zone can be determined more accurately by analyzing the change in hardness, from the edge of the surface into the depth of the sample. Analysis of the graphs (Fig. 3) shows that hardness decreases from the edge to the middle. After plasma hardening, the hardness is uneven (martensite + ferrite). The maximum hardness value at the surface edge is 153 HV (martensite grain); the minimum hardness value is 123 HV (ferrite). A noticeable decrease in hardness occurs after a depth of 400 μm. The maximum value of steel hardness after plasma cutting at the edge of the surface was 173 HV. At a distance of 300–400 μm from the surface edge, the hardness decreases sharply and corresponds to the hardness of ferrite, i. e. this is the depth of the hardened zone.

The zinc coating on the samples without treatment has matte and multi-colored spots (Fig. 4 a), while on the sample after plasma treatment, the coating had a glossy shine (Fig. 4 b).

Studies of the zinc coating microstructure, obtained on surfaces without treatment and after plasma cutting and hardening (Fig. 5), showed that the phase structures of the coatings are different. On the surface without treatment, a zinc coating is formed, which has a structure characteristic

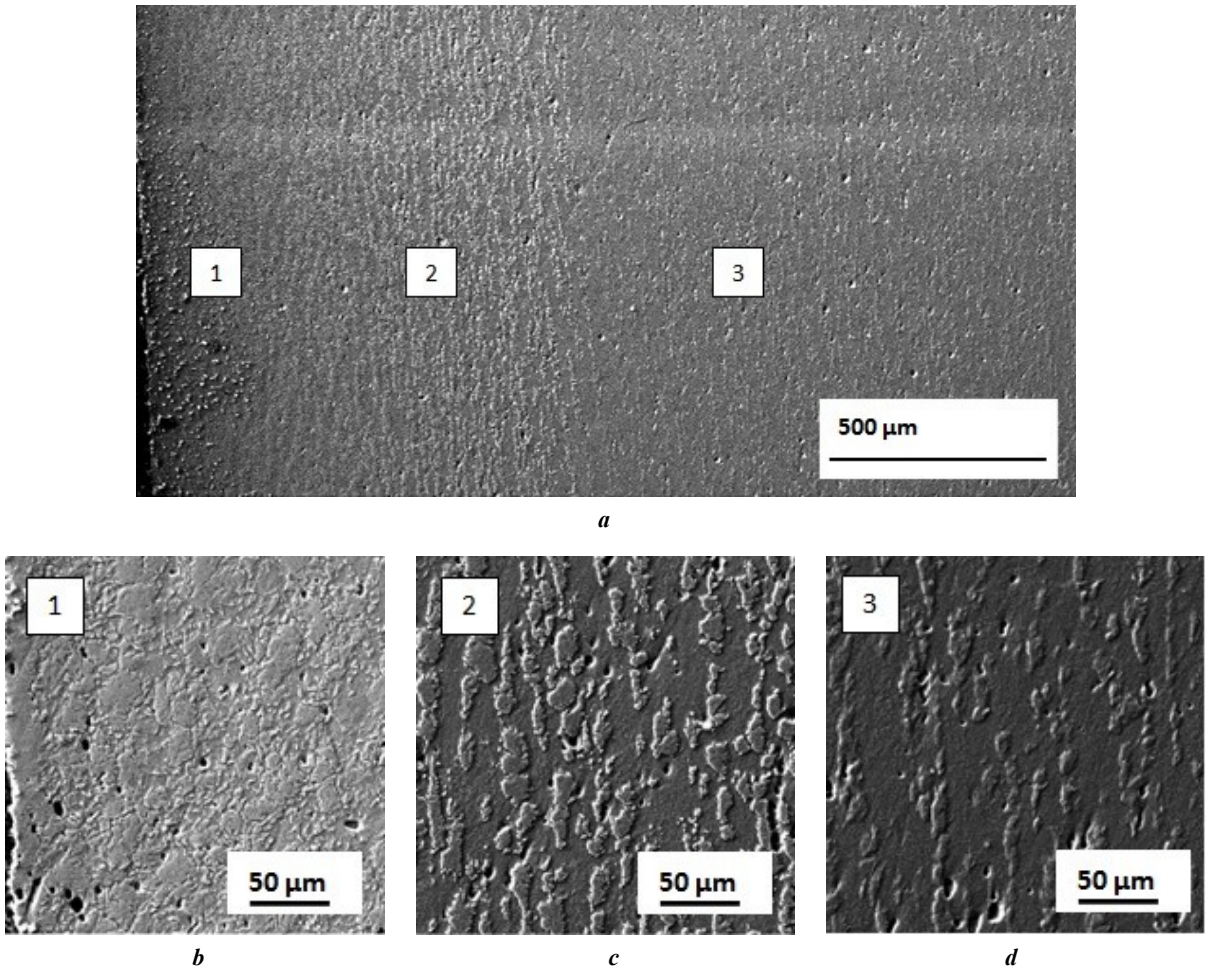

a ***b*** ***c*** ***d***

Fig. 1. *Microstructure of the sample after plasma hardening:*
a *– general view, ×100;* ***b*** *– surface layer, ×1000;* ***c*** *– transition layer, ×1000;* ***d*** *– middle, ×1000*
Рис. 1. *Микроструктура образца после плазменной закалки:*
а *– общий вид, ×100;* ***b*** *– поверхностный слой, ×1000;* ***c*** *– переходный слой, ×1000;* ***d*** *– середина, ×1000*

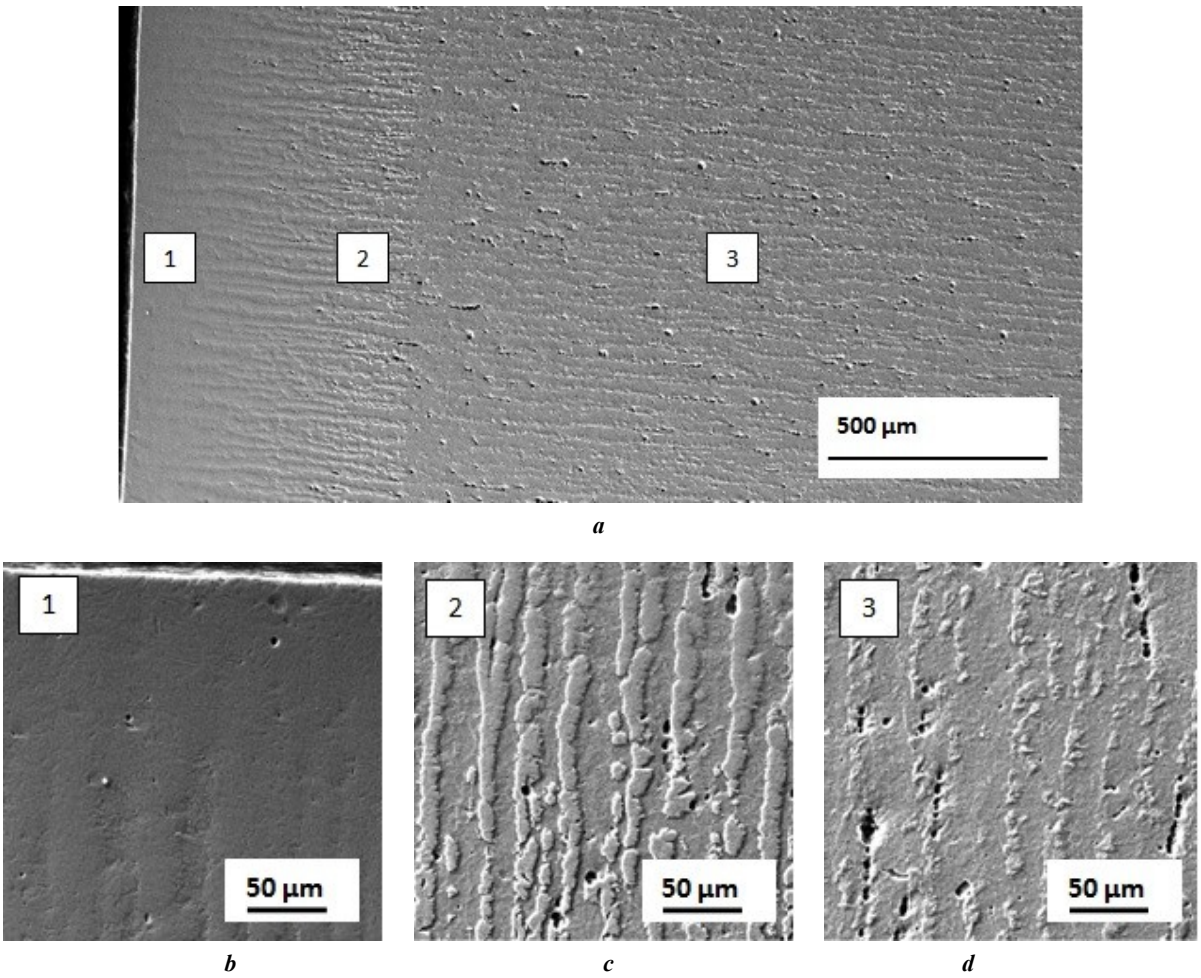

Fig. 2. *Microstructure of the sample after plasma cutting:*
a *– general view, ×100;* ***b*** *– surface layer, ×1000;* ***c*** *– transition layer, ×1000;* ***d*** *– middle, ×1000*
Рис. 2. *Микроструктура образца после плазменной резки:*
a *– общий вид, ×100;* ***b*** *– поверхностный слой, ×1000;* ***c*** *– переходный слой, ×1000;* ***d*** *– середина, ×1000*

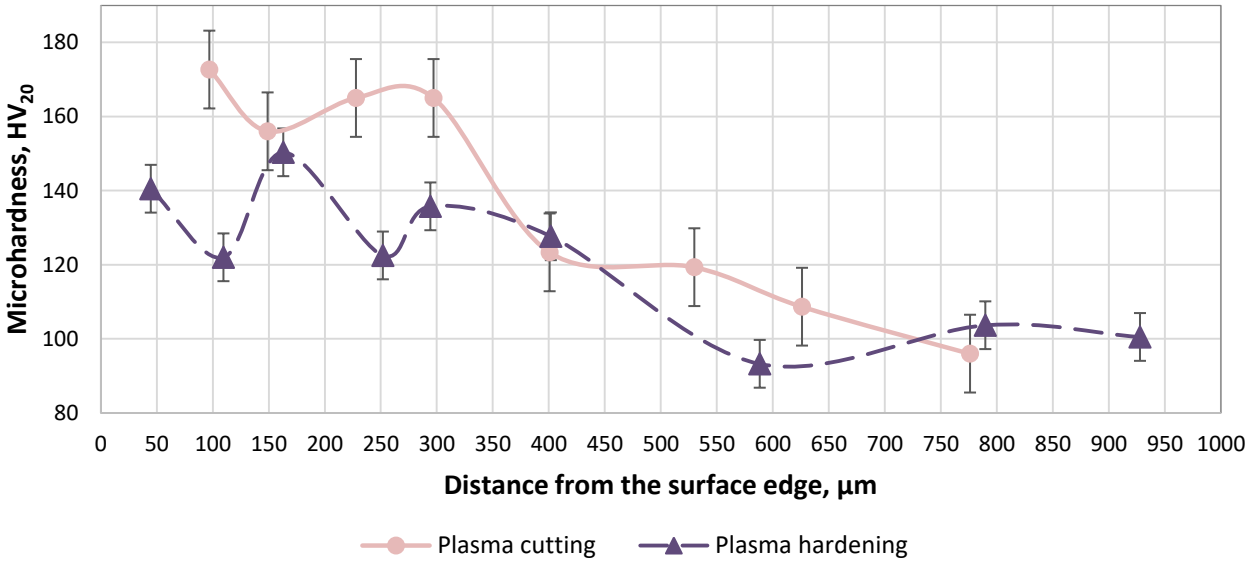

Fig. 3. *Change in microhardness from the edge of the treated surface to the middle*
Рис. 3. *Изменение микротвердости от края обработанной поверхности к середине*

for a coating on high-silicon steel: 80–90 % of the ζ-phase and a thin δ-phase layer, the η-phase is absent, which leads to a matte and multi-shaded coating surface (Fig. 5 a). After plasma treatment, all three main phases are observed in the microstructure of the zinc coating: the δ-phase is dense, columnar, the dendritic ζ-phase, and the η-phase is the coating zinc, which provides a glossy surface of the coating (Fig. 5 b, 5 c). This coating is typical for low-silicon steels. The thickness of the ζ-phase in the coating on the surface after plasma cutting is 30 % of the total coating thickness, and on the surface after plasma hardening – 50 % of the total coating thickness.

The analysis of the influence of preliminary plasma treatment, on the hardness of the sample surface, and the thickness of the forming zinc coating (Fig. 6), showed that the untreated sample with a ferrite-pearlite surface structure has the lowest hardness, and the greatest coating thickness, on average about 122 μm. After plasma hardening, the hardness of the ferrite-martensitic structure of the surface increased, and the thickness of the coating decreased by 29 % and amounted to about 87 μm. After plasma cutting, the hardness of the surface martensitic structure is maximum; the coating thickness decreased by 55 % relative to the untreated sample, and amounted to about 55 μm.

DISCUSSION

According to the Fe–Si equilibrium phase diagram, at low concentrations of silicon in iron, there are regions of the α-phase, which is a disordered solid solution of the substitution of iron by silicon in the body-centered cubic (bcc) lattice, and two ordered α1 (Fe_3Si) and α2 (FeSi) phases [19].

When silicon-containing steel, interacts with molten zinc, phase reactions are described by the Fe–Zn–Si ternary system. Researchers [20] showed that silicon present in steel in an amount of 0.5–1 %, forms the FeSi phase and shifts the equilibrium to the three-phase region: ζ-$FeZn_{13}$ – FeSi – liquid Zn. The presence of the liquid phase accelerates the growth of the ζ-$FeZn_{13}$ intermetallic layer.

As a result of the studies, it was found that the thickness and structure of the zinc coating, formed on 09G2S high-silicon steel, depends on the near-surface structure of the steel. If the structure is equilibrium, ferrite-pearlite, as in samples without heat treatment, then a thick zinc coating is formed with a well-developed ζ-phase, which is characteristic of high-silicon steel.

If the surface structure of the steel is martensite or martensite + ferrite, then the ζ-phase thickness decreases by 2 times, and a surface η-phase appears in the coating structure, which is typical for low-silicon steel. In this case, the near-surface structure of complete hardening (martensite), inhibits the growth of the coating ζ-phase more strongly than the incomplete hardening structure (martensite + ferrite).

One can assume that the martensite formation leads to the disappearance of the ordered FeSi phase. The martensite crystal lattice is greatly distorted compared to the ferrite lattice, and instead of cubic, it takes on a tetragonal shape. In the absence of the FeSi phase, the formation of a zinc coating occurs according to the Fe–Zn binary system, and phases specific to low-silicon steels are observed in the coating. It can be considered that the near-surface martensitic structure, is a diffusion barrier for silicon located in the steel, and influencing the formation and morphology of the zinc coating ζ-phase.

Thus, preliminary plasma treatment of the surface allows controlling the structure, and thickness of the zinc coating formed on this surface. In further research, it is planned to find the time of immersion of steel in the melt, during which the effect of the martensitic layer as a diffusion barrier is retained.

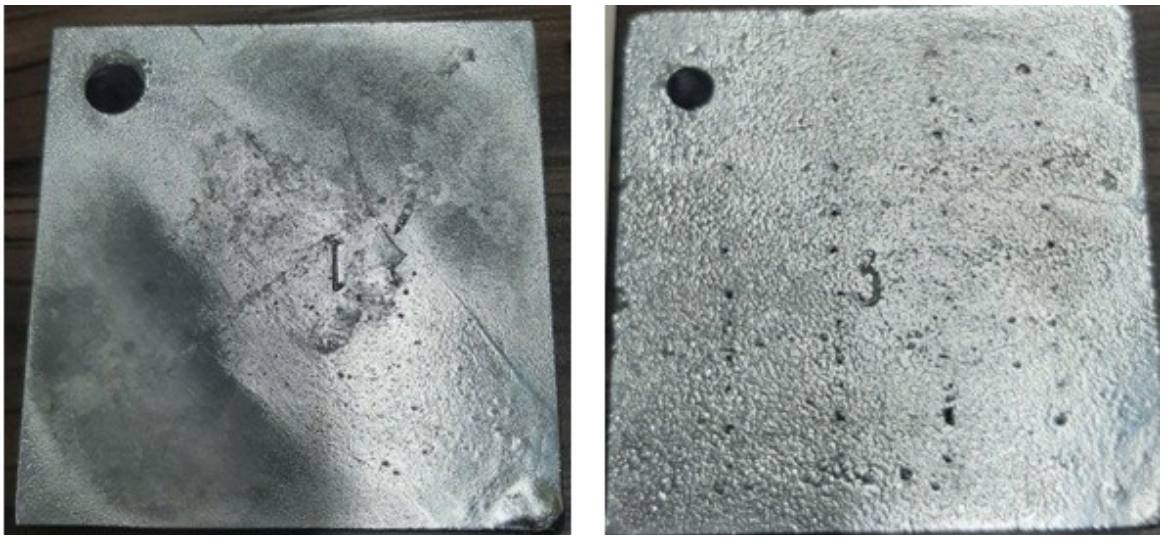

a ***b***

Fig. 4. *Coating surface after hot galvanizing:*
a *– without treatment;* ***b*** *– after plasma hardening*
Рис. 4. *Поверхность покрытия после горячего цинкования:*
a *– без обработки;* ***b*** *– после плазменной закалки*

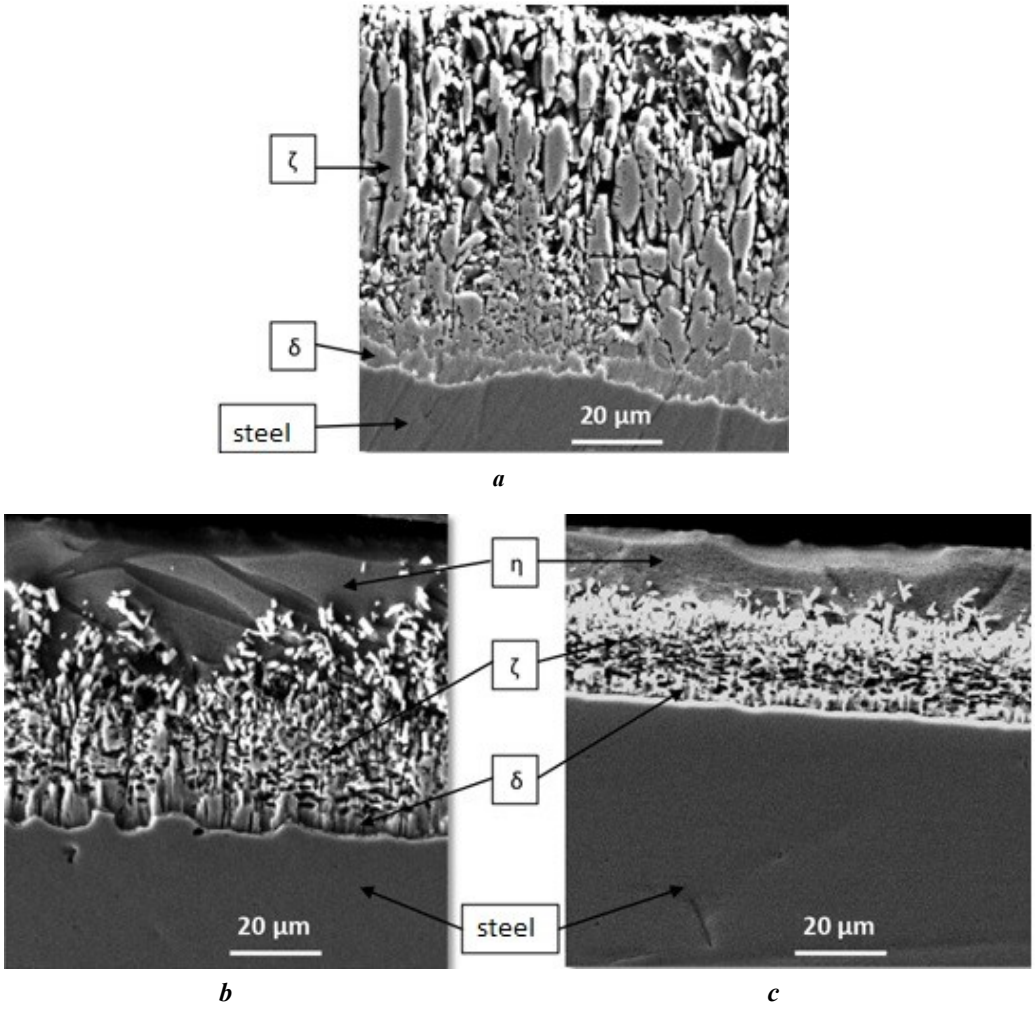

Fig. 5. *Microstructure of the sample zinc coating, ×2000:*
a *– without treatment;* ***b*** *– after plasma hardening;* ***c*** *– after plasma cutting*
Рис. 5. *Микроструктура цинкового покрытия образца, ×2000:*
a *– без обработки;* ***b*** *– после плазменной закалки;* ***c*** *– после плазменной резки*

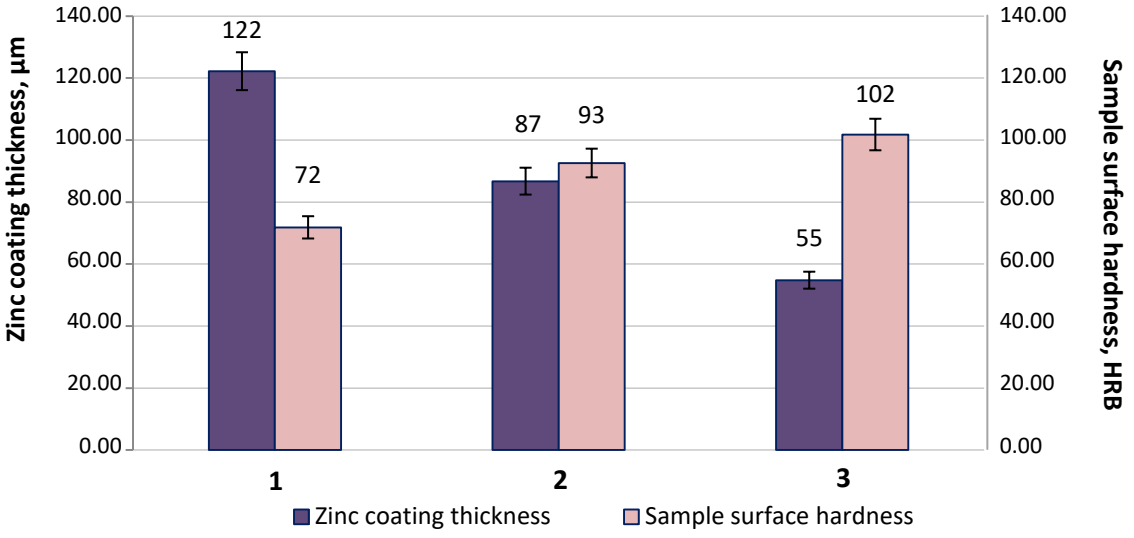

Fig. 6. *Diagram of the influence of treatment on the coating thickness and base hardness:*
1 – without treatment; 2 – plasma hardening; 3 – plasma cutting
Рис. 6. *Диаграмма влияния обработки на толщину покрытия и твердость основы:*
1 – без обработки; 2 – плазменная закалка; 3 – плазменная резка

CONCLUSIONS

The structure of individual sections of the heat-affected zone was determined, and their microstructure was studied. A completely hardened structure (martensite) was found on the surface after plasma cutting; an incompletely hardened structure (ferrite and martensite) was found on the surface after plasma hardening.

The maximum hardness of the sample surface after plasma cutting is 172 HV (increased by 42 %), and after plasma surface hardening – 153 HV (increased by 29 %). The hardened zone depth is 400 μm.

After plasma treatment, a coating with the pure zinc η-phase is formed on the surface, which gives the coating a glossy shine. The thickness of the zinc coating on the surface after plasma hardening is 29 % less, and on the surface after plasma cutting is 55 % less than on the untreated surface. The reduction in coating thickness occurs due to a decrease in the ζ-phase thickness.

A hypothesis was suggested, that the martensite formation on the steel surface leads to the ordered FeSi phase disappearance, and changes the phase equilibrium in the Fe–Zn–Si system. The zinc coating is formed according to the Fe–Zn binary system. Thus, the hardened layer serves as a diffusion barrier during the formation of the iron-zinc coating layers.

Preliminary plasma treatment of the 09G2S steel surface, leads to a reduction in the zinc consumption for the formation of a protective coating, and the formation of a glossy surface, therefore, the authors recommend to implement this method in the process of hot galvanizing of this steel grade.

REFERENCES

1. Gorlenko D.A., Konstantinov D.V., Polyakova M.A., Dabalá M. TRIP steels: the features of chemical composition and structure, prospects of application (overview). *CIS Iron and Steel Review*, 2022, vol. 23, pp. 67–75. DOI: 10.17580/cisisr.2022.01.13.
2. Min Sun, Packer J.A. Hot-dip galvanizing of cold-formed steel hollow sections: a state-of-the-art review. *Frontiers of Structural and Civil Engineering*, 2019, vol. 13, pp. 49–65. DOI: 10.1007/s11709-017-0448-0.
3. Arabaci U., Özdemir U. Effect of Filler Wire Composition on Hot-Dip Galvanizing Performance of S355JR Structural Steel Joints. *Transactions of the Indian Institute of Metals*, 2023, vol. 76, pp. 1583–1591. DOI: 10.1007/s12666-023-02878-5.
4. Bondareva O.S., Melnikov A.A. Effect of the silicon content in structural steels on the structure and growth rate of the zinc coating. *Izvestiya of Samara Scientific Center of the Russian Academy of Sciences*, 2017, vol. 19, no. 1-3, pp. 506–510. EDN: YPKJJJ.
5. Inoue J., Miwa S., Koseki T. Effect of Si content in steel on formation of Fe-Zn intermetallic compound layer at pure Zn melt/steel interface. *Tetsu-To-Hagane/Journal of the Iron and Steel Institute of Japan*, 2014, vol. 100, no. 3, pp. 390–396. DOI: 10.2355/tetsutohagane.100.390.
6. Han Seung-Chang, Sanchez D.F., Grolimund D., Uhm Sang-Ho, Choi Du-Youl, Jeong Hong-Chul, Jun Tea-Sung. Role of silicon on formation and growth of intermetallic phases during rapid Fe–Zn alloying reaction. *Materials Today Advances*, 2023, vol. 18, article number 100368. DOI: 10.1016/j.mtadv.2023.100368.
7. Minenkov A., Mörtlbauer T., Arndt M., Hesser G., Angeli G., Groiss H., Towards a dependable TEM characterization of hot-dip galvanized steels with low and high Si content. *Materials & Design*, 2023, vol. 227, article number 111684. DOI: 10.1016/j.matdes.2023.111684.
8. Marder A.R., Goodwin F.E. *The Metallurgy of Zinc Coated Steels*. Amsterdam, Elsevier Inc. Publ., 2023. 590 p. DOI: 10.1016/C2020-0-04502-0.
9. Marder A.R., Goodwin F.E. Chapter 15 – General galvanizing. *The Metallurgy of Zinc Coated Steels*. Amsterdam, Elsevier Inc. Publ., 2023, pp. 543–566. DOI: 10.1016/B978-0-323-99984-7.00020-8.
10. Bondareva O.S., Melnikov A.A. Influence of the temperature of a zinc melt on the coating thickness and structure during high-temperature zincplating steels with a high silicon content. *Powder Metallurgy and Functional Coatings*, 2015, no. 1, pp. 66–70. DOI: 10.17073/1997-308X-2015-1-66-70.
11. Verma A.R.B., Van Ooij W.J. High-temperature batch hot-dip galvanizing. Part 1. General description of coatings formed at 560 °C. *Surface and Coatings Technology*, 1997, vol. 89, no. 1-2, pp. 132–142. DOI: 10.1016/S0257-8972(96)02941-6.
12. Schmitz T. *Silicon-containing steel sheet chemical pretreatment prior to hot coating used in automobile structural part production involves degreasing and submersing in pickling bath containing fluorine ions to remove silicon from steel surface,* patent FR no. 9900126, 2002, 15 p.
13. Kania H., Mendala J., Kozuba J., Saternus M. Development of Bath Chemical Composition for Batch Hot-Dip Galvanizing-A Review. *Materials (Basel)*, 2020, vol. 13, no. 18, article number 4168. DOI: 10.3390/ma13184168.
14. He Z.-R., He Y., Zhang Y.-H., Liu J.-T., Xie K. Comparative on microstructure and properties of Zn and Zn–0.05Ni alloy coatings by hot-dip galvanizing. *Cailial Rechuli Xuebao/Transactions of Materials and Heat Treatment*, 2013, vol. 34, no. 2, pp. 152–156.
15. Chakraborty A., Ghosh R., Sudan M., Mondal A. Improvement in hot dip galvanized coating microstructure and properties by pre-metallic deposition on steel surface: A comprehensive review. *Surface and Coatings Technology*, 2022, vol. 449, article number 128972. DOI: 10.1016/j.surfcoat.2022.128972.
16. Che Chunshan, Lu Jintang, Kong Gang, Xu Qiaoyu. Role of silicon in steels on galvanized coatings. *Acta Metallurgica Sinica (English Letters)*, 2009, vol. 22, no. 2, pp. 138–145. DOI: 10.1016/s1006-7191(08)60081-2.
17. Toktar A.B., Ädilbekov K.E., Serikov S.E., Kombaev K.K. The influence of plasma cutting modes on the edge properties of 09G2S steel. *Bulletin of D. Serikbayev East Kazakhstan Technical University*, 2019, no. 4, pp. 160–170. EDN: VCTRBV.
18. Samotugin S.S., Gagarin V.A., Mazur V.A., Nesterov O.Yu. Metallographic examination of hardened layers after surface treatments by highly concentrated plasma jet. *Vestnik Priazovskogo gosudarstvennogo tekhnicheskogo universiteta. Seriya: Tekhnicheskie nauki*, 2017, no. 34, pp. 98–105. EDN: YLVILS.

19. Ershov N.V., Lukshina V.A., Chernenkov Y.P., Fedorov V.I. Structure of α-FeSi alloys with 8 and 10 at % silicon. *Physics of the Solid State*, 2012, vol. 54, no. 9, pp. 1935–1942. DOI: 10.1134/S1063783412090107.
20. Takata N., Hayano K., Suzki A., Kobashi M. Enhanced Interfacial Reaction of Fe–Si Alloy Sheets Hot-Dipped in Zn Melt at 460°C. *ISIJ International*, 2018, vol. 58, no. 9, pp. 1608–1615. DOI: 10.2355/isijinternational.ISIJINT-2018-036.

СПИСОК ЛИТЕРАТУРЫ

1. Gorlenko D.A., Konstantinov D.V., Polyakova M.A., Dabalá M. TRIP steels: the features of chemical composition and structure, prospects of application (overview) // CIS Iron and Steel Review. 2022. Vol. 23. P. 67–75. DOI: 10.17580/cisisr.2022.01.13.
2. Min Sun, Packer J.A. Hot-dip galvanizing of cold-formed steel hollow sections: a state-of-the-art review // Frontiers of Structural and Civil Engineering. 2019. Vol. 13. P. 49–65. DOI: 10.1007/s11709-017-0448-0.
3. Arabaci U., Özdemir U. Effect of Filler Wire Composition on Hot-Dip Galvanizing Performance of S355JR Structural Steel Joints // Transactions of the Indian Institute of Metals. 2023. Vol. 76. P. 1583–1591. DOI: 10.1007/s12666-023-02878-5.
4. Бондарева О.С., Мельников А.А. Влияние содержания кремния в конструкционных сталях на строение и скорость роста цинкового покрытия // Известия Самарского научного центра Российской академии наук. 2017. Т. 19. № 1-3. С. 506–510. EDN: YPKJJJ.
5. Inoue J., Miwa S., Koseki T. Effect of Si content in steel on formation of Fe–Zn intermetallic compound layer at pure Zn melt/steel interface // Tetsu-To-Hagane/Journal of the Iron and Steel Institute of Japan. 2014. Vol. 100. № 3. P. 390–396. DOI: 10.2355/tetsutohagane.100.390.
6. Han Seung-Chang, Sanchez D.F., Grolimund D., Uhm Sang-Ho, Choi Du-Youl, Jeong Hong-Chul, Jun Tea-Sung. Role of silicon on formation and growth of intermetallic phases during rapid Fe–Zn alloying reaction // Materials Today Advances. 2023. Vol. 18. Article number 100368. DOI: 10.1016/j.mtadv.2023.100368.
7. Minenkov A., Mörtlbauer T., Arndt M., Hesser G., Angeli G., Groiss H., Towards a dependable TEM characterization of hot-dip galvanized steels with low and high Si content // Materials & Design. 2023. Vol. 227. Article number 111684. DOI: 10.1016/j.matdes.2023.111684.
8. Marder A.R., Goodwin F.E. The Metallurgy of Zinc Coated Steels. Amsterdam: Elsevier Inc., 2023. 590 p. DOI: 10.1016/C2020-0-04502-0.
9. Marder A.R., Goodwin F.E. Chapter 15 – General galvanizing // The Metallurgy of Zinc Coated Steels. Amsterdam: Elsevier Inc., 2023. P. 543–566. DOI: 10.1016/B978-0-323-99984-7.00020-8.
10. Бондарева О.С., Мельников А.А. Влияние температуры цинкового расплава на толщину и структуру покрытия при высокотемпературном горячем цинковании сталей с высоким содержанием кремния // Известия высших учебных заведений. Порошковая металлургия и функциональные покрытия. 2015. № 1. С. 66–70. DOI: 10.17073/1997-308X-2015-1-66-70.
11. Verma A.R.B., Van Ooij W.J. High-temperature batch hot-dip galvanizing. Part 1. General description of coatings formed at 560 °C // Surface and Coatings Technology. 1997. Vol. 89. № 1-2. P. 132–142. DOI: 10.1016/S0257-8972(96)02941-6.
12. Schmitz T. Silicon-containing steel sheet chemical pretreatment prior to hot coating used in automobile structural part production involves degreasing and submersing in pickling bath containing fluorine ions to remove silicon from steel surface: patent FR № 9900126, 2002. 15 p.
13. Kania H., Mendala J., Kozuba J., Saternus M. Development of Bath Chemical Composition for Batch Hot-Dip Galvanizing-A Review // Materials (Basel). 2020. Vol. 13. № 18. Article number 4168. DOI: 10.3390/ma13184168.
14. He Z.-R., He Y., Zhang Y.-H., Liu J.-T., Xie K. Comparative on microstructure and properties of Zn and Zn–0.05Ni alloy coatings by hot-dip galvanizing // Cailial Rechuli Xuebao/Transactions of Materials and Heat Treatment. 2013. Vol. 34. № 2. P. 152–156.
15. Chakraborty A., Ghosh R., Sudan M., Mondal A. Improvement in hot dip galvanized coating microstructure and properties by pre-metallic deposition on steel surface: A comprehensive review // Surface and Coatings Technology. 2022. Vol. 449. Article number 128972. DOI: 10.1016/j.surfcoat.2022.128972.
16. Che Chunshan, Lu Jintang, Kong Gang, Xu Qiaoyu. Role of silicon in steels on galvanized coatings // Acta Metallurgica Sinica (English Letters). 2009. Vol. 22. № 2. P. 138–145. DOI: 10.1016/s1006-7191(08)60081-2.
17. Тоқтар А.Б., Әділбеков К.Е., Серіков С.Е., Комбаев К.К. Влияние режимов плазменной резки на свойства кромки стали марки 09Г2С // Вестник Восточно-Казахстанского государственного технического университета им. Д. Серикбаева. 2019. № 4. С. 160–170. EDN: VCTRBV.
18. Самотугин С.С., Гагарин В.А., Мазур В.А., Нестеров О.Ю. Металлографические исследования упрочненных слоев после поверхностной обработки высококонцентрированной плазменной струей // Вестник Приазовского государственного технического университета. Серия: Технические науки. 2017. № 34. С. 98–105. EDN: YLVILS.
19. Ершов Н.В., Черненков Ю.П., Лукшина В.А., Федоров В.И. Структура сплавов alpha-FeSi с 8 и 10 ат. % кремния // Физика твердого тела. 2012. Т. 54. № 9. С. 1813–1819. EDN: RCSSDL.
20. Takata N., Hayano K., Suzki A., Kobashi M. Enhanced Interfacial Reaction of Fe–Si Alloy Sheets Hot-Dipped in Zn Melt at 460°C // ISIJ International. 2018. Vol. 58. № 9. P. 1608–1615. DOI: 10.2355/isijinternational.ISIJINT-2018-036.

Влияние предварительной плазменной обработки поверхности стали 09Г2С на формирование покрытия в результате горячего цинкования

Бондарева Ольга Сергеевна*[1], кандидат технических наук,
доцент кафедры технологии металлов и авиационного материаловедения
Добычина Ольга Сергеевна, аспирант кафедры технологии металлов и авиационного материаловедения
Куканков Леонид Сергеевич, студент
Короткова Юлия Николаевна, студент
Третьяков Виталий Александрович, студент
Самарский национальный исследовательский университет имени академика С.П. Королева, Самара (Россия)

***E-mail:** osbondareva@ssau.ru, osbond@yandex.ru

[1]ORCID: https://orcid.org/0000-0002-4273-2483

Поступила в редакцию 27.06.2023 *Принята к публикации 22.11.2023*

Аннотация: В последние годы расширяется ассортимент кремнийсодержащих сталей, подвергаемых горячему цинкованию. Легирование стали 0,5–1 % кремния приводит к образованию цинкового покрытия большой толщины с матовой или разнотонной поверхностью. Это связано с изменением фазовых реакций между железом и цинком в системе Fe–Zn–Si. Актуальной задачей является разработка способов нейтрализации негативного влияния кремния на формирование цинкового покрытия. Цель работы – изучение влияния предварительной плазменной резки и плазменной поверхностной закалки стали 09Г2С (S355J2) на толщину и структуру цинкового покрытия, образующегося на обработанных поверхностях. Установлено, что после плазменной резки структура приповерхностного слоя стали представляет собой мартенсит, а после плазменной поверхностной закалки – мартенсит и феррит. Анализ изменения микротвердости от поверхности стали к середине показал, что глубина закаленного слоя составляет 400 мкм. На поверхности стали без предварительной обработки формируется цинковое покрытие, состоящее из δ-фазы и ζ-фазы. На поверхности стали после плазменной обработки формируется цинковое покрытие, характерное для малокремнистых сталей и состоящее из δ-фазы, ζ-фазы и η-фазы. Установлено, что толщина цинкового покрытия на поверхности после плазменной резки в два раза меньше, чем на необработанной поверхности, причем сокращение толщины покрытия происходит за счет уменьшения толщины ζ-фазы. Выдвинута гипотеза, что образование на поверхности стали мартенсита приводит к исчезновению упорядоченной фазы FeSi и изменяет фазовое равновесие в системе Fe–Zn–Si. Следовательно, предварительная плазменная обработка поверхности стали позволяет управлять структурой и толщиной образующегося цинкового покрытия и поэтому рекомендуется для внедрения в процесс горячего цинкования кремнийсодержащих сталей.

Ключевые слова: горячее цинкование; цинковое покрытие; кремнийсодержащие стали; Fe–Zn–Si; плазменная обработка; поверхностная закалка.

Для цитирования: Бондарева О.С., Добычина О.С., Куканков Л.С., Короткова Ю.Н., Третьяков В.А. Влияние предварительной плазменной обработки поверхности стали 09Г2С на формирование покрытия в результате горячего цинкования // Frontier Materials & Technologies. 2024. № 2. С. 23–31. DOI: 10.18323/2782-4039-2024-2-68-2.

doi: 10.18323/2782-4039-2024-2-68-3

Low-cycle fatigue of 10 % Cr steel with high boron content at room temperature

Ivan S. Brazhnikov*[1], engineer
of the Joint Research Center of Belgorod State National Research University "Technology and Materials"
Alexandra E. Fedoseeva[2], PhD (Engineering),
senior researcher of the Laboratory of Mechanical Properties of Nanostructured Materials and Superalloys
Belgorod State National Research University, Belgorod (Russia)

***E-mail:** 1216318@bsu.edu.ru

[1]ORCID: https://orcid.org/0009-0008-8069-7376
[2]ORCID: https://orcid.org/0000-0003-4031-463X

Received 22.06.2023 *Accepted 16.02.2024*

Abstract: High-chromium martensitic steels are a promising material for the production of elements of boilers and steam pipelines, as well as blades and rotors of steam turbines for new coal-burning thermal generating units. The use of such materials will give an opportunity for the transition to ultra-supercritical steam parameters (temperature of 600–620 °C and pressure of 25–30 MPa), which will allow increasing the efficiency of generating units to 45 %. Modifications of the chemical composition of high-chromium steels have led to significant improvements of high-temperature properties such as 100,000 h creep strength and 1 % creep limit, while resistance to softening due to low-cycle fatigue remains understudied in this field. This work covers the study of low-cycle fatigue at room temperature with different amplitudes of deformation of martensitic high-chromium 10%Cr–3%Co–2%W–0.5%Mo–0.2%Cu–0.2%Re–0.003%N–0.01%B steel. The steel was pre-subjected to normalizing at 1050 °C followed by tempering at 770 °C. After heat treatment, the steel structure was a tempered martensitic lath structure stabilised by the particles of secondary phases of $M_{23}C_6$ carbides, Nb*X* carbonitrides, and M_6C carbides. The average width of martensite laths was 380 nm, and the dislocation density was 1.4×10^{14} m^{-2}. At low-cycle fatigue, with an increase in the strain amplitude from 0.2 to 1 %, the number of cycles before failure significantly decreases, and the value of plastic deformation in the middle of the number of loading cycles significantly increases. Maximum softening (18 %) is observed at a strain amplitude of 1 % in the middle of the number of loading cycles. In general, the steel structure after low-cycle fatigue tests does not undergo significant changes: the width of the laths increases by 18 % at a strain amplitude of more than 0.3 %, while the dislocation density remains at a rather high level (about 10^{14} m^{-2}) at all strain amplitudes.

Keywords: martensitic heat-resistant steel; low-cycle fatigue; strain amplitude; fatigue softening; fatigue failure.

Acknowledgements: The work was financially supported by the Russian Science Foundation (Agreement No. 19-73-10089-П). Link to information about the project: https://rscf.ru/project/22-73-41001/.

The authors express their gratitude to the Joint Research Center of Belgorod State National Research University "Technology and Materials" for the equipment provided for carrying out structural studies.

The paper was written on the reports of the participants of the XI International School of Physical Materials Science (SPM-2023), Togliatti, September 11–15, 2023.

For citation: Brazhnikov I.S., Fedoseeva A.E. Low-cycle fatigue of 10 % Cr steel with high boron content at room temperature. *Frontier Materials & Technologies*, 2024, no. 2, pp. 33–42. DOI: 10.18323/2782-4039-2024-2-68-3.

INTRODUCTION

9–12 % Cr steels are considered as promising materials for the production of elements of new thermal generating units, operating at super-supercritical steam parameters (temperature of 600–620 °C, pressure of 25–30 MPa) [1]. The transition to new super-supercritical steam parameters will increase the efficiency of thermal generating units to 45 % [2; 3].

The structure of 9–12 % Cr steels is a tempered lath troostite, the boundaries of which are fixed by particles of $M_{23}C_6$ carbides (where M is Cr, Fe, and Mo), and the high density of dislocations inside the martensitic laths is held by fine *MX* carbonitrides (where *M* is V and/or Nb, *X* is C and/or N) [4; 5]. It has been found that adding a small amount of boron to chromium-molybdenum and chromium-tungsten steels can significantly increase creep resistance [6; 7]. Segregation of boron at the boundaries of the prior austenite grains (PAG) strengthens and prevents local softening of these boundaries under creep conditions [6; 7]. Moreover, adding boron reduces the rate of coarsening of $M_{23}C_6$ carbides precipitated at the boundaries of martensite laths, blocks, packets, and PAG [8]. On the other hand, in steels with a high nitrogen content, boron tends to form large particles of boron nitride BN, which act as sources of cracks and discontinuities during creep [1].

Along with the BN formation in steels with a high nitrogen content, small metastable particles of *MX* carbonitrides are transformed into large particles of the thermodynamically stable Z-phase (Cr(V,Nb)N) during creep, which negatively affects the properties [9]. Reducing the nitrogen content to very small values (less than 0.003 wt. %) solves two problems at once: 1) prevention of the formation of large BN and Z-phase particles, and 2) the possibility of increasing the boron content to 0.01 wt. %. In this case, a significant

increase in original austenite grains up to 50–60 μm occurs [10]. The addition of cobalt, tungsten, molybdenum, and rhenium to steel slows down diffusion-controlled processes during creep, such as the Laves phase formation, particle coarsening and lath coarsening, which also has a positive effect on creep resistance [11; 12]. This approach to alloying can make it possible to increase the long-term creep strength from 72 (for P92 steel [13]) to 100 MPa [14].

Good creep resistance is demonstrated by the new promising 10 % Cr martensitic steel, which was chosen to be studied in this work. Thus, the long-term strength limit of the steel under study was 93 MPa at 650 °C on a basis of 100,000 h; moreover, there is no discontinuity in the long-term strength curve [12]. However, during operation of steam turbine blades, low-cycle fatigue cracks can form [1].

Currently, there are quite a lot of works covering the study of low-cycle fatigue of high-chromium steels [15–17]. High-chromium steels typically exhibit three distinct stages during low-cycle fatigue tests: a rapid softening stage, a stable stage, and a stage of final failure due to the initiation and propagation of cracks [15; 18–20]. In [15], it was found that when increasing test temperature, the proportion of plastic deformation increases, especially at large strain amplitudes. The structure of the material with increasing temperature of low-cycle fatigue test also undergoes significant changes, such as the formation of subgrains and the evolution of the dislocation structure – from cellular at room temperature to wall-like at elevated temperatures [19]. An increase in test temperature causes an increase in the distance between martensitic laths [16]. When tested for low-cycle fatigue at room temperature, fatigue softening depends on the size of the laths and is associated with dynamic recrystallisation [20].

Since the steel under study is supposed to be used as a material for the production of steam turbine blades, a detailed study of the creep characteristics is not enough. Low-cycle fatigue behaviour should be included in the study. The results concerning the behaviour of 10%Cr–3%Co–2W–0.5Mo–0.2Cu–0.2Re–0.003N–0.01B steel when tested for low-cycle fatigue will be useful for determining permissible cyclic loads, during operation of parts of thermal power plants made from the steels under study.

The purpose of this work is to identify the influence of the strain amplitude magnitude during low-cycle fatigue on the structural changes of 10 % Cr martensitic steel at room temperature.

METHODS

Table 1 presents the chemical composition of the new 10 % Cr martensitic steel. The steel was cast at the LLC SMSM plant, Moscow, in a vacuum induction furnace. After peeling, the ingots were homogenised at a temperature of 1150 °C for 16 h, followed by forging at the same temperature into blanks in the form of square bars with a square side of 50 mm, followed by cooling in air. Heat treatment of steel included normalizing at a temperature of 1050 °C for 1 h, cooling in air, followed by tempering at a temperature of 770 °C for 3 h, cooling in air.

Low-cycle fatigue tests were carried out on cylindrical samples in accordance with GOST 25.502-79, with a working part diameter of 5 mm and a reduced gauge length of up to 18 mm. The decrease in the gauge length of the sample is caused by the tendency of martensitic steel samples to longitudinal bending during compression at high strain amplitudes. Tension-compression tests were carried out with an asymmetry coefficient (R) of −1 at room temperature, with strain amplitudes of 0.2, 0.3, 0.6, and 1 % and a frequency of 0.5 Hz using an Instron 8801 testing machine (Great Britain). One sample was used for each amplitude. The study of the microstructure in the initial state, and after low-cycle fatigue tests was carried out on a JEM JEOL-2100 transmission electron microscope (Japan), equipped with an energy-dispersive spectrometer, at an accelerating voltage of 200 kV. The foils for microstructure studies were cut from the area closest to the fracture zone. The density of free dislocations inside the laths was determined from the number of dislocation exit points on the foil surface. The size of martensite laths was determined by the random secant method in six randomly selected areas of the structure. The equilibrium volume fraction of secondary phase particles was determined using Thermo-Calc software (TCFE7 database) (Sweden).

RESULTS

Structure after heat treatment

As a result of heat treatment, a rather homogeneous tempered martensitic lath structure is formed in 10 % Cr steel (Fig. 1 a). The average transverse size of martensite laths was (380±30) nm. Inside the laths, both free dislocations (Fig. 1 c) and networks of dislocations (Fig. 1 b) are observed. The dislocation density inside the laths is quite high and amounts to $(1.4\pm0.5)\times10^{14}$ m^{-2}. Analysis of the replicas (Fig. 1 d) showed that during the heat treatment, particles of $M_{23}C_6$ carbides enriched in chromium, particles of *MX* carbonitrides enriched in niobium, and a very small amount of particles of M_6C carbides enriched in tungsten are released. $M_{23}C_6$ carbides are the dominant phase and precipitate along the boundaries of original austenite grains, packets, blocks and martensite laths. Their average size is (70±5) nm, volume fraction – 2.35 %.

Table 1. *Chemical composition of 10%Cr–3%Co–2W–0.5Mo–0.2Cu–0.2Re–0.003N–0.01B steel, wt. %*
Таблица 1. *Химический состав стали 10%Cr–3%Co–2W–0,5Mo–0,2Cu–0,2Re–0,003N–0,01B, вес. %*

Fe	C	Cr	Co	W	Mo	Cu	V	Nb	Re	B	N
Base	0.13	9.4	3.1	2.1	0.6	0.29	0.16	0.05	0.17	0.015	0.002

Nb*X* carbonitrides with an average size of 30 nm are uniformly distributed throughout the material volume (Fig. 1 d). M_6C carbides with an average size of 40 nm were found along the boundaries of martensite laths (Fig. 1 d). The volume fractions of the last two phases are insignificant and do not exceed 0.1 %.

Properties during low-cycle fatigue at room temperature

Fig. 2 presents the results of low-cycle fatigue tests at room temperature. At a minimum strain amplitude of 0.2 %, the number of cycles before failure was 213,822 (Fig. 2 a). For the steel under study, as the strain amplitude increases, the number of cycles before failure decreases significantly. Thus, even a slight increase in the strain amplitude from 0.2 to 0.3 % reduces the number of cycles by 1 order of magnitude (Fig. 2 a). A further increase in the strain amplitude from 0.3 to 0.6 % reduces the number of cycles by another 8 times (Fig. 2 a). At the largest strain amplitude of 1 %, the number of cycles before failure decreased to 488 cycles (Fig. 2 a).

When comparing the number of cycles before failure during low-cycle fatigue of the steel under study to other 9–10 % Cr steels [21–23] at strain amplitudes of 0.3 and 0.6 %, it was found that at a strain amplitude of 0.3 %, the steel under study demonstrates 14,411 cycles to failure (Fig. 2 b). This correlates well with the values of cycles before failure for other steels [21–23]. On the other hand, at a strain amplitude of 0.6 %, the steel under study shows 1,815 cycles before failure, which exceeds the number of cycles before failure for the steels presented in [21–23] more than 2 times.

The hysteresis loops during low-cycle fatigue tests have an asymmetry, and with increasing strain amplitude, the hysteresis loop asymmetry increases. At a strain amplitude of 0.2 %, fatigue failure occurs mainly during elastic deformation, which, combined with the number of cycles before failure exceeding 200,000, allows classifying this test as a high-cycle fatigue test (Fig. 3). The stress amplitude in this case is 396.3 MPa. With an increase in the strain amplitude from 0.2 to 1 %, the contribution of the strain plastic component increases, and destruction occurs in the elastoplastic area (Table 2). With an increase in the strain amplitude from 0.2 to 1 %, the increase in the stress amplitude was 30 %, while the amplitude of the strain plastic component increased by 95 times.

During low-cycle fatigue tests at room temperature, cyclic hardening of the steel under study occurs, which is expressed in an increase in the stress amplitude with an increase in the number of cycles in relation to the first cycle stress (Fig. 4 a). This is typical for all strain amplitudes. For example, at a strain amplitude of 0.2 %, the steel under study was hardened up to the 60^{th} cycle, and the same level of stress amplitude was maintained until failure. At a strain amplitude of 1 %, the steel strengthened up to 6 cycles, after which a decrease in the stress amplitude was observed relative to the first cycle (Fig. 4 a). A decrease in the stress amplitude relative to the first cycle stress indicates material softening. On the other hand, such a decrease in stress amplitude relative to the first cycle stress may be caused by a decrease in force due to necking (reduction in cross-sectional area).

One can see that at a strain amplitude of 0.2 %, the degree of softening is negative, which indicates that up to 50 % of the total number of cycles before failure, the stress amplitude is higher than the first cycle stress amplitude (Fig. 4 b). However, even with a slight increase in the strain amplitude to 0.3 %, the value of the material stress amplitude becomes lower than the first cycle stress by already 5 % of the total number of cycles before failure. In this case, the degree of softening increases twice at 50 % of the total number of cycles before failure.

It should be noted that with a strain amplitude of 0.6 %, the degree of fatigue softening even at 50 % of the total number of cycles before failure does not exceed 10 % and is comparable to an amplitude of 0.3 %. At an amplitude of 1 %, the maximum softening of the steel under study is observed, which is 18 % at 40 and 50 % of the total number of cycles before failure.

Fractography of fractures

The relative reduction of samples after low-cycle fatigue increases significantly from 5 to 20 % for an amplitude from 0.2 to 1 %, which is caused by an increase in the strain plastic component. On the fracture surface, two zones can be clearly distinguished: the fatigue failure area and the rupture area (final destruction) (Fig. 5). Fatigue grooves can be discerned in the fatigue failure area. The rupture area has a viscous character expressed by small pits. An evaluation of the proportion of the fatigue failure area in relation to the entire fracture surface, revealed that this value does not depend on the strain amplitude and ranges from 45 to 60 %.

Structure after low-cycle fatigue

After low-cycle fatigue tests at all strain amplitudes, the tempered martensitic lath structure formed during heat treatment is preserved (Fig. 6). After low-cycle fatigue tests with a strain amplitude of 0.2 % (the number of cycles is more than 200,000), the average width of the laths is (370±30) nm, which coincides with the value before the test (Table 3). In this case, the density of free dislocations inside martensite laths also does not change compared to the initial state and amounts to $(1.4\pm0.5)\times10^{14}$ m^{-2} (Table 3).

With an increase in the strain amplitude up to 1 %, an insignificant increase in the width of martensite laths up to (460±30) nm is observed (Table 2), which is caused by the appearance of a strain plastic component (Table 1). Let us remark, that the dislocation density changes at the error level with increasing strain amplitude. The absence of significant changes in the dispersions of particles of secondary phases after low-cycle fatigue tests is also worth noting.

DISCUSSION

The number of cycles before failure at a strain amplitude of 0.2 % has passed the conventional threshold of 5×10^4 cycles, which indicates a transition from the low-cycle fatigue area to the high-cycle fatigue area. However, when the strain amplitude increases to 1 %, the number of

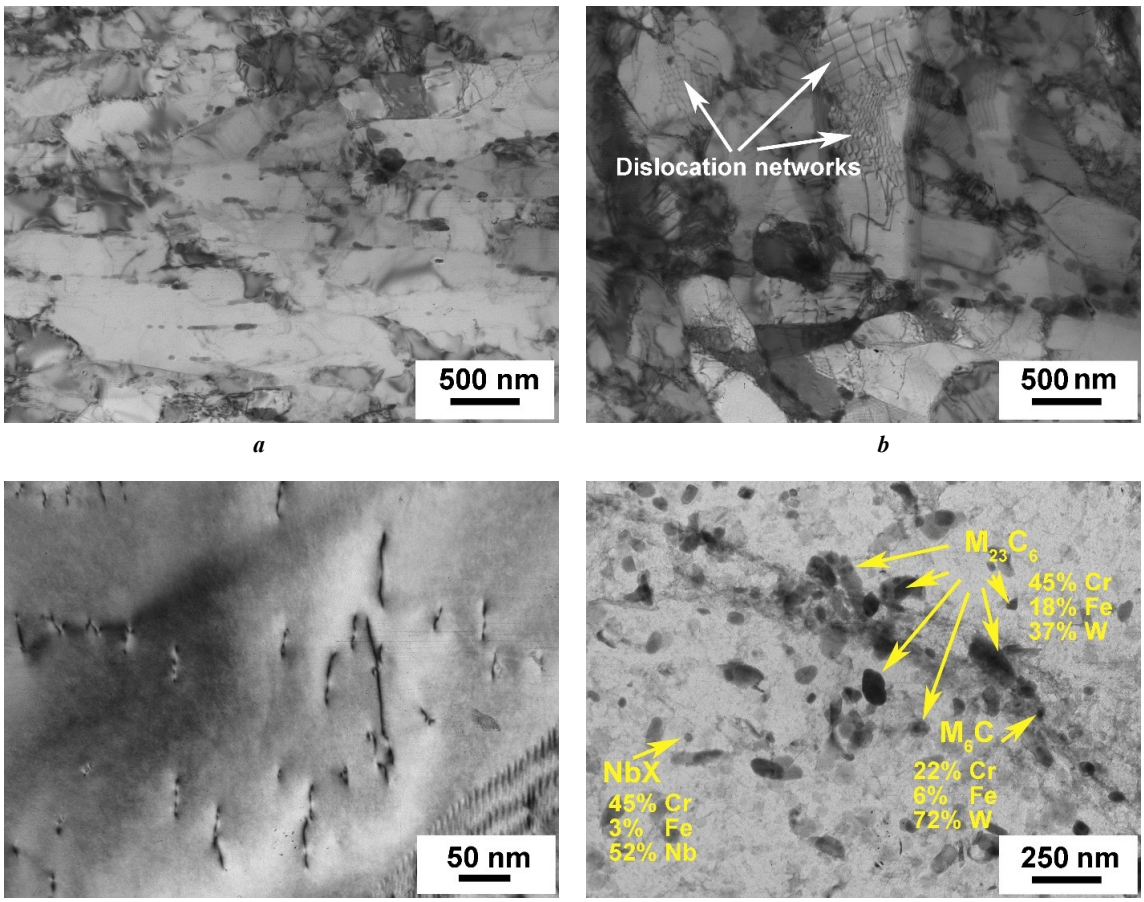

Fig. 1. *Images of the microstructure of the 10 % Cr steel under study after heat treatment, obtained by TEM method of thin foils (**a–c**) and carbon replicas (**d**)*
Рис. 1. *Изображения микроструктуры исследуемой 10 % Cr стали после термической обработки, полученные методом ПЭМ тонких фольг (**a–c**) и углеродных реплик (**d**)*

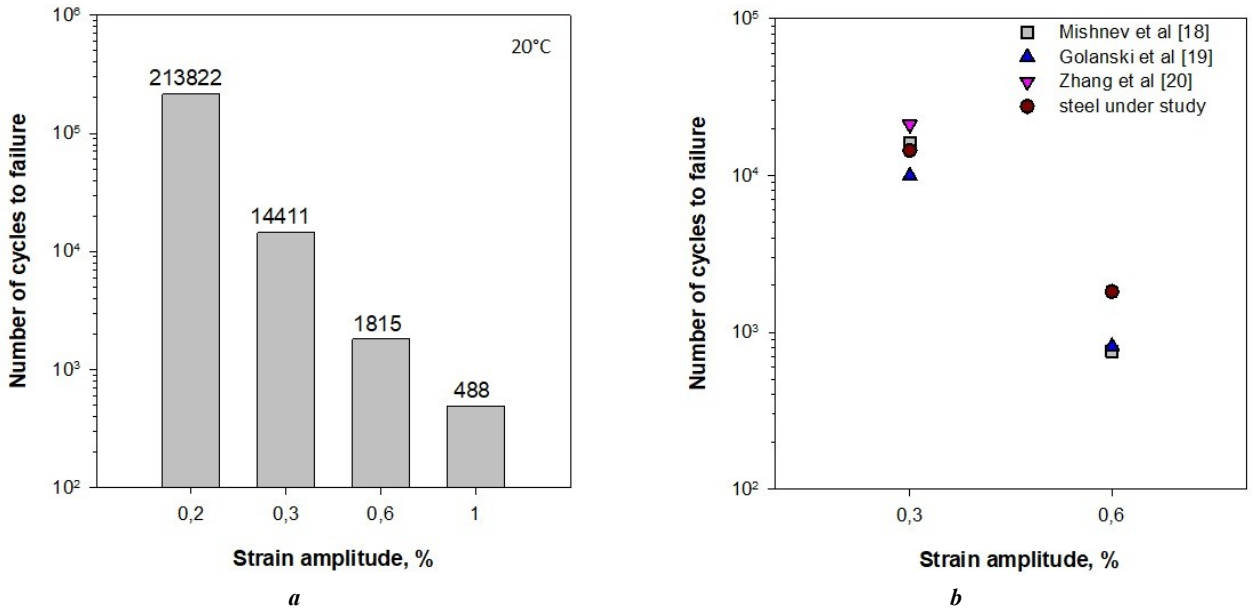

Fig. 2. *Dependence of the number of cycles to failure on the strain amplitude for the steel under study (**a**) and a comparison of the number of cycles to failure during low-cycle fatigue of the steel under study with other 9–10 % Cr steels [21–23] at strain amplitudes of 0.3 and 0.6 % (**b**)*
Рис. 2. *Зависимость количества циклов до разрушения от амплитуды деформации для исследуемой стали (**a**), а также сравнение количества циклов до разрушения при малоцикловой усталости исследуемой стали с другими 9–10 % Cr сталями [21–23] при амплитудах деформации 0,3 и 0,6 % (**b**)*

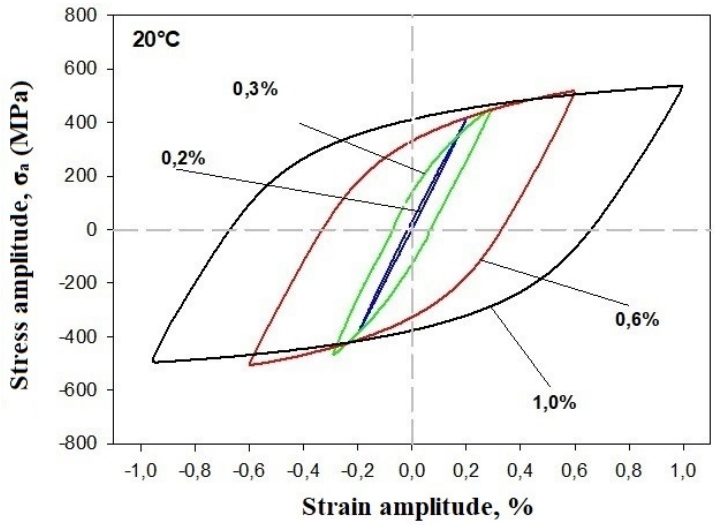

Fig. 3. *"Stress amplitude – strain amplitude" hysteresis loops in the middle of the number of loading cycles at a test temperature of 20 °C for 10 % Cr steel*
Рис. 3. *Петли гистерезиса «Амплитуда напряжения – амплитуда деформации» в середине количества циклов нагружения при температуре испытания 20 °C для 10 % Cr стали*

Table 2. *Data of low-cycle fatigue in the middle of the number of loading cycles*
Таблица 2. *Данные малоцикловой усталости в середине количества циклов нагружения*

Characteristics of low cycle fatigue	Strain amplitude ε_{ac}, %			
	0.2	0.3	0.6	1
Stress amplitude, $\sigma_a \frac{N}{2}$, MPa	396.3	459.8	511.1	515.7
Amplitude of strain plastic component ε_{ap}, %	0.007	0.073	0.33	0.666

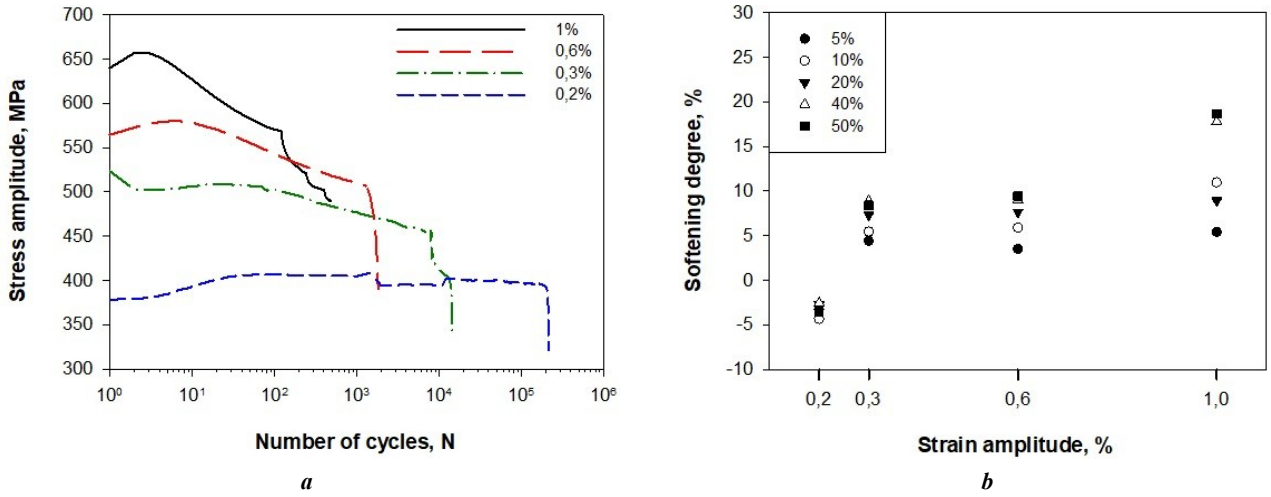

a ***b***

Fig. 4. *Dependence of the stress amplitude on the number of cycles at a strain amplitude of 0.2, 0.3, 0.6, and 1 % (**a**) together with the degree of fatigue softening in relation to the first cycle stress at different fractions of the maximum number of cycles before failure (**b**)*
Рис. 4. *Зависимость амплитуды напряжения от количества циклов при амплитуде деформации 0,2; 0,3; 0,6 и 1 % (**а**) совместно со степенью циклического разупрочнения по отношению к напряжению первого цикла при различных долях от максимального количества циклов до разрушения (**b**)*

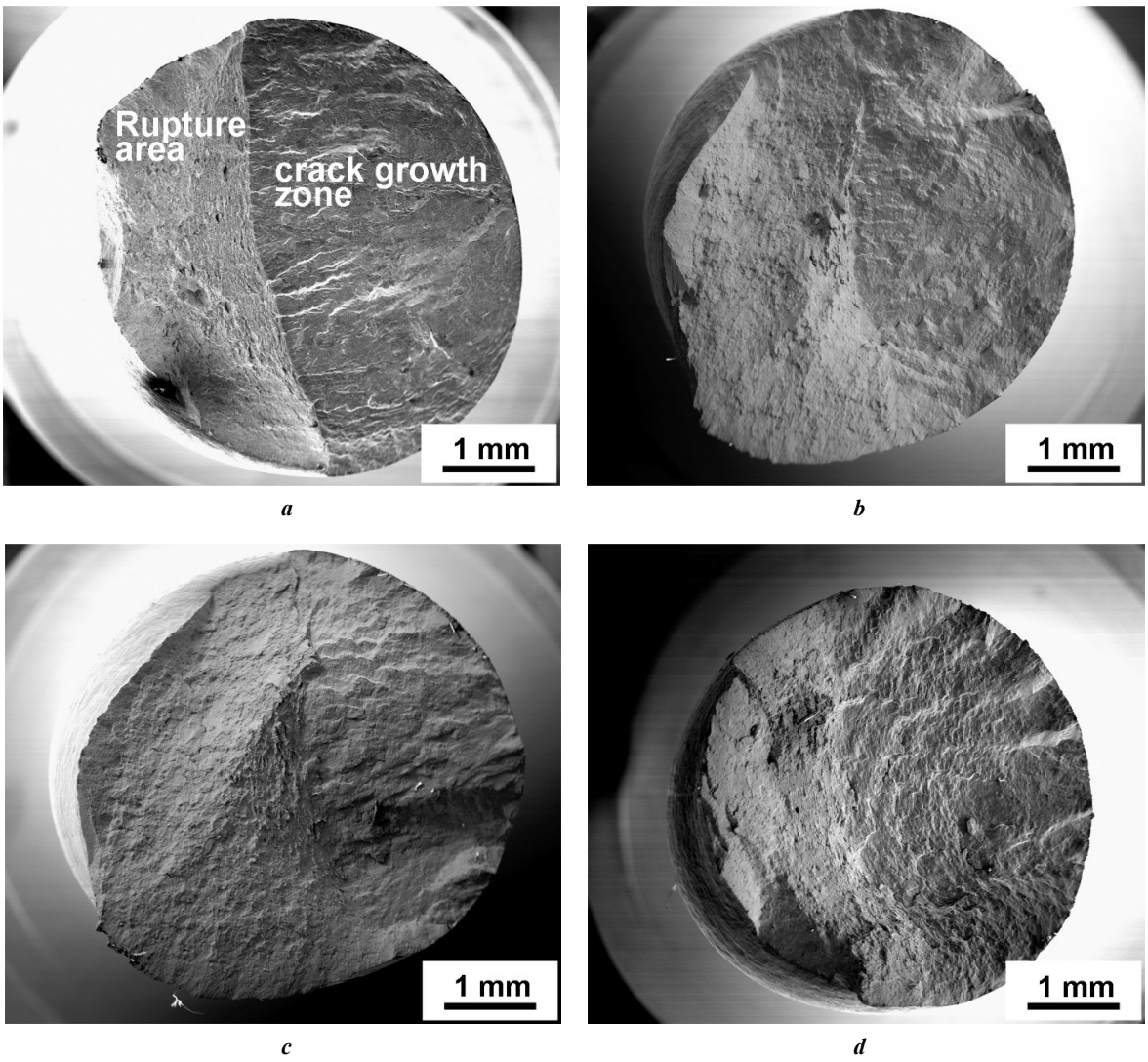

a *b*

c *d*

Fig. 5. *Fractography of fractures of destroyed samples after low-cycle fatigue tests at strain amplitudes of 0.2 % (**a**), 0.3 % (**b**), 0.6 % (**c**), and 1 % (**d**)*
Рис. 5. *Фрактография изломов разрушенных образцов после испытаний на малоцикловую усталость при амплитудах деформации 0,2 % (**a**), 0,3 % (**b**), 0,6 % (**c**) и 1 % (**d**)*

cycles before failure does not exceed 2×10^4 cycles, which indicates that for this steel, tests with a given strain amplitude above 0.3 % remain in the low-cycle fatigue area. Loop asymmetry in Fig. 3 is associated with the Bauschinger effect: the wider the loop, the greater the Bauschinger strain [21]. For the steel under study, one can note that with an increase in the strain amplitude in the middle of the number of loading cycles, the hysteresis loop width increases. It should be noted that at a strain amplitude of 0.2 %, the hysteresis loop is almost symmetrical, and accordingly, the Bauschinger strain in this case is extremely small. Thus, the loop width at a strain amplitude of 0.2 % clearly demonstrates, predominantly, elastic strain during the test.

The absence of transformations of lath boundaries into subgrain boundaries through the interaction of lath boundaries, and free dislocations is caused by the low test temperature. At room temperature, interaction even between free dislocations proceeds slowly [22]. Long-range fields of elastic stresses from dislocations and low-angle lath boundaries prevent the capture of dislocations by boundaries [21], which leads to the absence of visible changes in the structure after low-cycle fatigue tests at a strain amplitude of 0.2 %. Moreover, such a structure demonstrates cyclic hardening (Fig. 4). It is worth noting that cyclic hardening in the first cycles at room temperature is also observed in [21]. On the contrary, +24 % broadening of martensite laths after low-cycle fatigue testing at higher strain amplitudes, due to the appearance of a strain plastic component, can lead to fatigue softening (Fig. 4). Thus, substructural hardening from martensite laths can be assessed using the Langford–Cohen equation [24]:

$$\sigma_{\text{laths}} = \frac{k_h}{2l},$$

where k_h is the hardening coefficient (0.0862 MPa×m [24]); l is the width of martensite laths.

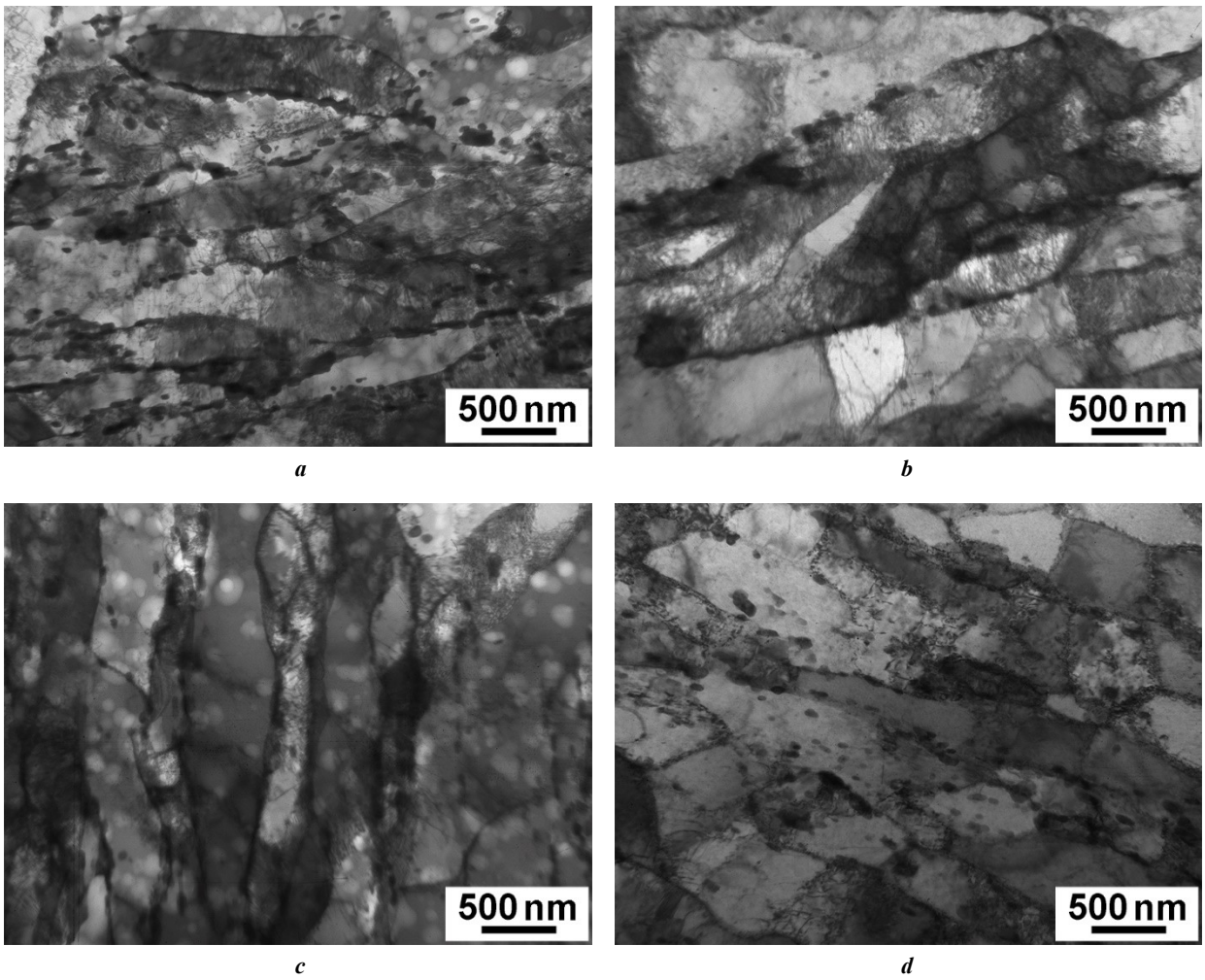

a *b*

c *d*

Fig. 6. *Microstructure of the steel under study after low-cycle fatigue testing at strain amplitudes of 0.2 % (**a**), 0.3 % (**b**), 0.6 % (**c**), and 1 % (**d**)*
Рис. 6. *Микроструктура исследуемой стали после испытания на малоцикловую усталость при амплитудах деформации 0,2 % (**a**), 0,3 % (**b**), 0,6 % (**c**) и 1 % (**d**)*

Table 3. *Microstructural parameters of 10%Cr–3%Co–2W–0.5Mo–0.2Cu–0.2Re–0.003N–0.01B steel after low-cycle fatigue tests*
Таблица 3. *Микроструктурные параметры стали 10%Cr–3%Co–2%W–0,5%Mo–0,2%Cu–0,2%Re–0,003%N–0,01%B после испытания на малоцикловую усталость*

Strain amplitude, %	0.2	0.3	0.6	1
Dislocation density, $\times 10^{14}$ m^{-2}	1.4±0.5	2.4±0.5	1.1±0.5	1.9±0.5
Lath width, nm	370±30	450±30	460±30	460±30

The magnitude of hardening in the initial state was 113 MPa (with a lath width of 380 nm (Table 3)), while lath broadening to 450–460 nm after low-cycle fatigue at 0.3–1 % of the strain amplitude (Table 3), leads to a decrease in substructural hardening up to 94–96 MPa. On the other hand, an increase in the relative reduction (reduction of cross-sectional area) causes a decrease in force rather than stress, which can be expressed as an apparent decrease in strain stress after necking. Thus, with an amplitude of 1 %, the relative reduction reaches 20 %, and softening occurs by approximately the same amount.

To identify the nature of the softening, Table 4 summarizes the values of softening caused by the broadening of the laths, the relative reduction values, and the values of the decrease in stress amplitude for a certain cycle in comparison with the first loading cycle. A comparison of the data from Table 4 showed that the softening of the material during low-cycle fatigue at high strain

Table 4. *The values of softening due to the widening of the laths, relative reduction and the decrease in the stress amplitude for a certain cycle compared to the first loading cycle for various strain amplitudes, %*
Таблица 4. *Величины разупрочнения из-за уширения реек, относительного сужения и значения снижения амплитуды напряжения для определенного цикла в сравнении с первым циклом нагружения для различных амплитуд деформаций, %*

Strain amplitude	0.2	0.3	0.6	1
Softening due to the widening of martensite laths	–	15	17	17
Relative reduction	5	12	8	20
Decrease in the stress amplitude relative to the first cycle stress at 50 % of the total number of cycles before failure	–	8	9	19

amplitudes is caused by the beginning of an increase in relative reduction (reduction of cross-sectional area), and not by a structural factor.

CONCLUSIONS

It has been found that an increase in the strain amplitude from 0.2 to 1 % reduces the number of cycles before failure by 3 orders of magnitude. The maximum softening of 18 % is observed at a strain amplitude of 1 % in the middle of the number of loading cycles. At the same time, the steel under study, after low-cycle fatigue tests, retains the tempered martensitic lath structure formed during heat treatment without significant changes. The material softening is caused by the beginning of an increase in the relative reduction of the samples.

REFERENCES

1. Kaybyshev R.O., Skorobogatykh V.N., Shchenkova I.A. New martensitic steels for fossil power plant: creep resistance. *The Physics of Metals and Metallography*, 2010, vol. 109, no. 2, pp. 186–200. EDN: MXPLYJ.
2. Abe F., Kern T.-U., Viswanathan R. *Creep-resistant steels*. Cambridge, Woodhead Publishing, 2008. 800 p.
3. Kern T.U., Staubli M., Scarlin B. The European efforts in material development for 650 °C USC power plants-COST522. *ISIJ international*, 2002, vol. 42, no. 12, pp. 1515–1519. DOI: 10.2355/isijinternational.42.1515.
4. Bladesha H.K.D.H., Design of ferritic creep-resistant steels. *ISIJ international*, 2001, vol. 41, no. 6, pp. 626–640. DOI: 10.2355/isijinternational.41.626.
5. Kostka A., Tak K.-G., Hellmig R.J., Estrin Y., Eggeler G. On the contribution of carbides and micrograin boundaries to the creep strength of tempered martensite ferritic steels. *Acta Materialia*, 2007, vol. 55, no. 2, pp. 539–550. DOI: 10.1016/j.actamat.2006.08.046.
6. Abe F. Effect of boron on microstructure and creep strength of advanced ferritic power plant steels. *Procedia Engineering*, 2011, vol. 10, pp. 94–99. DOI: 10.1016/j.proeng.2011.04.018.
7. Takahashi N., Fujita T. The Effect of Boron on the Long Period Creep Rupture Strength of the Modified 12% Chromium Heat Resisting Steel. *Transactions of the Iron and Steel Institute of Japan*, 1976, vol. 16, no. 11, pp. 606–613. DOI: 10.2355/isijinternational1966.16.606.
8. Kaibyshev R., Mishnev R., Fedoseeva A., Dudova N. The role of microstructure in creep strength of 9-12% Cr steels. *Materials Science Forum*, 2017, vol. 879, pp. 36–41. DOI: 10.4028/www.scientific.net/MSF.879.36.
9. Danielsen H.K. Review of Z phase precipitation in 9–12 wt-% Cr steels. *Materials Science and Technology*, 2016, vol. 32, no. 2, pp. 126–137. DOI: 10.1179/1743284715Y.0000000066.
10. Nikitin I.S., Fedoseeva A.E. Effect of the Normalizing Temperature on the Short-Time Creep of Martensitic 10Cr–3Co–3W–0.2Re Steel with a Low Nitrogen Content. *Russian Metallurgy (Metally)*, 2022, vol. 2022, pp. 753–763. DOI: 10.1134/S0036029522070102.
11. Knezevic V., Balun J., Sauthoff G., Inden G., Schneider A. Design of martensitic/ferritic heat-resistant steels for application at 923 K with supporting thermodynamic modeling. *Materials Science and Engineering: A*, 2008, vol. 477, no. 1-2, pp. 334–343. DOI: 10.1016/j.msea.2007.05.047.
12. Fedoseeva A.E. Creep Resistance and Structure of 10% Cr–3% Co–2% W–0.29% Cu–0.17% Re Steel with Low Nitrogen and High Boron Contents for Unit Components of Coal Power Plants. *Physical Mesomechanics*, 2024, vol. 27, pp. 88–101. DOI: 10.1134/S1029959924010090.
13. Haarmann K., Vaillant J.C., Vandenberghe B., Bendick W., Arbab A. *The T92/P92 Book*. Boulogne, Vallourec and Mannesmann tubes Publ., 1998. 62 p.
14. Dudova N., Mishnev R., Kaibyshev R. Creep behavior of a 10%Cr heat-resistant martensitic steel with low nitrogen and high boron contents at 650 °C. *Materials Science and Engineering: A*, 2019, vol. 766, article number 138353. DOI: 10.1016/j.msea.2019.138353.
15. Wang Quanyi, Wang Qingyuan, Gong Xiufang, Wang Tianjian, Zhang Wei, Li Lang, Liu Yongjie, He Chao, Wang Chong, Zhang Hong. A comparative study of low cycle fatigue behavior and microstructure of Cr-based steel at room and high temperatures. *Materials & Design*, 2020, vol. 195, article number 109000. DOI: 10.1016/j.matdes.2020.109000.
16. Zhang Zhe, Li Xiaofei, Yu Yaohua, Li Bingbing, Zhang Bo, Ma Yushan, Chen Xu. Effects of temperature and strain amplitude on low-cycle fatigue behavior of 12Cr13 martensitic stainless steel. *Journal of Materials Research and Technology*, 2024, vol. 29, pp. 1414–1427. DOI: 10.1016/j.jmrt.2024.01.162.
17. Mao Jianfeng, Zhu Jian, Li Xiangyang, Wang Dasheng, Zhong Fengping, Chen Jichang. Effect of strain ampli-

tude and temperature on creep-fatigue behaviors of 9–12% Cr steel. *Journal of Mechanical Science and Technology*, 2022, vol. 36, no. 5, pp. 2265–2276. DOI: 10.1007/s12206-022-0409-y.
18. Chen Furen, Zhang Wei, Zhang Kaihao, Yang Qiaofa, Wang Xiaoxiao, Zhou Changyu. Low cycle fatigue and creep-fatigue interaction behavior of 2.25CrMoV steel at high temperature. *Journal of Materials Research and Technology*, 2024, vol. 28, pp. 3155–3165. DOI: 10.1016/j.jmrt.2023.12.233.
19. Shi Shouwen, Cui Jianpeng, Li Haiyan, Chen Gang, Lin Qiang, Chen Xu. Cyclic stress response and microcrack initiation mechanism of modified 9Cr1Mo steel under low cycle fatigue at room temperature and 350 °C. *Fatigue and Fracture of Engineering Materials and Structures*, 2023, vol. 46, no. 7, pp. 2525–2538. DOI: 10.1111/ffe.14015.
20. Zhang Xiaodong, Wang Tianjian, Gong Xiufang, Li Qingsong, Liu Yongjie, Wang Quanyi, Zhang Hong, Wang Qingyuan. Low cycle fatigue properties, damage mechanism, life prediction and microstructure of MarBN steel: Influence of temperature. *International Journal of Fatigue*, 2021, vol. 144, article number 106070. DOI: 10.1016/j.ijfatigue.2020.106070.
21. Mishnev R., Dudova N., Kaibyshev R. Low cycle fatigue behavior of a 10Cr–2W–Mo–3Co–NbV steel. *International Journal of Fatigue*, 2016, vol. 83-2, pp. 344–355. DOI: 10.1016/j.ijfatigue.2015.11.008.
22. Golański G., Mroziński S. Low cycle fatigue and cyclic softening behaviour of martensitic cast steel. *Engineering Failure Analysis*, 2013, vol. 35, pp. 692–702. DOI: 10.1016/j.engfailanal.2013.06.019.
23. Zhang Zhen, Hu Zheng-fei, Fan Li-kun, Wang Bin. Low cycle fatigue behavior and cyclic softening of P92 ferritic-martensitic steel. *Journal of Iron and Steel Research International*, 2015, vol. 22, pp. 534–542. DOI: 10.1016/S1006-706X(15)30037-6.
24. Langford G., Cohen M. Strain hardening of iron by severe plastic deformation. *American Society for Metals Transactions*, 1969, vol. 62, pp. 623–638.

СПИСОК ЛИТЕРАТУРЫ

1. Кайбышев Р.О., Скоробогатых В.Н., Щенкова И.А. Новые стали мартенситного класса для тепловой энергетики. Жаропрочные свойства // Физика металлов и металловедение. 2010. Т. 109. № 2. С. 200–215. EDN: LOIWVD.
2. Abe F., Kern T.-U., Viswanathan R. Creep-resistant steels. Cambridge: Woodhead Publishing, 2008. 800 p.
3. Kern T.U., Staubli M., Scarlin B. The European efforts in material development for 650 °C USC power plants – COST522 // ISIJ international. 2002. Vol. 42. № 12. P. 1515–1519. DOI: 10.2355/isijinternational.42.1515.
4. Bladesha H.K.D.H., Design of ferritic creep-resistant steels // ISIJ international. 2001. Vol. 41. № 6. P. 626–640. DOI: 10.2355/isijinternational.41.626.
5. Kostka A., Tak K.-G., Hellmig R.J., Estrin Y., Eggeler G. On the contribution of carbides and micrograin boundaries to the creep strength of tempered martensite ferritic steels // Acta Materialia. 2007. Vol. 55. № 2. P. 539–550. DOI: 10.1016/j.actamat.2006.08.046.
6. Abe F. Effect of boron on microstructure and creep strength of advanced ferritic power plant steels // Procedia Engineering. 2011. Vol. 10. P. 94–99. DOI: 10.1016/j.proeng.2011.04.018.
7. Takahashi N., Fujita T. The Effect of Boron on the Long Period Creep Rupture Strength of the Modified 12% Chromium Heat Resisting Steel // Transactions of the Iron and Steel Institute of Japan. 1976. Vol. 16. № 11. P. 606–613. DOI: 10.2355/isijinternational1966.16.606.
8. Kaibyshev R., Mishnev R., Fedoseeva A., Dudova N. The role of microstructure in creep strength of 9-12% Cr steels // Materials Science Forum. 2017. Vol. 879. P. 36–41. DOI: 10.4028/www.scientific.net/MSF.879.36.
9. Danielsen H.K. Review of Z phase precipitation in 9–12 wt-% Cr steels // Materials Science and Technology. 2016. Vol. 32. № 2. P. 126–137. DOI: 10.1179/1743284715Y.0000000066.
10. Nikitin I.S., Fedoseeva A.E. Effect of the Normalizing Temperature on the Short-Time Creep of Martensitic 10Cr–3Co–3W–0.2Re Steel with a Low Nitrogen Content // Russian Metallurgy (Metally). 2022. Vol. 2022. P. 753–763. DOI: 10.1134/S0036029522070102.
11. Knezevic V., Balun J., Sauthoff G., Inden G., Schneider A. Design of martensitic/ferritic heat-resistant steels for application at 923 K with supporting thermodynamic modeling // Materials Science and Engineering: A. 2008. Vol. 477. № 1-2. P. 334–343. DOI: 10.1016/j.msea.2007.05.047.
12. Fedoseeva A.E. Creep Resistance and Structure of 10% Cr–3% Co–2% W–0.29% Cu–0.17% Re Steel with Low Nitrogen and High Boron Contents for Unit Components of Coal Power Plants // Physical Mesomechanics. 2024. Vol. 27. P. 88–101. DOI: 10.1134/S1029959924010090.
13. Haarmann K., Vaillant J.C., Vandenberghe B., Bendick W., Arbab A. The T92/P92 Book. Boulogne: Vallourec and Mannesmann tubes, 1998. 62 p.
14. Dudova N., Mishnev R., Kaibyshev R. Creep behavior of a 10%Cr heat-resistant martensitic steel with low nitrogen and high boron contents at 650 °C // Materials Science and Engineering: A. 2019. Vol. 766. Article number 138353. DOI: 10.1016/j.msea.2019.138353.
15. Wang Quanyi, Wang Qingyuan, Gong Xiufang, Wang Tianjian, Zhang Wei, Li Lang, Liu Yongjie, He Chao, Wang Chong, Zhang Hong. A comparative study of low cycle fatigue behavior and microstructure of Cr-based steel at room and high temperatures // Materials & Design. 2020. Vol. 195. Article number 109000. DOI: 10.1016/j.matdes.2020.109000.
16. Zhang Zhe, Li Xiaofei, Yu Yaohua, Li Bingbing, Zhang Bo, Ma Yushan, Chen Xu. Effects of temperature and strain amplitude on low-cycle fatigue behavior of 12Cr13 martensitic stainless steel // Journal of Materials Research and Technology. 2024. Vol. 29. P. 1414–1427. DOI: 10.1016/j.jmrt.2024.01.162.
17. Mao Jianfeng, Zhu Jian, Li Xiangyang, Wang Dasheng, Zhong Fengping, Chen Jichang. Effect of strain amplitude and temperature on creep-fatigue behaviors of 9–12% Cr steel // Journal of Mechanical Science and Technology. 2022. Vol. 36. № 5. P. 2265–2276. DOI: 10.1007/s12206-022-0409-y.
18. Chen Furen, Zhang Wei, Zhang Kaihao, Yang Qiaofa, Wang Xiaoxiao, Zhou Changyu. Low cycle fatigue and creep-fatigue interaction behavior of 2.25CrMoV steel at high temperature // Journal of Materials

Research and Technology. 2024. Vol. 28. P. 3155–3165. DOI: 10.1016/j.jmrt.2023.12.233.
19. Shi Shouwen, Cui Jianpeng, Li Haiyan, Chen Gang, Lin Qiang, Chen Xu. Cyclic stress response and microcrack initiation mechanism of modified 9Cr1Mo steel under low cycle fatigue at room temperature and 350 °C // Fatigue and Fracture of Engineering Materials and Structures. 2023. Vol. 46. № 7. P. 2525–2538. DOI: 10.1111/ffe.14015.
20. Zhang Xiaodong, Wang Tianjian, Gong Xiufang, Li Qingsong, Liu Yongjie, Wang Quanyi, Zhang Hong, Wang Qingyuan. Low cycle fatigue properties, damage mechanism, life prediction and microstructure of MarBN steel: Influence of temperature // International Journal of Fatigue. 2021. Vol. 144. Article number 106070. DOI: 10.1016/j.ijfatigue.2020.106070.
21. Mishnev R., Dudova N., Kaibyshev R. Low cycle fatigue behavior of a 10Cr–2W–Mo–3Co–NbV steel // International Journal of Fatigue. 2016. Vol. 83-2. P. 344–355. DOI: 10.1016/j.ijfatigue.2015.11.008.
22. Golański G., Mroziński S. Low cycle fatigue and cyclic softening behaviour of martensitic cast steel // Engineering Failure Analysis. 2013. Vol. 35. P. 692–702. DOI: 10.1016/j.engfailanal.2013.06.019.
23. Zhang Zhen, Hu Zheng-fei, Fan Li-kun, Wang Bin. Low cycle fatigue behavior and cyclic softening of P92 ferritic-martensitic steel // Journal of Iron and Steel Research International. 2015. Vol. 22. P. 534–542. DOI: 10.1016/S1006-706X(15)30037-6.
24. Langford G., Cohen M. Strain hardening of iron by severe plastic deformation // American Society for Metals Transactions. 1969. Vol. 62. P. 623–638.

Малоцикловая усталость 10 % Cr стали с высоким содержанием бора при комнатной температуре

Бражников Иван Сергеевич*[1], инженер
Центра коллективного пользования «Технологии и Материалы НИУ "БелГУ"»
Федосеева Александра Эдуардовна[2], кандидат технических наук,
старший научный сотрудник лаборатории механических свойств наноструктурных и жаропрочных материалов
Белгородский государственный национальный исследовательский университет, Белгород (Россия)

***E-mail:** 1216318@bsu.edu.ru

[1]ORCID: https://orcid.org/0009-0008-8069-7376
[2]ORCID: https://orcid.org/0000-0003-4031-463X

Поступила в редакцию 22.06.2023 *Принята к публикации 16.02.2024*

Аннотация: Высокохромистые стали мартенситного класса являются перспективным материалом для изготовления элементов котлов и паропроводов, а также лопаток и роторов паровых турбин новых энергоблоков тепловых электростанций, работающих на угле. Использование таких материалов даст возможность осуществить переход на суперсверхкритические параметры пара (температура 600–620 °C и давление 25–30 МПа), что позволит увеличить КПД энергоблоков до 45 %. Модификации химического состава высокохромистых сталей привели к существенному повышению жаропрочных характеристик, таких как предел длительной прочности – до 100 000 ч и предел ползучести – до 1 % на базе 100 000 ч, в то время как сопротивление разупрочнению в результате малоцикловой усталости остается недостаточно изученным в данной области. Настоящая работа посвящена исследованию малоцикловой усталости при комнатной температуре с различными амплитудами деформации высокохромистой стали мартенситного класса 10%Cr–3%Co–2%W–0,5%Mo–0,2%Cu–0,2%Re–0,003%N–0,01%B. Предварительно сталь была подвергнута нормализации с 1050 °C с последующим отпуском при 770 °C. После термической обработки структура стали представляла собой реечный троостит отпуска, стабилизированный частицами вторичных фаз карбидов $M_{23}C_6$, карбонитридов NbX и карбидов M_6C. Средняя ширина мартенситных реек составляла 380 нм, а плотность дислокаций – $1{,}4\times10^{14}$ м$^{-2}$. При малоцикловой усталости с увеличением амплитуды деформации с 0,2 до 1 % значительно снижается количество циклов до разрушения, а значение пластической деформации в середине количества циклов нагружения существенно увеличивается. Максимальное разупрочнение (18 %) наблюдается при амплитуде деформации 1 % в середине количества циклов нагружения. В целом структура стали после испытаний на малоцикловую усталость не претерпевает существенных изменений: ширина реек увеличивается на 18 % при амплитуде деформации более 0,3 %, при этом плотность дислокаций сохраняется на достаточно высоком уровне (около 10^{14} м$^{-2}$) при всех амплитудах деформации.

Ключевые слова: жаропрочная сталь мартенситного класса; малоцикловая усталость; амплитуда деформации; циклическое разупрочнение; усталостное разрушение.

Благодарности: Работа выполнена при финансовой поддержке Российского научного фонда (соглашение № 19-73-10089-П). Ссылка на информацию о проекте: https://rscf.ru/project/22-73-41001/.

Авторы выражают благодарность Центру коллективного пользования «Технологии и Материалы НИУ "БелГУ"» за предоставленное оборудование для проведения структурных исследований.

Статья подготовлена по материалам докладов участников XI Международной школы «Физическое материаловедение» (ШФМ-2023), Тольятти, 11–15 сентября 2023 года.

Для цитирования: Бражников И.С., Федосеева А.Э. Малоцикловая усталость 10 % Cr стали с высоким содержанием бора при комнатной температуре // Frontier Materials & Technologies. 2024. № 2. С. 33–42. DOI: 10.18323/2782-4039-2024-2-68-3.

doi: 10.18323/2782-4039-2024-2-68-4

Influence of tool geometry on the formation of welded joint during friction stir welding of the AA5083 aluminum alloy

Igor N. Zybin*[1], PhD (Engineering), Associate Professor,
assistant professor of Chair "Technologies of Connection and Processing of Materials"
Darya A. Buzyreva, graduate student
Kaluga Branch of Bauman Moscow State Technical University, Kaluga (Russia)

***E-mail:** igor.zybin@bmstu.ru,
igor.zybin@mail.ru

[1]ORCID: https://orcid.org/0000-0002-5738-4231

Received 18.10.2023 *Accepted 08.02.2024*

Abstract: One of the important parameters influencing the formation of a weld during friction stir welding is the tool geometry, which affects the processes of heat generation and stirring of metals in their connection zone. These processes influence the formation of a high quality and strength welded joint without continuity defects. In this regard, it is relevant to analyze the influence of tool geometry on the welding mode parameters, at which the welded joint is formed without continuity defects, as well as on the welded joint strength under static tension. The work considers the influence of the cylindrical and conical shapes of the tool pin, as well as the conical shape of the pin with a thread on its outer surface and a spiral groove on the end surface of the tool shoulder on the welding mode parameters, at which the welded joint is formed without continuity defects. The study shows that changing the shape of the pin working surface from cylindrical to a conical one had no effect on the range of welding mode parameters, at which the welded joint is formed without continuity defects. It has been found that the presence of a thread on the pin outer surface and a groove on the end surface of a tool shoulder allows producing welded joints without continuity defects in a wider range of welding mode parameters compared to a simpler tool geometry. The macrostructure of the resulting welded joints was considered. It has been found that the studied tool geometry has almost no influence on the maximum strength values of welded joints produced by friction stir welding and reaches 95 % of the strength of the base metal.

Keywords: friction stir welding; AA5083; tool geometry; strength of the welded joint without continuity defects.

For citation: Zybin I.N., Buzyreva D.A. Influence of tool geometry on the formation of welded joint during friction stir welding of the AA5083 aluminum alloy. *Frontier Materials & Technologies*, 2024, no. 2, pp. 43–52. DOI: 10.18323/2782-4039-2024-2-68-4.

INTRODUCTION

One of the modern advanced methods of joining metals is friction stir welding (FSW). Welding is performed without melting the materials being joined, which means the absence of defects in the joint that are characteristic of arc welding methods. High strength of the welded joint – up to 90–95 % of the base metal strength is ensured [1; 2], and the resulting welded joints are characterized by minimal deformations.

It is known that the tool geometry has a significant influence on the processes of plastic deformation and stirring of the metal, the formation of the structure, the processes of heat release in the welding zone, and the mechanical properties of the welded joint [3–5]. It plays an important role in the formation of a high-quality welded joint without defects.

Currently, tool geometry is characterized by a wide variety [6–8]. The tool consists of two main elements: a pin and a shoulder; both are involved in the process of stirring the metal [3], and have a strong influence on the flow of metal during the welding process [9].

The tool pin is mainly responsible for the direction of the plasticized material flow during welding, the trajectory of which is quite complex [10]. The geometric shape of the tool pin has a significant impact on the processes of heat release in the metal joining zone, and the amount of heat, in turn, affects the structure of a weld, the width of the heat-affected zone, and the quality of a welded joint. In addition, the shape of the tool pin affects the strength of a weld [11]. The pin, in most cases, has a cylindrical or conical surface. When using a pin with a conical surface, the cone angle, as a rule, does not exceed 20°, which is associated with a decrease in tensile strength and elongation at large angles. The pin conical surface may have grooves, threads, and other elements, controlling the plasticized material flow. The use of a conical pin with a thread ensures better stirring of the metal [12; 13]. Stirring the metal several times, before its deposition, helps to remove pores and destroy oxides.

It has been found that the presence of a thread on a pin causes a slight increase in temperature, near the pin, and enhances the flow and mixing of metal [14]. The pin diameter, as a rule, is comparable to the thickness of the samples to be connected, and its length is tenths of a millimeter less than the thickness of the metal. The end of a pin is usually flat or spherical. The former is easier to manufacture, while the latter provides less tool wear.

The shape of the tool shoulder can be flat, concave or convex. The shoulder end surface can be smooth or with notches, grooves and other elements. The presence of various projections on the tool shoulder surface, such as a spiral

groove, contributes to better stirring of the metal. The tool shoulder, along with the pin, provides the necessary heat generation in the zone of its friction with the parts to be welded. Moreover, it provides compaction of the metal and its forging during the welding process.

When selecting tool sizes, it is important to choose the ratio of the shoulder diameter to the tool pin diameter. This ratio plays an important role in the heat release as well as in the stirring of the metal during welding. According to works [15; 16], it is recommended to choose this ratio around 3:1. In this case, better grain refinement and high joint strength are ensured.

In the work [17], using the example of welded joints made of AA5083 aluminum alloy it is shown that the rolling direction influences the strength characteristics of the resulting welded joint. It is necessary to consider this fact when producing welded joints by FSW.

One of the important parameters of welding is the productivity of the process, which can be raised by increasing the welding speed. However, it is not always possible to increase the welding speed, and hereby to ensure a welded joint without continuity defects in the joint zone. Therefore, it is necessary to know whether increasing the complexity of the tool geometry allows expanding the range of parameters of the welding mode, which ensures the production of a welded joint without continuity defects, and whether it is possible to increase the welding speed. Note that during FSW, the welding speed and tool rotation frequency are interrelated. As a rule, when increasing the welding speed, it is necessary to adjust the tool rotation speed. These parameters directly affect the heat release processes in the metal joining zone. Insufficient or excessive heat generation in the welding zone can lead to defects.

In the literature, there is a significant number of works studying the influence of tool geometry on the production of a welded joint from the AA5083 aluminum alloy. In most cases, minor changes in process parameters (typically tool rotation speed and welding speed) are considered for this material. The depth of tool penetration into the sample is often assumed as a constant value, although it has a significant impact on the process of forming a welded joint. Therefore, it is of interest to study the influence of different tool geometry shapes on the welding mode parameters, at different depths of tool penetration into the sample.

The purpose of this work is to study the influence of tool geometry on the welding mode parameters, ensuring the absence of continuity defects in the metal joining zone, and on the strength of the welded joint under static tension.

METHODS

To carry out experimental studies on FSW, sheets of AA5083 aluminum alloy with a thickness of 5 mm were used, butt welding was performed. Tool geometric parameters: pin diameter at the base was 6.5 mm, shoulder diameter was 18.5 mm, and pin length was 4.75 mm. The pin end surface was rounded. The cone angle of the pin surface was 20°. The tool was made of H13 alloy steel, GOST 5950-2000, and hardened at a temperature of 1020 °C, and then tempered at a temperature of 500 °C. The hardness of the working surface of the tool was 53...57 HRC.

Three types of instruments were used during the study (Fig. 1).

Welding was performed on a FSS-400R vertical milling machine (Belarus), the spindle of which has the ability to rotate relative to the vertical axis at an angle of ±45°. The angle of tool inclination to the vertical was constant and amounted to 2°. The rotation frequency and welding speed were changed discretely. Welding of the samples was carried out on a substrate in the form of a Steel 20 sheet, with a thickness of 10 mm. The rolling direction for all samples was the same, and was chosen perpendicular to the weld. The edges of the surfaces to be joined were milled and degreased with acetone before welding. The welding mode parameters (Table 1) were considered in a wide range and were selected taking into account the capabilities of the equipment used at different values of tool shoulder penetration into the sample. The depth of shoulder penetration into the sample was in the range of 0.05...0.4 mm.

a ***b*** ***c***

Fig. 1. *Geometry of a tool for friction stir welding:*
a *– tool with a cylindrical shape of the pin;* ***b*** *– tool with a conical shape of the pin;*
c *– tool with a conical shape of the pin with a thread and a groove on the end surface of the tool shoulder*
Рис. 1. *Геометрические формы инструмента для СТП:*
a *– инструмент с цилиндрической формой пина;* ***b*** *– инструмент с конической формой пина;*
c *– инструмент с конической формой пина с резьбой и канавкой на торцевой поверхности заплечика*

Static tensile tests of welded samples were carried out on an IR 5092-100 universal tensile testing machine (Russia). The dimensions of the samples are shown in Fig. 2. At least three samples were prepared for testing in the same mode. Fig. 3 shows the examples of samples for static tensile tests.

RESULTS

After conducting experimental studies in the selected range of welding mode parameters, the appearance of the welded joints was examined, and macrosections of the cross sections of the welded samples were made to identify possible continuity defects.

Analysis of macrosections showed that when welding samples with tools with cylindrical and conical pin surfaces (Fig. 1 a, 1 b), a welded joint without continuity defects was produced under the following welding modes: tool rotation speed 450–560 rpm, welding speed 31.5–50 mm/min, depth of tool shoulder penetration into the sample 0.05–0.4 mm. One should note that at a tool rotation speed of 710 rpm, a welding speed of 50 mm/min, and a depth of tool shoulder penetration into the part from 0.1...0.15 to 0.4 mm, welded joints without defects in

Table 1. *Values of welding mode parameters for AA5083 aluminum alloy*
Таблица 1. *Значения параметров режимов сварки алюминиевого сплава АМг5*

Tool rotation frequency, rpm	Welding speed, mm/min	Tool angle of inclination to the vertical, °	Depth of tool shoulder penetration into the sample, mm
450–1400	31.5–120.0	2	0.05–0.40

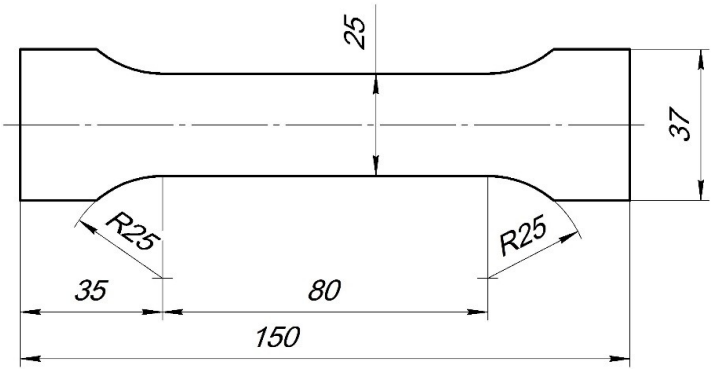

Fig. 2. *Geometrical dimensions of the specimen for static tensile tests*
Рис. 2. *Геометрические размеры образца для испытаний на статическое растяжение*

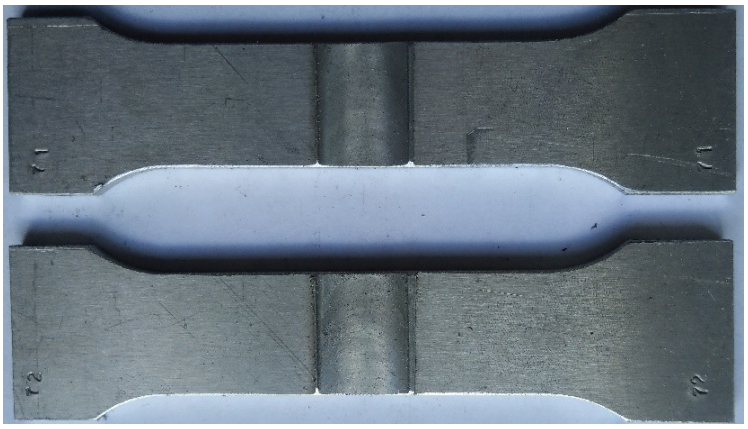

Fig. 3. *Specimens for static tensile tests*
Рис. 3. *Образцы для проведения испытаний на статическое растяжение*

the joint zone were also obtained. When the depth of tool shoulder penetration into the part was up to 0.1...0.15 mm, the lack of fusion was usually observed in the weld root. At a depth of more than 0.4 mm, significant burr was observed at the periphery of the welded joint, due to the extrusion of a large volume of metal into this zone. Examples of the appearance and macrosections of welded joints produced with tools with cylindrical and conical pin surfaces in different welding modes are shown in Fig. 4, 5.

Analysis of macrosections obtained by welding samples using a tool with a conical pin surface (Fig. 1 c), which has a thread on the outer surface and a spiral groove on the shoulder end surface, showed that a welded joint without continuity defects was produced under the following welding modes: rotation speed tool is 450–1120 rpm, welding speed is 31.5–125 mm/min. Fig. 6, 7 show the examples of the appearance and macrosections of welded joints produced using different welding modes.

The values of the ranges of mode parameters (tool rotation frequency and welding speed) for all considered tools are given in Fig. 8.

It was not possible to produce a welded joint without continuity defects outside zones 1 and 2 shown in Fig. 8. The types of main defects in welded joints produced during FSW are given in Fig. 9.

When using tools with a smooth pin surface (Fig. 1 a, 1 b), there was no onion ring structure on macrosections of cross sections of welded joints (Fig. 4 b, 5 b). When using a tool with a thread on the pin outer surface (Fig. 1 c), an onion ring structure was visible on macrosections (Fig. 6 b, 7 b).

When carrying out static tensile tests on welded samples without continuity defects produced using different tool shapes, the ultimate stress values shown in Table 2 were obtained. The table presents the ultimate stress values, indicating the ranges of welding modes.

According to experimental data, the static tension strength of the base metal was 327.1 MPa (average value). The rolling direction in these samples coincided with the tensile force direction during static tension tests.

DISCUSSION

Analysis of the results showed that in the case of all studied shapes of the tool working surface, welded joints without continuity defects were obtained.

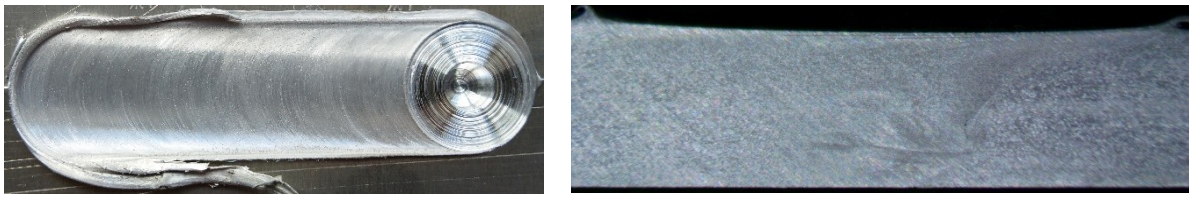

a ***b***

Fig. 4. *Appearance (**a**) and macrosection (**b**) of the cross section of the welded joint produced by a tool with a cylindrical pin shape (Fig. 1 a).*
Welding mode parameters: tool rotation frequency is 560 rpm, welding speed is 50 mm/min, and the depth of tool shoulder penetration into the sample is 0.07 mm
Рис. 4. *Внешний вид (**а**) и макрошлиф (**b**) поперечного сечения сварного соединения, полученного инструментом с цилиндрической формой пина (рис. 1 а).*
Параметры режимов сварки: частота вращения инструмента 560 об/мин, скорость сварки 50 мм/мин, глубина внедрения заплечика инструмента в образец 0,07 мм

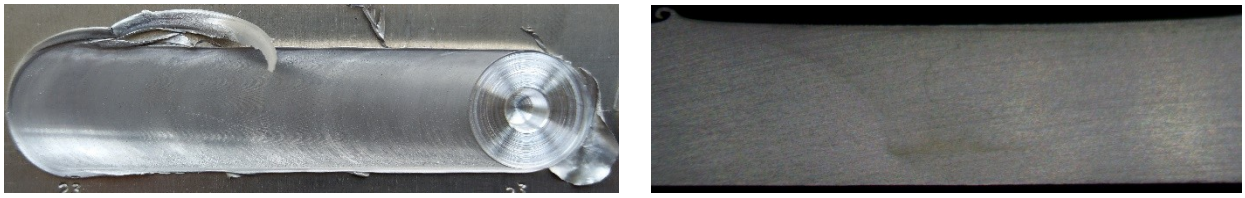

a ***b***

Fig. 5. *Appearance (**a**) and macrosection (**b**) of the cross section of the welded joint produced by a tool with a conical pin shape (Fig. 1 b).*
Welding mode parameters: tool rotation frequency is 450 rpm, welding speed is 31.5 mm/min, and the depth of tool shoulder penetration into the sample is 0.05 mm
Рис. 5. *Внешний вид (**а**) и макрошлиф (**b**) поперечного сечения сварного соединения, полученного инструментом с конической формой пина (рис. 1 b).*
Параметры режимов сварки: частота вращения инструмента 450 об/мин, скорость сварки 31,5 мм/мин, глубина внедрения заплечика инструмента в образец 0,05 мм

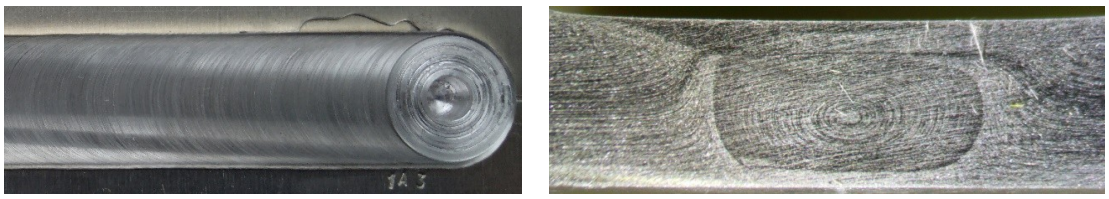

a ***b***

Fig. 6. *Appearance (**a**) and macrosection (**b**) of the cross section of the welded joint produced by a tool with a conical pin shape with a thread and a spiral groove on the end surface of the tool shoulder (Fig. 1 c). Welding mode parameters: tool rotation frequency is 710 rpm, welding speed is 50 mm/min, and the depth of tool shoulder penetration into the sample is 0.06 mm*

Рис. 6. *Внешний вид (**а**) и макрошлиф (**b**) поперечного сечения сварного соединения, полученного инструментом с конической формой пина с резьбой и спиральной канавкой на торцевой поверхности заплечика инструмента (рис. 1 с). Параметры режимов сварки: частота вращения инструмента 710 об/мин, скорость сварки 50 мм/мин, глубина внедрения заплечика инструмента в образец 0,06 мм*

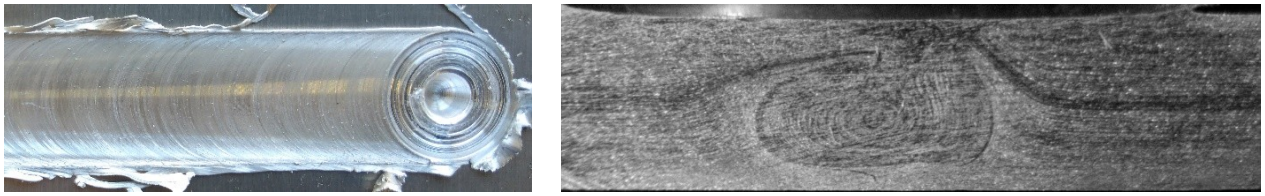

a ***b***

Fig. 7. *Appearance (**a**) and macrosection (**b**) of the cross section of the welded joint produced by a tool with a conical pin shape with a thread and a spiral groove on the end surface of the tool shoulder (Fig. 1 c). Welding mode parameters: tool rotation frequency is 1120 rpm, welding speed is 125 mm/min, and the depth of tool shoulder penetration into the sample is 0.07 mm*

Рис. 7. *Внешний вид (**а**) и макрошлиф (**b**) поперечного сечения сварного соединения, полученного инструментом с конической формой пина с резьбой и спиральной канавкой на торцевой поверхности заплечика инструмента (рис. 1 с). Параметры режимов сварки: частота вращения инструмента 1120 об/мин, скорость сварки 125 мм/мин, глубина внедрения заплечика инструмента в образец 0,07 мм*

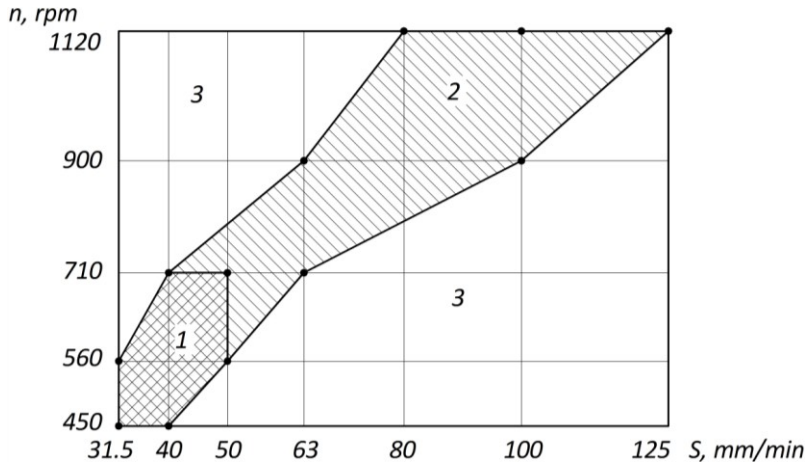

Fig. 8. *Rotation frequency (n) and welding speed (s) when producing butt joints by friction stir welding: 1 – zone without continuity defects (cylindrical and conical shapes of the tool pin without a thread); 2 – zone without continuity defects (conical shape of the pin with a thread and a spiral groove on the end surface of the tool shoulder), including zone 1; 3 – zone with continuity defects (for all tool types)*

Рис. 8. *Частота вращения (n) и скорость сварки (s) при получении стыковых соединений СТП: 1 – зона отсутствия дефектов сплошности (цилиндрическая и коническая форма пина инструмента без резьбы); 2 – зона отсутствия дефектов сплошности (коническая форма пина с резьбой и спиральной канавкой на торцевой поверхности заплечика инструмента), включающая в себя зону 1; 3 – зона наличия дефектов сплошности (для всех типов инструментов)*

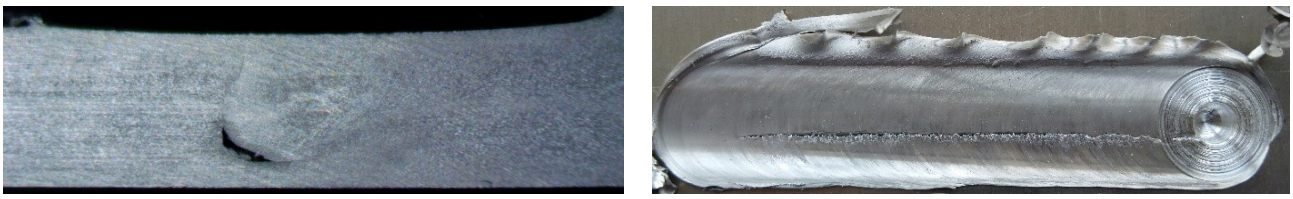

a *b*

Fig. 9. *Main types of defects of welded joints produced by friction stir welding:* ***a*** *– faulty root fusion;* ***b*** *– lack of fusion*
Рис. 9. *Основные виды дефектов сварных соединений, полученных при СТП:* ***a*** *– непровар в корне сварного шва;* ***b*** *– несплавление*

Table 2. *Welding mode parameters and ultimate stress limits of welded joints, which ensured the production of a welded joint without continuity defects*
Таблица 2. *Параметры режимов сварки и пределы прочности сварных соединений, при которых обеспечивалось получение сварного соединения без дефектов сплошности*

Welding mode parameters			Ultimate stress range, (average value), MPa
Tool rotation frequency, rpm	Welding speed, mm/min	Depth of tool shoulder penetration into the sample, mm	
Tool with a cylindrical pin shape (Fig. 1 a)			
450–560	31.5–50.0	0.05–0.40	304,3–318,8 (310,4)
710	50.0	(>0.10…0.15)–0.40	
Tool with a conical pin shape (Fig. 1 b)			
450–560	31.5–50.0	0.05–0.40	308.5–313.6 (311.5)
710	50.0	(>0.10…0.15)–0.40	
Tool with a conical pin shape with a thread and a spiral groove on the end surface of the tool shoulder (Fig. 1 c)			
450–1120	31.5–125.0	0.05–0.40	306.0–313.4 (309.7)

In the works of other authors, there is no information on changing the ranges of welding mode parameters (tool rotation frequency and welding speed) for the production of defect-free welded joints, including the values of these parameters when using a tool without a thread on the pin, as well as with a thread on the pin and a spiral groove at the tool shoulder end surface.

It is found that for cylindrical and conical pin shapes, the ranges of rotational speed and welding speed, at which a welded joint without continuity defects is ensured, coincide. The influence of replacing a cylindrical pin shape with a conical one on the parameters of welding modes for producing defect-free welded joints was not identified in this work.

The thread on the pin outer surface, and the spiral groove on the tool shoulder end surface (Fig. 1 c) significantly improve the conditions for forming a welded joint, which allowed producing welded joints without continuity defects in a wider range of welding mode parameters (rotation frequency and welding speed), compared to a simpler geometry tool (Fig. 1 a, 1 b). By increasing the welding speed, the process productivity can be increased.

Faulty root fusion (Fig. 9 a), as a rule, is characteristic of a low number of revolutions and high welding speed, which leads to insufficient mixing and plasticization of the metal, and heat supply to the welding zone. Lack of fusion (Fig. 9 b) was often observed at a large number of revolutions and different welding speeds, which is likely caused by the excessive heat generation in the metal joining zone.

The presence of an onion structure in welded joints produced by a tool with a pin, having a thread on the outer surface and a spiral groove on the shoulder end surface, is explained by the fact that layers of metal are extruded along the threaded groove of the pin with each revolution of the tool. The onion ring shape caused by different distribution of grain sizes along the spiral [18] is typical when using a tool with a pin having a thread on the surface to produce welded joints from aluminum alloys, including the AA5083 alloy [19]. When using a tool with a smooth

pin outer surface, the metal is stirred in the welding zone constantly and monotonously, and not intermittently. The presence of an onion structure characterizes better conditions for the formation of a weld, which allows using the higher welding speeds to produce welded joints without continuity defects.

The thread on the pin surface contributes to greater grain refinement in the welded joint area. According to the Hall–Petch equation, a decrease in grain size leads to an increase in tensile strength [20]. The experimental studies carried out in the work showed that the maximum values of the ultimate strength obtained for all considered tool geometry forms, are close to each other and amount to about 95 % of the strength of the base metal, i. e., the tool geometry did not affect the maximum values of the ultimate strength.

It was found that when using a cylindrical pin shape and a depth of tool shoulder penetration into the sample not exceeding 0.1...0.15 mm, the maximum value of the tensile strength reached 213.6 MPa (65 % of the strength of the base metal). For a conical pin shape with the same shoulder penetration depth, the maximum value of the ultimate strength reached 295.7 MPa (90 % of the strength of the base metal). In the work [21], when producing welded joints from aluminum alloys, including AA5083 aluminum alloy with a thickness of 0.8...3 mm, using a tool with a conical pin without a thread, it is recommended the tool shoulder to be penetrated into the sample to a depth of 0.1...0.15 mm, since at other depths, defects are formed in the weld. In our case, when using a pin with a thread on the outer surface and a spiral groove on the shoulder end surface, the maximum values of the tensile strength did not depend on the depth of tool shoulder penetration into the sample. It should be noted that, as a rule, when the shoulder penetration depth does not exceed 0.1...0.15 mm, subsequent mechanical processing of the welded joint to remove burr is not required.

The above indicates that at small depths of tool shoulder penetration into the sample, its geometry has a special influence on the processes of stirring metals in the welding zone. It is known that the tool shoulder is responsible for stirring the metal in the upper third of the sample thickness, and this stirring is enhanced in the presence of a spiral groove [9]. The presence of such a groove improves stirring due to the involvement of a larger volume of metal, in the process of plastic deformation, and stirring, a larger surface area of contact between the tool and the metal, which leads to a higher temperature in the joint zone, and lower viscosity of the metal. The use of a tool shoulder with a spiral groove on the end surface together with a threaded pin helps to achieve a higher tensile strength compared to the flat form of the shoulder, when penetrated into the sample to a depth of no more than 0.1...0.15 mm.

Studies aimed at analyzing the depth of tool penetration into the sample, which ensures maximum strength of the welded joint, have not been previously carried out for the cases of tool geometry and AA5083 aluminum alloy considered in the work. The results obtained are important in terms of performing welding with minimal amounts of tool shoulder penetration into the sample. In this case, there is no need for subsequent mechanical processing of the weld to remove flash, which reduces the cost of manufacturing welded products.

Experimental studies have shown that with a cylindrical tool without a thread on the pin, it is possible to obtain the strength of the welded joint at the same level as a tool with a thread on the pin, and a groove on the shoulder end surface.

The work [22], when analyzing the influence of the welding mode parameters of the AA5083 aluminum alloy on the defectiveness of the welded joint structure, noted the importance of the heat input coefficient defined as the ratio of the welding speed to the tool rotation frequency, and characterizing the heat introduced into the welding zone. In [23], defect-free welded joints from AA5083 aluminum alloy were produced at a given ratio in the range of 0.05...0.26 mm/rev. The author [21] found that the heat input coefficient when forming AA5083 aluminum alloy welded joints, without continuity defects, corresponded to the range of 0.058...0.187 mm/rev. Analysis of the results of experimental studies carried out in this work showed that the heat input coefficient in zones 1 and 2 (Fig. 8) corresponds to values in the range of 0.056...0.11, which is consistent with the data of [21; 23].

CONCLUSIONS

Changing the shape of the working surface of the tool pin from cylindrical to a conical one, had no effect on the choice of the range of welding mode parameters ensuring the absence of continuity defects, as well as on the static tensile strength.

The presence of a thread on the working surface of the tool pin, and a spiral groove on the shoulder end surface, leads to the formation of a welded joint without continuity defects in a wider range of mode parameters compared to tools without the above elements.

The maximum tensile strength values for joints produced using cylindrical and conical pins without threads, are ensured, when the shoulder penetrates into the sample to a depth of more than 0.1...0.15 mm, and for a conical pin with threads – from 0.05 mm.

For all considered forms of tool geometry, the maximum values of the static tensile strength reached 95 % of the strength of the base metal.

REFERENCES

1. Arbegast W.J. Friction stir welding after a decade of development. *Welding Journal*, 2006, vol. 85, no. 3, pp. 28–35.
2. Okamura H., Aota K., Ezumi M. Friction stir welding of aluminum alloy and application to structure. *Journal of Japan Institute of Light Metals*, 2000, vol. 50, no. 4, pp. 166–172. DOI: 10.2464/jilm.50.166.
3. Manigandan K., Senthilkumar S. Review of friction stir welding tools. *Journal of Advanced Engineering Research*, 2018, vol. 5, no. 1, pp. 41–51.
4. Chandrashekar A., Ajay Kumar B.S., Reddappa H.N. Friction stir welding: tool Material and geometry. *AKGEK International Journal of Technology*, 2015, vol. 6, no. 1, pp. 16–20.

5. Yang Min, Bao Rui-jun, Liu Xiu-zhong, Song Chao-qun. Thermo-mechanical interaction between aluminum alloy and tools with different profiles during friction stir wielding. *Transactions of Nonferrous Metals Society of China*, 2019, vol. 29, no. 3, pp. 495–506. DOI: 10.1016/S1003-6326(19)64958-7.
6. Kumar P.M., Anbumalar V., Ramesh Babu K.R. A review on progress of different types of friction stir welding tool geometry design. *Australian Journal of Basic and Applied Sciences*, 2014, vol. 16, no. 8, pp. 364–371.
7. Ratković N., Jovanović Pešić Ž., Arsić D., Pešić M., Džunić D. Tool geometry effect on material flow and mixture in FSW. *Advanced Technologies & Materials*, 2022, vol. 47, no. 2, pp. 33–36. DOI: 10.24867/ATM-2022-2-006.
8. Zhang Y.N., Cao X., Larose S., Wanjara P. Review of tools for friction stir welding and Processing. *Canadian Metallurgical Quarterly*, 2012, vol. 51, no. 3, pp. 250–261. DOI: 10.1179/1879139512Y.0000000015.
9. Ambrosio D., Morisada Y., Ushioda Y., Fujii H. Material flow in friction stir welding: A review. *Journal of Materials Processing Technology*, 2023, vol. 320, article number 118116. DOI: 10.1016/j.jmatprotec.2023.118116.
10. Kumar R., Pancholi V. Three-dimensional material flow during friction stir welding of AA5083. *Journal of Manufacturing Processes*, 2021, vol. 68-A, pp. 1214–1223. DOI: 10.1016/j.jmapro.2021.06.051.
11. Mohanty H.K., Mahapatra M.M., Kumar P., Biswas P., Mandal N.R. Effect of tool shoulder and pin probe profiles on friction stirred aluminum welds – a comparative study. *Journal of Marine Science and Application*, 2012, vol. 11, pp. 200–207. DOI: 10.1007/s11804-012-1123-4.
12. Meshram S., Madhusudhan Reddy G., Venugopal Rao V. Role of threaded tool pin profile and rotational speed on generation of defect free friction stir AA 2014 aluminium alloy welds. *Defence Science Journal*, 2016, vol. 66, no. 1, pp. 57–63. DOI: 10.14429/dsj.66.8566.
13. Hassan Kh.A.A., Prangnell P.B., Norman A.F., Price D.A., Williams S.W. Effect of welding parameters on nugget zone microstructure and properties in high strength aluminium alloy friction stir welds. *Science and Technology of Welding and Joining*, 2003, vol. 8, no. 4, pp. 257–268. DOI: 10.1179/136217103225005480.
14. Jiang Tao, Wu Chuan Song, Shi Lei. Effects of tool pin thread on temperature field and material mixing in friction stir welding of dissimilar Al/Mg alloys. *Journal of Manufacturing Processes*, 2022, vol. 74, pp. 112–122. DOI: 10.1016/j.jmapro.2021.12.008.
15. Vijayavel P., Balasubramanian V., Sundaram S. Effect of shoulder diameter to pin diameter (D/d) ratio on tensile strength and ductility of friction stir processed LM25AA-5% SiCp metal matrix composites. *Materials and Design*, 2014, vol. 57, pp. 1–9. DOI: 10.1016/j.matdes.2013.12.008.
16. Vijayavel P., Sundararajan T., Rajkumar I., Anantha-kumar K. Effect of tool diameter ratio of tapered cylindrical profile pin on wear characteristics of friction stir processing of Al–Si alloy reinforced with SiC ceramic particles. *Metal Powder Report*, 2021, vol. 76, no. 2, pp. 75–89. DOI: 10.1016/j.mprp.2020.04.005.
17. Gusarova A.V., Rubtsov V.E., Kolubaev E.A., Bakshaev V.A., Nikitin Yu.V. The influence of the rolling direction of AA5056 on the microstructure and properties of weld joints obtained by friction stir welding. *Obrabotka metallov / Metal working and material science*, 2020, vol. 22, no. 4, pp. 124–136. DOI: 10.17212/1994-6309-2020-22.4-124-136.
18. Alemdar A.S.A., Jalal S.R., Mulapeer M.M. Effect of exfoliation corrosion on the efficient hybrid joint of AA2024-T3 and AA2198-T8 formed by friction stir welding. *Heliyon*, 2023, vol. 9, no. 6, article number e16577. DOI: 10.1016/j.heliyon.2023.e16577.
19. Sizova O.V., Kolubaev A.V., Kolubaev E.A., Zaikina A.A., Rubtsov V.E. Fracture of friction stir welded butt joints structure of aluminum-magnesium alloy. *Obrabotka metallov / Metal working and material science*, 2014, no. 3, pp. 14–20. EDN: SKXOBD.
20. Dawood H.I., Mohammed K.S., Rahmat A., Uday M.B. Effect of small tool pin profiles on microstructures and mechanical properties of 6061 aluminum alloy by friction stir welding. *Transactions of Nonferrous Metal Society of China*, 2015, vol. 25, no. 9, pp. 2856−2865. DOI: 10.1016/S1003-6326(15)63911-5.
21. Poklyatskiy A.G. Parameters of FSW process of thin sheet aluminium alloys. *Vestnik of Polotsk State University. Part B. Industry. Applied Sciences*, 2015, no. 11, pp. 53–58. EDN: UOHBAH.
22. Sizova O.V., Kolubaev A.V., Kolubaev E.A., Zaikina A.A., Rubtsov V.E. Effect of main parameters of the friction stir welding on structure imperfections of welded joint. *Obrabotka metallov / Metal working and material science*, 2017, no. 4, pp. 19–29. DOI: 10.17212/1994-6309-2017-4-19-29.
23. Ovchinnikov V.V., Drits A.M. Technological peculiarities of friction welding with Al–Mg aluminum alloys stir. *Science intensive technologies in mechanical*, 2019, no. 3, pp. 7–20. DOI: 10.30987/article_5c7434ed5317f2.05345899.

СПИСОК ЛИТЕРАТУРЫ

1. Arbegast W.J. Friction stir welding after a decade of development // Welding Journal. 2006. Vol. 85. № 3. P. 28–35.
2. Okamura H., Aota K., Ezumi M. Friction stir welding of aluminum alloy and application to structure // Journal of Japan Institute of Light Metals. 2000. Vol. 50. № 4. P. 166–172. DOI: 10.2464/jilm.50.166.
3. Manigandan K., Senthilkumar S. Review of friction stir welding tools // Journal of Advanced Engineering Research. 2018. Vol. 5. № 1. P. 41–51.
4. Chandrashekar A., Ajay Kumar B.S., Reddappa H.N. Friction stir welding: tool Material and geometry // AKGEK International Journal of Technology. 2015. Vol. 6. № 1. P. 16–20.
5. Yang Min, Bao Rui-jun, Liu Xiu-zhong, Song Chao-qun. Thermo-mechanical interaction between aluminum alloy and tools with different profiles during friction stir wielding // Transactions of Nonferrous Metals Society of China. 2019. Vol. 29. № 3. P. 495–506. DOI: 10.1016/S1003-6326(19)64958-7.
6. Kumar P.M., Anbumalar V., Ramesh Babu K.R. A review on progress of different types of friction stir welding tool geometry design // Australian Journal of Basic and Applied Sciences. 2014. Vol. 16. № 8. P. 364–371.

7. Ratković N., Jovanović Pešić Ž., Arsić D., Pešić M., Džunić D. Tool geometry effect on material flow and mixture in FSW // Advanced Technologies & Materials. 2022. Vol. 47. № 2. P. 33–36. DOI: 10.24867/ATM-2022-2-006.
8. Zhang Y.N., Cao X., Larose S., Wanjara P. Review of tools for friction stir welding and Processing // Canadian Metallurgical Quarterly. 2012. Vol. 51. № 3. P. 250–261. DOI: 10.1179/1879139512Y.0000000015.
9. Ambrosio D., Morisada Y., Ushioda Y., Fujii H. Material flow in friction stir welding: A review // Journal of Materials Processing Technology. 2023. Vol. 320. Article number 118116. DOI: 10.1016/j.jmatprotec.2023.118116.
10. Kumar R., Pancholi V. Three-dimensional material flow during friction stir welding of AA5083 // Journal of Manufacturing Processes. 2021. Vol. 68-A. P. 1214–1223. DOI: 10.1016/j.jmapro.2021.06.051.
11. Mohanty H.K., Mahapatra M.M., Kumar P., Biswas P., Mandal N.R. Effect of tool shoulder and pin probe profiles on friction stirred aluminum welds – a comparative study // Journal of Marine Science and Application. 2012. Vol. 11. P. 200–207. DOI: 10.1007/s11804-012-1123-4.
12. Meshram S., Madhusudhan Reddy G., Venugopal Rao V. Role of threaded tool pin profile and rotational speed on generation of defect free friction stir AA 2014 aluminium alloy welds // Defence Science Journal. 2016. Vol. 66. № 1. P. 57–63. DOI: 10.14429/dsj.66.8566.
13. Hassan Kh.A.A., Prangnell P.B., Norman A.F., Price D.A., Williams S.W. Effect of welding parameters on nugget zone microstructure and properties in high strength aluminium alloy friction stir welds // Science and Technology of Welding and Joining. 2003. Vol. 8. № 4. P. 257–268. DOI: 10.1179/136217103225005480.
14. Jiang Tao, Wu Chuan Song, Shi Lei. Effects of tool pin thread on temperature field and material mixing in friction stir welding of dissimilar Al/Mg alloys // Journal of Manufacturing Processes. 2022. Vol. 74. P. 112–122. DOI: 10.1016/j.jmapro.2021.12.008.
15. Vijayavel P., Balasubramanian V., Sundaram S. Effect of shoulder diameter to pin diameter (D/d) ratio on tensile strength and ductility of friction stir processed LM25AA-5% SiCp metal matrix composites // Materials and Design. 2014. Vol. 57. P. 1–9. DOI: 10.1016/j.matdes.2013.12.008.
16. Vijayavel P., Sundararajan T., Rajkumar I., Anantha-kumar K. Effect of tool diameter ratio of tapered cylindrical profile pin on wear characteristics of friction stir processing of Al–Si alloy reinforced with SiC ceramic particles // Metal Powder Report. 2021. Vol. 76. № 2. P. 75–89. DOI: 10.1016/j.mprp.2020.04.005.
17. Гусарова А.В., Рубцов В.Е., Колубаев Е.А., Бакшаев В.А., Никитин Ю.В. Влияние направления проката АМг5 на микроструктуру и свойства сварных соединений, полученных сваркой трением с перемешиванием // Обработка металлов (технология, оборудование, инструменты). 2020. Т. 22. № 4. С. 124–136. DOI: 10.17212/1994-6309-2020-22.4-124-136.
18. Alemdar A.S.A., Jalal S.R., Mulapeer M.M. Effect of exfoliation corrosion on the efficient hybrid joint of AA2024-T3 and AA2198-T8 formed by friction stir welding // Heliyon. 2023. Vol. 9. № 6. Article number e16577. DOI: 10.1016/j.heliyon.2023.e16577.
19. Сизова О.В., Колубаев А.В., Колубаев Е.А., Заикина А.А., Рубцов В.Е. Разрушение стыковых соединений алюминиево-магниевого сплава, выполненных способом сварки трением с перемешиванием // Обработка металлов (технология, оборудование, инструменты). 2014. № 3. С. 14–20. EDN: SKXOBD.
20. Dawood H.I., Mohammed K.S., Rahmat A., Uday M.B. Effect of small tool pin profiles on microstructures and mechanical properties of 6061 aluminum alloy by friction stir welding // Transactions of Nonferrous Metal Society of China. 2015. Vol. 25. № 9. P. 2856−2865. DOI: 10.1016/S1003-6326(15)63911-5.
21. Покляцкий А.Г. Параметры процесса сварки трением с перемешиванием тонколистовых алюминиевых сплавов // Вестник Полоцкого государственного университета. Серия В: Промышленность. Прикладные науки. 2015. № 11. С. 53–58. EDN: UOHBAH.
22. Сизова О.В., Колубаев А.В., Колубаев Е.А., Заикина А.А., Рубцов В.Е. Влияние основных параметров процесса сварки трением с перемешиванием на дефектность структуры сварного соединения // Обработка металлов (технология, оборудование, инструменты). 2017. № 4. С. 19–29. DOI: 10.17212/1994-6309-2017-4-19-29.
23. Овчинников В.В., Дриц А.М. Технологические особенности сварки трением с перемешиванием соединений из алюминиевых сплавов системы Al–Mg // Наукоемкие технологии в машиностроении. 2019. № 3. С. 7–20. DOI: 10.30987/article_5c7434ed5317f2.05345899.

Влияние геометрии инструмента на формирование сварного соединения при сварке трением с перемешиванием алюминиевого сплава АМг5

Зыбин Игорь Николаевич*[1], кандидат технических наук, доцент,
доцент кафедры «Технологии соединения и обработки материалов»
Бузырева Дарья Алексеевна, магистрант
Калужский филиал Московского государственного технического университета имени Н.Э. Баумана, Калуга (Россия)

***E-mail:** igor.zybin@bmstu.ru,
igor.zybin@mail.ru

[1]ORCID: https://orcid.org/0000-0002-5738-4231

Поступила в редакцию 18.10.2023 *Принята к публикации 08.02.2024*

Аннотация: Одним из важных параметров, влияющих на формирование сварного шва при сварке трением с перемешиванием, является геометрия инструмента, которая влияет на процессы тепловыделения и перемешивания металлов в зоне соединения. От протекания этих процессов зависит получение качественного и прочного сварного соединения без дефектов сплошности. В связи с этим представляется актуальным анализ влияния геометрии инструмента на параметры режима сварки, при которых сварное соединение формируется без дефектов сплошности, а также на прочность сварного соединения при статическом растяжении. В работе рассмотрено влияние цилиндрической и конической форм пина инструмента, а также конической формы пина с резьбой на наружной поверхности и спиральной канавкой на торцевой поверхности заплечика инструмента на параметры режима сварки, при которых сварное соединение формируется без дефектов сплошности. Показано, что изменение формы рабочей поверхности пина с цилиндрической на коническую не оказало влияния на диапазон параметров режима сварки, при которых сварное соединение формируется без дефектов сплошности. Установлено, что наличие резьбы на наружной поверхности пина и канавки на торцевой поверхности заплечика позволяет получать сварные соединения без дефектов сплошности в более широком диапазоне параметров режима сварки по сравнению с более простой геометрией инструмента. Рассмотрена макроструктура сварных соединений, полученных при использовании различных геометрических форм инструмента. Установлено, что рассмотренная геометрия инструмента практически не влияет на максимальные значения прочности сварных соединений, полученных сваркой трением с перемешиванием, и достигает 95 % от прочности основного металла.

Ключевые слова: сварка трением с перемешиванием; АМг5; геометрия инструмента; прочность сварного соединения без дефектов сплошности.

Для цитирования: Зыбин И.Н., Бузырева Д.А. Влияние геометрии инструмента на формирование сварного соединения при сварке трением с перемешиванием алюминиевого сплава АМг5 // Frontier Materials & Technologies. 2024. № 2. С. 43–52. DOI: 10.18323/2782-4039-2024-2-68-4.

doi: 10.18323/2782-4039-2024-2-68-5

The study of transformations of supercooled austenite during step quenching of 20Cr2Mn2SiNiMo steel

Mikhail V. Maisuradze[1,3], PhD (Engineering), Associate Professor,
assistant professor of Chair "Heat Treatment and Physics of Metals"
Aleksandra A. Kuklina*[1,2,4], PhD (Engineering),
assistant professor of Chair "Physics",
Head of Scientific-Research and Testing Laboratory of Geocryology, Soil Physics and Materials,
engineer of Laboratory of Structural Methods of Analysis and Properties of Materials and Nanomaterials
Vera V. Nazarova[1], postgraduate student of Chair "Heat Treatment and Physics of Metals"
[1]*Ural Federal University named after the first President of Russia B.N. Yeltsin, Yekaterinburg (Russia)*
[2]*Ural State Mining University, Yekaterinburg (Russia)*

***E-mail:** kuklina@m.ursmu.ru,
Kuklina.aleksandra@rambler.ru

[3]ORCID: https://orcid.org/0000-0003-2850-2988
[4]ORCID: https://orcid.org/0000-0003-3779-3254

Received 26.06.2023 *Accepted 26.01.2024*

Abstract: Currently, step quenching of steels in the temperature range of martensitic transformation, including quenching – partitioning, has found wide application in the automotive industry. Step quenching technology is successfully used to increase a set of properties, which most often include temporary tensile strength and relative elongation. The authors carried out a dilatometric study of the supercooled austenite transformations occurring in the 20Cr2Mn2SiNiMo steel, when implementing various options of step quenching with holding in the martensitic region. It was found that after single-stage quenching, single-stage quenching followed by tempering, and two-stage quenching, primary martensite, isothermal bainite, and secondary martensite are formed in various quantitative ratios. Using X-ray diffraction phase analysis, the amount of residual austenite was determined during step quenching. It has been shown that two-stage quenching makes it possible to stabilise up to 14 % of residual austenite, in the structure of the studied steel, at room temperature. Research has revealed that 20Cr2Mn2SiNiMo steel is characterised by a decrease in the crystal lattice parameter of the residual austenite, with an increase in its content in the steel structure. Uniaxial tensile and impact bending tests were carried out, and the values of the mechanical properties were determined. It has been found that during two-stage quenching, higher strength and elongation values, with lower values of relative contraction and impact strength are achieved compared to oil quenching and low-temperature tempering. The study showed that, with regard to the structural reliability of machine-building parts, step quenching is not the optimal heat treatment mode for the steel under study. The best combination of strength, ductility and impact hardness is achieved after quenching and low-temperature tempering.

Keywords: supercooled austenite transformations; step quenching; 20Cr2Mn2SiNiMo steel; 20Cr2Mn2SiNiMo; quenching – partitioning; isothermal quenching; quenching and tempering; residual austenite; primary martensite; isothermal bainite; secondary martensite.

Acknowledgments: The study was supported by the Russian Science Foundation grant No. 22-29-00106, https://grant.rscf.ru/prjcard_int?22-29-00106.

The paper was written on the reports of the participants of the XI International School of Physical Materials Science (SPM-2023), Togliatti, September 11–15, 2023.

For citation: Maisuradze M.V., Kuklina A.A., Nazarova V.V. The study of transformations of supercooled austenite during step quenching of 20Cr2Mn2SiNiMo steel. *Frontier Materials & Technologies*, 2024, no. 2, pp. 53–65. DOI: 10.18323/2782-4039-2024-2-68-5.

INTRODUCTION

Step quenching of steels, in the temperature range of martensitic transformation, has found wide application in the automotive industry. In particular, the quenching – partitioning concept was developed, which is based on the assumption of the quasi-equilibrium of martensite α-phase, and austenite γ-phase during isothermal holding in the range from the beginning to the end of the M_n...M_k martensitic transformation [1]. If this condition is met, carbon from the supersaturated martensite α-phase diffuses into the surrounding unconverted austenite, thereby changing its chemical composition. As a result, upon further cooling to room temperature, no transformations occur, and the carbon-enriched residual austenite remains in a stable state. However, to implement such a scenario, it is necessary that there are no competing processes leading to a decrease in the residual austenite amount, and the degree of its enrichment with carbon (the formation of bainite and precipitation of carbide phase particles).

The quenching – partitioning technology of step quenching, in various variants is successfully used to increase a set of properties, which most often include tensile strength and relative elongation [2; 3], as the most important for the production of high-strength sheet parts for the automotive industry using deep drawing. For this

purpose, special grades of Quenching–Partitioning steels (QP steels) alloyed mainly with silicon, manganese and aluminium are being developed [4]. Step quenching is also used when producing mechanical engineering parts from structural steels [5]. In this case, as in the case of specially developed QP steels, significant deviations of the practically obtained results, from the theoretically predicted ones, are observed [6]. In particular, the volume fraction of residual austenite in the structure of steels after step quenching in the vast majority of cases turns out to be less than the calculated value [7]. This is related to the fact that it is almost impossible to exclude the formation of bainite and carbides in the steel structure during isothermal holding. The precipitation of carbides and the formation of bainite cannot but affect such properties of steel as impact strength and relative contraction. These characteristics are rarely analysed in published works, despite their practical significance in relation to constructional steels: the impact strength of steel has a certain correlation with wear resistance [8; 9], and the relative contraction – with the endurance limit [10; 11].

The purpose of this work is to study the transformations occurring in high-strength constructional 20Cr2Mn2SiNiMo steel during step quenching.

METHODS

The chemical composition of the steel under study is given in Table 1.

The transformation of supercooled austenite was studied using a LINSEIS L78 R.I.T.A dilatometer. Dilatometric samples had a diameter of 4 mm and a length of 10 mm. Heating and holding at the austenitisation temperature (900 °C, 20 min) were carried out in a vacuum; cooling of the samples to the isothermal holding temperature, was carried out at a given rate (20 °C/s) in a helium flow. Fig. 1 shows the diagram of heat treatment modes (QP1 – single-stage quenching; QP2 – two-stage quenching; QPT – single-stage quenching with tempering), of the steel under study during dilatometric studies.

To assess quantitatively the microstructure formed in 20Cr2Mn2SiNiMo steel during step quenching, the lever rule was used in relation to dilatometric curves [12; 13]. The temperature of the first quenching stage (280 °C), was determined according to the procedure used for QP steels [14; 15]. According to calculations, at a given cooling interruption temperature, the maximum amount of residual austenite (up to 25 %) should be stabilised in the structure of the steel under study. The temperature of the second stage of holding (350 °C) was chosen in the M_n temperature region of the steel under study (345±5 °C).

The indicated step quenching modes were implemented, during laboratory heat treatment of prismatic blanks with the dimensions of 12×12×65 mm, from which samples for mechanical uniaxial tension and impact bending tests were subsequently made. For heat treatment, SNOL laboratory chamber furnaces (austenitisation, tempering) and SShOL shaft crucible furnaces (isothermal holding) with molten salt (50 % KNO_3 + 50 % $NaNO_3$) were used. Cooling of the samples to room temperature was carried out in I20A quenching oil. After step quenching, all samples were subjected to low-temperature tempering at 180 °C for 2 h.

Mechanical properties under uniaxial tension, were determined in accordance with GOST 1497 on an Instron installation at room temperature. For the analysis, cylindrical samples (type III) with a working part diameter of 6 mm, and a working part length of 30 mm were used. Impact bending tests were carried out using a pendulum impact tester, in accordance with GOST 9454, at room temperature on standard samples, with a *V*-shaped stress concentrator (type 11).

X-ray structural phase analysis, was carried out on a Bruker D8 Advance X-ray diffractometer in Co–Kα radiation, in the range of reflection angles of 2θ=45...130° at voltage *U*=35 kV, tube current *I*=40 mA. Quantitative X-ray phase analysis was carried out according to the reference-free full-profile Rietveld analysis method using the TOPAS® 4.2 software package.

The microstructure was studied using a Jeol JSM 6490 scanning electron microscope.

RESULTS

A dilatometric study of the transformations occurring in 20Cr2Mn2SiNiMo steel during QP1 single-stage quenching showed that upon cooling to the first stage temperature (280 °C), a significant amount of M1 primary martensite is formed. The temperature at which primary martensite begins to form in the steel under study is 345 °C (arrow 1 in Fig. 2 a). During cooling interruption and holding for 10 min (arrow 2 in Fig. 2 a), the size of the sample continues to increase, which indicates the development of an isothermal bainite transformation (Fig. 2 b). Upon final cooling from a temperature of 280 °C, the formation of M2 secondary martensite is observed (arrow 3 in Fig. 2 a). The temperature at which the secondary martensitic transformation begins in the case of single-stage quenching is 215 °C.

Table 1. *Chemical composition of 20Cr2Mn2SiNiMo steel*
Таблица 1. *Химический состав стали 20Cr2Mn2SiNiMo*

Chemical element	C	Cr	Mn	Si	Ni	Mo	S	P
wt. %	0.220	1.960	2.020	0.960	1.090	0.310	0.002	0.010

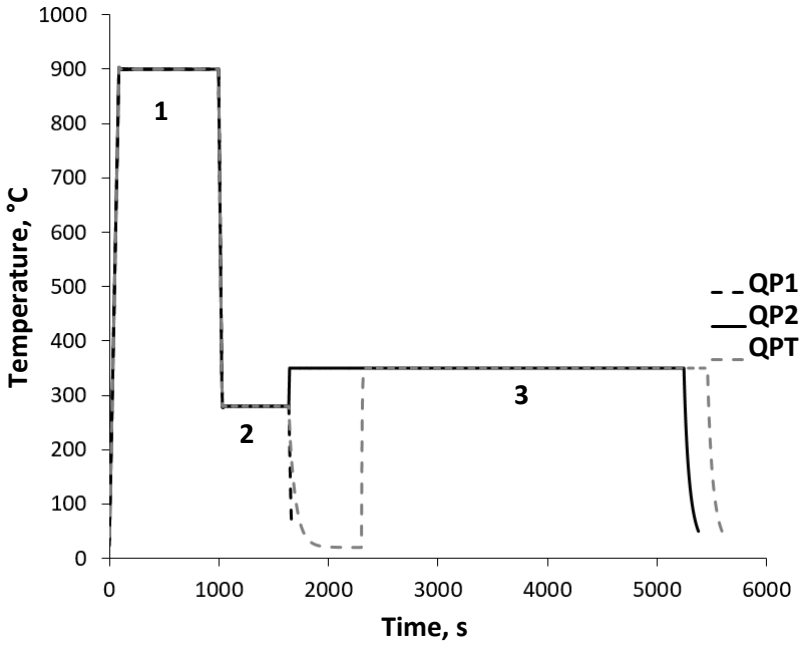

Fig. 1. *Scheme of implemented modes of step quenching of 20Cr2Mn2SiNiMo steel: QP1 – single-stage quenching; QP2 – two-stage quenching; QPT – single-stage quenching with tempering. 1 – austenitisation, 900 °C, 20 min; 2 – first stage, 280 °C, 10 min; 3 – second stage, 350 °C, 60 min*

Рис. 1. *Схема реализованных режимов ступенчатой закалки стали 20Х2Г2СНМА: QP1 – одноступенчатая закалка; QP2 – двухступенчатая закалка; QPT – одноступенчатая закалка с отпуском. 1 – аустенитизация, 900 °C, 20 мин; 2 – первая ступень, 280 °C, 10 мин; 3 – вторая ступень, 350 °C, 60 мин*

In the case of QP2 two-stage quenching, upon cooling from the austenitisation temperature to the first stage temperature (280 °C), just as in the case of QP1, the formation of M1 primary martensite occurs (the transformation onset temperature is 345 °C, arrow 1 in Fig. 3 a), after which some isothermal bainite is formed (arrow 2 in Fig. 3 a). After holding at a temperature of 280 °C for 10 min, the sample was heated to a temperature of 350 °C to increase the carbon diffusion rate. However, as dilatometric studies showed, when the second stage temperature was reached, the formation of bainite continued in the steel under study (Fig. 3 b).

In the case of QPT single-stage quenching with medium-temperature tempering, a mixture of M1 primary martensite (arrow 1 in Fig. 4 a), isothermal bainite formed at the first stage of treatment at a temperature of 280 °C (arrow 2 in Fig. 4 a), and M2 secondary martensite, the temperature of the formation onset which is 215 °C (arrow 3 in Fig. 4 a), was heated to a temperature of 350 °C. During holding at a temperature of 350 °C, no changes in the sample dimensions occur (Fig. 4 b), and upon subsequent cooling, only a slight deviation from the linear dependence is observed, associated with the formation of no more than 3 % of a new portion of M2 secondary martensite (arrow 5 in Fig. 4 a).

By calculations, dependences of the formed α-phase fraction on the temperature were obtained not taking into account residual austenite (Fig. 5). In particular, it was found that when implementing QP1 single-stage quenching, 73 % of primary martensite, 11 % of bainite and 16 % of secondary martensite are formed in the steel structure (Fig. 5 a); and with QP2 two-stage quenching – 75 % of primary martensite, 16 % of bainite (in total at the first and second stages of treatment), and 9 % of secondary martensite (Fig. 5 b).

After setting the structural-phase composition of the steel under study, taking into account the amount of residual austenite, the diagram shown in Fig. 6 was constructed.

Fig. 7 shows the lattice parameter values of residual austenite in the 20Cr2Mn2SiNiMo steel structure, after step quenching and isothermal quenching, at a temperature of 320 °C. The highest austenite lattice parameter is observed during single-stage quenching followed by tempering (Fig. 7 a). In 20Cr2Mn2SiNiMo steel at a holding temperature of 320 °C, the amount of residual austenite in the structure increases with increasing holding duration from 5 to 10 %, and the austenite crystal lattice parameter decreases from 3.6068 to 3.6037 Å.

The results of a metallographic study of the 20Cr2Mn2SiNiMo steel microstructure are shown in Fig. 8. In the case of QP1 single-stage quenching and QPT single-stage quenching with tempering, a pronounced edging of the primary martensite and bainite packets with

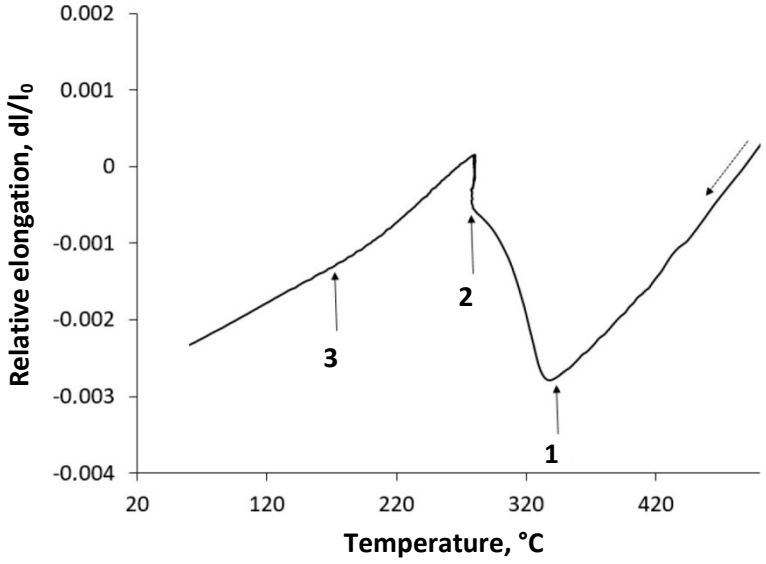

a

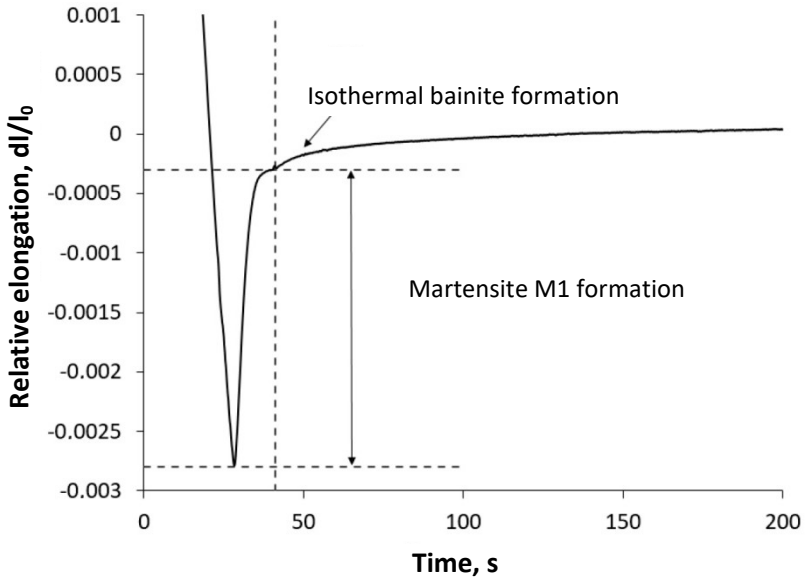

b

Fig. 2. *The dependence of relative elongation of the 20Cr2Mn2SiNiMo steel sample on the temperature (**a**) and time (**b**) when implementing QP1 single-stage quenching.*
1 – M1 primary martensite formation; 2 – isothermal holding at 280 °C, 10 min; 3 – M2 secondary martensite formation
Рис. 2. *Зависимость относительного удлинения образца стали 20Х2Г2СНМА от температуры (**а**) и времени (**b**) при реализации одноступенчатой закалки QP1.*
1 – образование первичного мартенсита М1; 2 – изотермическая выдержка при 280 °С, 10 мин; 3 – образование вторичного мартенсита М2

residual austenite, is observed (Fig. 8 a, 8 b). Moreover, in the case of QPT single-stage quenching with tempering (Fig. 8 b), the austenitic edging of the α-phase packets is more pronounced, which indicates an additional carbon outflow from martensite (primary and secondary) and bainite during the tempering process. In the case of two-stage quenching, no such pronounced boundaries were identified, and the secondary martensite/residual austenite areas have a diffuse structure (Fig. 8 c).

Table 2 shows the mechanical properties of the studied 20Cr2Mn2SiNiMo steel after step quenching, as well as after other heat treatment modes that provide a similar level of strength (isothermal quenching for 2 h at temperatures of 280 and 300 °C; oil quenching and tempering at temperatures of 200 and 300 °C).

Fig. 9 shows comparative diagrams of the mechanical properties of the steel under study after various heat treatment modes.

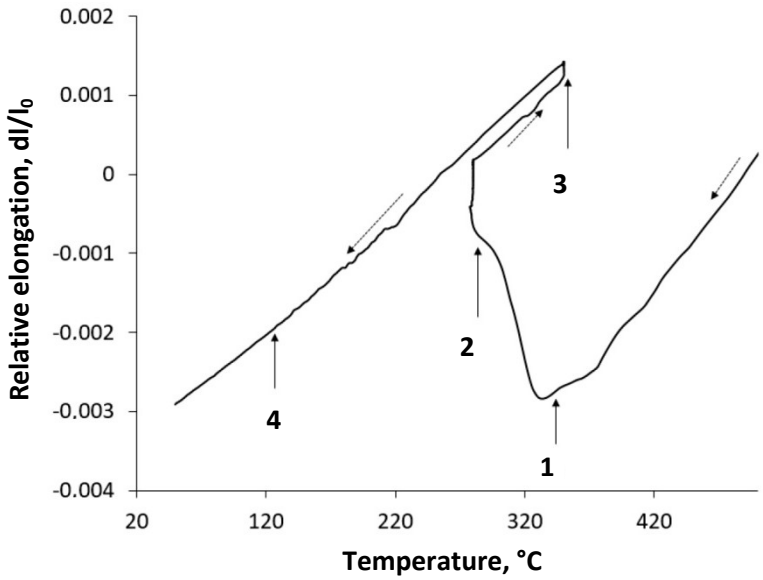

a

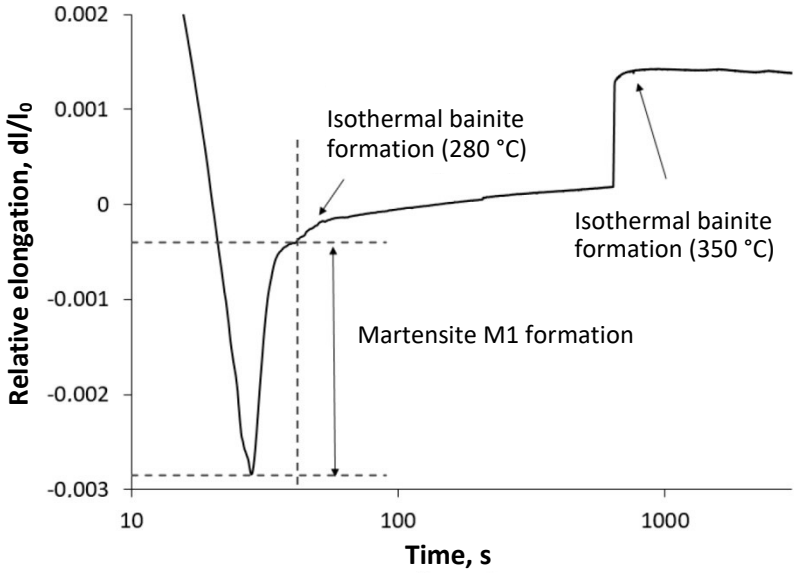

b

Fig. 3. *The dependence of relative elongation of the 20Cr2Mn2SiNiMo steel sample on the temperature (**a**) and time (**b**) when implementing QP2 two-stage quenching.*
1 – M1 primary martensite formation; 2 – isothermal holding at 280 °C, 10 min;
3 – isothermal holding at 350 °C, 60 min; 4 – M2 secondary martensite formation
Рис. 3. *Зависимость относительного удлинения образца стали 20Х2Г2СНМА от температуры (**а**) и времени (**b**) при реализации двухступенчатой закалки QP2.*
1 – образование первичного мартенсита М1; 2 – изотермическая выдержка при 280 °С, 10 мин;
3 – изотермическая выдержка при 350 °С, 60 мин; 4 – образование вторичного мартенсита М2

DISCUSSION

In 20Cr2Mn2SiNiMo steel, during QP1 single-stage hardening, the decrease in the martensitic transformation temperature after holding at a temperature of 280 °C (Fig. 2 a) is associated with the enrichment of unconverted austenite with carbon. Nevertheless, the presence of a secondary martensitic transformation indicates an insufficient carbon content in austenite to shift the M_n temperature below room temperature. This is a deviation from one of the main provisions of the quenching – partitioning theory (complete stabilisation of austenite during cooling suspension).

In the case of QP2 two-stage quenching during holding at 350 °C after the suspension of bainite formation, a decrease in sample size by 2 % is observed (Fig. 3 b), which is associated both with the processes of tempering the primary martensite and bainite α-phase, and with the diffusion carbon redistribution between the α-phase and austenite. With further cooling from the second stage temperature,

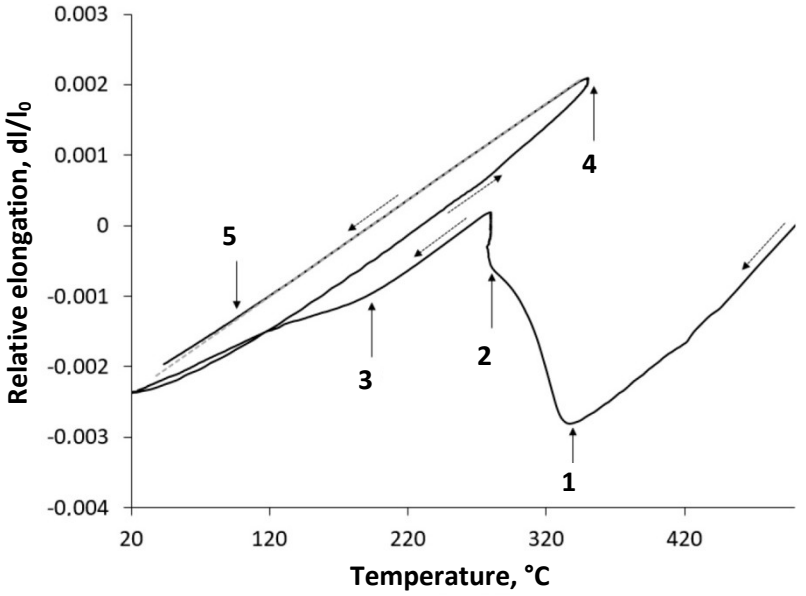

a

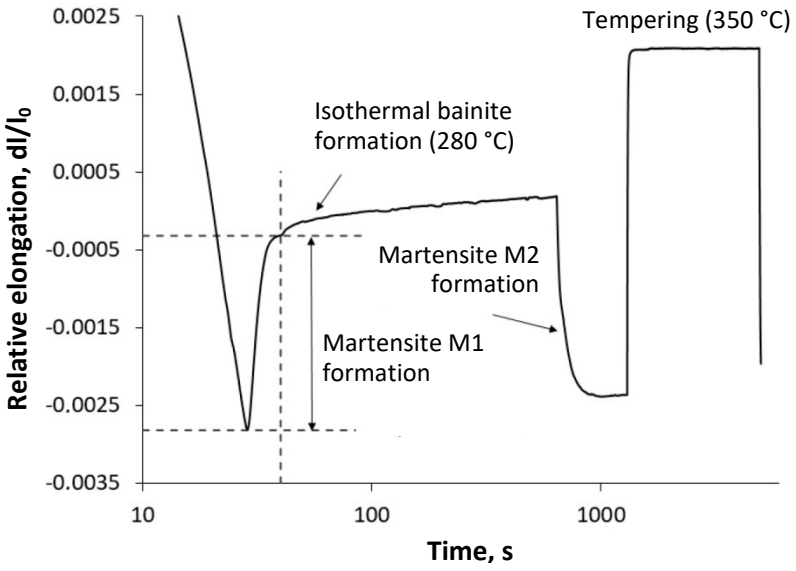

b

Fig. 4. *The dependence of relative elongation of the 20Cr2Mn2SiNiMo steel sample on the temperature (**a**) and time (**b**) when implementing QPT single-stage quenching with tempering.*
1 – M1 primary martensite formation; 2 – isothermal holding at 280 °C, 10 min; 3 – M2 secondary martensite formation; 4 – holding during tempering, 350 °C, 60 min; 5 – M2 secondary martensite formation
Рис. 4. *Зависимость относительного удлинения образца стали 20Х2Г2СНМА от температуры (**а**) и времени (**b**) при реализации одноступенчатой закалки с отпуском QPT.*
1 – образование первичного мартенсита М1; 2 – изотермическая выдержка при 280 °С, 10 мин; 3 – образование вторичного мартенсита М2; 4 – выдержка при отпуске, 350 °С, 60 мин; 5 – образование вторичного мартенсита М2

the secondary martensitic transformation begins at temperatures below 140 °C (Fig. 3 a). This is associated, firstly, with a smaller (compared to QP1) amount of unconverted austenite at the start of cooling, since the bainite transformation continues during holding at the second stage, and secondly, with a more effective stabilisation of residual austenite. As X-ray diffraction phase analysis showed, after QP1 single-stage quenching, the steel under study contains about 6 % of residual austenite, and when implementing QP2 two-stage quenching at room temperature, 14 % of residual austenite is stabilised.

In the case of QPT single-stage quenching, with medium-temperature tempering, the temperature at which the secondary martensite formation is observed is about 95 °C (Fig. 4 a). The amount of residual austenite stabilised in the structure of the steel under study, after QPT step quenching is practically no different from the result obtained with QP1, single-step quenching and is about 8 %. Thus, medium-

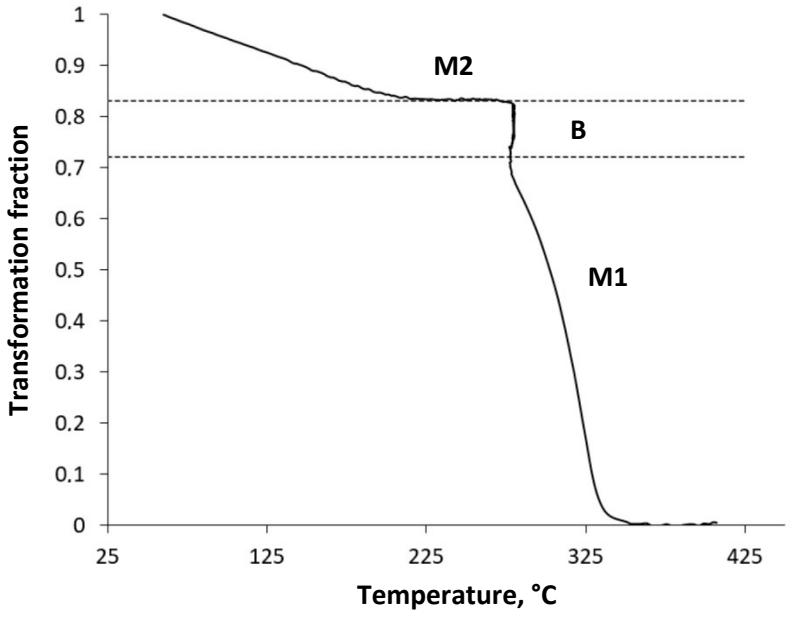

a

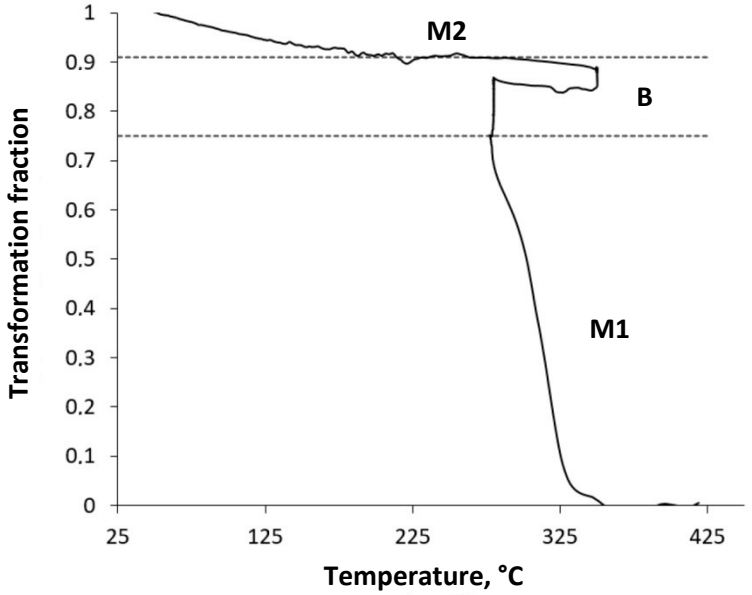

b

Fig. 5. *The dependence of the fraction of transformation of supercooled 20Cr2Mn2SiNiMo steel austenite, on the temperature, during step quenching (without taking into account residual austenite):* ***a*** *– QP1;* ***b*** *– QP2*
Рис. 5. *Зависимость доли превращения переохлажденного аустенита стали 20Х2Г2СНМА от температуры при реализации ступенчатой закалки (без учета остаточного аустенита):* ***a*** *– QP1;* ***b*** *– QP2*

temperature tempering after single-stage quenching does not lead to a noticeable change in the quantitative ratio of the structural components. During heating to a temperature of 350 °C, a nonlinear dependence of the relative elongation on the temperature is dilatometrically recorded, which indicates the occurrence of tempering and stress relaxation processes.

When implementing QPT single-stage quenching with tempering, the microstructure composition is practically no different from that obtained in the case of QP1 single-step quenching. Two-stage quenching leads to an increase in the residual austenite content in the structure, mainly due to a reduction in the secondary martensite amount (Fig. 6). In this case, the residual austenite lattice parameter after QP2 two-stage heat treatment, is less than after QP1 and QPT single-stage treatment (Fig. 7). Studies of 20Cr2Mn2SiNiMo steel have shown that it is characterised by a decrease in the residual austenite crystal lattice parameter, with an increase in its content in the steel structure. This phenomenon is associated with the fact that with an increase in the volume fraction of carbon-enriched unconverted austenite, present in the steel at the end of the isothermal holding, the carbon concentration in it is leveled out and averaged, which influences

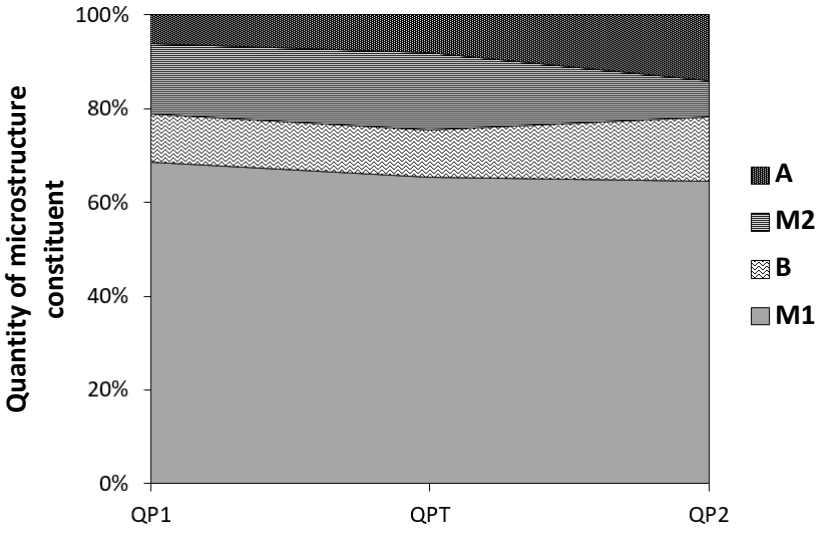

Fig. 6. *The ratio of the 20Cr2Mn2SiNiMo steel structural components after the implementation of various options of step quenching. M1 – primary martensite; B – bainite; M2 – secondary martensite; A – residual austenite*

Рис. 6. *Соотношение структурных составляющих стали 20Х2Г2СНМА после реализации различных вариантов ступенчатой закалки. М1 – первичный мартенсит; В – бейнит; М2 – вторичный мартенсит; А – остаточный аустенит*

the crystal lattice parameter value. In the case of QP1 single-stage quenching, the temperature and duration of isothermal holding (280 °C, 10 min) are insufficient for the bainite transformation completion and diffusion equalisation of the carbon concentration in unconverted austenite. As a result of this, austenite is significantly enriched in carbon only in volumes immediately adjacent to the martensite and bainite packets (which amounted to 6...8 % of the total metal volume), and in the remaining volume of unconverted austenite, the carbon concentration is insufficient to lower the M_n temperature below room temperature. Due to this, cooling from the isothermal holding temperature led to the formation of M2 secondary martensite at a temperature of 215 °C and below.

In the case of two-stage quenching, heating to a temperature of 350 °C ensured a more complete occurrence of the bainite transformation, due to which the volume of unconverted austenite was largely crushed by α-phase packets. Along with the increased temperature, this contributed to a more intense diffusion of carbon atoms from the boundaries with α-phase deep into the unconverted austenite volumes. As a result, the secondary martensitic transformation during cooling proceeded less intensely and at a lower temperature (140 °C) compared to the QP1 mode (single-stage quenching), and the volume of austenite enriched in carbon sufficiently to reduce the M_n temperature below 20 °C turned out to be significantly larger (14 %). This is confirmed by the results of metallographic research (Fig. 8).

QP2 two-stage quenching provides the maximum difference between the offset yield strength and tensile strength, as well as a rather high relative elongation, which is associated with the TRIP (Transformation-Induced Plasticity) effect. With regard to the PSE criterion, widely used in foreign practice, (the product of tensile strength and relative elongation, MPa×% [16, 17]) applied mainly for automotive sheet steels, the best result for the studied 20Cr2Mn2SiNiMo steel is provided by QP2 two-stage quenching (PSE=22,490 MPa×%). However, in terms of structural reliability required for mechanical engineering parts operating under conditions of alternating loads and wear, relative contraction and impact strength are also important characteristics. In this regard, the level of properties obtained during step, and isothermal quenching, is significantly inferior to the properties obtained after quenching and low-temperature tempering.

Thus, depending on the purpose of the part, the studied 20Cr2Mn2SiNiMo steel can provide a different combination of mechanical properties (strength, ductility, impact strength), and high stability of supercooled austenite of this steel [18; 19] allows implementing the heat treatment modes using only convective cooling media.

As one can see, to achieve both high strength and ductility, 20Cr2Mn2SiNiMo steel should be subjected to step quenching according to the QP2 mode. To achieve high impact strength and relative contraction, it is recommended to carry out quenching and low-temperature tempering at a temperature of no more than 200 °C. It is worth noting that the QPT single-stage quenching, and tempering mode provides the lowest impact strength, and the QP2 two-stage quenching mode provides the least contraction. The first is associated with the manifestation of the α-phase temper brittleness; the second is associated with the residual austenite transformation during deformation accompanied by an increase in the volume, and the formation of brittle high-carbon martensite.

CONCLUSIONS

1. A dilatometric study of the supercooled austenite transformations in the 20Cr2Mn2SiNiMo steel was carried out during step quenching in different modes: QP1 single-

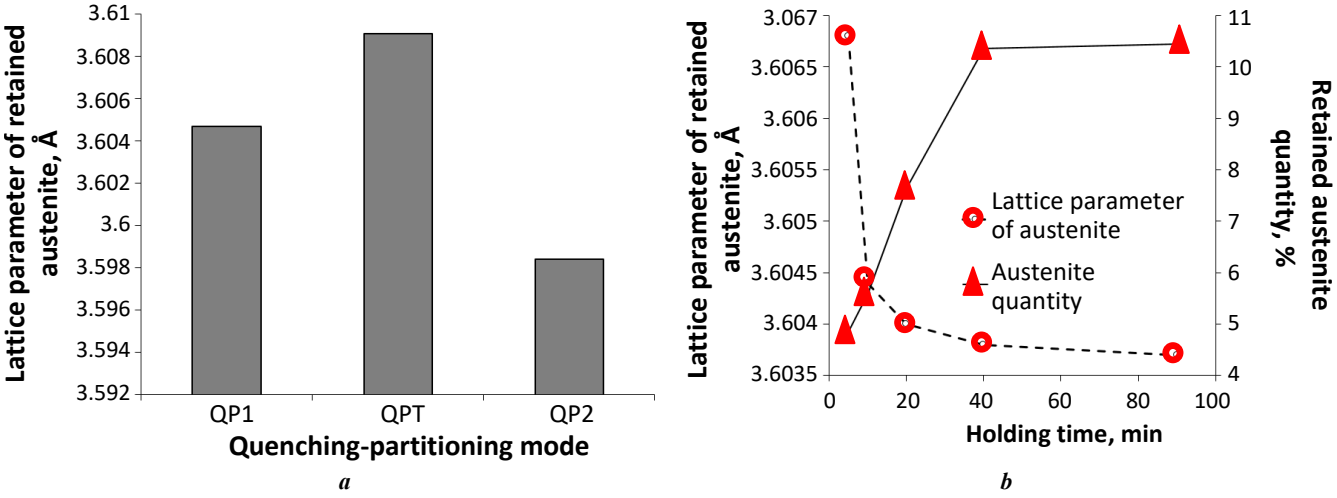

Fig. 7. *Values of the lattice parameter of residual austenite in the structure of 20Cr2Mn2SiNiMo steel after various heat treatment modes:*
a *– step quenching;* ***b*** *– isothermal quenching at 320 °C*
Рис. 7. *Значения параметра решетки остаточного аустенита в структуре стали 20Х2Г2СНМА после различных режимов термической обработки:*
а *– ступенчатая закалка;* ***b*** *– изотермическая закалка при 320 °С*

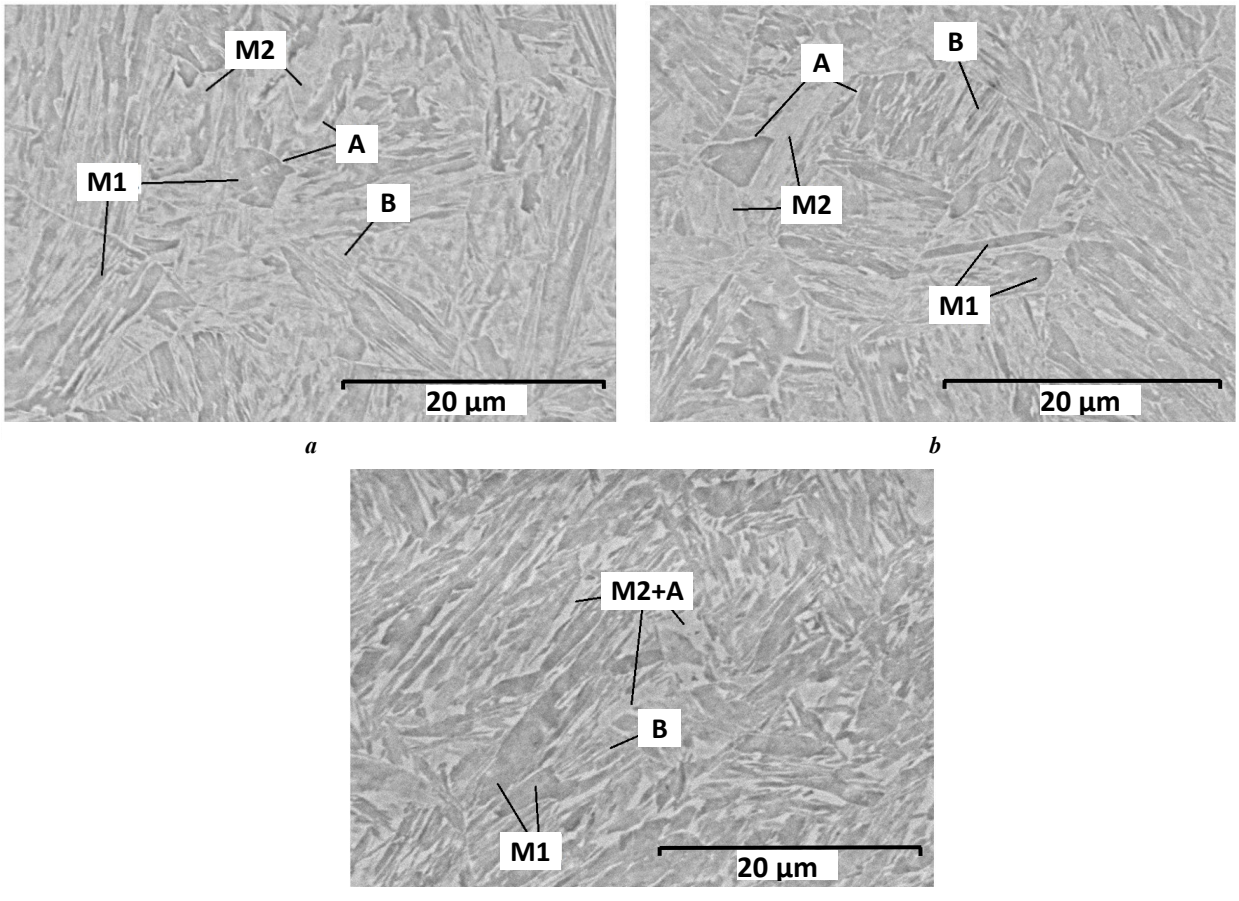

Fig. 8. *The microstructure of 20Cr2Mn2SiNiMo steel after various options of step quenching (scanning electron microscopy):* ***a*** *– QP1;* ***b*** *– QPT;* ***c*** *– QP2.*
M1 – primary martensite; B – bainite; M2 – secondary martensite; A – residual austenite
Рис. 8. *Микроструктура стали 20Х2Г2СНМА после различных вариантов ступенчатой закалки (растровая электронная микроскопия):* ***а*** *– QP1;* ***b*** *– QPT;* ***c*** *– QP2.*
М1 – первичный мартенсит; В – бейнит; М2 – вторичный мартенсит; А – остаточный аустенит

Table 2. *Mechanical properties of 20Cr2Mn2SiNiMo steel after various heat treatment modes*
Таблица 2. *Механические свойства стали 20Х2Г2СНМА после различных режимов термической обработки*

Technology	Mode	$\sigma_{0.2}$, MPa	σ_{UTS}, MPa	δ, %	ψ, %	KCV, MJ/m^2	PSE, MPa×%
Step quenching	QP1	1 292	1 558	12.3	52.1	0.68	19 157
	QPT	1 297	1 477	13.0	55.2	0.47	19 121
	QP2	945	1 551	14.5	39.9	0.70	22 490
Isothermal quenching	280 °C, 2 h	1 038	1 398	13.8	47.5	0.72	19 286
	300 °C, 2 h	1 045	1 430	15.2	51.9	0.61	21 665
Oil quenching and tempering	200 °C, 3 h	1 294	1 540	13.3	60.2	0.89	20 533
	300 °C, 3 h	1 269	1 494	12.2	59.5	0.76	18 273

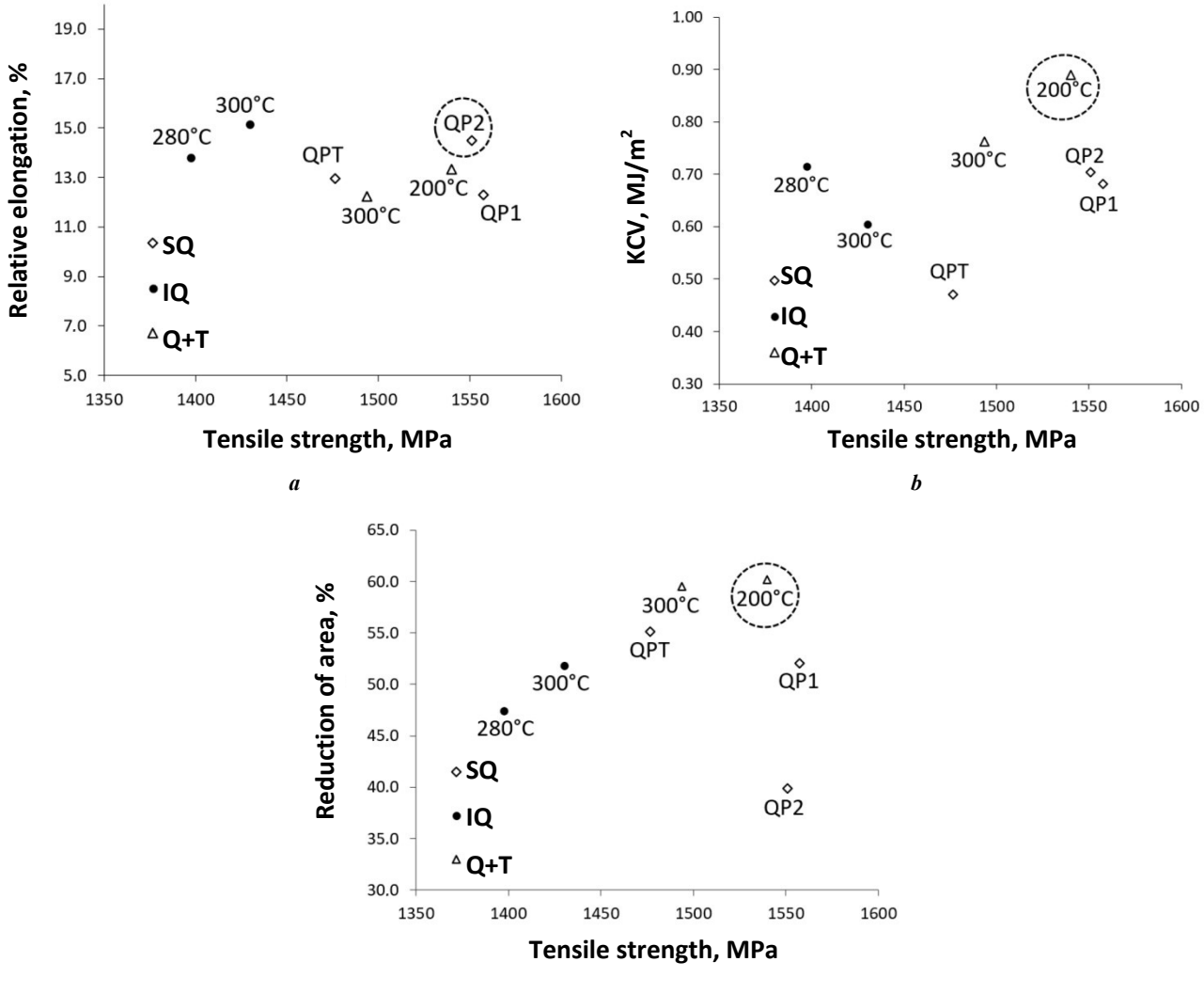

Fig. 9. *Diagrams of the mechanical properties of 20Cr2Mn2SiNiMo steel after various heat treatment options. SQ – step quenching; IQ – isothermal quenching; Q+T – quenching and tempering; parameters of heat treatment modes are indicated next to the corresponding markers*
Рис. 9. *Диаграммы механических свойств стали 20Х2Г2СНМА после различных вариантов термической обработки. SQ – ступенчатая закалка; IQ – изотермическая закалка; Q+T – закалка и отпуск; параметры режимов термообработки указаны возле соответствующих маркеров*

stage quenching, QPT single-stage quenching with tempering, and QP2 two-stage quenching. It was found that during the step quenching process, the following structural components are formed in steel: primary martensite at temperatures below 345 °C, isothermal bainite at temperatures of 280 and 350 °C, and secondary martensite at temperatures below 215 °C (for QP1, QPT) and 140 °C (QP2).

2. It is shown that QP2 two-stage quenching promotes stabilisation of 14 % of residual austenite in the steel structure at room temperature, and provides a smaller amount of secondary martensite. At the same time, the carbon content in residual austenite characterised by the crystal lattice parameter, after two-stage quenching is less than after one-stage quenching.

3. Based on the data of dilatometric and X-ray diffraction analysis, the structural-phase composition of the steel under study, was identified after the implementation of step quenching in different modes: 65...70 % of primary martensite; 10…14 % of bainite; 8…16 % of secondary martensite; 6…14 % of residual austenite.

4. The mechanical properties of the studied steel were determined after various types of step quenching. QP2 two-stage quenching provides a combination of high strength (1550 MPa) and relative elongation (14.5 %), but the contraction is minimal (40 %). Single-stage quenching and tempering leads to a significant decrease in impact strength (KCV 0.47 MJ/m^2), which is caused by the manifestation of tempering brittleness.

5. It is shown that, in terms of the structural reliability of machine-building parts, step quenching is not the optimal heat treatment mode for the steel under study. The best combination of strength (1540 MPa), ductility (relative elongation is 13 %, relative contraction is 60 %) and impact strength (KCV 0.89 MJ/m^2) is achieved after quenching and low-temperature tempering.

REFERENCES

1. Speer J.G. Phase transformations in quenched and partitioned steels. *Phase transformations in steels. Diffusionless Transformations, High Strength Steels, Modelling and Advanced Analytical Techniques*. Cambridge, Woodhead Publishing Limited, 2012. Vol. 2, pp. 247–270. DOI: 10.1533/9780857096111.2.247.
2. Liu Xingyu, Han Ying, Wei Junhu, Zu Guoqing, Zhao Yu, Zhu Weiwei, Ran Xu. Effect of tempering temperature on microstructure and mechanical properties of a low carbon bainitic steel treated by quenching-partitioning-tempering (QPT) process. *Journal of Materials Research and Technology*, 2023, vol. 23, pp. 911–918. DOI: 10.1016/j.jmrt.2023.01.061.
3. Zahrani M.M., Ketabchi M., Ranjbarnodeh E. Microstructure development and mechanical properties of a C–Mn–Si–Al–Cr cold rolled steel subjected to quenching and partitioning treatment. *Journal of Materials Research and Technology*, 2023, vol. 22, pp. 2806–2818. DOI: 10.1016/j.jmrt.2022.12.130.
4. Xu Wen-hua, Li Yang, Xiao Gui-yong, Gu Guo-chao, Lu Yu-peng. Effects of quenching and partitioning on microstructure and properties of high-silicon and high-aluminum medium carbon alloy steels. *Materials Today: Communications*, 2023, vol. 34, article number 105031. DOI: 10.1016/j.mtcomm.2022.105031.
5. Tian Yu, Tan Zhunli, Wang Jiong, Zhang Min. Realization of quenching & dynamic partitioning on large-size parts. *Materials and Manufacturing Processes*, 2022, vol. 37, no. 13, pp. 1490–1499. DOI: 10.1080/10426914.2021.2016815.
6. Samanta S., Das S., Chakrabarti D., Samajdar I., Singh S.B., Haldar A. Development of multiphase microstructure with bainite, martensite, and retained austenite in a Co-containing steel through quenching and partitioning (Q&P) treatment. *Metallurgical and Materials Transactions A*, 2013, vol. 44, pp. 5653–5664. DOI: 10.1007/s11661-013-1929-y.
7. Kumar S., Singh S.B. Evolution of microstructure during the "quenching and partitioning (Q&P)" treatment. *Materialia*, 2021, vol. 18, article number 101135. DOI: 10.1016/j.mtla.2021.101135.
8. Zambrano O.A. A Review on the Effect of Impact Toughness and Fracture Toughness on Impact-Abrasion Wear. *Journal of Materials Engineering and Performance*, 2021, vol. 30, pp. 7101–7116. DOI: 10.1007/s11665-021-05960-5.
9. Chintha A.R., Valtonen K., Kuokkala V.-T., Kundu S., Peet M.J., Bhadeshia H.K.D.H. Role of fracture toughness in impact-abrasion wear. *Wear*, 2019, vol. 428-429, pp. 430–437. DOI: 10.1016/j.wear.2019.03.028.
10. Pang J.C., Li S.X., Wang Z.G., Zhang Z.F. Relations between fatigue strength and other mechanical properties of metallic materials. *Fatigue and Fracture of Engineering Materials and Structures*, 2014, vol. 37, no. 9, pp. 958–976. DOI: 10.1111/ffe.12158.
11. Fleck N.A., Kang K.J., Ashby M.F. Overview no. 112: The cyclic properties of engineering materials. *Acta Metallurgica et Materialia*, 1994, vol. 42, no. 2, pp. 365–381. DOI: 10.1016/0956-7151(94)90493-6.
12. Maisuradze M.V., Ryzhkov M.A. Thermal Stabilization of Austenite During Quenching and Partitioning of Austenite for Automotive Steels. *Metallurgist*, 2018, vol. 62, pp. 337–347. DOI: 10.1007/s11015-018-0666-2.
13. Speer J.G., De Moor E., Clarke A.J. Critical Assessment 7: Quenching and partitioning. *Materials Science and Technology*, 2015, vol. 31, no. 1, pp. 3–9. DOI: 10.1179/1743284714Y.0000000628.
14. Maisuradze M.V., Ryzhkov M.A., Yudin Yu.V., Kuklina A.A. Transformations of supercooled austenite in a promising high-strength steel grade under continuous cooling conditions. *Metal Science and Heat Treatment*, 2017, vol. 59, pp. 486–490. DOI: 10.1007/s11041-017-0176-z.
15. Kop T.A., Sietsma J., Van Der Zwaag S. Dilatometric analysis of phase transformations in hypo-eutectoid steels. *Journal of Materials Science*, 2001, vol. 36, pp. 519–526. DOI: 10.1023/A:1004805402404.
16. Huang Fei, Chen Qiwei, Ding Hanlin, Wang Yongqiang, Mou Xiuting, Chen Jian. Automotive Steel with a High Product of Strength and Elongation used for Cold and Hot Forming Simultaneously. *Materials*, 2021, vol. 14, no. 5, article number 1121. DOI: 10.3390/ma14051121.
17. Yang Feng, Zhou Jian, Han Yun, Liu Peng, Luo Haiwen, Dong Han. A novel cold-rolled medium

Mn steel with an ultra-high product of tensile strength and elongation. *Materials Letters*, 2020, vol. 258, article number 126804. DOI: 10.1016/j.matlet.2019.126804.
18. Maisuradze M.V., Yudin Yu.V., Kuklina A.A. Formation of Microstructure in Advanced Low-Carbon Steel of Martensitic Class Under Heat Treatment. *Metal Science and Heat Treatment*, 2021, vol. 62, pp. 550–556. DOI: 10.1007/s11041-021-00601-z.
19. Maisuradze M.V., Ryzhkov M.A., Lebedev D.I. Microstructure and mechanical properties of martensitic high-strength engineering steel. *Metallurgist*, 2020, vol. 64, pp. 640–651. DOI: 10.1007/s11015-020-01040-6.

СПИСОК ЛИТЕРАТУРЫ

1. Speer J.G. Phase transformations in quenched and partitioned steels // Phase transformations in steels. Diffusionless Transformations, High Strength Steels, Modelling and Advanced Analytical Techniques. Vol. 2. Cambridge: Woodhead Publishing Limited, 2012. P. 247–270. DOI: 10.1533/9780857096111.2.247.
2. Liu Xingyu, Han Ying, Wei Junhu, Zu Guoqing, Zhao Yu, Zhu Weiwei, Ran Xu. Effect of tempering temperature on microstructure and mechanical properties of a low carbon bainitic steel treated by quenching-partitioning-tempering (QPT) process // Journal of Materials Research and Technology. 2023. Vol. 23. P. 911–918. DOI: 10.1016/j.jmrt.2023.01.061.
3. Zahrani M.M., Ketabchi M., Ranjbarnodeh E. Microstructure development and mechanical properties of a C–Mn–Si–Al–Cr cold rolled steel subjected to quenching and partitioning treatment // Journal of Materials Research and Technology. 2023. Vol. 22. P. 2806–2818. DOI: 10.1016/j.jmrt.2022.12.130.
4. Xu Wen-hua, Li Yang, Xiao Gui-yong, Gu Guo-chao, Lu Yu-peng. Effects of quenching and partitioning on microstructure and properties of high-silicon and high-aluminum medium carbon alloy steels // Materials Today: Communications. 2023. Vol. 34. Article number 105031. DOI: 10.1016/j.mtcomm.2022.105031.
5. Tian Yu, Tan Zhunli, Wang Jiong, Zhang Min. Realization of quenching & dynamic partitioning on large-size parts // Materials and Manufacturing Processes. 2022. Vol. 37. № 13. P. 1490–1499. DOI: 10.1080/10426914.2021.2016815.
6. Samanta S., Das S., Chakrabarti D., Samajdar I., Singh S.B., Haldar A. Development of multiphase microstructure with bainite, martensite, and retained austenite in a Co-containing steel through quenching and partitioning (Q&P) treatment // Metallurgical and Materials Transactions A. 2013. Vol. 44. P. 5653–5664. DOI: 10.1007/s11661-013-1929-y.
7. Kumar S., Singh S.B. Evolution of microstructure during the "quenching and partitioning (Q&P)" treatment // Materialia. 2021. Vol. 18. Article number 101135. DOI: 10.1016/j.mtla.2021.101135.
8. Zambrano O.A. A Review on the Effect of Impact Toughness and Fracture Toughness on Impact-Abrasion Wear // Journal of Materials Engineering and Performance. 2021. Vol. 30. P. 7101–7116. DOI: 10.1007/s11665-021-05960-5.
9. Chintha A.R., Valtonen K., Kuokkala V.-T., Kundu S., Peet M.J., Bhadeshia H.K.D.H. Role of fracture toughness in impact-abrasion wear // Wear. 2019. Vol. 428-429. P. 430–437. DOI: 10.1016/j.wear.2019.03.028.
10. Pang J.C., Li S.X., Wang Z.G., Zhang Z.F. Relations between fatigue strength and other mechanical properties of metallic materials // Fatigue and Fracture of Engineering Materials and Structures. 2014. Vol. 37. № 9. P. 958–976. DOI: 10.1111/ffe.12158.
11. Fleck N.A., Kang K.J., Ashby M.F. Overview no. 112: The cyclic properties of engineering materials // Acta Metallurgica et Materialia. 1994. Vol. 42. № 2. P. 365–381. DOI: 10.1016/0956-7151(94)90493-6.
12. Maisuradze M.V., Ryzhkov M.A. Thermal Stabilization of Austenite During Quenching and Partitioning of Austenite for Automotive Steels // Metallurgist. 2018. Vol. 62. P. 337–347. DOI: 10.1007/s11015-018-0666-2.
13. Speer J.G., De Moor E., Clarke A.J. Critical Assessment 7: Quenching and partitioning // Materials Science and Technology. 2015. Vol. 31. № 1. P. 3–9. DOI: 10.1179/1743284714Y.0000000628.
14. Maisuradze M.V., Ryzhkov M.A., Yudin Yu.V., Kuklina A.A. Transformations of supercooled austenite in a promising high-strength steel grade under continuous cooling conditions // Metal Science and Heat Treatment. 2017. Vol. 59. P. 486–490. DOI: 10.1007/s11041-017-0176-z.
15. Kop T.A., Sietsma J., Van Der Zwaag S. Dilatometric analysis of phase transformations in hypo-eutectoid steels // Journal of Materials Science. 2001. Vol. 36. P. 519–526. DOI: 10.1023/A:1004805402404.
16. Huang Fei, Chen Qiwei, Ding Hanlin, Wang Yongqiang, Mou Xiuting, Chen Jian. Automotive Steel with a High Product of Strength and Elongation used for Cold and Hot Forming Simultaneously // Materials. 2021. Vol. 14. № 5. Article number 1121. DOI: 10.3390/ma14051121.
17. Yang Feng, Zhou Jian, Han Yun, Liu Peng, Luo Haiwen, Dong Han. A novel cold-rolled medium Mn steel with an ultra-high product of tensile strength and elongation // Materials Letters. 2020. Vol. 258. Article number 126804. DOI: 10.1016/j.matlet.2019.126804.
18. Maisuradze M.V., Yudin Yu.V., Kuklina A.A. Formation of Microstructure in Advanced Low-Carbon Steel of Martensitic Class Under Heat Treatment // Metal Science and Heat Treatment. 2021. Vol. 62. P. 550–556. DOI: 10.1007/s11041-021-00601-z.
19. Maisuradze M.V., Ryzhkov M.A., Lebedev D.I. Microstructure and mechanical properties of martensitic high-strength engineering steel // Metallurgist. 2020. Vol. 64. P. 640–651. DOI: 10.1007/s11015-020-01040-6.

Исследование превращений переохлажденного аустенита при ступенчатой закалке стали 20Cr2Mn2SiNiMo

Майсурадзе Михаил Васильевич[1,3], кандидат технических наук, доцент,
доцент кафедры «Термообработка и физика металлов»
Куклина Александра Александровна*[1,2,4], кандидат технических наук, доцент кафедры «Физика»,
заведующий научно-исследовательской и испытательной лабораторией геокриологии, физики грунтов
и материалов, инженер лаборатории структурных методов анализа и свойств материалов и наноматериалов
Назарова Вера Вячеславовна[1], аспирант кафедры «Термообработка и физика металлов»
[1]*Уральский федеральный университет имени первого Президента России Б.Н. Ельцина, Екатеринбург (Россия)*
[2]*Уральский государственный горный университет, Екатеринбург (Россия)*

***E-mail:** kuklina@m.ursmu.ru,
Kuklina.aleksandra@rambler.ru

[3]ORCID: https://orcid.org/0000-0003-2850-2988
[4]ORCID: https://orcid.org/0000-0003-3779-3254

Поступила в редакцию 26.06.2023 *Принята к публикации 26.01.2024*

Аннотация: В настоящее время ступенчатая закалка сталей в температурном интервале мартенситного превращения, в т. ч. quenching – partitioning, нашла широкое применение в автомобильной промышленности. Технология ступенчатой закалки успешно применяется для повышения комплекса свойств, к которым чаще всего относят временное сопротивление разрыву и относительное удлинение. Проведено дилатометрическое исследование превращений переохлажденного аустенита, протекающих в стали 20Х2Г2СНМА, при реализации различных вариантов ступенчатой закалки с выдержкой в мартенситной области. Установлено, что после одноступенчатой закалки, одноступенчатой закалки с последующим отпуском, двухступенчатой закалки образуются первичный мартенсит, изотермический бейнит, вторичный мартенсит в различных количественных соотношениях. С помощью рентгеноструктурного фазового анализа определено количество остаточного аустенита при реализации ступенчатой закалки. Показано, что двухступенчатая закалка позволяет стабилизировать в структуре исследуемой стали при комнатной температуре до 14 % остаточного аустенита. Исследования выявили, что для стали 20Х2Г2СНМА характерно уменьшение параметра кристаллической решетки остаточного аустенита при увеличении его содержания в структуре стали. Проведены испытания при одноосном растяжении и на ударный изгиб, определены значения механических свойств. Установлено, что при двухступенчатой закалке достигаются более высокие по сравнению с закалкой в масле и низкотемпературным отпуском показатели прочности и относительного удлинения при меньших значениях относительного сужения и ударной вязкости. Показано, что с точки зрения конструктивной надежности машиностроительных деталей ступенчатая закалка не является оптимальным режимом термической обработки исследуемой стали. Наилучшее сочетание прочности, пластичности и ударной вязкости достигается после закалки и низкотемпературного отпуска.

Ключевые слова: превращения переохлажденного аустенита; ступенчатая закалка; сталь 20Х2Г2СНМА; 20Cr2Mn2SiNiMo; quenching – partitioning; изотермическая закалка; закалка и отпуск; остаточный аустенит; первичный мартенсит; изотермический бейнит; вторичный мартенсит.

Благодарности: Исследование выполнено за счет гранта Российского научного фонда № 22-29-00106, https://grant.rscf.ru/prjcard_int?22-29-00106.

Статья подготовлена по материалам докладов участников XI Международной школы «Физическое материаловедение» (ШФМ-2023), Тольятти, 11–15 сентября 2023 года.

Для цитирования: Майсурадзе М.В., Куклина А.А., Назарова В.В. Исследование превращений переохлажденного аустенита при ступенчатой закалке стали 20Cr2Mn2SiNiMo // Frontier Materials & Technologies. 2024. № 2. С. 53–65. DOI: 10.18323/2782-4039-2024-2-68-5.

doi: 10.18323/2782-4039-2024-2-68-6

Features of thermoreactivity of electrolytic nickel coatings with different surface morphologies

Nadezhda S. Matveeva, postgraduate student
Natalya N. Gryzunova*[1], Doctor of Sciences (Physics and Mathematics), Associate Professor, professor of Chair "Nanotechnology, Materials Science and Mechanics"
Togliatti State University, Togliatti (Russia)

***E-mail:** gryzunova@tltsu.ru [1]ORCID: https://orcid.org/0000-0003-2802-9537

Received 21.06.2023 *Accepted 07.12.2023*

Abstract: Nickel coatings consisting of oriented structures have unique catalytic properties. However, the temperature range for the use of such coatings is not determined, and a comprehensive study of their thermal properties in aggressive environments is required. This work studied the influence of the characteristics of the habit of nickel crystals on their reactivity with increasing temperature (thermoreactivity). The authors studied nickel coatings produced by electrodeposition with the addition of inhibitory additives, in the form of alkali metal chlorides to the electrolyte. Differential thermal analysis was used to study the reactivity of coatings in temperature fields. Oxygen was used as an aggressive medium. The phase composition of the samples after heating was determined, using a powder X-ray diffractometer. The introduced additives in the form of alkali metal chlorides allowed forming coatings consisting of crystals of a cone-shaped habit. It was found that the introduction of additives, in the form of alkali metal salts into the electrolyte, makes it possible to change the habit of nickel crystals, and increase the surface area of the coating by approximately 10–15 %. The study showed that electrodeposited nickel coatings, consisting of crystals in the form of micro- and nanocones, have (compared to the control coating) a reduced thermoreactivity. Experimental data allowed concluding that a decrease in the intensity of oxidation on the coatings under study, may be associated with the presence of a preferential development of certain crystallographic faces of the crystals, which causes a change in the nature of the nickel-oxygen interaction, and as a consequence, a change in the oxidation intensity.

Keywords: nickel coatings; nickel electrodeposition; cone-shaped crystals; thermoreactivity.

Acknowledgments: The paper was written on the reports of the participants of the XI International School of Physical Materials Science (SPM-2023), Togliatti, September 11–15, 2023.

For citation: Matveeva N.S., Gryzunova N.N. Features of thermoreactivity of electrolytic nickel coatings with different surface morphologies. Frontier Materials & Technologies, 2024, no. 2, pp. 67–75. DOI: 10.18323/2782-4039-2024-2-68-6.

INTRODUCTION

The development of modern technologies raises the requirements for electrodeposited metal coatings. Traditionally, nickel plating is used to protect against corrosion, increase the wear resistance and strength of parts, decorative surface finishing, etc. However, recently, the technology for producing nickel coatings or films, consisting of arrays of oriented structures has been actively developed. Among the large volume of scientific information, a significant number of publications covers, specifically the methods of forming nickel coatings with a developed surface, consisting of arrays of oriented structures [1–3]. In particular, in [1], magnetron sputtering of a nickel target was used to produce films from nickel nanocolumns. In [2–4], the electrodeposition method was used to create oriented structures on surfaces of various natures. In works [2; 5; 6], nickel coatings consisting of columnar structures were produced by modifying the electrolyte. The authors of [2] proposed to introduce a modifying agent, in the form of hydrochloric ethylenediamine into the electrolyte to obtain arrays of nickel nanocones. In works [6–8], calcium, sodium and potassium chlorides played the role of modifying agents. The authors of [9] produced vertically arranged arrays of nickel micro- and nanorods by galvanostatic electrolysis onto a titanium substrate, without any solid templates or surfactants.

Analysis of publications, allowed identifying works covering the study of the properties of coatings, made from arrays of oriented structures. In [10; 11], the corrosion properties of highly hydrophobic hierarchical nickel coatings were studied. Research showed that the corrosion resistance of coatings increases when using a chloride electrolyte, and nanostructured nickel as a matrix. In [12], it was proposed to use a nickel-cobalt developed surface, as a metal frame to create highly efficient supercapacitors. Studies [2] of the magnetic properties of arrays of nickel structures have demonstrated the existence of strong anisotropy. It was proposed to apply a silicon composite to nickel substrates, with a developed surface to increase the capacity of lithium-ion batteries [2; 13].

Nickel coatings with a developed surface, consisting of oriented structures or cone-shaped crystals, have high potential for practical application. In semiconductor technology, they are supposed to be used to create sensor devices and magnetic information storage devices [14]. Nickel coatings are used as ultrahydrophobic layers [10; 11], supercapacitors [12], and catalysts [15–17]. In [13], it was proposed to use electrodeposited nickel micro- and nano-

cones, to create a hierarchically structured current collector for lithium batteries.

In the above works, the magnetic, hydrophobic, corrosion, and catalytic properties of nickel coatings with a developed surface were studied, but there are no publications related to studies of their thermal properties in aggressive environments.

In this work, thermoreactivity will be understood to be the intensity of nickel oxidation in oxygen, under the influence of elevated temperatures. It is known [18] that reactivity can depend on the crystal structure, defect concentration, and the metal surface morphology.

The purpose of the research is to study the influence of the habit characteristics of nickel crystals in electrodeposited coatings on their reactivity when increasing temperature.

METHODS

Nickel coatings, consisting of cone-shaped crystals, were produced by electrodeposition from a nickel electrolyte based on grade Ch $NiSO_4 \cdot 7H_2O$ in a concentration of 3 mol/l. To produce coatings with different surface morphologies, alkali metal salts (sodium chloride and potassium chloride) taken in the same molar amount (3 mol/l of electrolyte), were introduced into the initial electrolyte.

Electrodeposition was carried out on substrates – stainless steel microgrids. The substrates were pre-prepared for electrodeposition: cleaned, degreased, washed, and dried. Nickel NPAN (semi-finished anode non-passivated nickel) was used as an anode. Electrodeposition was carried out at temperature of t=60 °C and current density of j=1.5 A/dm^2. Electrodeposition time was τ=600 s.

To assess the surface morphology of the resulting nickel coatings, a Carl Zeiss Sigma scanning electron microscope, and an Olympus LEXT OLS4000 laser scanning microscope were used. To identify the influence of crystal habit, and surface morphology of electrodeposited nickel coatings on their reactivity (nickel behaviour in an aggressive environment with increasing temperature), differential thermal analysis (DTA) was used, which was carried out on a DTG60/60H device. Oxygen was used as an aggressive medium. Heating was carried out from room temperature to 1100 °C at a rate of 10 deg/min, with a gas supply rate of 35 ml/min. To carry out differential thermal analysis of nickel coatings of different morphologies, disks with a diameter equal to the internal diameter of ceramic crucibles for direct annealing in the device were cut out. The weight of the samples was the same, and amounted to m=(7.0±0.5) mg. For each type of coating, at least 10 calorimetric studies were carried out.

The phase and approximate quantitative composition of the samples was determined, using a Shimadzu XRD-7000 powder X-ray diffractometer. Phase identification was performed using the JCPDS powder diffraction reference standard database, by comparing peak intensities and interplanar distances. The oxidation intensity was assessed using an X-ray diffractometer, based on changes in the quantitative composition of the phases of the samples after heating.

RESULTS

Fig. 1 presents microphotographs of the samples under study. Fig. 1 a shows the surface morphology of a sample produced from a pure electrolyte, without the addition of chlorides – a control sample. Scanning electron microscopy images showed that in this case, the nickel coating has a morphology without a pronounced surface microrelief (Fig. 1 a). When introducing the additives under study into the electrolyte, the surface relief changes significantly (Fig. 1 b–d), due to the formation of coatings consisting of cone-shaped habit crystals. In the coating with sodium chloride (Fig. 1 b), crystals with pentagonal symmetry are found in significant quantities (Fig. 1 c). At the same time, a more uniform surface morphology is observed in coatings, produced with the potassium chloride introduction into the electrolyte (Fig. 1 d).

Detailed microscopic studies showed that the potassium chloride introduction into the initial electrolyte, allows producing a coating, consisting of almost 100 % cone-shaped crystals (Fig. 1 d, 2 a). Of these, about 40 % of the crystals at the base in the transverse direction are nanosized ("a" parameter in Fig. 2 b). Determining the surface area of nickel coatings, using a laser scanning microscope, showed that the introduction of additives in the form of alkali metal salts into the electrolyte allows both changing the habit of nickel crystals in the coating, and increasing its surface area. Thus, if we take the control sample surface area (nickel coating produced from a pure electrolyte (Fig. 1 a)) as 100 %, then the surface area of coatings produced from electrolytes with NaCl and KCl additives increased by 10 and 15 %, respectively.

Using electron scanning microscopy, the average size of nickel cones in the coatings under study was assessed. Fig. 2 c presents a diagram of the dependence of the average size of cone-shaped crystals in the coating on the type of additive in the electrolyte. In Fig. 2 d, the ratio of the cone height to its base is estimated. The results obtained indicate that the potassium chloride addition to the electrolyte allows increasing the coating surface area, due to the pronounced anisotropy of crystal growth. Thus, the use of potassium chloride makes it possible to produce finer-crystalline coatings, consisting of cone-shaped habit crystals with an average size of 300–400 nm.

The results of DTA studies are presented in Fig. 3–5. In the graph (Fig. 3) of the control sample, no peaks of heat absorption and heat release are observed throughout the entire temperature range. The sodium chloride electrolyte sample exhibits two peaks. In the temperature range from 600 to 710 °C, there is an endothermic peak; in the temperature range from approximately 810 to 870 °C, there is an exothermic peak (Fig. 4). For another sample (from an electrolyte with potassium chloride), two similar peaks can also be observed, but shifted to a higher temperature range. Endothermic peak is from 630 to 740 °C, exothermic peak is from 830 to 880 °C (Fig. 5).

Fig. 6 shows diffraction patterns with marked phase lines for all three types of coatings. Due to the fact that the coating is applied to stainless steel microgrids, in addition to the nickel and nickel oxide phases, phases of other compounds can be observed. The noise present in the diffraction patterns is determined by the presence of fluorescent iron in the microgrid itself.

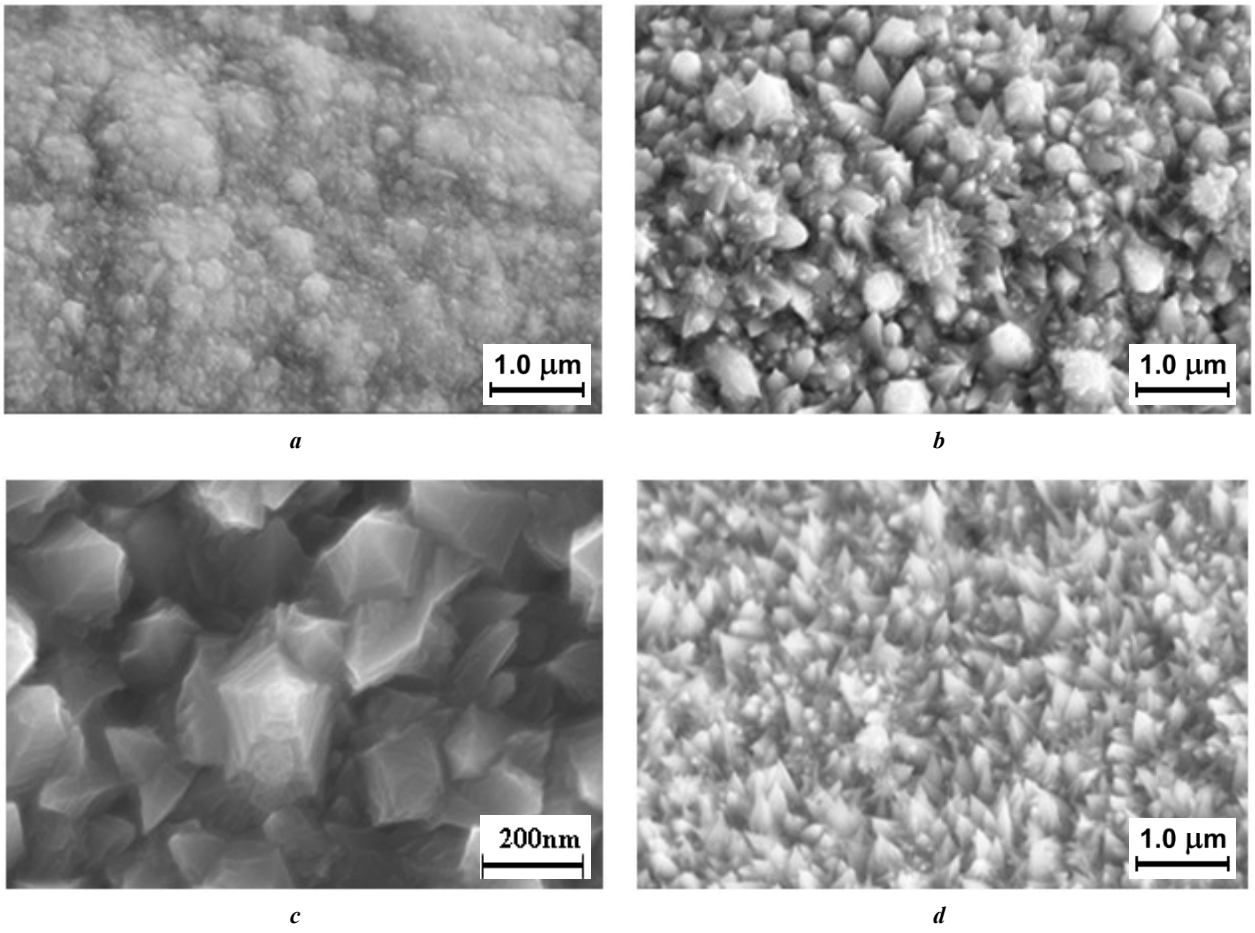

Fig. 1. *Electron micrographs of a nickel coating on a stainless steel microgrid:*
a *– sample of pure electrolyte;* ***b, c*** *– sample with added sodium chloride;* ***d*** *– sample with added potassium chloride*
Рис. 1. *Электронно-микроскопические снимки никелевого покрытия на микросетке из нержавеющей стали:*
a *– образец из чистого электролита;* ***b, c*** *– образец с добавлением хлорида натрия;* ***d*** *– образец с добавлением хлорида калия*

The approximate quantitative phase composition suggests that the control coating undergoes significant oxidation (approximately 53 % of nickel was oxidised), the oxidation intensity of coatings made of electrolytes with additives is lower (for coatings from an electrolyte with NaCl, it was approximately 17 %, for coatings from an electrolyte with KCl – approximately 39 %).

DISCUSSION

We associate the first peaks in the samples with the annealing of defects of growth origin and with the nickel recrystallisation processes within this temperature range. According to the Bochvar's formula (T_r=a×T_{melt}, where T_r is the recrystallisation temperature, a is a coefficient depending on the metal purity, T_{melt} is the melting temperature), the recrystallisation of nickel can begin already at a temperature of T_r=0.4T_{melt}. For nickel, this is (according to various sources) approximately 580–600 °C. In the nickel coating of the control sample, the recrystallisation process is not as pronounced as for the samples under study. In our opinion, this is associated with the fact that during the formation of coatings on the samples under study, selective inhibition of crystal growth occurs. Due to the inhibition of some crystallographic faces, others received preferential development. The work [13] presents the results of X-ray diffraction analysis of such coatings. They showed that when adding sodium chloride or potassium chloride to the electrolyte, the crystals formed in the coating exhibit preferential development of (111) faces and inhibition of the development of (200) faces.

Coatings with the addition of sodium chloride contain cone-shaped crystals with pentagonal symmetry [19; 20], which have large stored internal energy [21]. Therefore, in coatings made of electrolyte with NaCl, an intensive recrystallisation process begins at lower temperatures.

According to thermal analysis, the change in enthalpy (ΔH) at the occurrence of the first peaks for the coating with KCl is approximately 20 % greater than for the coating with NaCl. This may indicate that structural changes in these samples occur more actively, which may be associated with the dimensional characteristics of the crystals (Fig. 2).

We associate the further peaks (Fig. 3, 4) with phase transformations that occurred during the oxidation of nickel in oxygen. According to reference data, visible oxidation of nickel in an oxygen-containing environment is observed at temperatures above 700–800 °C. The occurrence of exothermic peaks in the thermograms of the samples is observed in a similar temperature range.

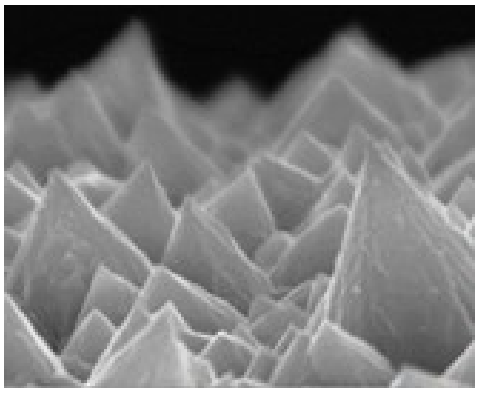

a

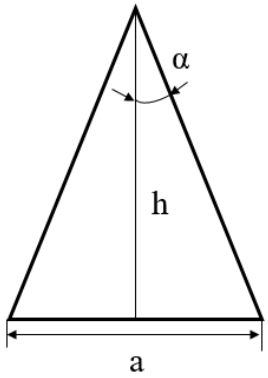

b

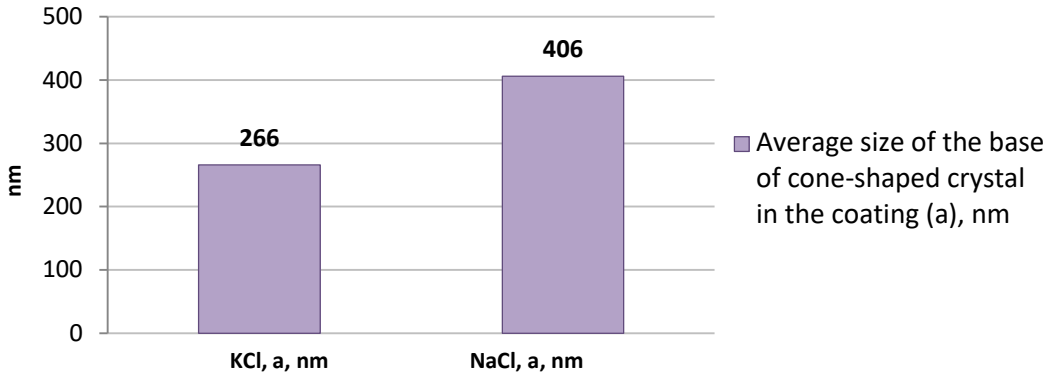

c

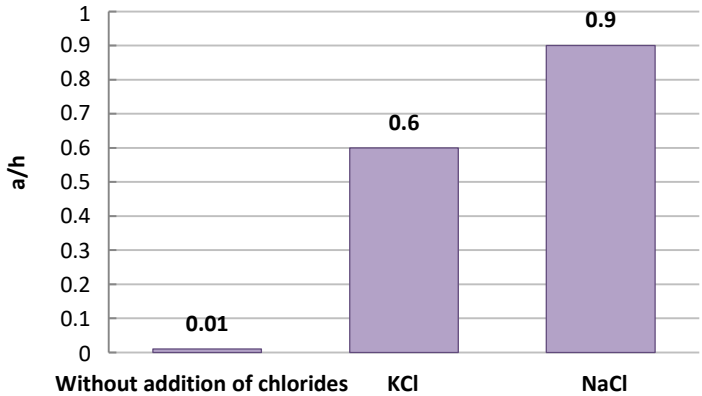

d

Fig. 2. *A view of cones in the coating, where a is the base, h is the cone height, α is the angle at the apex* ***(a)****; schematic representation of a cone-shaped nickel crystal and its geometric parameters* ***(b)****; diagram of the average size of nickel crystals in the coating with different additions to the electrolyte* ***(c)****; diagram of the ratio of the linear dimensions of cones in coatings of different morphologies* ***(d)***

Рис. 2. *Вид конусов в покрытии, где a – основание, h – высота конуса, α – угол при вершине* ***(a)****; схематичное изображение конусообразного кристалла никеля и его геометрических параметров* ***(b)****; диаграмма среднего размера кристаллов никеля в покрытии при разных добавках в электролит* ***(c)****; диаграмма отношения линейных размеров конусов в покрытиях разной морфологии* ***(d)***

X-ray phase studies of samples, showed that when heating nickel in oxygen, its surface oxidises. However, for the control coating, oxidation occurs gradually and more actively within the entire temperature range.

As late as in the middle of the 20th century, the oxygen adsorption on films of nickel, and other metals was studied. It was discovered that chemisorption on different crystallographic surfaces occurs with varying intensity degrees [22]. Later works [23] confirmed this specificity in terms of reaction rate. All this suggests that the decrease in the intensity of oxidation on the coatings, under study, may be associated exactly with the presence of preferential development of certain crystallographic facets in the crystals. This causes a change in the nature of the nickel-oxygen interaction and, as a consequence, a change in the oxidation reaction rate.

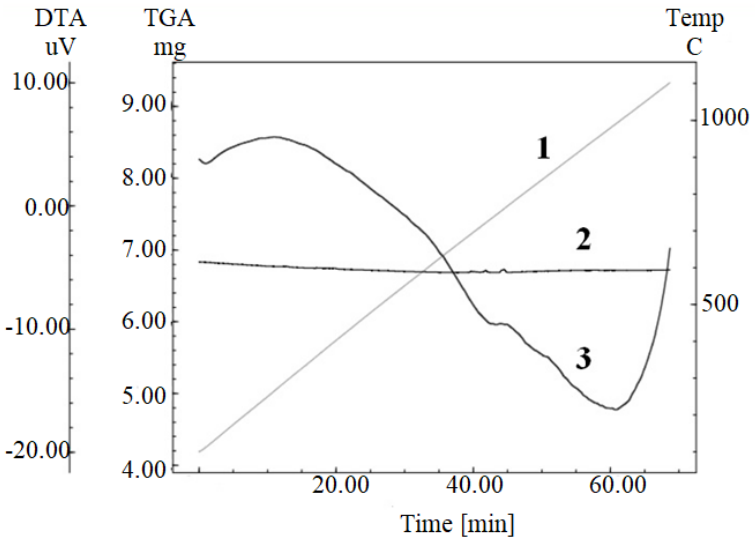

Fig. 3. *Thermogram after annealing of microgrids with a nickel coating produced from the pure electrolyte in oxygen.*
1 – graph of temperature changes in the device chamber;
2 – graph of changes in the mass of the studied samples during the heating process; 3 – DTA curve
Рис. 3. *Термограмма после отжига микросеток с никелевым покрытием, полученным из чистого электролита, в кислороде.*
1 – график изменения температуры в камере прибора;
2 – график изменения массы исследуемых образцов в процессе нагревания; 3 – кривая ДТА

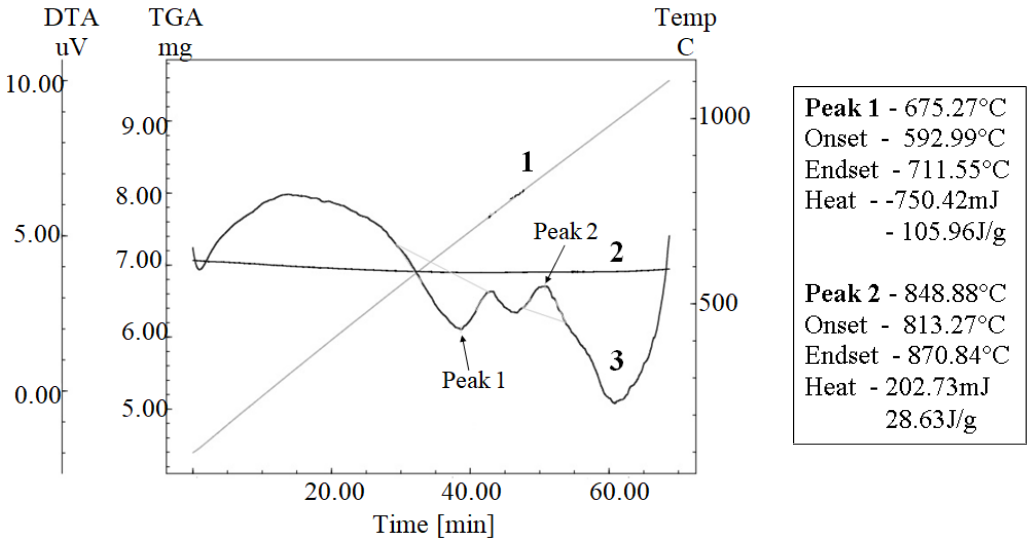

Fig. 4. *Thermogram after annealing of microgrids with a nickel coating produced with the addition of sodium chloride in oxygen.*
1 – graph of temperature changes in the device chamber;
2 – graph of changes in the mass of the studied samples during the heating process; 3 – DTA curve
Рис. 4. *Термограмма после отжига микросеток с никелевым покрытием,*
полученным с добавлением хлорида натрия, в кислороде.
1 – график изменения температуры в камере прибора;
2 – график изменения массы исследуемых образцов в процессе нагревания; 3 – кривая ДТА

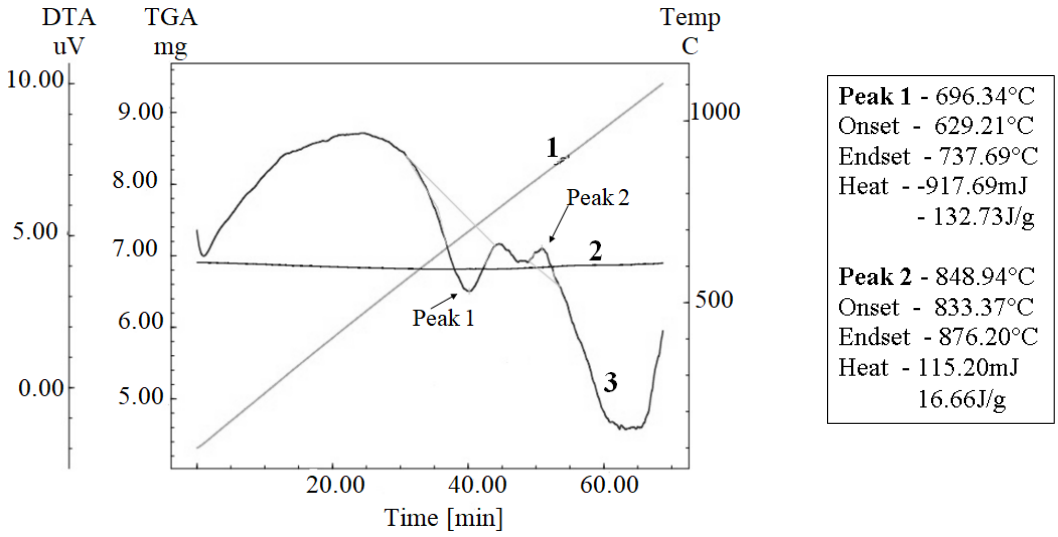

Fig. 5. *Thermogram after annealing of microgrids with a nickel coating produced with the addition of potassium chloride in oxygen.*
1 – graph of temperature changes in the device chamber;
2 – graph of changes in the mass of the studied samples during the heating process; 3 – DTA curve
Рис. 5. *Термограмма после отжига микросеток с никелевым покрытием,*
полученным с добавлением хлорида калия, в кислороде.
1 – график изменения температуры в камере прибора;
2 – график изменения массы исследуемых образцов в процессе нагревания; 3 – кривая ДТА

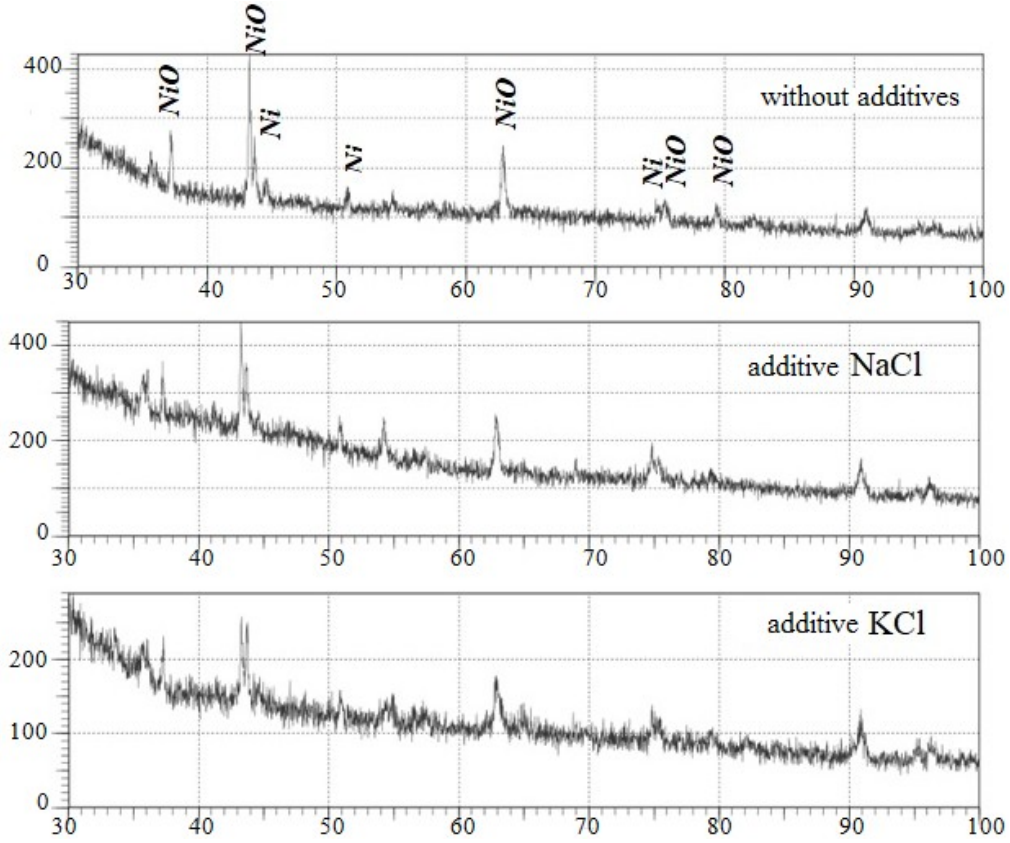

Fig. 6. *X-ray patterns of nickel coatings after differential thermal analysis*
Рис. 6. *Рентгенограммы никелевых покрытий после дифференциально-термического анализа*

CONCLUSIONS

It is possible to change the habit of growing crystals in the coating, and control their sizes, both by selecting the electrodeposition mode and by introducing various inhibitory additives into the electrolyte.

Differential thermal analysis of the behaviour of samples with additives in oxygen, showed the presence of two pronounced peaks. We associate the first of them with the recrystallisation of nickel, and the relaxation of large elastic stresses, caused by a high concentration of growth defects in the coating. We associate the second peak with selective chemisorption, with the result that the nickel oxidation (within a very narrow temperature range), first occurred at a high speed (a sharp change in enthalpy occurred), then slowed down significantly. This led to the fact that the intensity of nickel oxidation on the samples under study, was significantly lower.

Analysis of experimental data, allowed concluding that electrodeposited nickel coatings consisting of crystals, in the form of micro- and nanocones have (compared to the control coating) a reduced thermoreactivity even when heated to 1100 °C, which ensures additional possibilities for the use of such coatings, for example, as catalysts operating at high temperatures.

REFERENCES

1. Linnik A.I., Prudnikov A.M., Shalaev R.V., Varyukhin V.N., Kostyrya S.A., Burkhovetskii V.V. Synthesis and magnetic properties of nanocolumnar nickel films deposited in argon-nitrogen atmosphere. *Technical physics letters*, 2012, vol. 38, no. 6, pp. 499–502. EDN: RCVSKV.
2. Hang Tao, Li Ming, Fei Qin, Mao Dali. Characterization of nickel nanocones routed by electrodeposition without any template. *Nanotechnology*, 2008, vol. 19, article number 035201. DOI: 10.1088/0957-4484/19/03/035201.
3. Rahimi E., Davoodi A., Kiani Rashid A.R. Characterization of screw dislocation-driven growth in nickel micro-nanostructure electrodeposition process by AFM. *Materials Letters*, 2017, vol. 210, pp. 341–344. DOI: 10.1016/j.matlet.2017.09.057.
4. Ostanin N.I., Trofimov A.A., Ostanina T.N., Shnayder E.A. Electrodeposition of nickel coatings with developed surface in the diffusive regime. *Fundamental research*, 2017, no. 5, pp. 61–65. EDN: YRPIEV.
5. Hang Tao, Ling Huiqin, Hu Anmin, Li Ming. Growth Mechanism and Field Emission Properties of Nickel Nanocones Array Fabricated by One-Step Electrodeposition. *Journal of The Electrochemical Society*, 2010, vol. 157, no. 12, pp. 624–627. DOI: 10.1149/1.3499352.
6. Lee Jae Min, Jung Kyung Kuk, Lee Sung Ho, Ko Jong Soo. One-step fabrication of nickel nanocones by electrodeposition using $CaCl_2 \cdot 2H_2O$ as capping reagent. *Applied Surface Science*, 2016, vol. 369, pp. 163–169. DOI: 10.1016/j.apsusc.2016.02.006.
7. Yao Chen-zhong, Wei Bo-hui, Meng Li-xin, Hu Xiao-hua, Yao Ji-huan, Cui Ke-yong. Template-Free Electrochemical Deposition and Characterization of Ni Nano/Microrod Arrays. *Journal of the Electrochemical Society*, 2012, vol. 159, no. 7, pp. 425–430. DOI: 10.1149/2.027207jes.
8. Matveeva N.S., Gryzunova N.N., Yasnikov I.S. Formation of pentagonal nickel microcrystals in continuous electrodeposited coatings with a selective inhibition of the growth of their individual facets. *Physics of the Solid State*, 2022, pp. 64–70. DOI: 10.21883/FTT.2021.12.51681.168.
9. Lee Jae Min, Jung Kyung Kuk, Ko Jong Soo. Effect of NaCl in a nickel electrodeposition on the formation of nickel nanostructure. *Journal of Materials Science*, 2015, vol. 51, pp. 3036–3044. DOI: 10.1007/s10853-015-9614-8.
10. Salehikahrizsangi P., Raeissi K., Karimzadeh F., Calabrese L., Patane S., Proverbio E. Erosion-corrosion behavior of highly hydrophobic hierarchical nickel coatings. *Colloids and surfaces A: Physicochemical and Engineering Aspects*, 2018, vol. 558, pp. 446–454. DOI: 10.1016/j.colsurfa.2018.09.003.
11. Xiang Tengfei, Chen Depeng, Lv Zhong, Yang Zhiyan, Yang Ling, Li Cheng. Robust superhydrophobic coating with superior corrosion resistance. *Journal of Alloys and Compounds*, 2019, vol. 798, pp. 320–325. DOI: 10.1016/j.jallcom.2019.05.187.
12. Gao Shuwen, Sui Yanwei, Wei Fuxiang, Qi Jiqiu, Meng Qingkun, Ren Yaojian, He Yezeng. Dandelion-like nickel/cobalt metal-organic framework based electrode materials for high performance supercapacitors. *Journal of Colloid and Interface Science*, 2018, vol. 531, pp. 83–90. DOI: 10.1016/j.jcis.2018.07.044.
13. Hang Tao, Nara H., Yokoshima T., Momma T., Osaka T. Silicon composite thick film electrodeposited on a nickel micro-nanocones hierarchical structured current collector for lithium batteries. *Journal of Power Sources*, 2013, vol. 222, pp. 503–509. DOI: 10.1016/j.jpowsour.2012.09.008.
14. Navas D., Hernández-Vélez M., Vázquez M. Ordered Ni nanohole arrays with engineered geometrical aspects and magnetic anisotropy. *Applied Physics Letters*, 2007, vol. 90, article number 192501. DOI: 10.1063/1.2737373.
15. Peugeot A., Creissen Ch.E., Karapinar D., Tran H.N., Schreiber M., Fontecave M. Benchmarking of oxygen evolution catalysts on porous nickel supports. *Joule*, 2021, vol. 5, no. 5, pp. 1281–1300. DOI: 10.1016/j.joule.2021.03.022.
16. Kim J.H., Hansora D., Sharma P., Jang Ji-Wook, Lee Jae Sung. Toward practical solar hydrogen production – an artificial photosynthetic leaf-to-farm challenge. *Chemical Society Reviews*, 2019, vol. 48, pp. 1908–1971. DOI: 10.1039/c8cs00699g.
17. Kim Tae-Woo, Lee Eun-Han, Byun Segi, Seo Doo-Won, Hwang Hyo-Jung, Yoon Hyung-Chul, Kim Han-sung, Ryi Shin-Kun. Highly selective Pd composite membrane on porous metal support for high-purity hydrogen production through effective ammonia decomposition. *Energy*, 2022, vol. 260, article number 125209. DOI: 10.1016/j.energy.2022.125209.
18. Boldyrev V.V. *The Control of the Reactivity of Solids*. Amsterdam, Elsevier scientific publishing company Publ., 1979. 226 p.
19. Zou Ruiqing, Xiang Saidi, Wang Jian, Li Yuhe, Gu Lin, Wang Yanyan. Dialectical Observation of Control-

lable Electrodeposited Ni Nanocones: the Unification of Local Disorder and Overall Orde. *Nanoscale Research Letters*, 2020, vol. 15, article number 91. DOI: 10.1186/s11671-020-03321-0.
20. Yasnikov I.S., Gryzunova N.N. On the reasons for the formation and stability of single-component microcrystals of electrolytic origin with fullerene-like truncated icosahedral habit. *JETP Letters*, 2021, vol. 114, no. 5, pp. 284–288. DOI: 10.31857/S1234567821170080.
21. Vikarchuk A.A., Gryzunova N.N., Borgardt T.A. Evolution of icosahedral copper particles in the process of their growth during electrocrystallization. *Letters on materials*, 2019, vol. 9, no. 1, pp. 124–129. DOI: 10.22226/2410-3535-2019-1-124-129.
22. Ashmor P. *Kataliz i ingibirovanie khimicheskikh reaktsiy* [Catalysis and inhibition of chemical reactions]. Moscow, Mir Publ., 1966. 507 p.
23. Gadiyak G.V., Morokov Yu.N., Tomashek M. Calculation by the CNDO/2 method of chemisorption of some gases on the (111) and (100) faces of nickel. *Russian Journal of Physical Chemistry,* 1983, vol. 57, no. 2, pp. 221–224.

СПИСОК ЛИТЕРАТУРЫ

1. Линник А.И., Прудников А.М., Шалаев Р.В., Варюхин В.Н., Костыря С.А., Бурховецкий В.В. Синтез и магнитные свойства наноколонарных пленок никеля, осажденных в аргон-азотной атмосфере // Письма в журнал технической физики. 2012. Т. 38. № 11. С. 5–13. EDN: RCVSKV.
2. Hang Tao, Li Ming, Fei Qin, Mao Dali. Characterization of nickel nanocones routed by electrodeposition without any template // Nanotechnology. 2008. Vol. 19. Article number 035201. DOI: 10.1088/0957-4484/19/03/035201.
3. Rahimi E., Davoodi A., Kiani Rashid A.R. Characterization of screw dislocation-driven growth in nickel micro-nanostructure electrodeposition process by AFM // Materials Letters. 2017. Vol. 210. P. 341–344. DOI: 10.1016/j.matlet.2017.09.057.
4. Останин Н.И., Трофимов А.А., Останина Т.Н., Шнайдер Е.А. Электроосаждение никелевых покрытий с развитой поверхностью в диффузионном режиме // Фундаментальные исследования. 2017. № 5. С. 61–65. EDN: YRPIEV.
5. Hang Tao, Ling Huiqin, Hu Anmin, Li Ming. Growth Mechanism and Field Emission Properties of Nickel Nanocones Array Fabricated by One-Step Electrodeposition // Journal of The Electrochemical Society. 2010. Vol. 157. № 12. P. 624–627. DOI: 10.1149/1.3499352.
6. Lee Jae Min, Jung Kyung Kuk, Lee Sung Ho, Ko Jong Soo. One-step fabrication of nickel nanocones by electrodeposition using $CaCl_2 \cdot 2H_2O$ as capping reagent // Applied Surface Science. 2016. Vol. 369. P. 163–169. DOI: 10.1016/j.apsusc.2016.02.006.
7. Yao Chen-zhong, Wei Bo-hui, Meng Li-xin, Hu Xiao-hua, Yao Ji-huan, Cui Ke-yong. Template-Free Electrochemical Deposition and Characterization of Ni Nano/Microrod Arrays // Journal of the Electrochemical Society. 2012. Vol. 159. № 7. P. 425–430. DOI: 10.1149/2.027207jes.
8. Матвеева Н.С., Грызунова Н.Н., Ясников И.С. Особенности формирования пентагональных микрокристаллов никеля в сплошных электроосажденных покрытиях при избирательном ингибировании роста их отдельных граней // Физика твердого тела. 2022. Т. 63. № 12. С. 2178–2184. DOI: 10.21883/FTT.2021.12.51681.168.
9. Lee Jae Min, Jung Kyung Kuk, Ko Jong Soo. Effect of NaCl in a nickel electrodeposition on the formation of nickel nanostructure // Journal of Materials Science. 2015. Vol. 51. P. 3036–3044. DOI: 10.1007/s10853-015-9614-8.
10. Salehikahrizsangi P., Raeissi K., Karimzadeh F., Calabrese L., Patane S., Proverbio E. Erosion-corrosion behavior of highly hydrophobic hierarchical nickel coatings // Colloids and surfaces A: Physicochemical and Engineering Aspects. 2018. Vol. 558. P. 446–454. DOI: 10.1016/j.colsurfa.2018.09.003.
11. Xiang Tengfei, Chen Depeng, Lv Zhong, Yang Zhiyan, Yang Ling, Li Cheng. Robust superhydrophobic coating with superior corrosion resistance // Journal of Alloys and Compounds. 2019. Vol. 798. P. 320–325. DOI: 10.1016/j.jallcom.2019.05.187.
12. Gao Shuwen, Sui Yanwei, Wei Fuxiang, Qi Jiqiu, Meng Qingkun, Ren Yaojian, He Yezeng. Dandelion-like nickel/cobalt metal-organic framework based electrode materials for high performance supercapacitors // Journal of Colloid and Interface Science. 2018. Vol. 531. P. 83–90. DOI: 10.1016/j.jcis.2018.07.044.
13. Hang Tao, Nara H., Yokoshima T., Momma T., Osaka T. Silicon composite thick film electrodeposited on a nickel micro-nanocones hierarchical structured current collector for lithium batteries // Journal of Power Sources. 2013. Vol. 222. P. 503–509. DOI: 10.1016/j.jpowsour.2012.09.008.
14. Navas D., Hernández-Vélez M., Vázquez M. Ordered Ni nanohole arrays with engineered geometrical aspects and magnetic anisotropy // Applied Physics Letters. 2007. Vol. 90. Article number 192501. DOI: 10.1063/1.2737373.
15. Peugeot A., Creissen Ch.E., Karapinar D., Tran H.N., Schreiber M., Fontecave M. Benchmarking of oxygen evolution catalysts on porous nickel supports // Joule. 2021. Vol. 5. № 5. P. 1281–1300. DOI: 10.1016/j.joule.2021.03.022.
16. Kim J.H., Hansora D., Sharma P., Jang Ji-Wook, Lee Jae Sung. Toward practical solar hydrogen production – an artificial photosynthetic leaf-to-farm challenge // Chemical Society Reviews. 2019. Vol. 48. P. 1908–1971. DOI: 10.1039/c8cs00699g.
17. Kim Tae-Woo, Lee Eun-Han, Byun Segi, Seo Doo-Won, Hwang Hyo-Jung, Yoon Hyung-Chul, Kim Han-sung, Ryi Shin-Kun. Highly selective Pd composite membrane on porous metal support for high-purity hydrogen production through effective ammonia decomposition // Energy. 2022. Vol. 260. Article number 125209. DOI: 10.1016/j.energy.2022.125209.
18. Boldyrev V.V. The Control of the Reactivity of Solids. Amsterdam: Elsevier scientific publishing company, 1979. 226 p.
19. Zou Ruiqing, Xiang Saidi, Wang Jian, Li Yuhe, Gu Lin, Wang Yanyan. Dialectical Observation of Controllable Electrodeposited Ni Nanocones: the Unification of Lo-

cal Disorder and Overall Orde // Nanoscale Research Letters. 2020. Vol. 15. Article number 91. DOI: 10.1186/s11671-020-03321-0.
20. Ясников И.С., Грызунова Н.Н. О причинах формирования и стабильности однокомпонентных микрокристаллов электролитического происхождения с фуллереноподобным габитусом усеченного икосаэдра // Письма в журнал экспериментальной и теоретической физики. 2021. Т. 114. № 5-6. С. 284–288. DOI: 10.31857/S1234567821170080.
21. Викарчук А.А., Грызунова Н.Н., Боргардт Т.А. Эволюция икосаэдрических частиц меди в процессе их роста при электрокристаллизации // Письма о материалах. 2019. Т. 9. № 1. С. 124–129. DOI: 10.22226/2410-3535-2019-1-124-129.
22. Ашмор П. Катализ и ингибирование химических реакций. М.: Мир, 1966. 507 с.
23. Гадияк Г.В., Мороков Ю.Н., Томашек М. Расчет методом ППДП/2 хемосорбции некоторых газов на гранях (111) и (100) никеля // Журнал физической химии. 1983. Т. 57. № 2. С. 370–376.

Особенности термореакционной способности электролитических никелевых покрытий с различной морфологией поверхности

Матвеева Надежда Сергеевна, аспирант
Грызунова Наталья Николаевна*[1], доктор физико-математических наук, доцент,
профессор кафедры «Нанотехнологии, материаловедение и механика»
Тольяттинский государственный университет, Тольятти (Россия)

***E-mail:** gryzunova@tltsu.ru [1]ORCID: https://orcid.org/0000-0003-2802-9537

Поступила в редакцию 21.06.2023 *Принята к публикации 07.12.2023*

Аннотация: Никелевые покрытия, состоящие из ориентированных структур, обладают уникальными каталитическими свойствами. Однако температурный интервал применения таких покрытий не определен, и требуется всестороннее изучение их термических свойств в агрессивных средах. В работе изучалось влияние особенностей габитуса кристаллов никеля на их реакционную способность с повышением температуры (термореакционную способность). Исследовались никелевые покрытия, полученные методом электроосаждения с добавлением в электролит ингибирующих добавок в виде хлоридов щелочных металлов. Для исследования реакционной способности покрытий в температурных полях применялся дифференциальный термический анализ. В качестве агрессивной среды использовался кислород. Фазовый состав образцов после нагрева определялся при помощи порошкового рентгеновского дифрактометра. Введенные добавки в виде хлоридов щелочных металлов позволили сформировать покрытия, состоящие из кристаллов конусообразного габитуса. Обнаружено, что введение в электролит добавок в виде солей щелочных металлов позволяет изменить габитус кристаллов никеля и увеличить площадь поверхности покрытия примерно на 10–15 %. Показано, что электроосажденные никелевые покрытия, состоящие из кристаллов в виде микро- и наноконусов, обладают (по сравнению с контрольным покрытием) пониженной термореакционной способностью. Экспериментальные данные позволили сделать вывод, что уменьшение интенсивности окисления на исследуемых покрытиях может быть связано с наличием преимущественного развития определенных кристаллографических граней у кристаллов, что обуславливает изменение характера взаимодействия никеля с кислородом и, как следствие, изменение интенсивности окисления.

Ключевые слова: никелевые покрытия; электроосаждение никеля; конусообразные кристаллы; термореакционная способность.

Благодарности: Статья подготовлена по материалам докладов участников XI Международной школы «Физическое материаловедение» (ШФМ-2023), Тольятти, 11–15 сентября 2023 года.

Для цитирования: Матвеева Н.С., Грызунова Н.Н. Особенности термореакционной способности электролитических никелевых покрытий с различной морфологией поверхности // Frontier Materials & Technologies. 2024. № 2. С. 67–75. DOI: 10.18323/2782-4039-2024-2-68-6.

doi: 10.18323/2782-4039-2024-2-68-7

The influence of Cu additions on the microstructure and properties of Al–Fe system alloys produced by casting into electromagnetic crystallizer

Andrey E. Medvedev*[1], PhD (Physics and Mathematics), junior researcher
Olga O. Zhukova[2], postgraduate student
Aigul F. Shaikhulova[3], PhD (Engineering), Associate Professor, senior researcher
Maxim Yu. Murashkin[4], PhD (Engineering), senior researcher
Ufa University of Science and Technology, Ufa (Russia)

***E-mail:** medvedevae@uust.ru,
medvedevandreyrf@gmail.com

[1]ORCID: https://orcid.org/0000-0002-8616-0042
[2]ORCID: https://orcid.org/0000-0002-1879-9389
[3]ORCID: https://orcid.org/0000-0002-3340-3880
[4]ORCID: https://orcid.org/0000-0001-9950-0336

Received 26.06.2023 *Accepted 14.02.2024*

Abstract: The modern electrical engineering industry requires cheap and easily reproducible aluminum alloys with advanced mechanical strength and electrical conductivity. This work studies the influence of small (up to 0.3 wt. %) copper additions on the microstructure and physical and mechanical properties, as well as phase transformations in the Al–Fe system alloys with an iron content of 0.5 and 1.7 wt. %, produced by continuous casting into electromagnetic crystallizer. Alloys of the above chemical compositions were produced, and subsequently annealed at 450 °C for 2 h. In all states, the microstructure (via SEM), yield strength, ultimate tensile strength, elongation to failure, and electrical conductivity were studied. It has been shown that copper additions lead to an increase in the strength of both alloys and a slight decrease in their ductility compared to similar materials without copper. An increase in strength and a decrease in ductility due to the copper addition is associated with the formation of more dispersed intermetallic particles in copper-containing Al–Fe system alloys. Additional spheroidizing annealing leads to a decrease in the length of the interphase boundary between the aluminum matrix and iron aluminide particles due to a change in their morphology, which leads to an increase in electrical conductivity. In general, copper-containing alloys showed higher mechanical strength with lower electrical conductivity, as well as higher thermal stability.

Keywords: Al; Al–Fe–Cu; casting into electromagnetic crystallizer; phase transformations; mechanical properties; electrical conductivity; thermal stability.

Acknowledgements: The research was supported by the Russian Science Foundation grant No. 20-79-10133, https://rscf.ru/project/20-79-10133/.

The research part of the work was carried out on the equipment of the Core Facility Centre “Nanotech” of Ufa University of Science and Technology. The authors express their gratitude to Professor V.N. Timofeev (Siberian Federal University) for providing the research material.

The paper was written on the reports of the participants of the XI International School of Physical Materials Science (SPM-2023), Togliatti, September 11–15, 2023.

For citation: Medvedev A.E., Zhukova O.O., Shaikhulova A.F., Murashkin M.Yu. The influence of Cu additions on the microstructure and properties of Al–Fe system alloys produced by casting into electromagnetic crystallizer. *Frontier Materials & Technologies*, 2024, no. 2, pp. 77–85. DOI: 10.18323/2782-4039-2024-2-68-7.

INTRODUCTION

Today, the major consumers of aluminum alloys are high-tech sectors of the economy, such as locomotive, railcar and shipbuilding, aerospace, automotive, electrical industries, construction, and production of power lines [1]. The current trends in metallurgy and materials science are the need to reduce weight, metal consumption, and increase the efficiency of the materials’ use. These trends are largely determined by the development of new materials with the necessary performance characteristics and the introduction of technologies for their production.

Due to their distinctive performance characteristics and technical properties, aluminum alloys stand out from other metallic materials for structural and electrical purposes. Aluminum and its alloys are used in electrical engineering and usually are produced in the form of wire rod/wire obtained by the methods of combined casting and rolling, casting, rolling, and pressing, using subsequent rolling or drawing [2; 3]. However, despite relatively high level of electrical conductivity (52–62 % IACS), their strength and heat resistance are rather low [4], which is further complicated by the fact, that strength and electrical conductivity improvement in Al alloys usually exclude each other [5]. In this regard, modern research is aimed at finding new alloys and production technologies that will allow the use of aluminum more efficiently, both in terms of physical and mechanical properties, as well as from a financial standpoint.

A step towards the wider use of aluminum was the introduction of aluminum alloys of the Al–Fe system of such

grades as 8030 and 8176, from which conductors with a cross section of 2 to 10 mm are made[1]. These alloys have greater strength than pure aluminum, such as grade 1350, good ductility and an acceptable level of fire safety. Improvements in physical and mechanical properties in alloys of the Al–Fe system were achieved by introducing Fe (in the range of 0.4–1.0 wt. %) into the composition of aluminum [6; 7], as well as small additions of Cu (up to 0.3 wt. %) [8]. The presence of Fe provided an increase in the strength of the alloy after its heat treatment (annealing). Small additions of Cu also improve the strength characteristics of conductors based on Al–Fe alloys. However, a number of physical and technical-operational indicators limit their application, encouraging researchers to look for further ways to increase the strength and thermal stability of alloys of the Al–Fe system without losing their electrical conductivity.

In recent decades, attention has been paid to the formation of nanostructured, nanophase-containing, and ultrafine-grained structures in semi-finished products and products from aluminum alloys, which can significantly improve the complex of physical and mechanical, as well as functional and operational characteristics [9; 10]. In addition, traditional methods for obtaining and processing aluminum-based alloys are being improved and developed.

One of the promising methods for the production of wire rod and wire from aluminum alloys for electrical purposes is continuous casting into electromagnetic crystallizers (EMC), also known as casting into electromagnetic mold. The use of EMC makes it possible to provide unique physical and mechanical properties of the wire by achieving extremely high cooling rates (10^3–10^4 K/s), providing unique alloy structures and properties (high strength and high electrical conductivity), as it was shown on the example of the Al–Zr [11] and Al–Ca–Fe–Si [12] alloys.

In this paper, the results of studies are carried out, which are a continuation of the work carried out by a group of scientists from Ufa University of Science and Technology, aimed at creating new materials for electrical purposes based on Al alloys obtained by casting in EMC. In [13] the Al–La–Ce alloy was produced and then subjected to high-pressure torsion (HPT). It was demonstrated that HPT does not only result in the grain size refinement, but also in the formation of a solid solution of La and Ce in Al, although this system is considered to have zero solubility of the alloying elements. In [14] studies dedicated to the Al–Fe system were conducted, showing that Al–Fe alloys, produced via EMC, tend to have higher mechanical strength and finer grain size relatively to the alloys produced by conventional methods. Also, EMC resulted in the formation of the metastable Al_2Fe phase, usually not presented in the Al–Fe system alloys [15]. As research materials, Al–0.5Fe and Al–1.7Fe alloys (wt. %), obtained by casting in EMC, additionally alloyed with 0.3 wt. % Cu (hereinafter, Al–0.5Fe–0.3Cu and Al–1.7Fe–0.3Cu, respectively), were used.

Based on the previous research, the annealing for the studied materials was conducted. In [16; 17] it was demonstrated that the annealing in the range of 450–550 °C in the Al alloys with low immiscibility of the alloying elements leads to coagulation and spheroidization process of the intermetallic particles without phase transformations. The spheroidization of lamellar/plate-like intermetallic particles in alloys of the Al–Fe system obtained by casting in EMC is accompanied by a decrease in the area of the interfacial surface and an increase in their electrical conductivity. Such heat treatment also results in the increase of the material's ductility. Since addition of the Cu into Al–Fe alloy decreases the ductility of the alloy, the annealing at 450 °C may be performed as a ductility increasing measure.

The aim of this work is establishing the influence of copper additions and intermetallic particles morphology on the mechanical and electrical properties of the Al–0.5Fe and Al–1.7Fe alloys, produced by electromagnetic casting.

METHODS

Initial bars with a diameter of 11 mm and a length of more than 2 m from alloys of the Al–Fe system with an iron content of 0.5 and 1.7 wt. %, and the addition of copper 0.3 wt. % were made by continuous casting in EMC on the experimental laboratory casting equipment at the LLC "Scientific and Practical Center for Magnetic Hydrodynamics" (Krasnoyarsk, Russia). The chemical composition of the studied alloys is presented in Table 1.

The study samples were prepared from aluminum grade A85 and the addition of Fe80Al20 master alloy in proportions selected to match the required iron concentration. After reaching a melt temperature of more than 800 °C, continuous casting was carried out in an EMC equipment at a rate of 12.4 mm/s. Cast blanks were processed by cold drawing to a diameter of 3 mm in 8 passes.

Heat treatment of samples was carried out in an atmospheric Nabertherm B 180 (Lilienthal, Germany) furnace at 450 °C for 2 h.

Scanning electron microscopy (SEM) was performed on a JEOL JSM-6490LV (Tokyo, Japan) microscope at an accelerating voltage of 15 kV. For image processing and quantitative measurements of microstructural elements (average grain size, average particle size of the second phases), the "ImageJ" software and the "Grain Size" software package were used.

Tensile tests were carried out on an Instron 5982 (Norwood, USA) machine at room temperature and a strain rate of 10^{-3} s^{-1}. At least 3 samples of each test condition were tested to obtain statistically reliable results. Yield strength ($\sigma_{0.2}$), ultimate tensile strength (σ_{UTS}), and elongation to failure (δ) were obtained using flat specimens with dimensions of 2.0×1.0×6.0 mm.

Electrical conductivity (ω) was determined with an error of ±2 % by the eddy current method. The electrical conductivity relative to annealed copper (International Annealed Copper Standard, % IACS) was calculated using the equation:

$$IACS = \frac{\omega_{Al}}{\omega_{Cu}} \cdot 100\,\%, \quad (1)$$

[1] *GOST R 58019-2017. Rod aluminium wire of 8176 and 8030 alloys. Specifications. M.: Standartinform, 2018. 20 p.*

Table 1. *Chemical composition of Al–Fe alloys, wt. %*
Таблица 1. *Химический состав Al–Fe сплавов, мас. %*

Alloy	Cu	Fe	Si	Σ (Mn, Cr, Zn)	Al
Al–0.5Fe–Cu	0.30	0.50	0.02	<0.01	99.04
Al–1.7Fe–Cu	0.30	1.85	0.00	<0.01	97.71
AA8176 (ASTM B800)	–	0.40–0.50	0.07	<0.03	The rest
AA8030 (ASTM B800)	0.15–0.20	0.35–0.45	0.07	<0.03	The rest

Note. For comparison shows the chemical composition of AA8176 and AA8030 alloys currently used as a material for electrical conductors both in Russia and abroad.

Примечание. Для сравнения приведен химический состав сплавов AA8176 и AA8030, в настоящее время используемых в качестве материала для электропроводников в России и за рубежом.

where ω_{Al} is the measured electrical conductivity of the Al alloy;
ω_{Cu} is the electrical conductivity of annealed chemically pure copper (58 MS/m).

RESULTS

Evolution of the microstructure as a result of heat treatment

Fig. 1 shows the microstructure of billets of Al–0.5Fe–0.3Cu and Al–1.7Fe–0.3Cu alloys, obtained by casting into an electromagnetic mold. Analysis of the images, obtained by SEM, showed that the aluminum matrix contains inclusions of the intermetallic phase formed during crystallization. In the Al–1.7Fe–0.3Cu alloy, particles of the second phase form a continuous net with a cell size of (2.1±0.3) μm (Fig. 1 b), and in the Al–0.5Fe–0.3Cu alloy, the intermetallic network has the average cell size is (5.7±0.9) μm (Fig. 1 a). Judging by the size of the dendritic cells, the cooling rate during crystallization of the billet was at least 1000 °C/s. A detailed examination (Fig. 1 c, 1 d) shows that the intermetallic phase crystallized in the form of plates/needles up to (0.6±1.0) μm thick in Al–0.5Fe–0.3Cu and Al–1.7Fe–0.3Cu alloys. In addition, intermetallic particles in copper-containing alloys are more fragmented than in alloys without copper.

Fig. 2 shows the microstructure of Al–0.5Fe–0.3Cu and Al–1.7Fe–0.3Cu alloys obtained by casting in EMC and additional annealing at 450 °C for 2 h. Quantitative analysis showed that annealing does not lead to a noticeable change in the size of dendritic cells in both studied materials. However, due to annealing, the particles began to spheroidize – in the structure of both alloys, a change in the morphology of thin plates/needles of the intermetallic phase is observed – their spheroidization.

Fig. 3 shows the microstructure of Al–1.7Fe and Al–1.7Fe–0.3Cu alloys after casting in EMC and additional annealing at a temperature of 450 °C for 2 h. The presence of the copper in the alloy reduces the tendency of the alloy to spheroidization after annealing at a temperature of 450 °C – in Al–1.7Fe–0.3Cu alloys particles have sharper and rougher edges.

Evolution of mechanical and electrical properties as a result of deformation processing

Table 2 shows the physical and mechanical properties of alloys of the Al–Fe system. In the initial state the ultimate tensile strength of the Al–0.5Fe–0.3Cu alloy is (106±4) MPa, in the Al–1.7Fe–0.3Cu alloy the σ_{UTS} is (174±11) MPa. With the addition of 0.3 wt. % Cu – the electrical conductivity of the Al–0.5Fe alloy is reduced by 1.7 % IACS, while the electrical conductivity of the Al–1.7Fe alloy is reduced by 8.2 % IACS (1). Such a change in electrical conductivity indicates that it is mainly controlled by the content of iron, and, accordingly, the proportion of particles of iron aluminides in alloys.

Spheroidizing annealing, aimed at reducing the length of the interfacial boundary in the alloys, led to a decrease in strength and an increase in plasticity and electrical conductivity in the study materials. Thus, in the Al–0.5Fe–0.3Cu alloy, ductility, and electrical conductivity after annealing at 450 °C for 2 h increased from 33.7 to 37.8 % and from 56.1 to 60.9 % IACS, respectively, while the tensile strength decreased from 106 to 100 MPa (within the error value). At the same time, as a result of similar annealing, it increases the ductility and electrical conductivity in the Al–1.7Fe–0.3Cu alloy from 23.3 to 23.6 %, respectively, and from 41.4 to 55.9 % IACS, and the tensile strength decreases from 175 to 150 MPa.

DISCUSSION

This paper discusses the effect of Cu alloying on the microstructure and physical and mechanical properties of alloys of the Al–Fe system, obtained by casting in EMC. It has been established that the introduction of 0.3 wt. % Cu leads to a change in the morphology of intermetallic particles formed during crystallization at rates higher than 10^3 °C/s. In alloys without Cu, the particles form dendritic cells crystallize in the shape of long plates/needles with evenly rounded edges, and in in copper-containing alloys, such particles have a noticeably shorter length, forming "fragmented" clusters. Most likely, the rough shape of the intermetallic particles forms due to the casting method, since in [18] it is demonstrated, that in additively manufactured

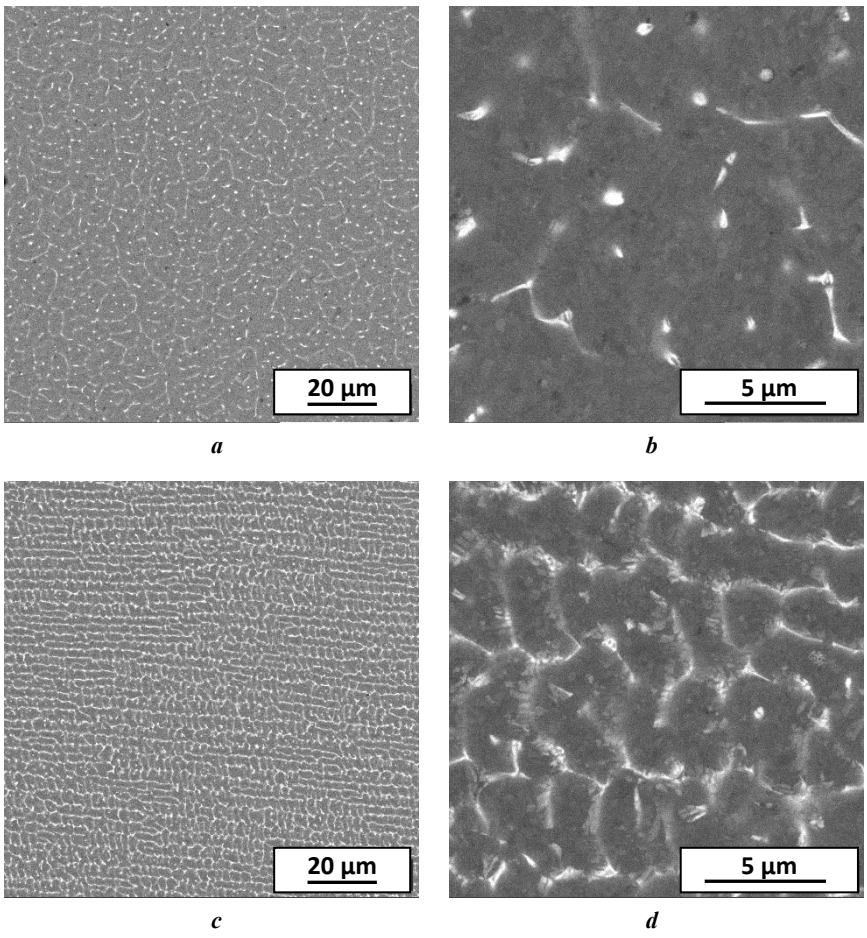

Fig. 1. *Microstructure of electromagnetically cast alloys:* ***a, b*** *– Al–0.5Fe–0.3Cu;* ***c, d*** *– Al–1.7Fe–0.3Cu, SEM*
Рис. 1. *Микроструктура сплавов, полученных литьем в электромагнитный кристаллизатор:* ***a, b*** *– Al–0,5Fe–0,3Cu;* ***c, d*** *– Al–1,7Fe–0,3Cu, РЭМ*

Al–Cu–Fe alloy intermetallic particles have smooth rounded edges. The other production methods demonstrate similar difference [19; 20].

Addition of the copper also increases the number of intermetallic particles nuclei, decreasing the distance between them, thus shortening the free dislocation path and increasing the strength of the alloy. The addition of 0.3 wt. % Cu in alloys with a selected Fe content leads to an increase in the tensile strength (from 90 to 106 MPa in the Al–0.5Fe alloy and from 150 to 174 MPa in the Al–1.7Fe alloy) and a decrease in electrical conductivity (from 57.8 to 56.1 % IACS in Al–0.5Fe alloy and from 49.6 to 41.4 % IACS in Al–1.7Fe alloy). This change in mechanical strength and electrical conductivity is sensitive to the Fe content – the value of the difference in properties is proportional to the iron content. Thus, it might be assumed that the copper doesn't have the leading role in the properties' changes of the studied alloys.

It can also be noted that additional alloying with Cu, along with an increase in strength (which is probably due to the formation of a solid solution in aluminum by copper atoms), led to an insignificant decrease in the plasticity of the study materials.

It is important to note that the addition of the same amount of copper to a commercially available 8030 alloy does not lead to a similar increase in its strength, in comparison with an 8176 alloy in which copper is absent (Table 2). Most likely, the difference in mechanical strength noted in this study is due to the difference in the methods for obtaining semi-finished products. As noted above, in alloys obtained by continuous casting in EMC, the wires/rods/blanks are rapidly cooled, and thus, during the crystallization process, most of the copper remains in the aluminum solid solution. In mass-produced semi-finished products, obtained by the method of continuous casting and rolling [21], the copper content in the solid solution of aluminum is noticeably lower, due to the lower crystallization rate (by ~2 orders of magnitude) and slow cooling during subsequent rolling.

The nature of the intermetallic particles is an open question. It is considered that iron has near-to-zero solid solution concentration in aluminium [22; 23], thus no solid solution of Fe should be presented in the Al–Fe alloys, and all the Fe should be bounded in the Al_xFe_y intermetallic particles. Copper, however, can form the solid solution in aluminium with the concentration up to 0.2 wt. % (~0.1 at. %) at a normal condition. According to the ternary Al–Cu–Fe diagram [24], at a given concentration the intermetallic particles are presented by $Al_{13}Fe_4$ and Al_7Cu_2Fe phases. Since the total amount of Cu in the Al–0.5Fe–0.3Cu alloy is 0.3 wt. % and could even be considered impurity, it would be quite hard to separate the strengthening effect of Cu solid solution in aluminium

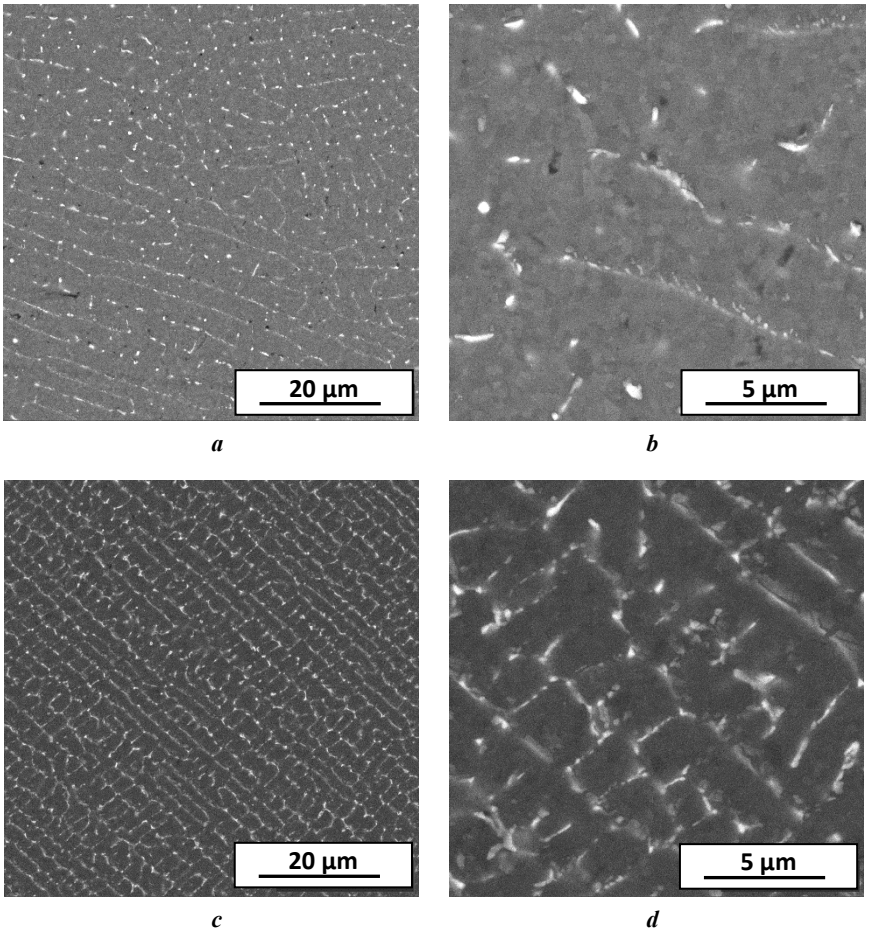

Fig. 2. *Microstructure of alloys after casting into electromagnetic crystallizer and additional annealing at 450 °C, 2 h:* ***a, b*** *– Al–0.5Fe–0.3Cu;* ***c, d*** *– Al–1.7Fe–0.3Cu, SEM*
Рис. 2. *Микроструктура сплавов после литья в электромагнитный кристаллизатор и дополнительного отжига при 450 °С, 2 ч:* ***a, b*** *– Al–0,5Fe–0,3Cu;* ***c, d*** *– Al–1,7Fe–0,3Cu, РЭМ*

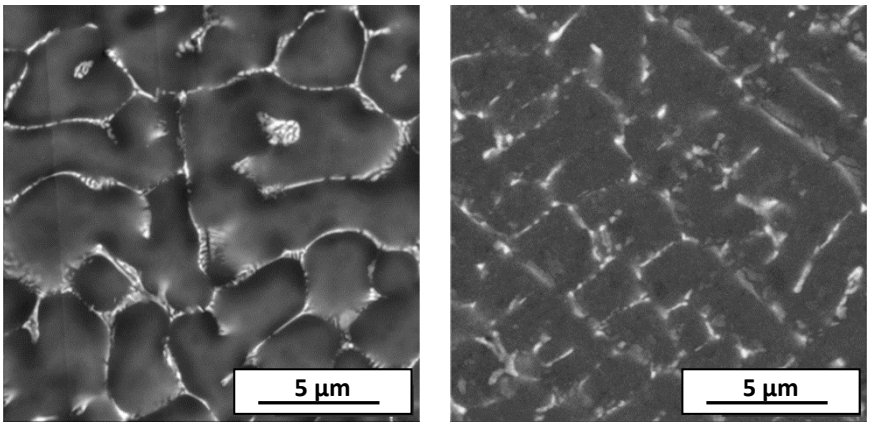

Fig. 3. *Microstructure of Al–1.7Fe (**a**) and Al–1.7Fe–0.3Cu (**b**) alloys after casting in electromagnetic crystallizer and additional annealing at 450 °C, 2 h (SEM)*
Рис. 3. *Микроструктура сплавов Al–1,7Fe (**a**) и Al–1,7Fe–0,3Cu (**b**) после литья в электромагнитный кристаллизатор и дополнительного отжига при 450 °С, 2 ч (РЭМ)*

Table 2. *Physical and mechanical properties of alloys of the Al–Fe system*
Таблица 2. *Физические и механические свойства сплавов системы Al–Fe*

Alloy	State	Electrical properties		Mechanical properties		
		ω, MS/m	IACS, %	$\sigma_{0.2}$, MPa	σ_{UTS}, MPa	δ, %
Al–0.5Fe–0.3Cu	EMC	32.54±0.21	56.1±0.4	72±8	106±4	33.7±6.5
	EMC + 450 °C, 2 h	35.32±0.20	60.9±0.6	65±8	100±13	37.8±2.8
Al–1.7Fe–0.3Cu	EMC	24.01±0.16	41.4±0.3	113±9	174±11	23.6±2.1
	EMC + 450 °C, 2 h	32.42±0.18	55.9±0.5	85±5	149±4	23.9±2.1
Al–0.5Fe [14]	EMC	29.83±0.19	57.8±0.5	35±3	90±7	32.5±3.4
	EMC + 450 °C, 2 h	–	–	–	–	–
Al–1.7Fe [14]	EMC	28.77±0.21	49.6±0.6	60±6	150±11	28.8±2.1
	EMC + 450 °C, 2 h	33.04±0.17	57.0±0.4	68±5	133±3	33.5±2.8
AA8176 (ASTM B800)	–	–	60.6	–	103–152	–
AL2 (EN 50183:2000)	–	–	52.5	–	315	–
AT2 (IEC 62641:2023)	–	–	55.0	–	225–248	–
8030 (GOST R 58019-2017)	–	–	60.0	–	115–140	12
8176 (GOST R 58019-2017)	–	–	60.0	–	115–140	12

and Al_7Cu_2Fe phase with the acceptable tolerance. So, in this study the effect of Cu additions is considered as synergetic of all Cu-containing features.

It would be safe to assume that copper, at least in the cast state, is both presented in the solid solution, intermetallic particles, and grain boundaries segregations. Additional spheroidizing annealing showed that additional alloying with Cu makes alloys of the Al–Fe system obtained by casting in EMC more sensitive to changes in strength and electrical conductivity as a result, and this effect increases with an increase in the Fe content in aluminum. Comparing to the Al–1.7Fe alloy, Al–1.7Fe–0.3Cu alloy demonstrates better thermal stability – it loses mechanical strength to a lesser value. The nature of this effect is yet to be studied.

An annealing at 450 °C for 2 h that was carried out for copper-containing alloys Al–0.5Fe–0.3Cu and Al–1.7Fe–0.3Cu showed result, similar to one observed before [14]. The coagulation of the particles, occurred during the heat treatment, resulted in the smoothing of the particles' sharp edges, making the specimens ess likely to crack during the deformation.

Due to the use of EMC, we can gain the pronounced effect of the influence of copper on the morphology of the phases and the properties of semi-finished products, relative to those obtained by conventional methods. It would be interesting to find out if this effect transfers to the final product, such as wire/stripe. Future studies will be focused on this question as well.

CONCLUSIONS

1. It was established, that addition of 0.3 wt. % copper to the electromagnetically cast Al–0.5Fe and Al–1.7Fe alloys results in smaller size of the intermetallic particles.

2. Addition of the copper into Al–0.5Fe and Al–1.7Fe alloys increases their ultimate tensile strength (by 16 MPa in Al–0.5Fe alloy and by 24 MPa in Al–1.7Fe alloy). It also resulted in the decrease of the electrical conductivity (by 1.7 % IACS in Al–0.5Fe alloy and by 8.2 % IACS in Al–1.7Fe alloy).

3. Iron content in the studied alloys has higher effect on the properties of the alloy that copper content.

4. Annealing at 450 °C for 2 h leads to spheroidizing of the intermetallic particles, smoothing their edges and decreasing particle-matrix interphase area. Such heat treatment, resulting in decrease of the mechanical strength and increase of electrical conductivity, has seemingly no effect on the ductility of the alloys.

5. Alloys, containing additional copper, demonstrate higher thermal stability – they have less value of softening during heat treatment compared to the non-copper alloys. The EMC technique provides the emphasized effect of the Cu presence, that would be negligible in case of traditional cast methods.

REFERENCES

1. Aamir M., Giasin K., Tolouei-Rad M., Vafadar A. A review: drilling performance and hole quality of aluminium alloys for aerospace applications. *Journal of*

Materials Research and Technology, 2020, vol. 9, no. 6, pp. 12484–12500. DOI: 10.1016/j.jmrt.2020.09.003.
2. Belov N.A., Korotkova N.O., Akopyan T.K., Pesin A.M. Phase composition and mechanical properties of Al–1.5%Cu–1.5%Mn–0.35%Zr(Fe,Si) wire alloy. *Journal of Alloys and Compounds*, 2019, vol. 782, pp. 735–746. DOI: 10.1016/j.jallcom.2018.12.240.
3. Cai S.L., Wan J.C., Hao Y.J., Koch C.C. Dual gradient microstructure to simultaneously improve strength and electrical conductivity of aluminum wire. *Materials Science and Engineering: A*, 2020, vol. 783, article number 139308. DOI: 10.1016/j.msea.2020.139308.
4. Lee Keunwon, Song Yongwook, Kim Sehoon, Kim Minsang, Seol Jaebok, Cho Kisub, Choi Hyunjoo. Genetic design of new aluminum alloys to overcome strength-ductility trade-off dilemma. *Journal of Alloys and Compounds*, 2023, vol. 947, article number 169546. DOI: 10.1016/j.jallcom.2023.169546.
5. Genc M., Eloi P., Blandin J.-J., Pascal C., Donnadieu P., De Geuser F., Lhuissier P., Desrayaud C., Martin G. Optimization of the strength vs. conductivity trade-off in an aluminium alloy designed for laser powder bed fusion. *Materials Science and Engineering: A*, 2022, vol. 858, article number 144139. DOI: 10.1016/j.msea.2022.144139.
6. Sasaki T.T., Ohkubo T., Hono K. Microstructure and mechanical properties of bulk nanocrystalline Al-Fe alloy processed by mechanical alloying and spark plasma sintering. *Acta Materialia*, 2009, vol. 57, no. 12, pp. 3529–3538. DOI: 10.1016/j.actamat.2009.04.012.
7. Zhao Qingru, Qian Zhao, Cui Xiaoli, Wu Yuying, Liu Xiangfa. Optimizing microstructures of dilute Al-Fe-Si alloys designed with enhanced electrical conductivity and tensile strength. *Journal of Alloys and Compounds*, 2015, vol. 650, pp. 768–776. DOI: 10.1016/j.jallcom.2015.08.052.
8. Jiang Xinyang, Zhang Ying, Yi Danqing, Wang Haisheng, Deng Xianbo, Wang Bin. Low-temperature creep behavior and microstructural evolution of 8030 aluminum cables. *Materials Characterization*, 2017, vol. 130, pp. 181–187. DOI: 10.1016/j.matchar.2017.05.040.
9. Valiev R.Z., Langdon T.G. Principles of equal-channel angular pressing as a processing tool for grain refinement. *Progress in Materials Science*, 2006, vol. 51, no. 7, pp. 881–981. DOI: 10.1016/j.pmatsci.2006.02.003.
10. Zhilyaev A.P., Langdon T.G. Using high-pressure torsion for metal processing: Fundamentals and applications. *Progress in Materials Science*, 2008, vol. 53, no. 6, pp. 893–979. DOI: 10.1016/j.pmatsci.2008.03.002.
11. Belov N., Murashkin M., Korotkova N., Akopyan T., Timofeev V. Structure and properties of Al–0.6 Wt.%Zr wire alloy manufactured by direct drawing of electromagnetically cast wire rod. *Metals (Basel)*, 2020, vol. 10, no. 6, pp. 1–11. DOI: 10.3390/met10060769.
12. Belov N., Akopyan T., Korotkova N., Murashkin M., Timofeev V., Fortuna A. Structure and properties of Ca and Zr containing heat resistant wire aluminum alloy manufactured by electromagnetic casting. *Metals (Basel)*, 2021, vol. 11, no. 2, article number 236. DOI: 10.3390/met11020236.
13. Murashkin M.Y., Sabirov I., Medvedev A.E., Enikeev N.A., Lefebvre W., Valiev R.Z., Sauvage X. Mechanical and electrical properties of an ultrafine grained Al-8.5wt. % RE (RE=5.4wt.% Ce, 3.1wt.% La) alloy processed by severe plastic deformation. *Materials and Design*, 2016, vol. 90, pp. 433–442. DOI: 10.1016/j.matdes.2015.10.163.
14. Medvedev A.E., Zhukova O.O., Fedotova D.D., Murashkin M.Yu. The mechanical properties, electrical conductivity, and thermal stability of a wire made of Al–Fe alloys produced by casting into an electromagnetic crystallizer. *Frontier Materials & Technologies*, 2022, no. 3-1, pp. 96–105. DOI: 10.18323/2782-4039-2022-3-1-96-105.
15. Medvedev A., Zhukova O., Enikeev N., Kazykhanov V., Timofeev V., Murashkin M. The Effect of Casting Technique and Severe Straining on the Microstructure, Electrical Conductivity, Mechanical Properties and Thermal Stability of the Al–1.7 wt.% Fe Alloy. *Materials*, 2023, vol. 16, article number 3067. DOI: 10.3390/ma16083067.
16. Mogucheva A.A., Zyabkin D.V., Kaibyshev R.O. Effect of annealing on the structure and properties of aluminum alloy Al–8% MM. *Metal Science and Heat Treatment*, 2012, vol. 53, pp. 450–454 DOI: 10.1007/s11041-012-9414-6.
17. Akopyan T.K., Letyagin N.V., Belov N.A., Koshmin A.N., Gizatulin D.S. Analysis of the Microstructure and Mechanical Properties of a New Wrought Alloy Based on the ((Al) + Al_4(Ca,La)) Eutectic. *Physics of Metals and Metallography*, 2020, vol. 121, pp. 914–919. DOI: 10.1134/S0031918X20080025.
18. Cheng Yue, Miyawaki T., Wang Wenyuan, Takata N., Suzuki A., Kobashi M., Kato M. Laser-beam powder bed fusion of Al–Fe–Cu alloy to achieve high strength and thermal conductivity. *Additive Manufacturing Letters*, 2024, vol. 8, article number 100191. DOI: 10.1016/j.addlet.2023.100191.
19. Aghaali V., Rahimipour M.R., Faraji A., Ebadzadeh T. The effect of microwave radiation on the formation of quasi-crystalline phases in the Al-Cu-Fe system prepared by induction furnace. *Materials Today Communications*, 2024, vol. 38, article number 107499. DOI: 10.1016/j.mtcomm.2023.107499.
20. Zhao Yuliang, He Weixiang, Medina J., Song Dongfu, Sun Zhenzhong, Xue Yanlin, González-Doncel G., Fernández R. Contribution of the Fe-rich phase particles to the high temperature mechanical behaviour of an Al-Cu-Fe alloy. *Journal of Alloys and Compounds*, 2024, vol. 973, article number 172866. DOI: 10.1016/j.jallcom.2023.172866.
21. Belyy D.I. Aluminum alloys for conductors of cable products. *Kabeli i provoda*, 2012, no. 1, pp. 8–15. EDN: PWOFCV.
22. Mondolfo L.F. *Aluminum Alloys Structure and Properties*. Oxford, Butterworth Publ., 1976. 971 p.
23. Jiang Hongxiang, Li Shixin, Zhang Lili, He Jie, Zheng Qiuju, Song Yan, Li Yanqiang, Zhao Jiuzhou. The influence of rare earth element lanthanum on the microstructures and properties of as-cast 8176 (Al-0.5Fe) aluminum alloy. *Journal of Alloys and Compounds*, 2021, vol. 859, article number 157804. DOI: 10.1016/j.jallcom.2020.157804.
24. Draissia M., Debili M.-Y. Study of solid-solution hardening in binary aluminium-based alloys. *Open Physics*, 2005, vol. 3, no. 3, pp. 395–408. DOI: 10.2478/BF02475646.

СПИСОК ЛИТЕРАТУРЫ

1. Aamir M., Giasin K., Tolouei-Rad M., Vafadar A. A review: drilling performance and hole quality of aluminium alloys for aerospace applications // Journal of Materials Research and Technology. 2020. Vol. 9. № 6. P. 12484–12500. DOI: 10.1016/j.jmrt.2020.09.003.
2. Belov N.A., Korotkova N.O., Akopyan T.K., Pesin A.M. Phase composition and mechanical properties of Al–1.5%Cu–1.5%Mn–0.35%Zr(Fe,Si) wire alloy // Journal of Alloys and Compounds. 2019. Vol. 782. P. 735–746. DOI: 10.1016/j.jallcom.2018.12.240.
3. Cai S.L., Wan J.C., Hao Y.J., Koch C.C. Dual gradient microstructure to simultaneously improve strength and electrical conductivity of aluminum wire // Materials Science and Engineering: A. 2020. Vol. 783. Article number 139308. DOI: 10.1016/j.msea.2020.139308.
4. Lee Keunwon, Song Yongwook, Kim Sehoon, Kim Minsang, Seol Jaebok, Cho Kisub, Choi Hyunjoo. Genetic design of new aluminum alloys to overcome strength-ductility trade-off dilemma // Journal of Alloys and Compounds. 2023. Vol. 947. Article number 169546. DOI: 10.1016/j.jallcom.2023.169546.
5. Genc M., Eloi P., Blandin J.-J., Pascal C., Donnadieu P., De Geuser F., Lhuissier P., Desrayaud C., Martin G. Optimization of the strength vs. conductivity trade-off in an aluminium alloy designed for laser powder bed fusion // Materials Science and Engineering: A. 2022. Vol. 858. Article number 144139. DOI: 10.1016/j.msea.2022.144139.
6. Sasaki T.T., Ohkubo T., Hono K. Microstructure and mechanical properties of bulk nanocrystalline Al-Fe alloy processed by mechanical alloying and spark plasma sintering // Acta Materialia. 2009. Vol. 57. № 12. P. 3529–3538. DOI: 10.1016/j.actamat.2009.04.012.
7. Zhao Qingru, Qian Zhao, Cui Xiaoli, Wu Yuying, Liu Xiangfa. Optimizing microstructures of dilute Al-Fe-Si alloys designed with enhanced electrical conductivity and tensile strength // Journal of Alloys and Compounds. 2015. Vol. 650. P. 768–776. DOI: 10.1016/j.jallcom.2015.08.052.
8. Jiang Xinyang, Zhang Ying, Yi Danqing, Wang Haisheng, Deng Xianbo, Wang Bin. Low-temperature creep behavior and microstructural evolution of 8030 aluminum cables // Materials Characterization. 2017. Vol. 130. P. 181–187. DOI: 10.1016/j.matchar.2017.05.040.
9. Valiev R.Z., Langdon T.G. Principles of equal-channel angular pressing as a processing tool for grain refinement // Progress in Materials Science. 2006. Vol. 51. № 7. P. 881–981. DOI: 10.1016/j.pmatsci.2006.02.003.
10. Zhilyaev A.P., Langdon T.G. Using high-pressure torsion for metal processing: Fundamentals and applications // Progress in Materials Science. 2008. Vol. 53. № 6. P. 893–979. DOI: 10.1016/j.pmatsci.2008.03.002.
11. Belov N., Murashkin M., Korotkova N., Akopyan T., Timofeev V. Structure and properties of Al–0.6 Wt.%Zr wire alloy manufactured by direct drawing of electromagnetically cast wire rod // Metals (Basel). 2020. Vol. 10. № 6. P. 1–11. DOI: 10.3390/met10060769.
12. Belov N., Akopyan T., Korotkova N., Murashkin M., Timofeev V., Fortuna A. Structure and properties of Ca and Zr containing heat resistant wire aluminum alloy manufactured by electromagnetic casting // Metals (Basel). 2021. Vol. 11. № 2. Article number 236. DOI: 10.3390/met11020236.
13. Murashkin M.Y., Sabirov I., Medvedev A.E., Enikeev N.A., Lefebvre W., Valiev R.Z., Sauvage X. Mechanical and electrical properties of an ultrafine grained Al-8.5wt. % RE (RE=5.4wt.% Ce, 3.1wt.% La) alloy processed by severe plastic deformation // Materials and Design. 2016. Vol. 90. P. 433–442. DOI: 10.1016/j.matdes.2015.10.163.
14. Медведев А.Е., Жукова О.О., Федотова Д.Д., Мурашкин М.Ю. Механические свойства, электропроводность и термостабильность проволоки из сплавов системы Al–Fe, полученных литьем в электромагнитный кристаллизатор // Frontier Materials & Technologies. 2022. № 3-1. С. 96–105. DOI: 10.18323/2782-4039-2022-3-1-96-105.
15. Medvedev A., Zhukova O., Enikeev N., Kazykhanov V., Timofeev V., Murashkin M. The Effect of Casting Technique and Severe Straining on the Microstructure, Electrical Conductivity, Mechanical Properties and Thermal Stability of the Al–1.7 wt.% Fe Alloy // Materials. 2023. Vol. 16. Article number 3067. DOI: 10.3390/ma16083067.
16. Mogucheva A.A., Zyabkin D.V., Kaibyshev R.O. Effect of annealing on the structure and properties of aluminum alloy Al–8% MM // Metal Science and Heat Treatment. 2012. Vol. 53. P. 450–454 DOI: 10.1007/s11041-012-9414-6.
17. Akopyan T.K., Letyagin N.V., Belov N.A., Koshmin A.N., Gizatulin D.S. Analysis of the Microstructure and Mechanical Properties of a New Wrought Alloy Based on the ((Al) + Al_4(Ca,La)) Eutectic // Physics of Metals and Metallography. 2020. Vol. 121. P. 914–919. DOI: 10.1134/S0031918X20080025.
18. Cheng Yue, Miyawaki T., Wang Wenyuan, Takata N., Suzuki A., Kobashi M., Kato M. Laser-beam powder bed fusion of Al–Fe–Cu alloy to achieve high strength and thermal conductivity // Additive Manufacturing Letters. 2024. Vol. 8. Article number 100191. DOI: 10.1016/j.addlet.2023.100191.
19. Aghaali V., Rahimipour M.R., Faraji A., Ebadzadeh T. The effect of microwave radiation on the formation of quasi-crystalline phases in the Al-Cu-Fe system prepared by induction furnace // Materials Today Communications. 2024. Vol. 38. Article number 107499. DOI: 10.1016/j.mtcomm.2023.107499.
20. Zhao Yuliang, He Weixiang, Medina J., Song Dongfu, Sun Zhenzhong, Xue Yanlin, González-Doncel G., Fernández R. Contribution of the Fe-rich phase particles to the high temperature mechanical behaviour of an Al-Cu-Fe alloy // Journal of Alloys and Compounds. 2024. Vol. 973. Article number 172866. DOI: 10.1016/j.jallcom.2023.172866.
21. Белый Д.И. Алюминиевые сплавы для токопроводящих жил кабельных изделий // Кабели и провода. 2012. № 1. С. 8–15. EDN: PWOFCV.
22. Mondolfo L.F. Aluminum Alloys Structure and Properties. Oxford: Butterworth, 1976. 971 p.
23. Jiang Hongxiang, Li Shixin, Zhang Lili, He Jie, Zheng Qiuju, Song Yan, Li Yanqiang, Zhao Jiuzhou. The influence of rare earth element lanthanum on

the microstructures and properties of as-cast 8176 (Al-0.5Fe) aluminum alloy // Journal of Alloys and Compounds. 2021. Vol. 859. Article number 157804. DOI: 10.1016/j.jallcom.2020.157804.

24. Draissia M., Debili M.-Y. Study of solid-solution hardening in binary aluminium-based alloys // Open Physics. 2005. Vol. 3. № 3. P. 395–408. DOI: 10.2478/BF02475646.

Влияние добавок Cu на микроструктуру и свойства сплавов системы Al–Fe, полученных методом литья в электромагнитный кристаллизатор

Медведев Андрей Евгеньевич*[1], кандидат физико-математических наук, младший научный сотрудник
Жукова Ольга Олеговна[2], аспирант
Шайхулова Айгуль Фазировна[3], кандидат технических наук, доцент, старший научный сотрудник
Мурашкин Максим Юрьевич[4], кандидат технических наук, старший научный сотрудник
Уфимский университет науки и технологий, Уфа (Россия)

***E-mail:** medvedevae@uust.ru, medvedevandreyrf@gmail.com

[1]ORCID: https://orcid.org/0000-0002-8616-0042
[2]ORCID: https://orcid.org/0000-0002-1879-9389
[3]ORCID: https://orcid.org/0000-0002-3340-3880
[4]ORCID: https://orcid.org/0000-0001-9950-0336

Поступила в редакцию 26.06.2023 *Принята к публикации 14.02.2024*

Аннотация: Современная электротехническая промышленность требует дешевых и легко воспроизводимых алюминиевых сплавов – материалов с повышенной механической прочностью и электропроводностью. В работе исследовано влияние малых (до 0,3 мас. %) добавок меди на микроструктуру и физико-механические свойства, а также фазовые трансформации в сплавах системы Al–Fe с содержанием железа 0,5 и 1,7 мас. %, полученных методом непрерывного литья в электромагнитный кристаллизатор. Были получены сплавы указанных выше химических составов, впоследствии отожженные при 450 °C в течение 2 ч. Во всех состояниях были изучены микроструктура (с помощью РЭМ), предел текучести, предел прочности при растяжении, удлинение до разрушения и электропроводность. Показано, что добавки меди приводят к увеличению прочности обоих сплавов и некоторому снижению их пластичности по сравнению с аналогичными материалами без меди. Повышение прочности и снижение пластичности за счет добавки меди связано с образованием более дисперсных интерметаллидных частиц в медьсодержащих сплавах системы Al–Fe. Дополнительный сфероидизирующий отжиг приводит к уменьшению протяженности межфазной границы между алюминиевой матрицей и частицами алюминида железа за счет изменения их морфологии, что ведет к увеличению электропроводности. В целом медьсодержащие сплавы показали более высокую механическую прочность при меньшей электропроводности, а также повышенную термическую стабильность.

Ключевые слова: Al; Al–Fe–Cu; литье в электромагнитный кристаллизатор; фазовые превращения; механические свойства; электрическая проводимость; термическая стабильность.

Благодарности: Исследование выполнено за счет гранта Российского научного фонда № 20-79-10133, https://rscf.ru/project/20-79-10133/.

Исследовательская часть работы выполнена на оборудовании ЦКП «Нанотех» Уфимского университета науки и технологий. Авторы выражают благодарность профессору В.Н. Тимофееву (Сибирский федеральный университет) за предоставленный материал исследования.

Статья подготовлена по материалам докладов участников XI Международной школы «Физическое материаловедение» (ШФМ-2023), Тольятти, 11–15 сентября 2023 года.

Для цитирования: Медведев А.Е., Жукова О.О., Шайхулова А.Ф., Мурашкин М.Ю. Влияние добавок Cu на микроструктуру и свойства сплавов системы Al–Fe, полученных методом литья в электромагнитный кристаллизатор // Frontier Materials & Technologies. 2024. № 2. С. 77–85. DOI: 10.18323/2782-4039-2024-2-68-7.

doi: 10.18323/2782-4039-2024-2-68-8

Acoustic properties of 15-5 PH maraging steel after energy deposition

Olga V. Muravieva[1,2,3], Doctor of Sciences (Engineering), Professor,
professor of Chair "Instruments and Methods of Measurements, Testing, Diagnostics"
Vitaly V. Muraviev[1,2,4], Doctor of Sciences (Engineering), Professor,
professor of Chair "Instruments and Methods of Measurements, Testing, Diagnostics"
Lyudmila V. Volkova[1,5], PhD (Engineering), Associate Professor,
assistant professor of Chair "Instruments and Methods of Measurements, Testing, Diagnostics"
Aleksey L. Vladykin*[1,6], postgraduate student
Konstantin Yu. Belosludtsev[1], graduate student
[1]*Kalashnikov Izhevsk State Technical University, Izhevsk (Russia)*
[2]*Udmurt Federal Research Center of the Ural branch of the RAS, Izhevsk (Russia)*

***E-mail:** pmkk@istu.ru,
vladykin-ndt@mail.ru

[3]ORCID: https://orcid.org/0000-0003-3442-8163
[4]ORCID: https://orcid.org/0000-0001-8590-1382
[5]ORCID: https://orcid.org/0000-0001-5128-6465
[6]ORCID: https://orcid.org/0009-0006-1813-2011

Received 05.07.2023 *Accepted 28.11.2023*

Abstract: The study of the acoustic properties of maraging steels operated under various energy force and temperature actions is a critical task, since it is the method of acoustic structuroscopy that provides the most reliable connection with the structure, stress-strain state and mechanical properties of steels. The paper is devoted to research of the acoustic properties of the 15-5 PH maraging steel samples under various types of heat treatment under the conditions of mechanical tensile and cyclic loads. Samples of the 15-5 PH maraging steel were studied in three structural states: solid solution annealing and subsequent aging at 470 and 565 °C; during tensile tests; during cyclic tension-compression loading. The research used a unique scientific installation "Information-measuring complex for investigation of acoustic properties of materials and products". It implements the acoustic mirror-shadow multiple reflections method using electromagnetic-acoustic and piezoelectric transducers based on polyvinylidene fluoride film to excite and receive waves and allows determining the velocity of wave propagation with an error of no more than 2 m/s. The acoustic (wave velocity, elastic moduli, electromagnetic-acoustical (EMA) transformation coefficients, acoustic anisotropy coefficients, acoustoelastic coupling coefficients) and electromagnetic (coercive force and electrical conductivity) characteristics of the samples were examined. The samples were studied in the initial state (before loading); stepwise in the process of tensile loads and subsequent unloading; after tensile tests; during cyclic tension-compression loading. It was revealed that the following acoustic parameters of 15-5 PH steel samples are the greatest structural sensitivity to mechanical tensile load and cyclic loading: transverse wave velocity, Poisson's ratio, double EMA-transformation coefficient, and acoustic anisotropy coefficient.

Keywords: 15-5 PH maraging steel; acoustic properties; heat treatment; mechanical tensile load; cyclic loading.

Acknowledgements: The study was supported by the grant of the Russian Science Foundation (project No. 22-19-00252, https://rscf.ru/project/22-19-00252/) using the Unique Scientific Installation "Information-measuring complex for investigation of acoustic properties of materials and products" (registration number 586308).

The paper was written on the reports of the participants of the XI International School of Physical Materials Science (SPM-2023), Togliatti, September 11–15, 2023.

For citation: Muravieva O.V., Muraviev V.V., Volkova L.V., Vladykin A.L., Belosludtsev K.Yu. Acoustic properties of 15-5 PH maraging steel after energy deposition. *Frontier Materials & Technologies*, 2024, no. 2, pp. 87–100. DOI: 10.18323/2782-4039-2024-2-68-8.

INTRODUCTION

Maraging steels are widely used in many industries due to their high strength and toughness without loss of ductility and increased heat resistance with a low cold brittleness threshold. High mechanical properties of these steels are achieved by the use of alloying elements, an important component of which is nickel, as well as chromium, copper, cobalt, titanium, manganese, silicon, etc. Heat treatment of maraging steels consists of solid solution annealing and subsequent aging in the temperature range of 400...550 °C, which makes the greatest contribution to strengthening [1]. Maraging steels are used for heavy-duty parts operated under conditions of cyclic force and temperature exposure, at extremely high and low temperatures.

The KhM-12 steel discussed in this paper, also known as 15-5 PH or UNS S15500, contains chromium, nickel and copper as alloying elements. Its unique structure ensures increased strength and corrosion resistance, improved

toughness and a quenching temperature lower than its predecessor, 17-4 PH steel, does [2].

In many foreign publications dealing with 15-5 PH maraging steel, the influence of heat treatment modes on the microstructure and mechanical properties of this steel is studied using destructive methods on special samples cut from industrial products [3–7]. In particular, in [3], using electron microscopy, it was shown that the microstructure of martensitic stainless steel undergoes a complex evolution during long-term aging. This evolution includes the possible development of a minor austenitic phase, copper-rich precipitates, and the precipitation of chromium and silicon from the solid solution. Precipitates several nm in size coherently nucleate during aging at the interfaces with the matrix. With longer aging, clusters are uniformly formed in the matrix.

It was shown in [4] that the tensile strength of a martensitic steel weld first increases with the growth of aging temperature after welding, which is associated with the size and distribution of the copper-rich phase, and then decreases with the growth of aging temperature after welding, probably due to an increase in amount of residual austenite.

The results of [5] showed that the tensile strength of stainless steel first decreased with increasing aging temperature from 440 to 540 °C, and then increased with increasing aging temperature from 540 to 610 °C. The authors believe that hardening mechanisms caused by the dislocation density and deposition of a second phase enriched in copper precipitates at various aging temperatures are the predominant strengthening mechanisms.

In [6], cyclic bending tests were carried out on samples made of martensitic stainless steel to determine fatigue strength. The study showed that the influence of the compressive sublayer on fatigue strength is much more important than the influence of surface roughness or microstructure. In [7], electron microscopic studies identified that the strengthening of grain boundaries by dislocations and the resulting copper precipitates in 15-5 PH martensitic stainless steel is the main factor determining the increase in the tensile strength and yield of tempered martensite.

Many recent studies deal with the analysis of the microstructure and mechanical properties of maraging steels produced using additive technologies [8–10], including during cyclic tests [11]. For example, the work [8] notes that the hardness of the metal produced by direct laser sintering varies along the upper and lower parts of the finished samples and the hardness of the upper part of the samples is higher due to the finer grain size. However, aging of the alloy promotes further increase in its hardness and strength. The work [9] shows that the amount of residual austenite is significantly reduced after heat treatment, and the remaining minor residual austenite is completely converted to martensite during mechanical tension in samples produced by selective laser melting. Standard aging conditions increase the yield stress, hardness and corrosion resistance of steel through the formation of fine spherical copper-rich deposits, but make the samples brittle, which leads to a decrease in impact resistance [10]. The work [11] reports on the effect of heat treatment (aging and overaging) on the fatigue life of age-hardened 15-5 PH stainless steel produced by selective laser melting. It is shown that aging leads to dispersion strengthening of the matrix, while the sensitivity to defects in the high-cycle fatigue mode increases. Overaging makes the sample ductile due to the coarsening of copper-rich precipitates and increases the amount of residual austenite.

The use of nondestructive testing methods to analyze the structure and properties of chromium-nickel steels, as well as the influence of mechanical loading and fatigue tests on them is limited to electromagnetic nondestructive testing methods: magnetic [12] and eddy current [13].

The study of the acoustic properties of steels operated under various energy force and temperature actions is a critical task, since it is the method of acoustic structuroscopy providing the most reliable connection with the structure, stress-strain state and mechanical properties of steels [14–19]. In particular, the authors proposed using the parameters of Poisson's ratio and acoustic anisotropy to assess the structural state of plastically deformed 09G2S steel [14], to assess microstructural changes during plastic deformation with subsequent heat treatment and low-cycle fatigue of 12KM8N10T austenitic steel [15; 16]. The acoustoelasticity method was used to assess residual stresses when manufacturing the axisymmetric parts from 03N17K10V10MT maraging steel [17], as well as to assess residual stresses when manufacturing rails [18]. The work [19] shows the possibility of determining the degree of damage of flat 12Kh18N10T austenitic steel samples in the region of low-cycle fatigue by the velocity of propagation of elastic waves and coercive force.

All the above-described studies in the field of acoustic structuroscopy can be implemented on specially made flat samples. In relation to round-bar samples of maraging steels, it is promising to use the non-contact electromagnetic-acoustic (EMA) method of emitting and receiving acoustic waves and the echo-shadow technique of multiple reflections due to the high accuracy and reliability of the obtained acoustic characteristics [20; 21]. This is also evidenced by the results obtained in [22; 23] dealing with assessing the influence of heat treatment and high-cycle loading by cantilever bending with rotation on the velocity of shear and Rayleigh waves in samples of 45 steel and 40H steel. One should note that martensitic steels were practically not studied previously by acoustic methods. There is also no information on the influence of heat treatment (solid solution annealing, aging) and mechanical (including cyclic) loading on the acoustic characteristics of round-bar samples used for most highly loaded parts in the oil industry.

The purpose of the work is to study the acoustic properties of samples of KhM-12 (15-5 PH) maraging steel after various types of energy impacts: heat treatment, mechanical tensile and cyclic loads.

METHODS

For the research, the authors used samples of dispersion-aging KhM-12 steel with the addition of copper (the alloy is also known as 15-5 PH and UNS S15500). The samples were subjected to various types of heat treatment:

solid solution annealing at a temperature of 1040 °C for 30 min with cooling at air and aging at temperatures of 470 and 565 °C for 3 h.

The chemical composition of 15-5 PH low-carbon steel complies with the ASTM A564 standard and contains the following alloying elements: 14 % Cr, 4 % Ni, 3 % Cu, 1 % Mn, and 1 % Si.

The samples are made in the form of cylinders with a working part diameter of 10 mm and a length of 150 mm with the fillets to a diameter of 20 mm for grippers.

The studies were carried out on a unique scientific installation “Information-measuring complex for investigation of acoustic properties of materials and products” (registration number 586308) as part of the DEMA-P information-measuring system and the DIO-1000 PA ultrasonic detector (Fig. 1). The installation provides excitation and reception of bulk transverse waves of longitudinal and radial polarization propagating along the diametric directions of the sample cross-section and a surface Rayleigh wave propagating along the sample envelope curve (Fig. 2 a). The uniqueness of the equipment is the use of a non-contact electromagnetic-acoustic method of wave emission and reception, which allows increasing significantly the reliability and accuracy of measurement results and using the EMA-transformation efficiency as an additional informative parameter. The emission and reception of a longitudinal radial-polarization wave is carried out using a flexible piezo-film such as polyvinylidene fluoride (PVDF) and a DIO-1000 PA ultrasonic detector. The installation allows recording the resulting oscillograms with a high sampling frequency and contains specific Prince IX software for calculating the main informative parameters. Typical oscillograms of the recorded series of transverse and longitudinal wave pulses re-reflected along the sample diameter are presented in Fig. 2 b, 2 c.

The velocities of longitudinal and transverse waves were calculated using the formula:

$$C_{t,l} = \frac{d \cdot n}{\Delta t},$$

where d is the average value of the object diameter at the transducer location point (determination error is 5 μm);
n is the number of analyzed reflections;
Δt is the time corresponding to n reflections.

The Rayleigh wave velocity was calculated using the formula:

$$C_R = \frac{\pi \cdot d \cdot n}{\Delta t}.$$

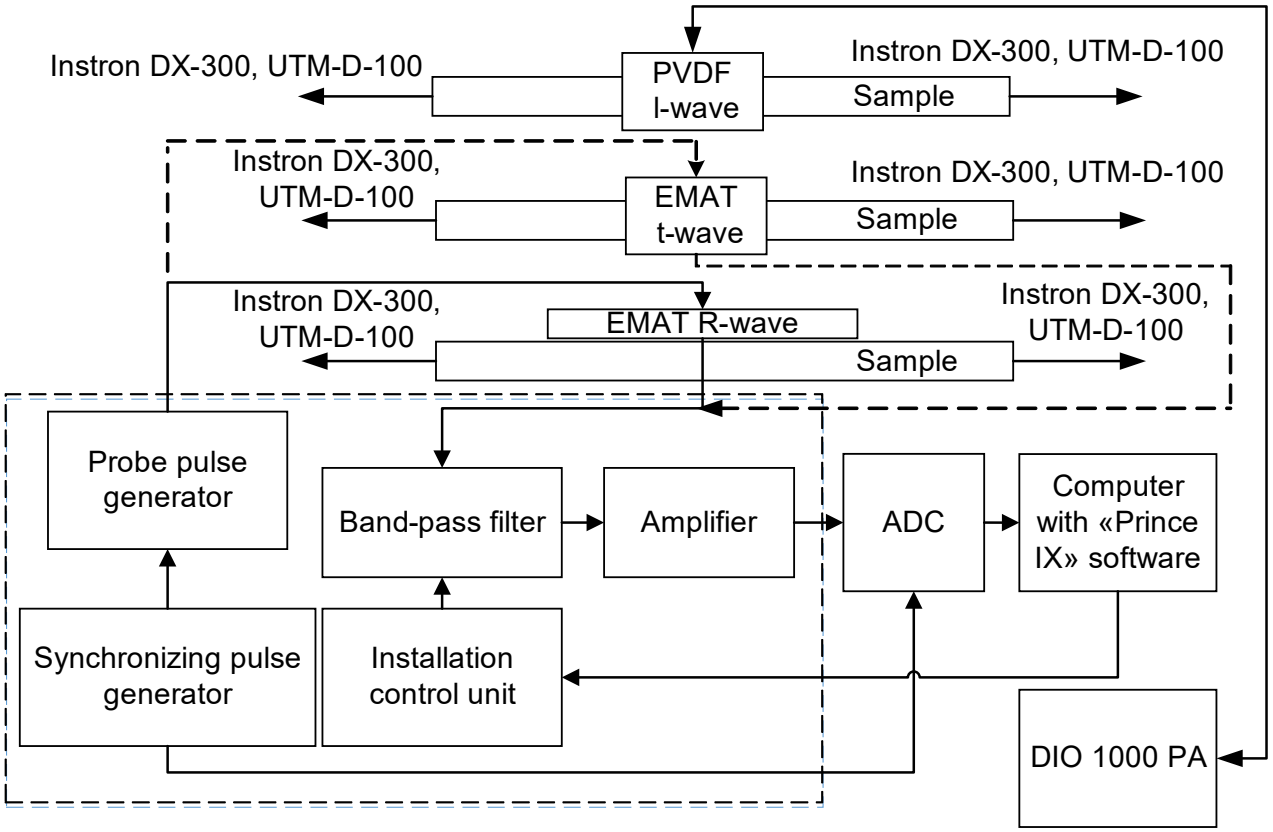

Fig. 1. *Block scheme of the experimental installation,*
where ADC is an analog-to-digital converter (LAn10-12PCI-U); SW is software;
EMAT is an electromagnetic acoustic transducer; UTM-D is a universal dynamic testing machine
Рис. 1. *Блок-схема экспериментальной установки,*
где ADC – аналого-цифровой преобразователь (ЛАн10-12PCI-У); SW – программное обеспечение;
EMAT – электромагнитно акустический преобразователь; UTM-D – универсальная испытательная машина динамическая

When determining dynamic elastic moduli (Young’s modulus E, shear modulus G, Poisson’s ratio ν), their relationship with the velocities of longitudinal and transverse waves and the material density ρ was used:

$$E = \rho \cdot C_t^2 \cdot \frac{3 - 4 \cdot C_t^2 / C_l^2}{1 - C_t^2 / C_l^2};$$

$$G = \rho \cdot C_t^2;$$

$$\nu = \frac{C_l^2 - 2 \cdot C_t^2}{2 \cdot \left(C_l^2 - C_t^2\right)}.$$

Special aspect of the acoustic method of measuring Poisson’s ratio through the velocities of elastic waves is its high accuracy determined by its independence from the sample diameter. The error in its measurements is predominant in the method of determining wave velocity.

Knowledge of the propagation velocities of transverse waves of different polarizations (axial C_{tos} and radial C_{trad}) allowed estimating the magnitude of acoustic anisotropy according to the GOST R 55805 standard:

$$A = \frac{2 \cdot \left[C_{trad} - C_{tos}\right]}{C_{trad} + C_{tos}}.$$

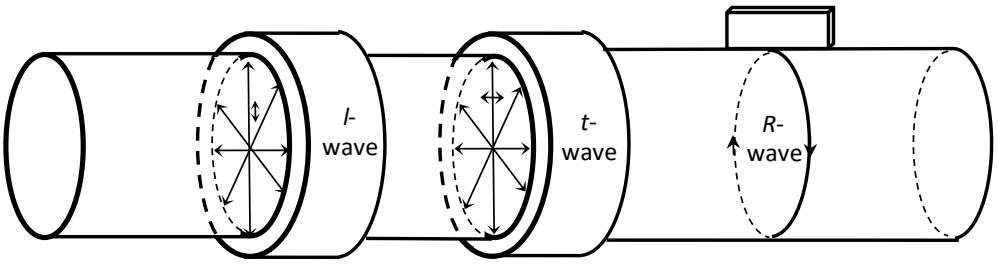

a

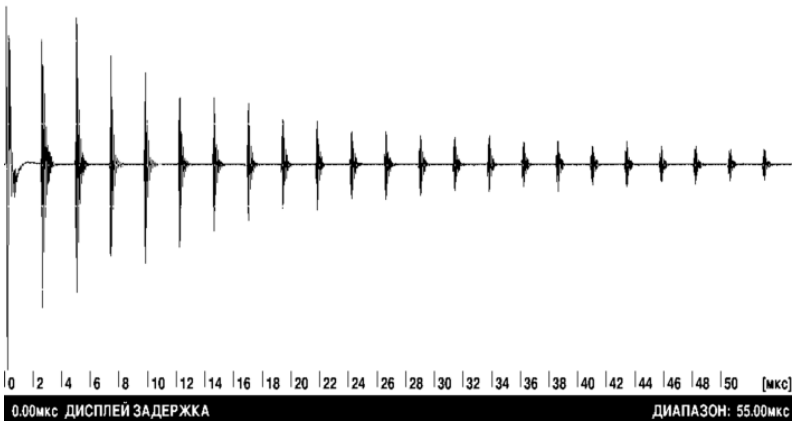

b

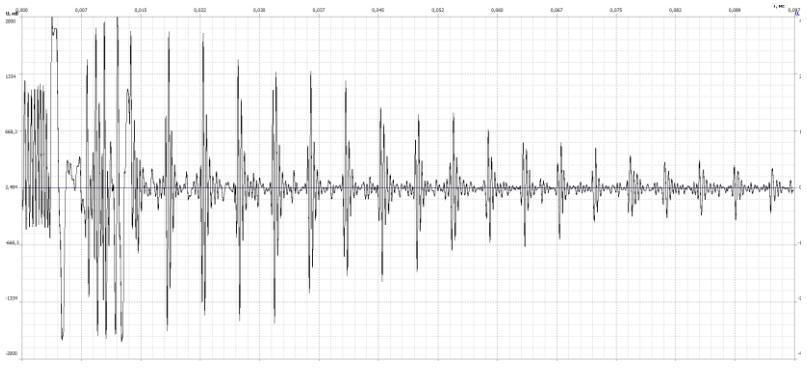

c

Fig. 2. *Scheme of propagation of bulk longitudinal l-waves, transverse t-waves and surface R-waves along the diameter of the sample (**a**); characteristic oscillograms of a series of multiple reflections of transverse waves (**b**) and longitudinal waves (**c**)*

Рис. 2. *Схема распространения объемных продольных l-волн, поперечных t-волн и поверхностных R-волн по диаметру образца (**a**); характерные осциллограммы серии многократных отражений поперечных волн (**b**) и продольных волн (**c**)*

The random error in determining the wave velocity was calculated using the formula:

$$\Delta C_r = t_{ST} \cdot \sqrt{\frac{\sum_{i=1}^{n} (C_i - C_{av})^2}{n \cdot (n-1)}},$$

where t_{ST} is the Student's coefficient (assumed equal to 2.776);
C_i is a velocity value for the i-th calculation, m/s;
C_{av} is an average velocity value based on the results of n measurements, m/s;
n is the number of measurements.

The random error in determining the velocity does not exceed 2 m/s and is comparable to the systematic error caused by the error in determining the sample diameter (5 μm) and the error in measuring time intervals (1 ns).

The EMA-transformation efficiency and the wave attenuation during propagation can be indirectly assessed by the dispersion parameter of the data array of a series of multiple reflections [24]:

$$D_x = \frac{1}{N-1} \cdot \sum_{n=0}^{N-1} (x_n - m_x)^2,$$

where N is the amount of data in the array represented as a sample sequence $\{x_n, n=0 \ldots N-1\}$;

m_x is mathematical expectation, $m_x = \frac{1}{N} \cdot \sum_{n=0}^{N-1} x_n$.

Fig. 3 shows the diagram of the physical measurement block. In addition to acoustic measurements, magnetic measurements were carried out using a KIFM-1N coercimeter (coercive force is an informative parameter), and electrical measurements were carried out using an MVP-2M eddy-current multifunctional device (relative electrical conductivity is an informative parameter). At the initial stage of the research, the density of the samples was measured by hydrostatic weighing on an HR-AG analytical balance with an accuracy of 0.5 kg/m^3.

The samples were studied in three structural states for the following loading options: the initial state (no load); with a tensile load and subsequent unloading at each step; under cyclic tension-compression load (Fig. 3).

The study of bulk wave velocity and elastic moduli of samples during uniaxial tension was carried out on an Instron DX-300 testing machine with a load increment of 10 kN and a gradual unloading in increments of 20 kN. The maximum load was 1000 MPa for the sample with solid solution annealing heat treatment, 1400 MPa for the sample aged at 470 °C, and 1200 MPa for the sample aged at 565 °C.

Studying the behavior of wave velocities during stretching allows determining the acoustoelasticity coefficient as the degree of influence of the mechanical load σ on the velocities of bulk waves:

$$k = \frac{\frac{\Delta C}{C_0}}{\sigma},$$

where k is the acoustoelastic coupling coefficient;
σ is the applied load, MPa;
$\frac{\Delta C}{C_0}$ is relative change in velocity.

The cyclic tension-compression experiment was carried out on a UIM-D-100 testing machine. A zero (pulsating) cycle with the following characteristics was used: maximum cycle stress $\sigma_{max}=\sigma$, minimum stress $\sigma_{min}=0$, average stress $\sigma_m=\sigma/2$, amplitude $\sigma_a=\sigma/2$, and asymmetry coefficient $r=0$. The maximum cycle stress was 70 % of the yield strength: for the sample after annealing – $\sigma_{max}=700$ MPa, after aging – $\sigma_{max}=1200$ MPa; cycle frequency is 5 Hz, step is from 1000 to 10 000 cycles increasing with the number of cycles.

At each step of the experimental studies, the sample average diameter was measured at control points using an MP 25 micrometer with an accuracy of 5 μm.

RESULTS

The results of studying the microstructure of the samples show that after annealing the structure is predominantly austenitic with the presence of martensite. After aging, the structure of the samples is represented by low-carbon martensite, residual austenite and a small amount of delta ferrite (0–2 %) elongated along the rolled product axis. There are precipitates of a finely dispersed structure (a strengthening phase), the amount of which determines the strength of the steel. Fig. 4 shows the 15-5 PH microstructure.

The mechanical properties of the 15-5 PH steel samples after different types of heat treatment are shown in Table 1. The results of testing the mechanical characteristics show that the strength properties and hardness of the samples after solid solution annealing are minimal. Aging at 470 °C increases strength properties and hardness to maximum values. Aging at 565 °C leads to a slight decrease in strength properties and hardness, but the highest impact strength is achieved.

Table 2 presents the physical characteristics of the samples for three heat treatment modes measured in the central region of the studied samples.

The results of acoustic structuroscopy of the 15-5 PH steel samples under various heat treatment modes (Table 2) showed:

– the minimum values of the velocities of longitudinal, transverse and Rayleigh waves, as well as elastic moduli for the 15-5 PH alloy are observed after solid solution annealing;

– Poisson's ratio, on the contrary, takes maximum values for sample No. 1 and minimum values for sample No. 3;

– wave velocities increase after aging due to the solid solution decomposition with the release of copper deposits, as well as the release of chromium and silicon from the solid solution;

– acoustic anisotropy of properties is more significant for sample No. 1 and decreases by more than twice for samples No. 2 and 3.

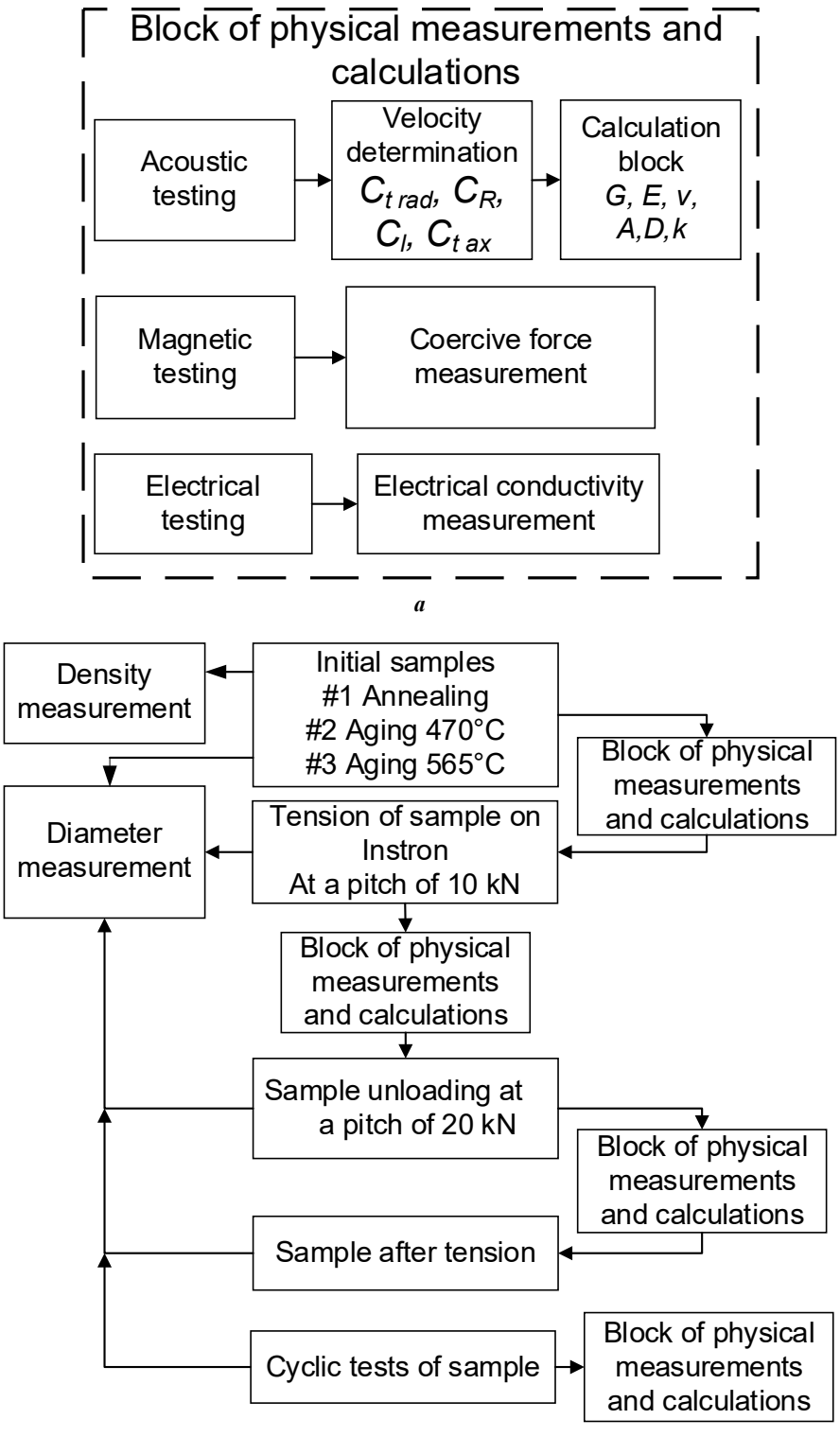

Fig. 3. *Diagram of physical measurement block (**a**); diagram of block of tests during loading (**b**)*
Рис. 3. *Схема блока физических измерений (**a**); схема блока испытаний в процессе нагружения (**b**)*

Fig. 5 shows the distribution of Poisson's ratio and anisotropy coefficient along the length of the studied samples after heat treatment.

Changes in the wave velocity and Poisson's ratio when stretching the samples lead to a smooth linear decrease in the velocity of the transverse axial-polarization wave over the entire range of applied loads (Fig. 6).

The tension-compression influence on the relative change in the rate of cyclic loading is presented in Fig. 7. The nature of the curves is nonlinear.

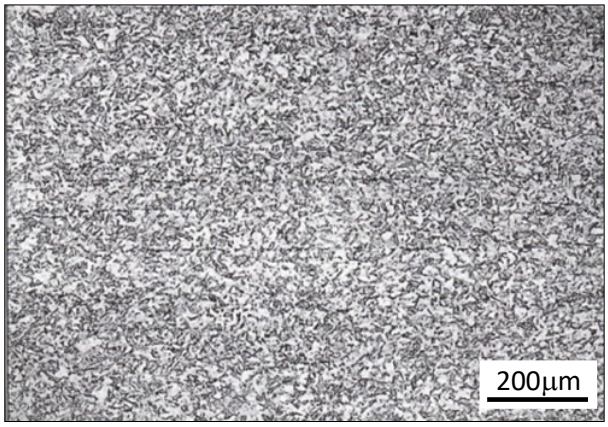

Fig. 4. *Microstructure of the 15-5 PH steel after aging*
Рис. 4. *Микроструктура стали ХМ-12 после старения*

Table 1. *Mechanical properties of the 15-5 PH steel after various types of heat treatment*
Таблица 1. *Механические свойства стали ХМ-12 после различных термических обработок*

Type and mode of heat treatment	Solid solution annealing at 1040 °C, 0.5 h in the air	Aging at 470 °C, 3 h	Aging at 565 °C, 3 h
	Sample No.		
	1	2	3
Tensile strength σ_{UTS}, MPa	1 070	1 455	1 230
Yield strength $\sigma_{0.2}$, MPa	990	1 420	1 200
Percentage elongation, %	13.5	12.5	12.5
Percentage reduction, %	67	60	65
Impact strength KCU, J/cm^2	168	110	190
Hardness, HRC	30	45	39

DISCUSSION

The data in Table 2 show that with increasing aging temperature, the steel structure becomes ordered with the appearance of new phases [3], and the size of the copper-enriched phase increases. According to [5], the microstructure of steel during long-term aging undergoes a complex evolution, including the development of a minor austenitic phase, copper-rich deposits, as well as the release of chromium and silicon from the solid solution.

Electrical conductivity decreases relative to solid solution annealing after aging at 470 °C, and at 565 °C, it increases to values corresponding to annealing. The coercive force relative to solid solution annealing increases slightly after aging at 470 °C. An increase in the aging temperature to 565 °C leads to a decrease in coercive force values, which may be associated with a decrease in internal stresses caused by the crystal lattice distortion. This is confirmed in [25], which shows that the coercive force of a maraging iron-chromium-nickel alloy depends on the structure morphology, stresses, grain size, and shape.

From the analysis of Fig. 5 and 6 it is clear that, despite the change in Poisson's ratio within a very small range (no more than 0.25 %), there are significant differences in the acoustic anisotropy coefficient along the length of the sample, which indicates the presence of heterogeneity in the sample. The most significant deviation in velocity is 0.96 % for sample No. 2 after aging at 470 °C; the least significant is 0.67 % for sample No. 3 after aging at 565 °C. The high sensitivity of transverse waves to tensile loads is explained by the coincidence of the axial direction of wave polarization with the force direction. The velocity of a longitudinal wave polarized across the direction of tensile stresses practically does not change (changes are within the error). The corresponding calculated coefficients of the studied samples are presented in Table 3.

One should note that during the stretching process, an increase in the EMA-transformation efficiency is observed

Table 2. *Physical characteristics of the 15-5 PH steel samples before loading*
Таблица 2. *Физические характеристики образцов стали ХМ-12 до нагружения*

Physical characteristic	Heat treatment modes		
	Annealing	Aging at 470 °C	Aging at 565 °C
Wave velocity C_l, m/s	5 798	5 838	5 866
Wave velocity C_{trad}, m/s	3 136	3 154	3 192
Wave velocity C_{tos}, m/s	3 123	3 150	3 186
Wave velocity C_R, m/s	2 907	2 922	2 956
Density ρ, kg/m^3	7 687	7 677	7 689
Young’s modulus E, GPa	194.6	200.0	202.7
Shear modulus G, GPa	75.2	77.4	78.4
Poisson’s ratio ν	0.2947	0.2913	0.2896
Electrical conductivity, mkV	3 860	3 907	3 947
Coercive force, A/cm	23.2	17.5	17.1
Anisotropy coefficient, %	0.417	0.127	0.208
Dispersion, mV^2	6 755	6 851	6 371

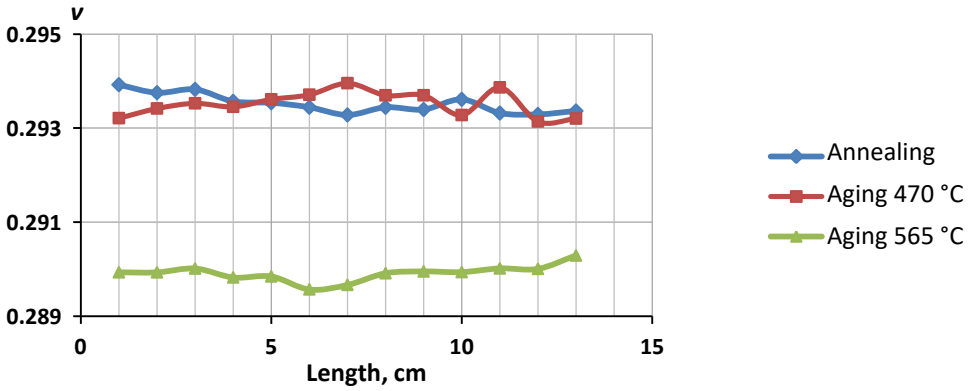

a

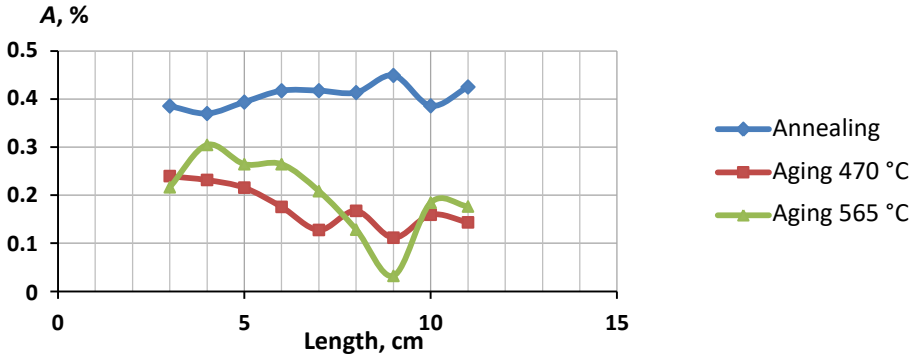

b

Fig. 5. *Distribution of Poisson’s ratio* ***(a)*** *and acoustic anisotropy coefficient* ***(b)*** *along the length of samples subjected to various heat treatment modes*
Рис. 5. *Распределение коэффициента Пуассона* ***(а)*** *и коэффициента акустической анизотропии* ***(b)*** *по длине образцов, подвергнутых различным режимам термообработки*

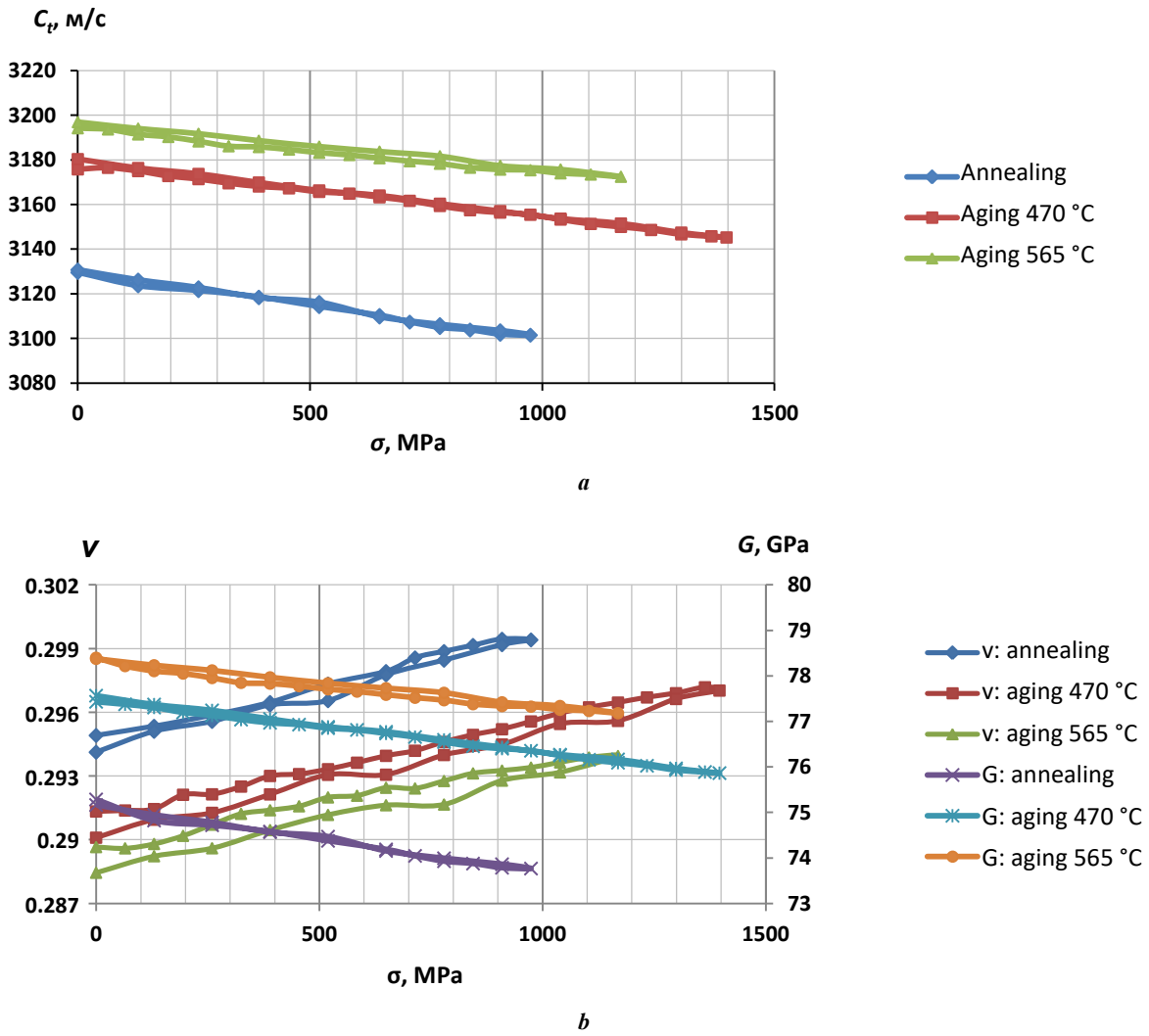

Fig. 6. *Change in the transverse wave velocity (**a**), shear elastic modulus and Poisson’s ratio (**b**) during tension process*
Рис. 6. *Изменение скорости поперечной волны (**a**), упругого модуля сдвига и коэффициента Пуассона (**b**) в процессе растяжения*

(Fig. 8). It is nonlinear in nature: a slow increase at low loads, a sharper increase at loads approaching the yield strength of the material. In the area of high loads, a decrease in the EMA-transformation coefficient is observed, which is explained by a decrease in the sample radius near the yield point, and, consequently, an increase in the gap between the EMA transducer and the test object, which leads to a decrease in eddy currents in the sample surface layer. Other things being equal, the EMA-transformation coefficient has a maximum value for sample No. 2 (aging at 470 °C) (Table 3) and correlates with the maximum values of sample hardness (Table 1) and maximum coercive force (Table 2), which corresponds to conventional beliefs about the influence of the material magnetic properties on the EMA-transformation efficiency.

After unloading, virtually no changes in the velocities of the acoustic waves are observed. At the same time, electrical conductivity increases significantly for all types of heat treatment.

The linear decrease in the relative change in the transverse wave velocity (Fig. 7) to 0.32 % for the sample after annealing and to 0.14 % for the sample after aging observed at the initial stage (10 cycles) is a consequence of preloading the sample (up to 359 MPa for the sample after annealing and up to 490 MPa for the sample after aging) and corresponds to the value obtained under static uniaxial tension. For a sample after annealing, a subsequent increase in the number of cycles leads to a less significant decrease in the transverse wave velocity and further stabilization of the values in the region of 1000 cycles and above. Changes in velocity with a number of cycles greater than 1000 are within the measurement error and primarily determined by small temperature fluctuations. For the sample after aging, a similar pattern is observed with a more nonlinear curve nature. One should note that with a small number of cycles, there is a slight (in comparison with the transverse wave) increase in the longitudinal wave velocity, followed by its decrease with a large number of cycles. The indicated differences in the behavior of longitudinal and transverse waves lead to changes in the elastic moduli during the cyclic tests presented in Fig. 7 b, 7 c as the loading cycles increase.

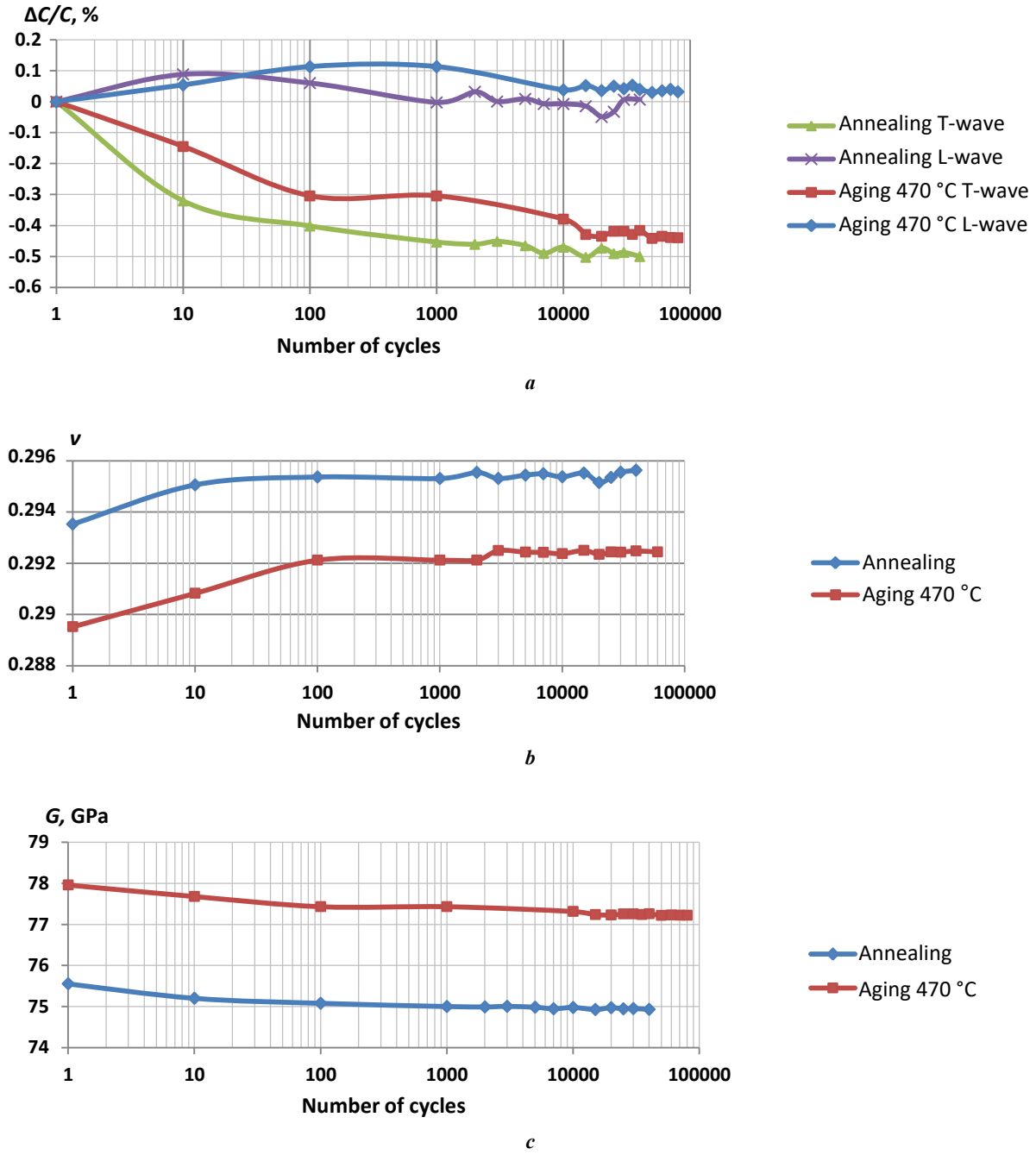

Fig. 7. *Change in bulk wave velocity (**a**), shear modulus (**b**), and Poisson’s ratio (**c**) depending on the number of tension-compression cycles*
Рис. 7. *Изменение скоростей объемных волн (**a**), модуля сдвига (**b**) и коэффициента Пуассона (**c**) от количества циклов растяжения-сжатия*

Table 3. *Acoustoelasticity coefficients and EMA-transformation coefficient of the studied samples*
Таблица 3. *Коэффициенты акустоупругости и коэффициента ЭМА-преобразования исследованных образцов*

Characteristic	Heat treatment mode		
	Annealing	Aging at 470 °C	Aging at 565 °C
Acoustoelasticity coefficient, k, TPa^{-1}	−9.2	−6.9	−5.7
EMA-transformation coefficient, K_{EMA}, mV	966	1 128	666

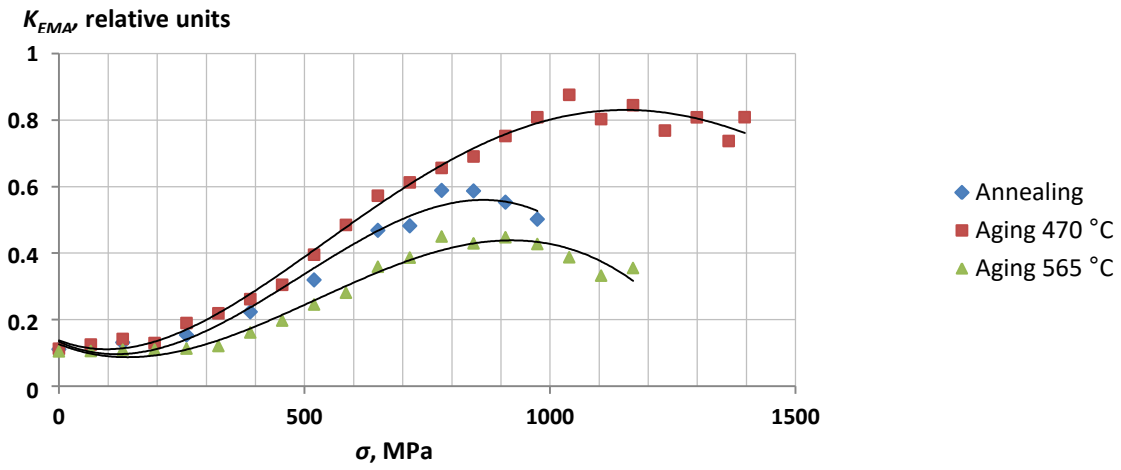

Fig. 8. *Change in relative EMA-transformation coefficient in the process of tension*
Рис. 8. *Изменение относительного коэффициента ЭМА-преобразования в процессе растяжения*

One should note that a further increase in the number of cycles to $4 \cdot 10^5$ and an increase in the loading amplitude to 0.8 of the yield strength did not lead to the destruction of any of the samples. Considering that the process of nucleation and accumulation of microcracks should lead to a decrease in velocity with increasing load [19; 22], one can assume that it is not decisive in the behavior of these curves. Probably, the stabilization of the behavior of the curves during loading is determined by the appearance in the 15-5 PH steel microstructure of the strain martensite hardening phase characteristic of these materials, which can replace residual austenite.

CONCLUSIONS

The study of the acoustic characteristics of KhM-12 (15-5 PH) maraging steel samples after heat treatment of solid solution annealing and subsequent aging under mechanical tensile and cyclic loads showed the presence of the following structure-sensitive parameters: transverse axial-polarization wave velocity, elastic shear modulus, Poisson's ratio, acoustic anisotropy coefficient, acoustoelasticity coefficient, double electromagnetic-acoustic transformation, electrical conductivity and coercive force coefficients.

It was found that the minimum values of the velocities of longitudinal, transverse and Rayleigh waves for the KhM-12 (15-5 PH) alloy are observed after solid solution annealing. The velocity of a transverse wave with polarization in the direction of the force in the elastic region of mechanical loading decreases in direct proportion to the load, while the maximum value of the acoustoelastic coefficient corresponds to the sample after annealing (-9.2 TPa^{-1}). Young's and shear moduli decrease linearly, while Poisson's ratio, on the contrary, increases linearly in the range of loads under study. Increasing the number of cycles leads to a decrease in the transverse wave velocity in the range of up to 1000 cycles and further stabilization of values in the region of higher values.

The non-contact acoustic echo-shadow method developed for research based on multiple reflections and the equipment implementing it using non-contact EMA principles of excitation and reception of waves can be effectively used for tasks of acoustic structuroscopy, when assessing the stress-strain state, in cyclic tests and other types of impacts for a wide class of metals and alloys with special properties.

REFERENCES

1. Eremin E.N., Losev A.S., Ponomarev I.A., Borodikhin S.A. Thermal treatment impact upon structure, properties and phase structure of steel 10G7M3S2AFTYU weld with powder wire. *Science intensive technologies in mechanical engineering*, 2020, no. 5, pp. 3–8. DOI: 10.30987/2223-4608-2020-5-3-8.
2. Gromov V.I., Yakusheva N.A., Polunov I.L. Evaluation of the effect of heat treatment on mechanical properties of maraging steels in the alloying system Fe–Ni–Mo–Ti–Al. *Trudy VIAM (Proceedings of VIAM)*, 2017, no. 11, pp. 12–20. DOI: 10.18577/2307-6046-2017-0-11-2-2.
3. Couturier L., De Geuser F., Deschamps A. Microstructural evolution during long time aging of 15–5PH stainless steel. *Materialia*, 2020, vol. 9, article number 100634. DOI: 10.1016/j.mtla.2020.100634.
4. Niu Jingpeng, Cui Bing, Jin Huijin, Yan Jialing, Meng Wei, Min Chunying, Xu Dong. Effect of Post-Weld Aging Temperature on Microstructure and Mechanical Properties of Weld Metal of 15-5 PH. *Journal of Materials Engineering and Performance*, 2020, vol. 29, pp. 7026–7033. DOI: 10.1007/s11665-020-05193-y.
5. Jin Chunhui, Zhou Honglin, Lai Yuan, Li Bei, Zhang Kewei, Chen Huiqin Zhao Jinhua. Microstructure and mechanical properties of 15-5 PH stainless steel under different aging temperature. *Metallurgical Research and Technology*, 2021, vol. 118, no. 6, article number 601. DOI: 10.1051/metal/2021078.

6. Valiorgue F., Zmelty V., Dumas M., Chomienne V., Verdu C., Lefebvre F., Rech J. Influence of residual stress profile and surface microstructure on fatigue life of a 15-5PH. *Procedia Engineering*, 2018, vol. 213, pp. 623–629. DOI: 10.1016/j.proeng.2018.02.058.
7. Zhou Tao, Faleskog J., Babu R.P., Odqvist J., Yu Hao, Hedström P. Exploring the relationship between the microstructure and strength of fresh and tempered martensite in a maraging stainless steel Fe–15Cr–5Ni. *Materials Science and Engineering: A*, 2019, vol. 745, pp. 420–428. DOI: 10.1016/j.msea.2018.12.126.
8. Avula I., Arohi A.Ch., Kumar Ch.S., Sen I. Microstructure, Corrosion and Mechanical Behavior of 15-5 PH Stainless Steel Processed by Direct Metal Laser Sintering. *Journal of Materials Engineering and Performance*, 2021, vol. 30, pp. 6924–6937. DOI: 10.1007/s11665-021-06069-5.
9. Nong X.D., Zhou X.L., Li J.H., Wang Y.D., Zhao Y.F., Brochu M. Selective laser melting and heat treatment of precipitation hardening stainless steel with a refined microstructure and excellent mechanical properties. *Scripta Materialia*, 2020, vol. 178, pp. 7–12. DOI: 10.1016/j.scriptamat.2019.10.040.
10. Sarkar S., Mukherjee S., Kumar Ch.S., Nath A.K. Effects of heat treatment on microstructure, mechanical and corrosion properties of 15-5 PH stainless steel parts built by selective laser melting process. *Journal of Manufacturing Processes*, 2020, vol. 150, pp. 279–294. DOI: 10.1016/j.jmapro.2019.12.048.
11. Sarkar S., Kumar Ch.S., Nath A.K. Effects of heat treatment and build orientations on the fatigue life of selective laser melted 15-5 PH stainless steel. *Materials Science and Engineering: A*, 2019, vol. 755, pp. 235–245. DOI: 10.1016/j.msea.2019.04.003.
12. Gorkunov E.S., Povolotskaya A.M., Zadvorkin S.M., Putilova E.A., Mushnikov A.N., Bazulin E.G., Vopilkin A.K. Some features in the behavior of magnetic and acoustic characteristics of hot-rolled 08G2B steel under cyclic loading. *Russian Journal of Nondestructive Testing*, 2019, vol. 55, no. 11, pp. 827–836. DOI: 10.1134/S0130308219110034.
13. Takeda S., Uchimoto T., Kita A., Matsumoto T., Sasaki T. Mechanism study of the residual stress evaluation of low-carbon steels using the eddy current magnetic signature method. *Journal of Magnetism and Magnetic Materials*, 2021, vol. 538, article number 168268. DOI: 10.1016/j.jmmm.2021.168268.
14. Mishakin V.V., Gonchar A.V., Klyushnikov V.A., Kurashkin K.V. Study of the effect of plastic deformation on the crystallographic texture and acoustic characteristics of low-alloy steel. *Problems of Strength and Plasticity / Problemy prochnosti i plastichnosti*, 2021, vol. 83, no. 3, pp. 255–264. DOI: 10.32326/1814-9146-2021-83-3-255-264.
15. Gonchar A.V., Klyushnikov V.A., Mishakin V.V. The effect of plastic deformation and subsequent heat treatment on the acoustic and magnetic properties of 12Khl8N10T steel. *Industrial laboratory. Diagnostics of materials*, 2019, vol. 85, no. 2, pp. 23–28. DOI: 10.26896/1028-6861-2019-85-2-23-28.
16. Mishakin V.V., Gonchar A.V., Kurashkin K.V., Klyushnikov V.A., Kachanov M. On low-cycle fatigue of austenitic steel. Part I: Changes of Poisson’s ratio and elastic anisotropy. *International Journal of Engineering Science*, 2021, vol. 168, article number 103567. DOI: 10.1016/j.ijengsci.2021.103567.
17. Uglov A.L., Khlybov A.A., Bychkov A.L., Kuvshinov M.O. About Non-Destructive Control of Residual Stresses in Axisymmetric Parts Made of Steel 03Ni17Co10W10MoTi. *Vestnik IzhGTU imeni M.T. Kalashnikova*, 2019, vol. 22, no. 4, pp. 3–9. DOI: 10.22213/2413-1172-2019-4-3-9.
18. Muravev V.V., Lenkov S.V., Tapkov K.A. In-production nondestructive testing of internal stresses in rails using acoustoelasticity method. *Russian Journal of Nondestructive Testing*, 2019, vol. 55, no. 1, pp. 8–14. DOI: 10.1134/S01303082190100020.
19. Khlybov A.A., Kabaldin Yu.G., Ryabov D.A., Anosov M.S., Shagatin D.A. Study of the damage to 12Cr18Ni10Ti steel samples under low cycle fatigue using methods of nondestructive control. *Industrial laboratory. Diagnostics of materials*, 2021, vol. 87, no. 5, pp. 61–67. DOI: 10.26896/1028-6861-2021-87-5-61-67.
20. Muraveva O.V., Muravev V.V., Basharova A.F., Sintsov M.A., Bogdan O.P. Thermal treatment effect and structural state of rod-shaped assortment 40Kh steel on the speed of ultrasound waves and poisson coefficient. *Steel in Translation*, 2020, vol. 50, no. 8, pp. 579–584. EDN: MKTWDN.
21. Muravev V.V., Muraveva O.V., Vagapov T.R., Makarova V.E., Stepanova E.A. Acoustic and electromagnetic properties of civilian gun blanks. *Intelligent Systems in Manufacturing*, 2023, vol. 21, no. 1, pp. 59–70. EDN: KBBVGW.
22. Muravev V.V., Budrin A.Yu., Sintsov M.A. Influence of high-cycle fatigue on the speed of shear and Rayleigh waves in steel bars of different heat treatment. *Intelligent Systems in Manufacturing*, 2020, vol. 18, no. 4, pp. 4–10. DOI: 10.22213/2410-9304-2020-4-10.
23. Muravev V.V., Budrin A.Yu., Sintsov M.A. Structuroscopy of heat-treated steel bars by the speed of propagation of Rayleigh waves. *Intelligent Systems in Manufacturing*, 2020, vol. 18, no. 2, pp. 37–43. DOI: 10.22213/2410-9304-2020-2-37-43.
24. Muraveva O.V., Brester A.F., Muravev V.V. Comparative sensitivity of informative parameters of electromagnetic-acoustic mirror-shadow multiple reflections method during bar stock testing. *Russian Journal of Nondestructive Testing*, 2022, vol. 58, no. 8, pp. 689–704. EDN: BQEKGO.
25. Kazantseva N.V., Merkushev A.G., Shishkin D.A., Ezhov I.V., Davidov D.I., Rigmant M.B., Terentev P.B., Egorova L.Yu. Magnetic Properties and Structure of Products from 1.4540 Stainless Steel Manufactured by 3D Printing. *Physics of Metals and Metallography*, 2019, vol. 120, pp. 1270–1275. DOI: 10.1134/S0031918X19130118.

СПИСОК ЛИТЕРАТУРЫ

1. Еремин Е.Н., Лосев А.С., Пономарев И.А., Бородихин С.А. Влияние режимов термической обработки на структуру, свойства и фазовый состав стали 10Г7М3С2АФТЮ, наплавленной порошковой проволокой // Наукоемкие технологии в машиностроении. 2020. № 5. С. 3–8. DOI: 10.30987/2223-4608-2020-5-3-8.

2. Громов В.И., Якушева Н.А., Полунов И.Л. Оценка влияния режимов термической обработки на уровень механических свойств мартенситостареющих сталей системы легирования Fe–Ni–Mo–Ti–Al // Труды ВИАМ. 2017. № 11. С. 12–20. DOI: 10.18577/2307-6046-2017-0-11-2-2.
3. Couturier L., De Geuser F., Deschamps A. Microstructural evolution during long time aging of 15–5PH stainless steel // Materialia. 2020. Vol. 9. Article number 100634. DOI: 10.1016/j.mtla.2020.100634.
4. Niu Jingpeng, Cui Bing, Jin Huijin, Yan Jialing, Meng Wei, Min Chunying, Xu Dong. Effect of Post-Weld Aging Temperature on Microstructure and Mechanical Properties of Weld Metal of 15-5 PH // Journal of Materials Engineering and Performance. 2020. Vol. 29. P. 7026–7033. DOI: 10.1007/s11665-020-05193-y.
5. Jin Chunhui, Zhou Honglin, Lai Yuan, Li Bei, Zhang Kewei, Chen Huiqin, Zhao Jinhua. Microstructure and mechanical properties of 15-5 PH stainless steel under different aging temperature // Metallurgical Research and Technology. 2021. Vol. 118. № 6. Article number 601. DOI: 10.1051/metal/2021078.
6. Valiorgue F., Zmelty V., Dumas M., Chomienne V., Verdu C., Lefebvre F., Rech J. Influence of residual stress profile and surface microstructure on fatigue life of a 15-5PH // Procedia Engineering. 2018. Vol. 213. P. 623–629. DOI: 10.1016/j.proeng.2018.02.058.
7. Zhou Tao, Faleskog J., Babu R.P., Odqvist J., Yu Hao, Hedström P. Exploring the relationship between the microstructure and strength of fresh and tempered martensite in a maraging stainless steel Fe–15Cr–5Ni // Materials Science and Engineering: A. 2019. Vol. 745. P. 420–428. DOI: 10.1016/j.msea.2018.12.126.
8. Avula I., Arohi A.Ch., Kumar Ch.S., Sen I. Microstructure, Corrosion and Mechanical Behavior of 15-5 PH Stainless Steel Processed by Direct Metal Laser Sintering // Journal of Materials Engineering and Performance. 2021. Vol. 30. P. 6924–6937. DOI: 10.1007/s11665-021-06069-5.
9. Nong X.D., Zhou X.L., Li J.H., Wang Y.D., Zhao Y.F., Brochu M. Selective laser melting and heat treatment of precipitation hardening stainless steel with a refined microstructure and excellent mechanical properties // Scripta Materialia. 2020. Vol. 178. P. 7–12. DOI: 10.1016/j.scriptamat.2019.10.040.
10. Sarkar S., Mukherjee S., Kumar Ch.S., Nath A.K. Effects of heat treatment on microstructure, mechanical and corrosion properties of 15-5 PH stainless steel parts built by selective laser melting process // Journal of Manufacturing Processes. 2020. Vol. 150. P. 279–294. DOI: 10.1016/j.jmapro.2019.12.048.
11. Sarkar S., Kumar Ch.S., Nath A.K. Effects of heat treatment and build orientations on the fatigue life of selective laser melted 15-5 PH stainless steel // Materials Science and Engineering: A. 2019. Vol. 755. P. 235–245. DOI: 10.1016/j.msea.2019.04.003.
12. Горкунов Э.С., Поволоцкая А.М., Задворкин С.М., Путилова Е.А., Мушников А.Н., Базулин Е.Г., Вопилкин А.Х. Особенности поведения магнитных и акустических характеристик горячекатаной стали 08Г2Б при циклическом нагружении // Дефектоскопия. 2019. № 11. С. 21–31. DOI: 10.1134/S0130308219110034.
13. Takeda S., Uchimoto T., Kita A., Matsumoto T., Sasaki T. Mechanism study of the residual stress evaluation of low-carbon steels using the eddy current magnetic signature method // Journal of Magnetism and Magnetic Materials. 2021. Vol. 538. Article number 168268. DOI: 10.1016/j.jmmm.2021.168268.
14. Мишакин В.В., Гончар А.В., Клюшников В.А., Курашкин К.В. Исследование влияния пластического деформирования на кристаллографическую текстуру и ультразвуковые характеристики низколегированной стали // Проблемы прочности и пластичности. 2021. Т. 83. № 3. С. 255–264. DOI: 10.32326/1814-9146-2021-83-3-255-264.
15. Гончар А.В., Клюшников В.А., Мишакин В.В. Влияние пластического деформирования и последующей термообработки на акустические и электромагнитные свойства стали 12Х18Н10Т // Заводская лаборатория. Диагностика материалов. 2019. Т. 85. № 2. С. 23–28. DOI: 10.26896/1028-6861-2019-85-2-23-28.
16. Mishakin V.V., Gonchar A.V., Kurashkin K.V., Klyushnikov V.A., Kachanov M. On low-cycle fatigue of austenitic steel. Part I: Changes of Poisson’s ratio and elastic anisotropy // International Journal of Engineering Science. 2021. Vol. 168. Article number 103567. DOI: 10.1016/j.ijengsci.2021.103567.
17. Углов А.Л., Хлыбов А.А., Бычков А.Л., Кувшинов М.О. О неразрушающем контроле остаточных напряжений в деталях осесимметричной формы из стали 03Н17К10В10МТ // Вестник ИжГТУ имени М.Т. Калашникова. 2019. Т. 22. № 4. С. 3–9. DOI: 10.22213/2413-1172-2019-4-3-9.
18. Муравьев В.В., Тапков К.А., Леньков С.В. Неразрушающий контроль внутренних напряжений в рельсах при изготовлении с использованием метода акустоупругости // Дефектоскопия. 2019. № 1. С. 10–16. DOI: 10.1134/S0130308219010020.
19. Хлыбов А.А., Кабалдин Ю.Г., Рябов Д.А., Аносов М.С., Шагатин Д.А. Исследование поврежденности образцов из стали 12Х18Н10Т при малоцикловой усталости методами неразрушающего контроля // Заводская лаборатория. Диагностика материалов. 2021. Т. 87. № 5. С. 61–67. DOI: 10.26896/1028-6861-2021-87-5-61-67.
20. Муравьева О.В., Муравьев В.В., Башарова А.Ф., Синцов М.А., Богдан О.П. Влияние термической обработки и структурного состояния стали 40Х прутkового сортамента на скорость ультразвуковых волн и коэффициент Пуассона // Сталь. 2020. № 8. С. 63–68. EDN: MKTWDN.
21. Муравьев В.В., Муравьева О.В., Вагапов Т.Р., Макарова В.Е., Степанова Е.А. Акустические и электромагнитные свойства заготовок стволов гражданских ружей // Интеллектуальные системы в производстве. 2023. Т. 21. № 1. С. 59–70. EDN: KBBVGW.
22. Муравьев В.В., Будрин А.Ю., Синцов М.А. Влияние циклически изменяющихся нагрузок на скорости сдвиговых и рэлеевских волн в стальных прутках разной термической обработки // Интеллектуальные системы в производстве. 2020. Т. 18. № 4. С. 4–10. DOI: 10.22213/2410-9304-2020-4-10.
23. Муравьев В.В., Будрин А.Ю., Синцов М.А. Структуроскопия термически обработанных стальных

прутков по скорости распространения рэлеевских волн // Интеллектуальные системы в производстве. 2020. Т. 18. № 2. С. 37–43. DOI: 10.22213/2410-9304-2020-2-37-43.
24. Муравьева О.В., Брестер А.Ф., Муравьев В.В. Сравнительная чувствительность информативных параметров электромагнитно-акустического зеркально-теневого метода на многократных отражениях при контроле пруткового проката // Дефектоскопия. 2022. № 8. С. 36–51. EDN: BQEKGO.
25. Kazantseva N.V., Merkushev A.G., Shishkin D.A., Ezhov I.V., Davidov D.I., Rigmant M.B., Terentev P.B., Egorova L.Yu. Magnetic Properties and Structure of Products from 1.4540 Stainless Steel Manufactured by 3D Printing // Physics of Metals and Metallography. 2019. Vol. 120. P. 1270–1275. DOI: 10.1134/S0031918X19130118.

Акустические свойства мартенситно-стареющей стали ХМ-12 после энергетических воздействий

Муравьева Ольга Владимировна[1,2,3], доктор технических наук, профессор, профессор кафедры «Приборы и методы измерений, контроля, диагностики»
Муравьев Виталий Васильевич[1,2,4], доктор технических наук, профессор, профессор кафедры «Приборы и методы измерений, контроля, диагностики»
Волкова Людмила Владимировна[1,5], кандидат технических наук, доцент, доцент кафедры «Приборы и методы измерений, контроля, диагностики»
Владыкин Алексей Леонидович*[1,6], аспирант
Белослудцев Константин Юрьевич[1], магистрант
[1]*Ижевский государственный технический университет имени М.Т. Калашникова, Ижевск (Россия)*
[2]*Удмуртский федеральный исследовательский центр Уральского отделения РАН, Ижевск (Россия)*

***E-mail:** pmkk@istu.ru, vladykin-ndt@mail.ru

[3]ORCID: https://orcid.org/0000-0003-3442-8163
[4]ORCID: https://orcid.org/0000-0001-8590-1382
[5]ORCID: https://orcid.org/0000-0001-5128-6465
[6]ORCID: https://orcid.org/0009-0006-1813-2011

Поступила в редакцию 05.07.2023 *Принята к публикации 28.11.2023*

Аннотация: Исследование акустических свойств мартенситно-стареющих сталей, эксплуатируемых в условиях различных энергетических силовых и температурных воздействий, является актуальной задачей, так как именно метод акустической структуроскопии обеспечивает наиболее достоверную связь со структурой, напряженно-деформированным состоянием и механическими свойствами сталей. Работа посвящена исследованию акустических свойств образцов мартенситно-стареющей стали ХМ-12 при различных термических обработках в условиях механических растягивающих и циклических нагрузок. Исследованы образцы мартенситно-стареющей стали ХМ-12 в трех структурных состояниях: после отжига на твердый раствор и последующего старения при 470 и 565 °С; при испытаниях на растяжение; в процессе циклической нагрузки растяжения-сжатия. В исследованиях использована уникальная научная установка «Информационно-измерительный комплекс для исследований акустических свойств материалов и изделий». Она реализует акустический зеркально-теневой метод на многократных отражениях с применением электромагнитно-акустического и пьезоэлектрического преобразователей на основе поливинилиденфторидной пленки для возбуждения и приема волн и позволяет определить скорости распространения волн с погрешностью не более 2 м/с. Исследованы акустические (скорость волн, упругие модули, коэффициенты электромагнитно-акустического (ЭМА) преобразования, коэффициенты акустической анизотропии, коэффициенты акустоупругой связи) и электромагнитные (коэрцитивная сила и электропроводность) характеристики образцов: в исходном состоянии (до нагружения); пошагово в процессе растягивающих нагрузок и последующего разгружения; после испытаний на растяжение; в процессе циклической нагрузки растяжения-сжатия. Выявлено, что наибольшей структурной чувствительностью к механической растягивающей нагрузке и циклическому нагружению являются следующие акустические параметры образцов стали ХМ-12: скорость поперечной волны, коэффициент Пуассона, коэффициент двойного ЭМА-преобразования и коэффициент акустической анизотропии.

Ключевые слова: мартенситно-стареющая сталь ХМ-12; акустические свойства; термическая обработка; механическая растягивающая нагрузка; циклическое нагружение.

Благодарности: Исследование выполнено за счет гранта Российского научного фонда (грант № 22-19-00252, https://rscf.ru/project/22-19-00252/) с использованием УНУ «Информационно-измерительный комплекс для исследований акустических свойств материалов и изделий» (рег. номер 586308).

Статья подготовлена по материалам докладов участников XI Международной школы «Физическое материаловедение» (ШФМ-2023), Тольятти, 11–15 сентября 2023 года.

Для цитирования: Муравьева О.В., Муравьев В.В., Волкова Л.В., Владыкин А.Л., Белослудцев К.Ю. Акустические свойства мартенситно-стареющей стали ХМ-12 после энергетических воздействий // Frontier Materials & Technologies. 2024. № 2. С. 87–100. DOI: 10.18323/2782-4039-2024-2-68-8.

doi: 10.18323/2782-4039-2024-2-68-9

Surface finish and cutting efficiency in gingelly oil during machining: regression analysis

Shailesh Rao A., PhD, Professor, Department of Mechanical Engineering
NITTE Meenkshi Institute of Technology, Bangalore (India)

E-mail: shailesh.rao@nmit.ac.in ORCID: https://orcid.org/0000-0001-6190-9857

Received 31.08.2023 *Accepted 19.02.2024*

Abstract: This study evaluates the use of gingelly oil as an eco-friendly cutting fluid for the turning operation. Experiments were conducted to determine the effect of nose radius, and rake angle on tool wear, surface formation, and cutting force. In addition, different lubrication techniques, such as cutting fluids and bio-oils, were investigated to determine their potential for minimising friction, heat generation, and tool wear during machining. In comparison to dry cutting, and conventional petroleum-based lubricants, the results demonstrate that gingelly oil consistently produces smoother surface finishes, and reduces cutting forces. The relationships between cutting parameters, and surface finish were analysed using statistical modelling, with *R*-square and *p*-values used to quantify correlations and predictor significance. The findings highlight the viability of gingelly oil as a cutting fluid and the significance of optimising process parameters for increased machining efficiency.

Keywords: cutting efficiency in gingelly; mechanical processing in gingelly oil; cutting fluid; sustainable machining; surface finish; tool wear; rake angle; nose radius.

For citation: Shailesh Rao A. Surface finish and cutting efficiency in gingelly oil during machining: regression analysis. *Frontier Materials & Technologies*, 2024, no. 2, pp. 101–111. DOI: 10.18323/2782-4039-2024-2-68-9.

INTRODUCTION

The choice of cutting fluid is critical in machining operations, since it directly affects surface quality and cutting efficacy. Generally, the cutting fluid creates a protective barrier between the cutting tool and the workpiece, reducing tool wear and friction. The use of bio-oils in the machining process has recently shown an improvement in the cutting efficiency and surface quality. Here the lubricating characteristics improve the overall surface quality, by allowing for a more seamless interaction between the tool and the workpiece.

In conventional machining processes, the dynamic interplay between the cutting tool, and the workpiece is critical to achieving the desired surface polish and form. This contact, defined by a ploughing motion, results in the removal of metals, shaping the workpiece with the accuracy of sharp tools, and sparking an investigation into cutting mechanisms [1]. The cutting processes have a wide range of performance implications, including surface quality, precision, tool wear, chip formation, burr development, material selection, and more [2]. These characteristics, taken together, define the research focus, with the goal of gaining a full understanding of industrial machining. A key difficulty in this arena is energy efficiency in manufacturing. Inappropriate process parameters can lead to increased energy consumption and production costs [3]. As a result, a thorough examination into the optimal process parameter selection becomes necessary.

In the field of improved machining process, the degradation of the nose radius, and other tool surfaces is a cause for worry. Defining workpiece process parameters is critical to achieving the specified machine surface and other desirable characteristics. The standard turning parameters, if not carefully chosen, might result in suboptimal machine surfaces and unnecessary tool wear. To address this, the vibration and instability of turning tools have been thoroughly investigated [4]. The consequences of tool vibration are poor surface polish, detectable noise, and edge blunting, emphasising the complex interaction of elements in achieving machining precision.

The authors [5] investigated tool wear and longevity in the turning of aluminium alloys. The study incorporates systematic variations in the rake angle and other relevant process variables to determine their impact on tool longevity. The positive rake angle improved the tool life during the machining process. Establishing an appropriate tool configuration improves turning conditions, with machinability gains gained by precisely aligning the tool point, angle, height, and deflection [6]. The nose radius is a critical parameter to consider when evaluating turning processes, as it has a significant impact on the outcome of machining operations. There are detailed studies on heat generation, surface development to the rake angle utility, and tool life for machining hard materials [7]. Further, the cutting forces are determined using a lathe tool dynamometer for the various negative and positive rake angles. Notably, positive rake angles helped in reducing the cutting force [8].

Changes to machining process parameters, such as spindle speed and feed rate, cause the tool profile and nose radius to become blunted. This tendency is most pronounced when the parameters are changed, resulting in higher tool wear and degradation, particularly with deeper cuts [9; 10]. The incorrect parameter selection has significant consequences beyond tool wear, including increased temperatures and a degraded surface finish. The rake angle is an important aspect in determining tool performance, and when maximised, it adds to longer tool life. However, it introduces the trade-off of dulling and creating tool clatter,

emphasising the delicate balance required for parameter selection [11–13]. The interplay between the tool's nose radius and rake angle has a substantial impact on the tool profile during machining, altering the smoothness of the machined surface. Hence, maintaining a specified nose radius range, such as 0.4–0.5 mm, has been shown in improving surface quality, especially when cutting high-strength AISI 1040 stainless steel [14]. The deeper incisions, as well as the presence of a nose radius, contribute to crater development and tool flank wear. The inappropriate turning process settings can result in discontinuous chips [15; 16]. An alternate method, magnetic cutting, has shown promise in improving turning machinability, surface characteristics, and tool life [10]. These advanced methods highlight the complex link between machining parameters and their significant influence on tool performance and surface properties in metalworking operations.

The chip-tool interface contact area is determined by the rake angle of a cutting tool. It is difficult to select the rake angle, since any deviation from the optimal value impacts the tool profile and machined surface. An increase in rake angle results in an increase in chip-tool friction. The cutting force, and contact area are both reduced by the rake angle. Many studies are being conducted to determine how process parameters influence rake angle, and machining processes. It is difficult to comprehend its impact on machining parameters. An investigation, of the ways in which rake angle affects machining parameters in ductile and brittle materials, was carried out by the researchers. During the procedure, a comprehensive study was done to identify the machining settings [14]. The rake angle and feed rate both contribute to a reduction in cutting force, when machining steel alloys. Here an in-depth investigation was conducted into the connection that exists between vibration and rake angle. The amplitude of vibration decreased as the rake angle increased [17]. An investigation was conducted on the modifications to the tool life rake angle. By reducing the rake angle, the nose radius was blunted. It was determined that a rake angle of 20° produced the greatest results in terms of tool life and surface finish [18].

Cutting fluids are critical for reducing heat generated at the chip-tool interface because of cutting forces. These fluids have the dual function of cooling and lubricating the cutting operation, resulting in longer tool life. Cutting fluids passing over the chip-tool interface, contribute to lower cutting temperatures [19]. The current research is focused on alternate cooling and lubrication technologies such as bio-oils, cryogenics, and chilled air, to address environmental problems and optimise milling operations [20; 21].

In the continued pursuit of sustainable machining methods, current research efforts are mostly focused on the usage of bio-oils. The researchers are currently investigating the viability of replacing petroleum-based lubricants with bio-oils, which are known for their non-hazardous properties. Some studies on the usefulness of vegetable oils, such as palm and shear butter oils during turning operations are carried out to determine their impact on surface quality and tool performance. They found an improvement in the surface quality and improvement in the tool life during the machining process [22]. The comparative investigation of palm and shear butter oils demonstrated significant improvements in chip thickness, and tool lifespan, with the added benefit of reducing the disagreeable aromas associated with traditional petroleum-based lubricants [23]. Similarly, the extraction of jatropha seed oil during machining resulted in lower surface temperatures, and better surface finishes, demonstrating the potential of bio-oils in improving machined surfaces [24]. Notably, as compared to mineral-based cutting solutions, coconut oil produced better surface quality and related to less tool wear [25].

The comparative examination of diverse bio-oils, as mentioned by researchers [26; 27] has become a focus point in comprehending their individual properties and performance characteristics. Using statistical techniques such as Anova, researchers are improving process parameters in experimental designs, to improve the use of bio-oils in machining operations [28; 29].

The investigation and prediction of the performance of various bio-oils as cutting fluids, in machining operations, can be accomplished by implementing advanced data analytics approaches [30]. Here a comprehensive predictive model can be created to systematically evaluate the feasibility and effectiveness of various bio-oils. The researcher created a model that contains complicated factors, such as bio-oil classification, machining parameters (e. g., cutting speed, input rate), material properties, and specific targeted machining outcomes [31]. The prediction model uses advanced statistical approaches, and machine learning algorithms to identify complicated patterns, and relationships in the dataset. This permits the estimate of the impact of using specific bio-oils as cutting fluids based on available data [32]. The model expands its predictive capabilities to measure critical performance indicators, such as surface finish quality, tool wear rate, and chip formation, for each bio-oil under changing machining settings [33]. The use of predictive modelling in the study of bio-oils, as cutting fluids, provides researchers with profound insights into the nuanced benefits and drawbacks of certain bio-oils [34]. This analytical method supports informed decision-making processes, machining operation optimisation, and environmental impact mitigation, by encouraging the use of non-hazardous and sustainable cutting fluids.

According to the available literature, a thorough evaluation of the feasibility, and performance of various bio-oils as cutting fluids in machining processes, involves rigorous experimental investigations as well, as the use of predictive modelling methodologies. The impact of bio-oils on essential metrics such as surface finish, tool wear, chip formation, and environmental consequences should be thoroughly investigated in this research. The bio-oils shows potential as practical and environmentally benign replacements, to petroleum-based lubricants in machining operations, according to the existing literature. However, in-depth experimental research combined with advanced predictive modelling techniques, are required to gain a deeper knowledge of their performance characteristics.

This study is required to perform extensive trials, and build accurate predictive models capable of comprehensively assessing the efficacy of bio-oils as cutting fluids. Fur-

thermore, these initiatives not only encourage sustainable practices and minimise reliance on petroleum-based lubricants, but they also help to expand bio-oil knowledge and its use in the manufacturing sector.

METHODS

This study identified gingelly oil, an edible vegetable oil derived from gingelly grains, as a viable substitute for mineral oils in the machining process. Table 1 compares the characteristics of gingelly oil and petroleum-based oil. In the investigation, a BALAJI Model 215 Super Series medium-duty lathe was utilised. 20 mm in diameter and 100 mm in length AISI 1014 mild steel workpieces were securely held in a three-jaw chuck, and spun at 328 and 750 rpm. The feed rates were held constant at 0.23 mm/rev for both experiments. For the machining process, an INDIAN TOOL manufacturer produced an HSS tool with 10 % cobalt, a 12.7 mm square section, and a 50 mm length. The experimental work was carried out with a variety of tool rake angles (5, 8, and 11°), and tool tip radii (1, 1.5, and 2 mm). The gingelly oil was delivered at a constant rate of 50 ml/min, while the petroleum-based oil (SAE 20W-40) served as a cutting fluid, and lubricant at a rate of 72 ml/min. The experiments were conducted in three distinct ways: without any cutting fluid (dry running), with a cutting fluid derived from petroleum (SAE 20W-40), and with gingelly oil as the cutting fluid. The surface roughness (Ra) of the workpieces was determined using a portable MITUTOYO SJ-210 surface roughness measuring device. This experimental setup enabled a thorough evaluation of gingelly oil's effectiveness as a cutting fluid, comparing its impacts on surface roughness to those of dry running, and standard petroleum-based cutting fluids. The cutting forces were measured using a lathe tool dynamometer. The cutting tool was inserted into the Contact-type Lathe Tool Dynamometer, and secured to the lathe's cross slide. Before starting the lathe machine, both the speed and feed were set to zero, and the feed was automatically applied to the tool. The surface roughness measurements were taken using a talysurf (MITUTOYO brand) under varied cutting conditions.

RESULTS

Fig. 1 demonstrates a notable disparity in surface smoothness, depending on the size of the workpiece, and the type of cutting operations used, especially when utilising a 5° rake angle, and 1 mm nose radius. The employment of the dry cutting technique resulted in a lower level of surface roughness, in comparison to the utilisation of cutting fluids, regardless of whether the cutting fluids were derived from petroleum or gingelly oil. Despite this, the surface roughness values increased with the increase in specimen diameter. Here the amount of sharpness over the cutting tool tip did not have any impact on the quality of the surface finish. Although some of the examples revealed surface qualities that were remarkable, others displayed levels of roughness that were far higher. Considering this, it appears that the surface finish is determined by a greater number of elements than the sharpness of the cutting tool in these conditions.

Fig. 2 depicts the effect of a higher cutting speed (750 rpm) on surface irregularity for various diameters of workpieces based on experimental data. When the cutting speed was increased to 750 rpm with a 5° rake angle, a remarkable increase in surface irregularity from 5.4 to 8.7 μm was observed. The increased rake angle and a 2 mm nose radius resulted in smoother surface finishes, and decreased cutting forces, as surface roughness improved. Notably, lower nose radii exhibited insufficient tool-to-workpiece adhesion, resulting in dispersed cutting force values for dry and petroleum-based cutting fluids. With its triglyceride content, gingelly oil displayed superior lubrication properties, generating a robust lubricant film that reduced friction and tool wear during machining. Consequently, this contributed to the finer formation of the machined workpiece's surfaces.

DISCUSSION

Effect of surface finish on different lubrication conditions

Further investigation indicated that raising the cutting tool's nose radius, resulted in increased adhesiveness between the tool and the workpiece, resulting in better and

Table 1. *Characteristics of petroleum based oil and gingelly oil*
Таблица 1. *Характеристики смазочно-охлаждающей жидкости на нефтяной основе и кунжутного масла*

Characteristics	Petroleum based oil (SAE 20W-40)	Gingelly oil
Flash point	210 °C	255 °C
Fire point	215 °C	280 °C
Density at 50 °C	774 kg/m^3	780 kg/m^3
Kinematic viscosity at 50 °C	2.39×10^{-5} m^2/s	3.72×10^{-5} m^2/s
Dynamic viscosity at 50 °C	1.86×10^{-3} N-s/m^2	2.67×10^{-3} N-s/m^2
Colour	Red	Clear yellow

more consistent surface finish values. The smoother surface finishes of 4.9 to 6 μm were attained with a tool nose radius of 1.5 mm, when gingelly oil was utilised as the cutting fluid. Furthermore, using a larger tool nose radius of 2 mm resulted in a 20 % reduction in surface roughness measurements, demonstrating the beneficial effect of increased nose radius on surface quality. Moving to an 8° rake angle, a limited variation range of cutting forces resulted in a significant difference in surface finish between the dry cutting procedure and the usage of petroleum-based cutting fluid. This is due to probable flaws in the machining process during turning operations. When gingelly oil was used as the cutting fluid, however, there was a considerable improvement in contact between the cutting tool and the workpiece, resulting in smoother surface finish values. Notably, increasing the tool nose radius improved the surface polish even more, due to increased ploughing area, and longer contact time between the tool and workpiece.

Further, the increase in the rake angle effectively reduced burr formation at the tool-workpiece interface, allowing the tool to glide through the material with greater ease. However, dynamic forces must be considered in a balanced manner, as exceedingly steep rake angles may not guarantee smoother operation. An optimal rake angle of 8°, appeared to accomplish favorable dynamic force balancing, reducing tangential force, while increasing thrust force at the interface of the tool tip. During this procedure, slight increases in surface roughness were observed. As a cutting fluid, gingelly oil demonstrated superior lubrication and cooling properties compared to cryogenic fluids, allowing for improved tool-to-workpiece slippage and thereby enhancing machinability. In addition, the use of higher cutting

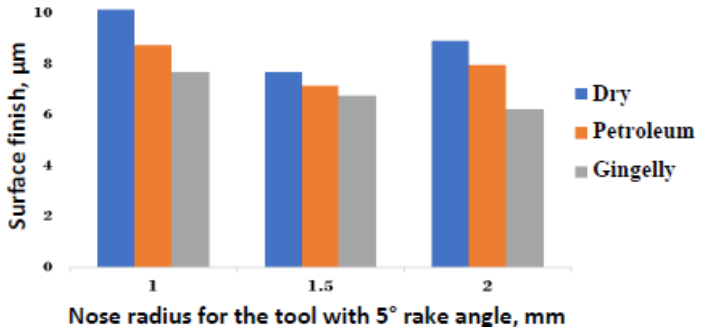

a

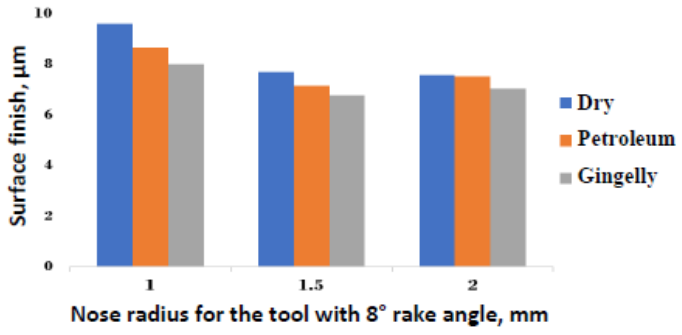

b

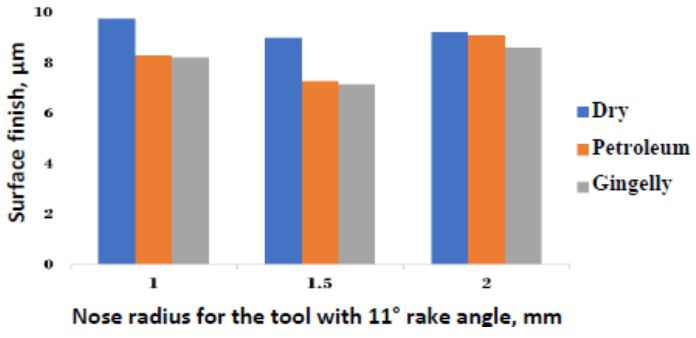

c

Fig. 1. *Effect of the surface finish over nose radius for the varying rake angles 5° (**a**), 8° (**b**), 11° (**c**), and cutting speed 328 rpm*
Рис. 1. *Влияние на качество поверхности радиуса закругления вершины при передних углах инструмента 5° (**a**), 8° (**b**), 11° (**c**) и скорости резания 328 об/мин*

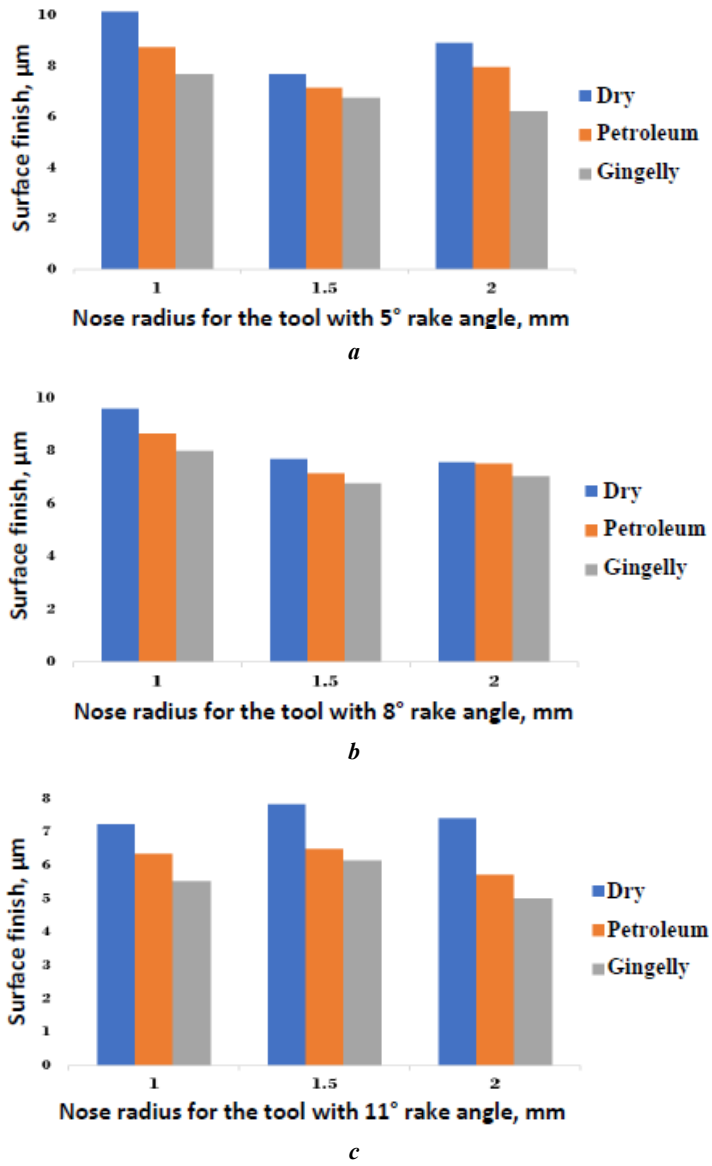

Fig. 2. *Effect of the surface finish over nose radius for the varying rake angles 5° (**a**), 8° (**b**), 11° (**c**), and cutting speed 720 rpm*
Рис. 2. *Влияние на качество поверхности радиуса закругления вершины при передних углах инструмента 5° (**a**), 8° (**b**), 11° (**c**) и скорости резания 720 об/мин*

speeds (750 rpm) with gingelly oil, led to significant advances in cutting processes, resulting in superior surface finishes, when compared to lower cutting speeds. Combining a higher cutting speed (750 rpm), a rake angle of 8°, and a nose radius of 2 mm with gingelly oil as the cutting fluid, resulted in significant improvements in machining performance. Compared to other process parameters, these enhancements included reduced cutting forces (approximately 5 to 25 % reduction), and enhanced surface roughness (approximately 2 to 15 % improvement).

Statistical model

The objective of the statistical model proposed in this research is to examine the impact of process factors on the quality of the output in the machining process. Here the cutting force, and roughness data from the experimental work is tabulated in Excel sheet and R software was used to determine the correlation and regression studies. Table 2 presents the dataset for 20 mm diameter specimen, encompassing factors such as nose radius, rake angle, cutting force, and surface finish.

The experimental study showed a statistically significant inverse link between surface finish, and various lubrication conditions, particularly in relation to nose radius and rake angle. The rake angle correlation coefficients ranged from −0.2 to −0.4, whereas the nose radius correlation coefficients ranged from −0.3 to −0.6. The discovered negative relationships, suggest that increasing the rake angle and nose radius improves the surface quality. A regression model was created to improve understanding of the relationship between different machining parameters and surface finish. This study focused on the interaction between several independent variables, such as cutting speed, cutting force, rake angle, and nose

radius, and the dependent variable, surface finish. However, the built multiple regression model was ineffective, as demonstrated by *R*-square values, ranging from −0.1 to −0.3. The more independent process parameters were added to the model, its overall stability and accuracy decreased. On the other side, investigating the effect of rake angle and cutting force while maintaining constant cutting speed surfaced as a potentially valuable route for enhancing the model. This phenomenon is most likely due to the increased complexity and interdependence brought about by the integration of several variables.

Furthermore, the *p*-values produced from the multiple regression model were found to be greater than the 0.05 significance level. This shows that the predictors utility in clarifying surface finish variability, did not approach statistical significance, possibly due to intricate interactions among variables that were not fully accounted for by the model.

This research aims to understand the intricate correlation between surface finish and critical cutting factors in machining processes. It utilises regression methods to address the shortcomings of conventional methodologies. Conventional approaches have faced difficulties in accurately capturing the complex non-linear relationships and interactions between important factors such as cutting speed, cutting force, rake angle, and nose radius. To overcome this deficiency, we have implemented divided strategies, which are effective in handling complex interconnections, and assessing the combined effect of these dividing elements on the evenness of the surface. To cover a wider range of cutting circumstances, trials were carried out with several diameters (8, 12, and 15 mm). The experimental data was then organised and analysed for various nose radius, and rake angle settings.

The influence of cutting force, diameter, and rake angle on surface polish while keeping a consistent nose

Table 2. *Cutting force and surface roughness values for the different process parameters*
Таблица 2. *Значения силы резания и шероховатости поверхности при разных параметрах процесса обработки*

Rake angle	Nose radius	Cutting force (N)			Cutting speed (rpm)	Surface roughness (μm)		
		dry turning	petroleum based lubrication	gingelly oil lubrication		dry turning	petroleum based lubrication	gingelly oil lubrication
5	1	459	451	448	328	9.350	7.388	7.455
5	1.5	466	441	438	328	9.350	7.388	7.455
5	2	452	444	319	328	8.948	7.021	5.331
8	1	444	432	420	328	6.967	6.521	5.335
8	1.5	458	451	450	328	7.161	6.661	6.117
8	2	430	437	318	328	5.636	7.963	6.548
11	1	466	458	447	328	9.788	8.327	8.221
11	1.5	473	469	446	328	9.017	7.287	7.171
11	2	441	438	318	328	9.248	9.132	8.626
5	1	470	462	444	750	10.152	8.758	7.682
5	1.5	477	461	448	750	7.682	7.152	6.758
5	2	382	343	327	750	8.920	7.980	6.230
8	1	469	450	444	750	9.596	8.651	7.989
8	1.5	476	460	454	750	7.682	7.152	6.758
8	2	360	323	310	750	7.560	7.510	7.030
11	1	472	461	457	750	7.249	6.351	5.532
11	1.5	483	462	434	750	7.847	6.490	6.143
11	2	356	317	311	750	7.420	5.730	5.020

radius was successfully investigated. The results of these analyses were evaluated using statistical metrics, notably *R*-square values, and *p*-values, which reveal the strength of the correlations and the importance of the predictors. The *R*-square and *p*-values for the various rake angle and nose radius are shown in Tables 3 and 4.

It was found that a rake angle of 8°, and a nose radius of 2 mm, resulted in higher surface finish performance in their testing. Among all the trial settings investigated, these exact combinations of cutting parameters produced the greatest results. It is understood that chatter (vibrations during cutting), climatic conditions, machine parameters, and other unknown variables, all influence the variation in cutting force and surface finish. These variables can cause variability in the machining process, resulting in variations in cutting force, and surface finish quality. Despite the influence of these and other elements, it is found that the rake angle, nose radius, cutting speed, and diameter all played important roles in enhancing surface polish, and cutting force. These critical cutting parameters were found to have a major impact on final surface smoothness, and guaranteeing adequate cutting force levels during the machining process.

Statistical metrics, such as *R*-square and *p*-values are used to quantify the associations, and assess the relevance of the identified predictors. The *R*-square value quantifies the amount of variance in the dependent variable (surface finish), explained by the independent variables (rake angle, nose radius, cutting speed, and diameter). The *p*-value, on the other hand, reveals the statistical significance of the predictors' effects. Based on the *R*-square and *p*-value data, the greatest values were associated with an 8° rake angle, and a 2 mm nose radius. This understands that these precise rake angle and nose radius combinations, have a significant and favourable impact on surface finish quality. Working under these optimised conditions resulted in significantly improved surface finish, when compared to other experimental settings, according to the data. In contrast, weak *R*-square and *p*-values were obtained for other working circumstances. This implies that the machining process operated poorly under these conditions, resulting in worse surface finish quality, and possibly larger cutting pressures. Finally, the experimental work demonstrated the significance of optimising the rake angle, and nose radius to create a superior surface quality and regulate cutting forces throughout the machining process.

CONCLUSIONS

In conclusion, this study examined gingelly oil as a cutting fluid in machining, and its effects on surface finish and cutting forces. Gingelly oil outperformed petroleum-based lubricants in machining, providing better lubrication and cooling. Gingelly oil consistently produced smoother surfaces and lower cutting forces, than dry cutting and petroleum-based lubrication.

Statistical analysis showed that optimising process parameters, especially rake angle and nose radius, improves surface finish quality. Surface finish and cutting forces were improved with an 8° rake angle and 2 mm nose radius. These optimised cutting conditions, outperformed other experimental settings, demonstrating the importance of cutting parameter selection and control in machining operations. Predictive modelling can evaluate bio-oils as cutting fluids, according to the study. Predictive models can estimate bio-oil effects on surface finish quality, tool wear rate, chip formation, and other performance indicators using historical data and experimental results. This method optimises machining, guides decision-making, and promotes sustainable cutting fluids.

Table 3. *R-square and p-values for different values of nose radius*
Таблица 3. *R-квадрат и p-значения при разных значениях радиуса закругления вершины*

Nose radius	*R*-square	*p*-value	Lubrication method
1	0.014	0.36	Dry
1	0.01	0.03	Petroleum
1	0.3	0.015	Gingelly
1.5	0.1579	0.09447	Dry
1.5	0.3	0.1243	Petroleum
1.5	0.5	0.0005	Gingelly
2	0.3	0.04	Dry
2	0.5	0.003	Petroleum
2	0.66	0.019	Gingelly

Table 4. *R-square and p-values for different values of rake angle*
Таблица 4. *R-квадрат и p-значения для разных значений переднего угла инструмента*

Rake angle	*R*-square	*p*-value	Lubrication method
5	0.17	0.05	Dry
5	0.3046	0.008478	Petroleum
5	0.3351	0.005295	Gingelly
8	0.3394	0.002	Dry
8	0.3409	0.009779	Petroleum
8	0.5878	0.0004	Gingelly
11	0.32	0.04	Dry
11	−0.115	0.08926	Petroleum
11	0.44	0.008	Gingelly

Gingelly oil and other bio-oils appear to be viable and environmentally being replacements to petroleum-based lubricants in manufacturing. However, more research is needed to understand the complicated connections between cutting parameters, and surface polish and cutting forces. Predictive modelling can help the industry implement sustainable practices by revealing bio-oil performance in certain machining settings.

REFERENCES

1. Beyer F., Willner K. Surface Deformation due to Shear and Ploughing in a Halfspace. *PAMM*, 2014, vol. 14, no. 1, pp. 239–240. DOI: 10.1002/pamm.201410107.
2. Hatna A., Grieve B. Cartesian machining versus parametric machining: A comparative study. *International Journal of Production Research*, 2000, vol. 38, no. 13, pp. 3043–3065. DOI: 10.1080/00207540050117431.
3. Oda Y., Kawamura Y., Fujishima M. Energy Consumption Reduction by Machining Process Improvement. *Procedia CIRP*, 2012, vol. 4, pp. 120–124. DOI: 10.1016/j.procir.2012.10.022.
4. Balevicius G., Ostasevicius V., Jurenas V., Baskutiene J., Zakrasas R. Investigation of vibration assisted drilling prospects for improving machining characteristics of hard to machine materials at high and low frequency ranges. *Mechanics*, 2016, vol. 22, no. 2, pp. 125–131. DOI: 10.5755/j01.mech.22.2.14431.
5. Nagasaka K., Hashimoto F. The establishment of a tool life equation considering the amount of tool wear. *Wear*, 1982, vol. 81, no. 1, pp. 21–31. DOI: 10.1016/0043-1648(82)90301-5.
6. Guney M., Seker U. Investigation of the Effect of Cutting Tool Rake Angle on Feed Force. *Journal of Polytechnic*, 2005, vol. 8, no. 4, pp. 323–328. DOI: 10.2339/y2005.v8.n4.p323-328.
7. Naves V.T.G., Da Silva M.B., Da Silva F.J. Evaluation of the effect of application of cutting fluid at high pressure on tool wear during turning operation of AISI 316 austenitic stainless steel. *Wear*, 2013, vol. 302, no. 1-2, pp. 1201–1208. DOI: 10.1016/j.wear.2013.03.016.
8. Neşeli S., Yaldız S., Türkeş E. Optimization of tool geometry parameters for turning operations based on the response surface methodology. *Measurement*, 2011, vol. 44, no. 3, pp. 580–587. DOI: 10.1016/j.measurement.2010.11.018.
9. Sewailem M.R., Mobarak I.M. The practical estimation of tool wear in turning. *Wear*, 1981, vol. 67, no. 3, pp. 261–269. DOI: 10.1016/0043-1648(81)90041-7.
10. Patwari A.U., Mahmood M.N., Arif M.D. Improvement of Machinability of Mild Steel during Turning Operation by Magnetic Cutting. *International Journal on Advanced Science, Engineering and Information Technology*, 2012, vol. 2, no. 3, pp. 207–210. DOI: 10.18517/ijaseit.2.3.187.
11. Ghani A.K., Choudhury I.A., Husni. Study of tool life, surface roughness and vibration in machining nodular cast iron with ceramic tool. *Journal of Materials Processing Technology*, 2002, vol. 127, no. 1, pp. 17–22. DOI: 10.1016/s0924-0136(02)00092-4.
12. Dahlman P., Gunnberg F., Jacobson M. The influence of rake angle, cutting feed and cutting depth on residual stresses in hard turning. *Journal of Materials Processing Technology*, 2004, vol. 147, no. 2, pp. 181–184. DOI: 10.1016/j.matprotec.2003.12.014.
13. Verma A., Sharma S. Analysis of Cutting Forces for Different Work Materials and Tool Material: Effect of Rake Angle in Turning Process. *International Journal of Scientific Research*, 2014, vol. 3, no. 7, pp. 172–173. DOI: 10.15373/22778179/july2014/54.
14. Radhika A., Shailesh Rao A., Yogesha K.B. Evaluating machining performance of AISI 1014 steel using gingelly oil as cutting fluid. *Australian Journal of Mechanical Engineering*, 2019, vol. 19, no. 4, pp. 445–456. DOI: 10.1080/14484846.2019.1636517.
15. Dodla S. Experimental Investigations of Tool Wear in Vibration-Assisted Turning of Inconel 718. *Archives of*

Metallurgy and Materials, 2022, vol. 67, no. 3, pp. 949–953. DOI: 10.24425/amm.2022.139687.
16. Shailesh Rao A. Effect of nose radius on the chip morphology, cutting force and tool wear during dry turning of Inconel 718. *Tribology - Materials, Surfaces & Interfaces*, 2023, vol. 17, no. 1, pp. 62–71. DOI: 10.1080/17515831.2022.2160161.
17. Yan Pei, Rong Yiming, Wang Gang. The effect of cutting fluids applied in metal cutting process. *Proceedings of the Institution of Mechanical Engineers, Part B: Journal of Engineering Manufacture*, 2015, vol. 230, no. 1, pp. 19–37. DOI: 10.1177/0954405415590993.
18. Haygreen L.H. Selection of cutting fluids. *Tribology International*, 1977, vol. 10, no. 1, pp. 13–16. DOI: 10.1016/0301-679x(77)90146-3.
19. Bartarya G., Choudhury S.K. Effect of Cutting Parameters on Cutting Force and Surface Roughness During Finish Hard Turning AISI52100 Grade Steel. *Procedia CIRP*, 2012, vol. 1, pp. 651–656. DOI: 10.1016/j.procir.2012.05.016.
20. Shashidhara Y.M., Jayaram S.R. Vegetable oils as a potential cutting fluid - An evolution. *Tribology International*, 2010, vol. 43, no. 5-6, pp. 1073–1081. DOI: 10.1016/j.triboint.2009.12.065.
21. Rapeti P., Pasam V.K., Rao Gurram K.M., Revuru R.S. Performance evaluation of vegetable oil based nano cutting fluids in machining using grey relational analysis – A step towards sustainable manufacturing. *Journal of Cleaner Production*, 2018, vol. 172, pp. 2862–2875. DOI: 10.1016/j.jclepro.2017.11.127.
22. Kumar B.S., Padmanabhan G., Krishna P.V. Experimental Investigations of Vegetable Oil Based Cutting Fluids with Extreme Pressure Additive in Machining of AISI 1040 Steel. *Manufacturing Science and Technology*, 2015, vol. 3, no. 1, pp. 1–9. DOI: 10.13189/mst.2015.030101.
23. Ozcelik B., Kuram E., Huseyin Cetin M., Demirbas E. Experimental investigations of vegetable based cutting fluids with extreme pressure during turning of AISI 304L. *Tribology International*, 2011, vol. 44, no. 12, pp. 1864–1871. DOI: 10.1016/j.triboint.2011.07.012.
24. Cetin M.H., Ozcelik B., Kuram E., Demirbas E. Evaluation of vegetable based cutting fluids with extreme pressure and cutting parameters in turning of AISI 304L by Taguchi method. *Journal of Cleaner Production*, 2011, vol. 19, no. 17-18, pp. 2049–2056. DOI: 10.1016/j.jclepro.2011.07.013.
25. Gunjal S.U., Patil N.G. Experimental Investigations into Turning of Hardened AISI 4340 Steel using Vegetable based Cutting Fluids under Minimum Quantity Lubrication. *Procedia Manufacturing*, 2018, vol. 20, pp. 18–23. DOI: 10.1016/j.promfg.2018.02.003.
26. Katna R., Suhaib M., Agrawal N. Nonedible vegetable oil-based cutting fluids for machining processes – a review. *Materials and Manufacturing Processes*, 2019, vol. 35, no. 1, pp. 1–32. DOI: 10.1080/10426914.2019.1697446.
27. Sredanovic B., Cica D. Comparative Study of ANN and ANFIS Prediction Models For Turning Process in Different Cooling and Lubricating Conditions. *SAE International Journal of Materials and Manufacturing*, 2015, vol. 8, no. 2, pp. 586–591. DOI: 10.4271/2015-01-9082.
28. Cica D., Sredanovic B., Tesic S., Kramar D. Predictive modeling of turning operations under different cooling/lubricating conditions for sustainable manufacturing with machine learning techniques. *Applied Computing and Informatics*, 2024, vol. 20, no. 1/2, pp. 162–180. DOI: 10.1016/j.aci.2020.02.001.
29. Shailesh R.A. Regression Analysis of Cutting Forces in Machining - Impact of Cutting Conditions and Fluids. *Comadem Journal*, 2024, vol. 27, no. 1, pp. 31–39.
30. Nagaraj A., Uysal A., Gururaja S., Jawahir I.S. Analysis of surface integrity in drilling carbon fiber reinforced polymer composite material under various cooling/lubricating conditions. *Journal of Manufacturing Processes*, 2022, vol. 82, pp. 124–137. DOI: 10.1016/j.jmapro.2022.07.065.
31. Arapoglu R.A., Sofuoglu M.A., Orak S. An ANN-Based Method to Predict Surface Roughness in Turning Operations. *Arabian Journal for Science and Engineering*, 2017, vol. 42, pp. 1929–1940. DOI: 10.1007/s13369-016-2385-y.
32. Veeranaath V., Nandana Mohanty M., Kumar A., Kumar P. ANN modeling of the significance of constraints in turning superalloys using coated PCBN tools. *Materials Today: Proceedings*, 2022, vol. 65-1, pp. 20–28. DOI: 10.1016/j.matpr.2022.03.559.
33. Agari S.R. Wear and surface characteristics on tool performance with CVD coating of Al_2O_3/TiCN inserts during machining of Inconel 718 alloys. *Archive of Mechanical Engineering*, 2022, vol. 69, no. 1, pp. 59–75.
34. Prasad K., Chakraborty S. A decision-making model for non-traditional machining processes selection. *Decision Science Letters*, 2014, vol. 3, pp. 467–478. DOI: 10.5267/j.dsl.2014.7.002.

СПИСОК ЛИТЕРАТУРЫ

1. Beyer F., Willner K. Surface Deformation due to Shear and Ploughing in a Halfspace // PAMM. 2014. Vol. 14. № 1. P. 239–240. DOI: 10.1002/pamm.201410107.
2. Hatna A., Grieve B. Cartesian machining versus parametric machining: A comparative study // International Journal of Production Research. 2000. Vol. 38. № 13. P. 3043–3065. DOI: 10.1080/00207540050117431.
3. Oda Y., Kawamura Y., Fujishima M. Energy Consumption Reduction by Machining Process Improvement // Procedia CIRP. 2012. Vol. 4. P. 120–124. DOI: 10.1016/j.procir.2012.10.022.
4. Balevicius G., Ostasevicius V., Jurenas V., Baskutiene J., Zakrasas R. Investigation of vibration assisted drilling prospects for improving machining characteristics of hard to machine materials at high and low frequency ranges // Mechanics. 2016. Vol. 22. № 2. P. 125–131. DOI: 10.5755/j01.mech.22.2.14431.
5. Nagasaka K., Hashimoto F. The establishment of a tool life equation considering the amount of tool wear // Wear. 1982. Vol. 81. № 1. P. 21–31. DOI: 10.1016/0043-1648(82)90301-5.
6. Guney M., Seker U. Investigation of the Effect of Cutting Tool Rake Angle on Feed Force // Journal of Polytechnic. 2005. Vol. 8. № 4. P. 323–328. DOI: 10.2339/y2005.v8.n4.p323-328.
7. Naves V.T.G., Da Silva M.B., Da Silva F.J. Evaluation of the effect of application of cutting fluid at high pressure on tool wear during turning operation of AISI 316

austenitic stainless steel // Wear. 2013. Vol. 302. № 1-2. P. 1201–1208. DOI: 10.1016/j.wear.2013.03.016.
8. Neşeli S., Yaldız S., Türkeş E. Optimization of tool geometry parameters for turning operations based on the response surface methodology // Measurement. 2011. Vol. 44. № 3. P. 580–587. DOI: 10.1016/j.measurement.2010.11.018.
9. Sewailem M.R., Mobarak I.M. The practical estimation of tool wear in turning // Wear. 1981. Vol. 67. № 3. P. 261–269. DOI: 10.1016/0043-1648(81)90041-7.
10. Patwari A.U., Mahmood M.N., Arif M.D. Improvement of Machinability of Mild Steel during Turning Operation by Magnetic Cutting // International Journal on Advanced Science, Engineering and Information Technology. 2012. Vol. 2. № 3. P. 207–210. DOI: 10.18517/ijaseit.2.3.187.
11. Ghani A.K., Choudhury I.A., Husni. Study of tool life, surface roughness and vibration in machining nodular cast iron with ceramic tool // Journal of Materials Processing Technology. 2002. Vol. 127. № 1. P. 17–22. DOI: 10.1016/s0924-0136(02)00092-4.
12. Dahlman P., Gunnberg F., Jacobson M. The influence of rake angle, cutting feed and cutting depth on residual stresses in hard turning // Journal of Materials Processing Technology. 2004. Vol. 147. № 2. P. 181–184. DOI: 10.1016/j.matprotec.2003.12.014.
13. Verma A., Sharma S. Analysis of Cutting Forces for Different Work Materials and Tool Material: Effect of Rake Angle in Turning Process // International Journal of Scientific Research. 2014. Vol. 3. № 7. P. 172–173. DOI: 10.15373/22778179/july2014/54.
14. Radhika A., Shailesh Rao A., Yogesha K.B. Evaluating machining performance of AlSI 1014 steel using gingelly oil as cutting fluid // Australian Journal of Mechanical Engineering. 2019. Vol. 19. № 4. P. 445–456. DOI: 10.1080/14484846.2019.1636517.
15. Dodla S. Experimental Investigations of Tool Wear in Vibration-Assisted Turning of Inconel 718 // Archives of Metallurgy and Materials. 2022. Vol. 67. № 3. P. 949–953. DOI: 10.24425/amm.2022.139687.
16. Shailesh Rao A. Effect of nose radius on the chip morphology, cutting force and tool wear during dry turning of Inconel 718 // Tribology - Materials, Surfaces & Interfaces. 2023. Vol. 17. № 1. P. 62–71. DOI: 10.1080/17515831.2022.2160161.
17. Yan Pei, Rong Yiming, Wang Gang. The effect of cutting fluids applied in metal cutting process // Proceedings of the Institution of Mechanical Engineers, Part B: Journal of Engineering Manufacture. 2015. Vol. 230. № 1. P. 19–37. DOI: 10.1177/0954405415590993.
18. Haygreen L.H. Selection of cutting fluids // Tribology International. 1977. Vol. 10. № 1. P. 13–16. DOI: 10.1016/0301-679x(77)90146-3.
19. Bartarya G., Choudhury S.K. Effect of Cutting Parameters on Cutting Force and Surface Roughness During Finish Hard Turning AISI52100 Grade Steel // Procedia CIRP. 2012. Vol. 1. P. 651–656. DOI: 10.1016/j.procir.2012.05.016.
20. Shashidhara Y.M., Jayaram S.R. Vegetable oils as a potential cutting fluid - An evolution // Tribology International. 2010. Vol. 43. № 5-6. P. 1073–1081. DOI: 10.1016/j.triboint.2009.12.065.
21. Rapeti P., Pasam V.K., Rao Gurram K.M., Revuru R.S. Performance evaluation of vegetable oil based nano cutting fluids in machining using grey relational analysis – A step towards sustainable manufacturing // Journal of Cleaner Production. 2018. Vol. 172. P. 2862–2875. DOI: 10.1016/j.jclepro.2017.11.127.
22. Kumar B.S., Padmanabhan G., Krishna P.V. Experimental Investigations of Vegetable Oil Based Cutting Fluids with Extreme Pressure Additive in Machining of AISI 1040 Steel // Manufacturing Science and Technology. 2015. Vol. 3. № 1. P. 1–9. DOI: 10.13189/mst.2015.030101.
23. Ozcelik B., Kuram E., Huseyin Cetin M., Demirbas E. Experimental investigations of vegetable based cutting fluids with extreme pressure during turning of AISI 304L // Tribology International. 2011. Vol. 44. № 12. P. 1864–1871. DOI: 10.1016/j.triboint.2011.07.012.
24. Cetin M.H., Ozcelik B., Kuram E., Demirbas E. Evaluation of vegetable based cutting fluids with extreme pressure and cutting parameters in turning of AISI 304L by Taguchi method // Journal of Cleaner Production. 2011. Vol. 19. № 17-18. P. 2049–2056. DOI: 10.1016/j.jclepro.2011.07.013.
25. Gunjal S.U., Patil N.G. Experimental Investigations into Turning of Hardened AISI 4340 Steel using Vegetable based Cutting Fluids under Minimum Quantity Lubrication // Procedia Manufacturing. 2018. Vol. 20. P. 18–23. DOI: 10.1016/j.promfg.2018.02.003.
26. Katna R., Suhaib M., Agrawal N. Nonedible vegetable oil-based cutting fluids for machining processes – a review // Materials and Manufacturing Processes. 2019. Vol. 35. № 1. P. 1–32. DOI: 10.1080/10426914.2019.1697446.
27. Sredanovic B., Cica D. Comparative Study of ANN and ANFIS Prediction Models For Turning Process in Different Cooling and Lubricating Conditions // SAE International Journal of Materials and Manufacturing. 2015. Vol. 8. № 2. P. 586–591. DOI: 10.4271/2015-01-9082.
28. Cica D., Sredanovic B., Tesic S., Kramar D. Predictive modeling of turning operations under different cooling/lubricating conditions for sustainable manufacturing with machine learning techniques // Applied Computing and Informatics. 2024. Vol. 20. № 1/2. P. 162–180. DOI: 10.1016/j.aci.2020.02.001.
29. Shailesh R.A. Regression Analysis of Cutting Forces in Machining - Impact of Cutting Conditions and Fluids // Comadem Journal. 2024. Vol. 27. № 1. P. 31–39.
30. Nagaraj A., Uysal A., Gururaja S., Jawahir I.S. Analysis of surface integrity in drilling carbon fiber reinforced polymer composite material under various cooling/lubricating conditions // Journal of Manufacturing Processes. 2022. Vol. 82. P. 124–137. DOI: 10.1016/j.jmapro.2022.07.065.
31. Arapoglu R.A., Sofuoglu M.A., Orak S. An ANN-Based Method to Predict Surface Roughness in Turning Operations // Arabian Journal for Science and Engineering. 2017. Vol. 42. P. 1929–1940. DOI: 10.1007/s13369-016-2385-y.
32. Veeranaath V., Nandana Mohanty M., Kumar A., Kumar P. ANN modeling of the significance of constraints in turning superalloys using coated PCBN tools // Materials Today: Proceedings. 2022. Vol. 65-1. P. 20–28. DOI: 10.1016/j.matpr.2022.03.559.

33. Agari S.R. Wear and surface characteristics on tool performance with CVD coating of Al_2O_3/TiCN inserts during machining of Inconel 718 alloys // Archive of Mechanical Engineering. 2022. Vol. 69. № 1. P. 59–75.

34. Prasad K., Chakraborty S. A decision-making model for non-traditional machining processes selection // Decision Science Letters. 2014. Vol. 3. P. 467–478. DOI: 10.5267/j.dsl.2014.7.002.

Качество обработки поверхности и эффективность резания в кунжутном масле во время механической обработки: регрессионный анализ

Шайлеш Рао А., кандидат наук, профессор, кафедра машиностроения
Политехнический институт Нитте Минакши, Бангалор (Индия)

E-mail: shailesh.rao@nmit.ac.in ORCID: https://orcid.org/0000-0001-6190-9857

Поступила в редакцию 31.08.2023 *Принята к публикации 19.02.2024*

Аннотация: В исследовании оценивается возможность использования кунжутного масла в качестве экологически чистой смазочно-охлаждающей жидкости при токарной обработке. Проведены эксперименты для определения влияния радиуса закругления вершины и переднего угла инструмента на износ инструмента, формирование поверхности и силу резания. Кроме того, были исследованы различные смазочные материалы, такие как смазочно-охлаждающие жидкости на нефтяной основе и биомасла, с целью определения их потенциала для минимизации трения, выделения тепла и износа инструмента во время обработки. Установлено, что по сравнению с сухим резанием и обычными смазками на нефтяной основе кунжутное масло обеспечивает более гладкую поверхность и снижает силу резания. Взаимосвязь между параметрами резания и качеством обработки поверхности анализировалась с использованием статистического моделирования. Для количественной оценки корреляций и значимости предиктора использовались коэффициент детерминации (R-квадрат) и p-значения. Результаты подчеркивают эффективность использования кунжутного масла в качестве смазочно-охлаждающей жидкости и важность оптимизации параметров процесса для повышения эффективности обработки.

Ключевые слова: эффективность резания в кунжутном масле; механическая обработка в кунжутном масле; смазывающе-охлаждающая жидкость; надежная обработка; качество обработки поверхности; износ инструмента; передний угол; радиус закругления вершины.

Для цитирования: Шайлеш Рао А. Качество обработки поверхности и эффективность резания в кунжутном масле во время механической обработки: регрессионный анализ // Frontier Materials & Technologies. 2024. № 2. С. 101–111. DOI: 10.18323/2782-4039-2024-2-68-9.

doi: 10.18323/2782-4039-2024-2-68-10

Comparative analysis of the chemical composition and mechanical properties of duralumin welded joint produced by friction stir welding

Gennady V. Shchapov[1], postgraduate student, junior researcher
Nataliya V. Kazantseva*[2], Doctor of Sciences (Physics and Mathematics), Associate Professor, chief researcher
M.N. Mikheev Institute of Metal Physics of the Ural Branch of RAS, Yekaterinburg (Russia)

***E-mail:** kazantseva@imp.uran.ru

[1]ORCID: https://orcid.org/0009-0000-2106-6381
[2]ORCID: https://orcid.org/0000-0002-4143-1064

Received 27.06.2023 *Accepted 21.11.2023*

Abstract: Friction stir welding is an advanced method of joining various metals and alloys in the aircraft and mechanical engineering industries. This type of welding is used to join materials that are difficult to weld or not weldable by conventional methods. The high-strength D16 aluminum alloy is difficult to weld by fusion, which is associated with the formation of a dendritic structure in the fusion zone leading to a decrease in the mechanical strength of the joint. In the work, the microstructure and microhardness of a welded seam of the D16 aluminum alloy produced by friction stir welding was studied. Using scanning electron microscopy and optical metallography, the authors identified the presence of three zones: the weld core, the thermomechanical impact zone, and the heat effected zone. In the central part of the welded joint (in the core), a laminated onion ring structure was discovered. A change in the chemical composition of the aluminum solid solution was identified in different areas of the weld zones, as well as the presence of a concentration gradient within each zone. In the upper part of the welded seam, the solid solution is silicon-enriched and depleted in copper. Due to the solid solution depletion in alloying elements, the aluminum content in the solid solution in the zone of the welded joint is higher compared to the initial state. The microhardness values in different areas of the welded joint correlate with changes in the chemical composition. In the welded joint zone, a significant decrease in microhardness was found compared to the initial state, and a change in microhardness associated with the chemical composition gradient within each zone was also observed.

Keywords: friction stir welding; duralumin; aluminum; laminated structure; onion ring structure.

Acknowledgments: The work was carried out within the state assignment of the Ministry of Education and Science of the Russian Federation (topic “Additivity”, No. 121102900049-1).

The paper was written on the reports of the participants of the XI International School of Physical Materials Science (SPM-2023), Togliatti, September 11–15, 2023.

For citation: Shchapov G.V., Kazantseva N.V. Comparative analysis of the chemical composition and mechanical properties of duralumin welded joint produced by friction stir welding. *Frontier Materials & Technologies*, 2024, no. 2, pp. 113–119. DOI: 10.18323/2782-4039-2024-2-68-10.

INTRODUCTION

Friction stir welding (FSW) is a relatively new method for producing permanent joints of materials, proposed in 1991 by the Welding Institute of Great Britain. Friction stir welding is a solid-state joining process, when no volumetric melting of the base material occurs [1; 2]. Research in recent years has shown that FSW is an effective way to produce high-quality connections of structures of various sizes and shapes, including sheets, three-dimensional profiles, and pipes. It is used to restore worn parts and to weld cracks and casting defects. Compared to conventional fusion welding methods, during FSW, there are no signs of a cast structure in the joint zone, the joined parts have little deformation and residual stress, there is no need to carry out operations to clean the surface from oxides before the welding process, and there are no defects resulting from melting and hardening.

To join parts, frictional heating and plastic deformation are used, as a rule, at temperatures below the absolute melting point of the alloys being joined. This is achieved through the interaction of a rotating tool consisting of a pin and a shoulder (pin) with the faying surfaces into which it is immersed until the shoulder contacts with the upper surface of the blanks, and then moves along the interface between the blanks (Fig. 1). Due to wide technological capabilities for producing permanent joints of parts or assemblies, FSW can be used as an alternative to rivet joints, electric arc welding, electron beam and laser welding, as well as for welding dissimilar materials.

A large number of works deals with the issue of selecting friction stir welding modes. Usually, the speed of tool rotation and movement [3; 4], pin shape [5], and sample preheating [6] are varied. However, no detailed study of changes in the chemical composition and mechanical properties in different welded joint areas, including its upper and lower parts, has been found in the literature.

High-strength D16 grade duralumin for aviation purposes, as a rule, is difficult to be welded by fusion, since, when using this type of welding, a dendritic structure is formed in the fusion zone leading to a sharp decrease in mechanical strength [7]. According to [8–10], during FSW, the metal

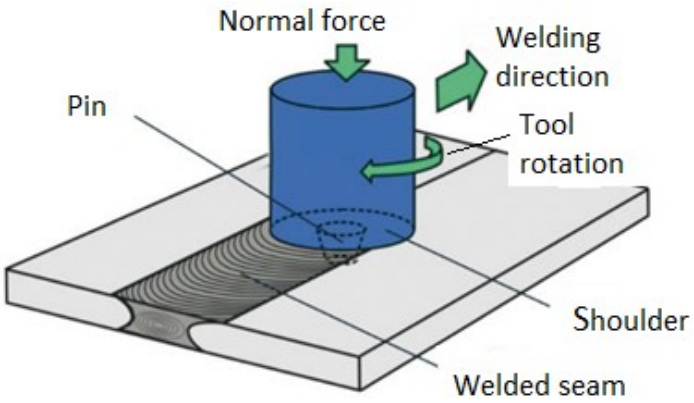

Fig. 1. *The diagram of the process of friction stir welding*
Рис. 1. *Схема процесса сварки трением с перемешиванием*

does not reach the melting temperature, so FSW can produce high-quality, defect-free welds when properly selecting the welding parameters for high-strength D16 alloys, as well as avoiding severe heating and cooling cycles that occur during fusion welding.

When using FSW, it is important to study the mechanisms and identify the physical patterns of the formation of the structural state, and factors leading to the formation of structural heterogeneities and discontinuities in the weld. Identification of such patterns will allow selecting the optimal FSW characteristics and making a forecast of the welded product operational properties. A change in the chemical composition of the alloy solid solution has a great influence on the mechanical properties. For dispersion-hardening aluminium alloys, except for the main strengthening intermetallic phases, the presence of secondary phases is possible. Under certain thermomechanical interactions, they can significantly deplete the solid solution, and due to coagulation of particles, reduce the general strength properties of the material [11; 12].

The purpose of this study is to analyse the distribution of the chemical composition and mechanical properties in the weld zone of a D16 alloy butt joint produced by friction stir welding.

METHODS

The authors used for the study the D16 GOST 4784-2019 (foreign analogues AA2024, $AlCuMg_2$) duralumin plates. A direct butt welded joint was produced by friction stir welding using a test stand. A welding tool made of high-speed R6M5 steel was used, the tool rotation speed range was 400–600 rpm, and the tool movement speed was 320 mm/min. Samples cut using an electrical discharge machine were examined in the transverse and longitudinal sections of the welded joint. Table 1 presents the chemical composition of the original D16 alloy plates and the chemical composition according to GOST 4784-2019.

Structural studies were carried out using a JSM 6490 scanning electron microscope with the Oxford Inca system for energy dispersive and wave microanalysis and a Micromed MET optical microscope, with the ability of imaging in polarized light. Analysis of the solid solution structure, and chemical composition in the weld zone was carried out along the A, B, C lines every 4 mm. The centre of the lower edge of the weld was taken as the first reference point. The area with a zero position corresponded to the original material. The size of the analysed area, which does not include the precipitation of intermetallic phases, was 5×5 μm, the diameter of the probe in a scanning electron microscope was 3 μm. Microhardness was measured using a Metalab-502 device, the load was 0.490 N, the time was 10 s. The microhardness value was determined from five measurements.

RESULTS

Fig. 2 shows an optical photograph of the cross section of the weld of the studied D16 alloy. In the optical image, differing in colour: the core zone, the thermomechanical impact zone, and the heat effected

Table 1. *Chemical composition of the D16 alloy, wt. %*
Таблица 1. *Химический состав сплава Д16, мас. %*

Composition	Al	Mg	Cu	Fe	Si	Mn	Zn	Ti	Cr
According to GOST 4784-2019	Base	1.2–1.8	3.8–4.9	<0.5	<0.5	0.3–0.9	<0.25	<0.15	<0.1
Original sample	93.34	1.31	4.23	0.3	0.16	0.54	0.08	0.04	0.004

zone. In the central part of the welded joint (in the core), the laminated onion ring structure is observed (Fig. 2, lines A, B). In our case, line C passes through the thermomechanical impact zone, and line D passes through the heat effected zone (Fig. 2).

Fig. 3 presents the results of measuring the chemical composition of the solid solution in various areas of the weld (along the selected lines) obtained using a scanning microscope. In the thermomechanical impact zone (region 7) in the lower part of the joint, an increase in silicon content (Fig. 3 a) and a decrease in aluminium (Fig. 3 b) are observed. Compared to the initial state, the aluminium content in the solid solution of the weld zone is generally higher (Fig. 3 b).

It is possible to note, as well, an increase in the copper content in the solid solution in the welded joint core, and in the thermomechanical impact zone compared to the initial state. At the same time, in the centre of the core (areas 2 and 3), the copper content decreases, and the silicon content increases. The main strengthening phase of the D16 alloy is the *S*-phase. However, we did not detect macroprecipitates of this phase.

Fig. 4 shows the results of measuring microhardness in various areas of the welded joint. In the zone of the welded joint, microhardness significantly decreases, compared to the initial state (point 0) (Fig. 4). Point 9 is the boundary between the core, and the thermomechanical zone, where a sharp increase in microhardness is observed.

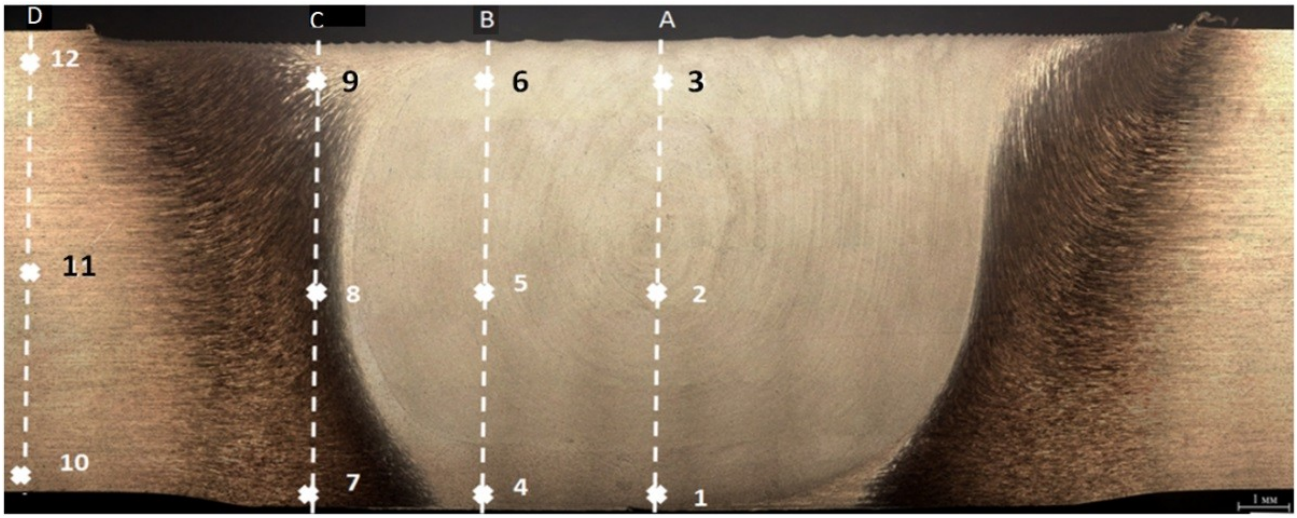

Fig. 2. *Microstructure of the welded joint cross section indicating areas of study*
Рис. 2. *Микроструктура поперечного сечения сварного соединения с указанием областей исследования*

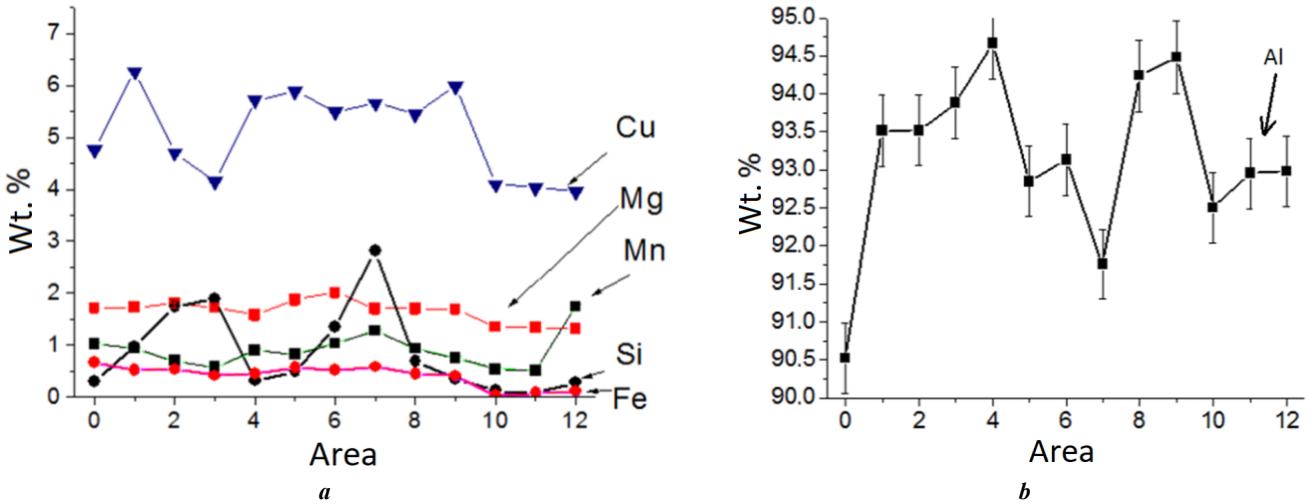

Fig. 3. *Distribution of alloying elements (**a**) and aluminium (**b**) in the welded joint area*
Рис. 3. *Распределение легирующих элементов (**a**) и алюминия (**b**) в зоне сварного соединения*

DISCUSSION

According to the literature, three zones can be distinguished in a welded joint: the weld core, the thermomechanical impact zone, and the heat effected zone [12]. These three zones are clearly visible in Fig. 2. According to [12], the laminated onion ring structure is formed when the tool rotates in the plasticised metal, which was observed in the centre of the welded joint.

Only using transmission electron microscopy, nanosised precipitations of the strengthening *S*-phase in the AA2024 alloy (Russian analogue is D16) after friction stir welding were detected in local areas of the welded joint, with increased microhardness [13]. This explains the absence of the *S*-phase in our case during optical and scanning electron microscopy studies.

The change in the chemical composition of the solid solution in the welded joint can be explained by the precipitation of secondary phases enriched in copper and silicon. In [14; 15], in the AA2024 alloy of the Al–Cu–Mg system (Russian analogue is D16) secondary intermetallic microcrystalline phases containing silicon and copper were discovered: Al_2Cu, AlCuFeMnSi, Mg_2Si, Al_7Cu_2Fe, $Al_{12}(Fe,Mn)_3Si$, $Al_{20}Mg_3Cu_2$. Both in the thermomechanical impact zone, and in the core of the welded joint, according to the literature, an increase in temperature up to 500 °C is possible [16–18], which can cause precipitation of secondary intermetallic phases leading to a change in the solid solution content.

An increase in temperature accelerates the diffusion of chemical elements in aluminium alloys. Table 2 presents the coefficients of diffusion of chemical elements in aluminium obtained in [16], from which it can be seen that silicon is the most mobile element at a temperature of 500 °C. Aluminium self-diffusion coefficient is close to the copper diffusion coefficient. Manganese is the "slowest" element. Considering the fact that the diffusion front moves at the speed of the "slowest" element, at this temperature, a slow growth of phases containing manganese can be expected. Therefore, the appearance of such phases can be caused both by thermal impact and by deformation.

Changes in the microstructure in various zones influence greatly the mechanical properties of the joint after welding [19]. A change in microhardness in the welded joint zone similar to that found in our work was observed in [20; 21]. In the work [3], it was found that the aluminium alloy microhardness depends on the rotation frequency of the pin and the speed of its movement. Comparing the results obtained in our work with the data of [3], one can talk of different rates of stirring the material in different areas of the welded joint. According to the literature, phase ageing in aluminium alloys leads to both strengthening, and softening of the material. Softening is associated with coagulation of particles of secondary strengthening phases [12]. A significant decrease in microhardness in the lower part of the thermomechanical impact zone (area 8 in Fig. 2),

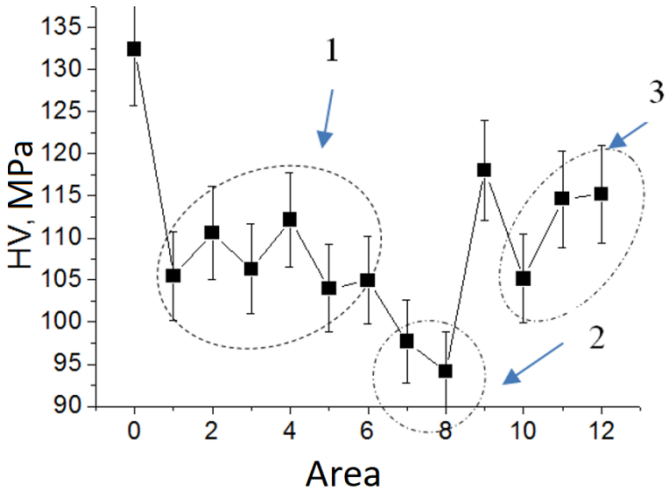

Fig. 4. *The results of measuring microhardness in the welded joint area:*
1 – core; 2 – thermomechanical impact zone; 3 – heat effected zone
Рис. 4. *Результаты измерения микротвердости в зоне сварного соединения:*
1 – ядро; 2 – зона термомеханического воздействия; 3 – зона термического воздействия

Table 2. *Coefficients of diffusion of elements in aluminium at 500 °C, m^2/s [Repr. from 16, p. 10]*
Таблица 2. *Коэффициенты диффузии элементов в алюминии при 500 °C, $м^2/с$ [Привод. по 16, с. 10]*

Al	Mg	Cu	Fe	Si	Mn
4.3×10^{-14}	9.9×10^{-14}	4.0×10^{-14}	8.9×10^{-16}	13×10^{-13}	7.4×10^{-18}

may be associated exactly with the enlargement of the precipitated secondary phases enriched in copper and silicon. In this case, the increase in microhardness in the upper part of the thermomechanical impact zone (area 9 in Fig. 2) may be associated with the precipitation of small secondary phases. These assumptions are consistent with the results of studies of the chemical composition of the solid solution in these areas (Fig. 3).

CONCLUSIONS

1. A change in aluminium content and a redistribution of alloying elements (Si, Cu) in the solid solution in various areas of the weld zones were detected. Compared to the initial state, the aluminium content in the zone of the welded joint in the solid solution is higher. An increase in the copper content in the solid solution in the welded joint core and in the thermomechanical impact zone was detected, compared to the initial state. At the same time, the copper content decreases and the silicon content increases in the core centre, which is probably associated with the precipitation of secondary phases such as $Al_{12}(Fe,Mn)_3Si$ or AlCuFeMnSi, enriched in copper and silicon, under the influence of deformation.

2. In the welded joint zone, a significant decrease in microhardness compared to the initial state is observed, which may be caused by the coagulation of particles of secondary strengthening phases enriched in copper and silicon.

3. Within each zone of the weld, a gradient in the solid solution chemical composition is observed, which also correlates with a change in microhardness.

REFERENCES

1. Thomas W.M., Nicholas E.D., Needham J.C., Murch M.G., Templesmith P., Smith C.J. *Friction stir butt welding*: patent USA no. 5460317, 1995, 10 p.
2. Drits A.M., Ovchinnikov V.V., Vasilev P.A. Studies of structure and mechanical properties of Al–Cu–Mg alloy joints made by friction stir welding. *Tekhnologiya legkikh splavov*, 2019, no. 4, pp. 17–25. EDN: NVFMZO.
3. Radhika Ch., Shyam Kumar N. Process Parameters Optimization of Aa2024 Alloy Friction Stir Welding using Taguchi's Technique. *International Journal of Innovative Technology and Exploring Engineering*, 2019, vol. 8, no. 11, pp. 1940–1945. DOI: 10.35940/ijitee.K2138.0981119.
4. Ridha M.H., Alkhazraji S.K., Abdull I.T. Investigation of Friction Stir Welding of AA2024-T4 Thin Sheets for Industrial Applications. *IOP Conference Series: Materials Science and Engineering*, 2020, vol. 881, article number 012074. DOI: 10.1088/1757-899X/881/1/012074.
5. Luo Jian, Wang Jiafa, Lin Hongxin, Yuan Lei, Gao Jianjun, Geng Haibin. Study on the Relationship between Root Metal Flow Behavior and Root Flaw Formation of a 2024 Aluminum Alloy Joint in Friction Stir Welding by a Multiphysics Field Model. *Metals*, 2020, vol. 10, no. 7, article number 913. DOI: 10.3390/met10070913.
6. Kubit A., Kluz R., Ochaek K., Wydrzyñski D., Trzepieciñski T. Friction stir welding of 2024-T3 aluminium alloy sheet with sheet pre-heating. *Materials and technology*, 2018, vol. 52, no. 3, pp. 283–288. DOI: 10.17222/mit.2017.084.
7. Genri A., Loginova I.S., Kravchenko K.V., Daubarayte D.K., Ryabov D.K. An effect of yttrium on hot cracking resistance, microstructure and properties of D16 alloy produced by laser melting. *Tekhnologiya legkikh splavov*, 2019, no. 4, pp. 26–34. EDN: NZTBBX.
8. Cavaliere P., Nobile R., Pannela F.W., Squillace A. Mechanical and microstructural behaviour of 2024–7075 aluminium alloy sheets joined by friction stir welding. *International Journal of Machine Tools & Manufacture*, 2006, vol. 46, no. 6, pp. 588–594. DOI: 10.1016/J.IJMACHTOOLS.2005.07.010.
9. Cavaliere P., Cerri E., Squillace A. Mechanical response of 2024–7075 aluminium alloys joined by friction stir welding. *Journal of Material Science*, 2005, vol. 40, pp. 3669–3676. DOI: 10.1007/s10853-005-0474-5.
10. Zadpoor A.A., Sinke J., Benedictus R., Pieters R. Mechanical properties and microstructure of friction stir welded tailor-made blanks. *Materials Science and Engineering: A*, 2008, vol. 494, no. 1-2, pp. 281–290. DOI: 10.1016/j.msea.2008.04.042.
11. Vorobev R.A., Sorokina S.A., Evstifeeva V.V. Phase composition of deformable D16 and B95 aluminium alloys with the quantitative assessment of overburning of different stages of development. *Izvestiya. Non-Ferrous Metallurgy / Izvestiya Vuzov. Tsvetnaya metallurgiya,* 2020, no. 1, pp. 68–78. DOI: 10.17073/0021-3438-2020-1-68-78.
12. Krishnan K.N. On the formation of onion rings in friction stir welds. *Materials Science and Engineering: A*, 2002, vol. 327, no. 2, pp. 246–251. DOI: 10.1016/S0921-5093(01)01474-5.
13. Morozova I., Królicka A., Obrosov A., Yang Y., Doynov N., Weiß S., Michailov V. Precipitation phenomena in impulse friction stir welded 2024 aluminium alloy. *Materials Science and Engineering: A*, 2022, vol. 852, article number 143617. DOI: 10.1016/j.msea.2022.143617.
14. Zhang Fan, Levine L.E., Allen A.J., Campbell C.E., Creuziger A.A., Kazantseva N., Ilavsky J. In situ structural characterization of ageing kinetics in aluminum alloy 2024 across angstrom-to-micrometer length scales. *Acta Materialia*, 2016, vol. 111, pp. 385–398. DOI: 10.1016/j.actamat.2016.03.058.
15. Mrówka-Nowotnik G., Sieniawsk J. Analysis of intermetallic phases in 2024 aluminium alloy. *Solid State Phenomena*, 2013, vol. 197, pp. 238–243. DOI: 10.4028/www.scientific.net/SSP.197.238.
16. Czerwinski F. Thermal Stability of Aluminum Alloys. *Materials*, 2020, vol. 13, no. 15, article number 3441. DOI: 10.3390/ma13153441.
17. Tang W., Guo X., Mcclure J., Murr L., Nunes A.C. Heat input and temperature distribution in friction stir welding. *Journal of Materials Processing and Manufacturing Science*, 1998, vol. 7, no. 2, pp. 163–172.
18. Chen C.M., Kovacevic R. Finite element modeling of friction stir welding-thermal and thermomechanical analysis. *International Journal of Machine Tools & Manufacture*, 2003, vol. 43, no. 13, pp. 1319–1326. DOI: 10.1016/S0890-6955(03)00158-5.

19. Mishra R.S., Ma Z.Y. Friction stir welding and processing. *Materials Science and Engineering: R: Reports*, 2005, vol. 50, no. 1-2, pp. 1–78. DOI: 10.1016/j.mser.2005.07.001.
20. Dawes C.J. An introduction to friction stir welding and its development. *Welding and Metal fabrication*, 1995, pp. 14–16.
21. Dawes C.J., Thomas W.M. Friction stir joining of aluminium alloys. *TWI Bulletin*, 1995, vol. 6, pp. 124–127.

СПИСОК ЛИТЕРАТУРЫ

1. Thomas W.M., Nicholas E.D., Needham J.C., Murch M.G., Templesmith P., Smith C.J. Friction stir butt welding: patent USA № 5460317, 1995. 10 p.
2. Дриц А.М., Овчинников В.В., Васильев П.А. Исследование структуры и механических свойств соединений сплавов системы Al–Cu–Mg, полученных сваркой трением с перемешиванием // Технология легких сплавов. 2019. № 4. С. 17–25. EDN: NVFMZO.
3. Radhika Ch., Shyam Kumar N. Process Parameters Optimization of Aa2024 Alloy Friction Stir Welding using Taguchi’s Technique // International Journal of Innovative Technology and Exploring Engineering. 2019. Vol. 8. № 11. P. 1940–1945. DOI: 10.35940/ijitee.K2138.0981119.
4. Ridha M.H., Alkhazraji S.K., Abdull I.T. Investigation of Friction Stir Welding of AA2024-T4 Thin Sheets for Industrial Applications // IOP Conference Series: Materials Science and Engineering. 2020. Vol. 881. Article number 012074. DOI: 10.1088/1757-899X/881/1/012074.
5. Luo Jian, Wang Jiafa, Lin Hongxin, Yuan Lei, Gao Jianjun, Geng Haibin. Study on the Relationship between Root Metal Flow Behavior and Root Flaw Formation of a 2024 Aluminum Alloy Joint in Friction Stir Welding by a Multiphysics Field Model // Metals. 2020. Vol. 10. № 7. Article number 913. DOI: 10.3390/met10070913.
6. Kubit A., Kluz R., Ochaek K., Wydrzyñski D., Trzepieciñski T. Friction stir welding of 2024-T3 aluminium alloy sheet with sheet pre-heating // Materials and technology. 2018. Vol. 52. № 3. P. 283–288. DOI: 10.17222/mit.2017.084.
7. Генри А., Логинова И.С., Кравченко К.В., Даубарайте Д.К., Рябов Д.К. Влияние иттрия на сопротивление образованию горячих трещин, микроструктуру и свойства сплава Д16 при лазерном плавлении // Технология легких сплавов. 2019. № 4. С. 26–34. EDN: NZTBBX.
8. Cavaliere P., Nobile R., Pannela F.W., Squillace A. Mechanical and microstructural behaviour of 2024–7075 aluminium alloy sheets joined by friction stir welding // International Journal of Machine Tools & Manufacture. 2006. Vol. 46. № 6. P. 588–594. DOI: 10.1016/J.IJMACHTOOLS.2005.07.010.
9. Cavaliere P., Cerri E., Squillace A. Mechanical response of 2024–7075 aluminium alloys joined by friction stir welding // Journal of Material Science. 2005. Vol. 40. P. 3669–3676. DOI: 10.1007/s10853-005-0474-5.
10. Zadpoor A.A., Sinke J., Benedictus R., Pieters R. Mechanical properties and microstructure of friction stir welded tailor-made blanks // Materials Science and Engineering: A. 2008. Vol. 494. № 1-2. P. 281–290. DOI: 10.1016/j.msea.2008.04.042.
11. Воробьев Р.А., Сорокина С.А., Евстифеева В.В. Фазовый состав деформируемых алюминиевых сплавов Д16 с количественной оценкой пережога разных стадий развития // Известия высших учебных заведений. Цветная металлургия. 2020. № 1. С. 68–78. DOI: 10.17073/0021-3438-2020-1-68-78.
12. Krishnan K.N. On the formation of onion rings in friction stir welds // Materials Science and Engineering: A. 2002. Vol. 327. № 2. P. 246–251. DOI: 10.1016/S0921-5093(01)01474-5.
13. Morozova I., Królicka A., Obrosov A., Yang Y., Doynov N., Weiß S., Michailov V. Precipitation phenomena in impulse friction stir welded 2024 aluminium alloy // Materials Science and Engineering: A. 2022. Vol. 852. Article number 143617. DOI: 10.1016/j.msea.2022.143617.
14. Zhang Fan, Levine L.E., Allen A.J., Campbell C.E., Creuziger A.A., Kazantseva N., Ilavsky J. In situ structural characterization of ageing kinetics in aluminum alloy 2024 across angstrom-to-micrometer length scales // Acta Materialia. 2016. Vol. 111. P. 385–398. DOI: 10.1016/j.actamat.2016.03.058.
15. Mrówka-Nowotnik G., Sieniawsk J. Analysis of intermetallic phases in 2024 aluminium alloy // Solid State Phenomena. 2013. Vol. 197. P. 238–243. DOI: 10.4028/www.scientific.net/SSP.197.238.
16. Czerwinski F. Thermal Stability of Aluminum Alloys // Materials. 2020. Vol. 13. № 15. Article number 3441. DOI: 10.3390/ma13153441.
17. Tang W., Guo X., Mcclure J., Murr L., Nunes A.C. Heat input and temperature distribution in friction stir welding // Journal of Materials Processing and Manufacturing Science. 1998. Vol. 7. № 2. P. 163–172.
18. Chen C.M., Kovacevic R. Finite element modeling of friction stir welding-thermal and thermomechanical analysis // International Journal of Machine Tools & Manufacture. 2003. Vol. 43. № 13. P. 1319–1326. DOI: 10.1016/S0890-6955(03)00158-5.
19. Mishra R.S., Ma Z.Y. Friction stir welding and processing // Materials Science and Engineering: R: Reports. 2005. Vol. 50. № 1-2. P. 1–78. DOI: 10.1016/j.mser.2005.07.001.
20. Dawes C.J. An introduction to friction stir welding and its development // Welding and Metal fabrication. 1995. P. 14–16.
21. Dawes C.J., Thomas W.M. Friction stir joining of aluminium alloys // TWI Bulletin. 1995. Vol. 6. P. 124–127.

Сравнительный анализ химического состава и механических свойств различных участков сварного соединения дюралюмина, полученного сваркой трением с перемешиванием

Щапов Геннадий Валерьевич[1], аспирант, младший научный сотрудник
Казанцева Наталия Васильевна*[2], доктор физико-математических наук, доцент, главный научный сотрудник
Институт физики металлов имени М.Н. Михеева Уральского отделения РАН, Екатеринбург (Россия)

***E-mail:** kazantseva@imp.uran.ru

[1]ORCID: https://orcid.org/0009-0000-2106-6381
[2]ORCID: https://orcid.org/0000-0002-4143-1064

Поступила в редакцию 27.06.2023 *Принята к публикации 21.11.2023*

Аннотация: Сварка трением с перемешиванием в авиастроении и машиностроении является передовым способом соединения различных металлов и сплавов, плохо свариваемых или несвариваемых обычными способами. Активно используемый в авиастроении высокопрочный алюминиевый сплав Д16 плохо поддается сварке плавлением, что связано с образованием дендритной структуры в зоне сплавления, приводящей к снижению механической прочности соединения. В работе исследована микроструктура и микротвердость сварного шва алюминиевого сплава Д16, полученного методом сварки трением с перемешиванием. Методами сканирующей электронной микроскопии и оптической металлографии выявлено наличие трех зон: ядра шва, зоны термомеханического воздействия и зоны термического воздействия. В центральной части сварного соединения (в ядре) обнаружена слоистая структура «луковичных колец». Обнаружено изменение химического состава твердого раствора алюминия в различных областях зон сварного шва, а также присутствие концентрационного градиента внутри каждой зоны. В верхней части сварного шва наблюдается обогащение твердого раствора кремнием и обеднение медью. Благодаря обеднению твердого раствора легирующими элементами содержание алюминия в зоне сварного соединения в твердом растворе выше по сравнению с исходным состоянием. Значения микротвердости в различных областях сварного соединения коррелируют с изменением химического состава. В зоне сварного соединения обнаружено значительное снижение микротвердости по сравнению с исходным состоянием, а также наблюдается изменение микротвердости, связанное с градиентом химического состава внутри каждой зоны.

Ключевые слова: сварка трением с перемешиванием; дюралюмин; алюминий; слоистая структура; структура «луковичных колец».

Благодарности: Работа выполнена в рамках государственного задания Министерства науки и высшего образования Российской Федерации (тема «Аддитивность», № 121102900049-1).

Статья подготовлена по материалам докладов участников XI Международной школы «Физическое материаловедение» (ШФМ-2023), Тольятти, 11–15 сентября 2023 года.

Для цитирования: Щапов Г.В., Казанцева Н.В. Сравнительный анализ химического состава и механических свойств различных участков сварного соединения дюралюмина, полученного сваркой трением с перемешиванием // Frontier Materials & Technologies. 2024. № 2. С. 113–119. DOI: 10.18323/2782-4039-2024-2-68-10.

OUR AUTHORS

Abdrakhmanova Elmira Damirovna, student.
Address: Ufa University of Science and Technology,
450076, Russia, Ufa, Zaki Validi Street, 32.
E-mail: elmira.abdr2019@mail.ru

Belosludtsev Konstantin Yurievich, graduate student.
Address: Kalashnikov Izhevsk State Technical University,
426069, Russia, Izhevsk, Studencheskaya Street, 7.
E-mail: kostya.belka99@yandex.ru

Bondareva Olga Sergeevna, PhD (Engineering),
assistant professor of Chair of Metal Technology and Aviation Materials Science.
Address: Academician S.P. Korolev Samara National Research University,
443086, Russia, Samara, Moskovskoye Shosse, 34.
E-mail: osbondareva@ssau.ru

Brazhnikov Ivan Sergeevich, engineer of the Joint Research Center
of Belgorod State National Research University "Technology and Materials".
Address: Belgorod State National Research University,
308015, Russia, Belgorod, Pobedy Street, 85.
E-mail: 1216318@bsu.edu.ru

Buzyreva Darya Alekseevna, graduate student.
Address: Kaluga Branch of Bauman Moscow State Technical University,
248000, Russia, Kaluga, Bazhenov Street, 2.
E-mail: dasha.buzyreva@bk.ru

Dobychina Olga Sergeevna, postgraduate student
of Chair of Metal Technology and Aviation Materials Science.
Address: Academician S.P. Korolev Samara National Research University,
443086, Russia, Samara, Moskovskoye Shosse, 34.
E-mail: o.dobychina@zvpm.ru

Fedoseeva Alexandra Eduardovna, PhD (Engineering),
senior researcher of the Laboratory of Mechanical Properties
of Nanostructured Materials and Superalloys.
Address: Belgorod State National Research University,
308015, Russia, Belgorod, Pobedy Street, 85.
E-mail: fedoseeva@bsu.edu.ru

Gryzunova Natalya Nikolaevna, Doctor of Sciences (Physics and Mathematics), Associate Professor,
professor of Chair "Nanotechnology, Materials Science and Mechanics".
Address: Togliatti State University,
445020, Russia, Togliatti, Belorusskaya Street, 14.
E-mail: gryzunova@tltsu.ru

Kazantseva Nataliya Vasilievna, Doctor of Sciences (Physics and Mathematics), Associate Professor,
chief researcher.
Address: M.N. Mikheev Institute of Metal Physics of the Ural Branch of RAS,
620108, Russia, Yekaterinburg, Sofya Kovalevskaya Street, 18.
E-mail: kazantseva@imp.uran.ru

Khafizova Elvira Dinifovna, PhD (Engineering),
assistant professor of Chair of Materials Science and Physics of Metals,
senior researcher of Scientific Research Laboratory "Metals and Alloys under Extreme Impacts".
Address: Ufa University of Science and Technology,
450076, Russia, Ufa, Zaki Validi Street, 32.
E-mail: KhafizovaED@uust.ru

Korotkova Yuliya Nikolaevna, student.
Address: Academician S.P. Korolev Samara National Research University,
443086, Russia, Samara, Moskovskoye Shosse, 34.
E-mail: korotkova.y.n@gmail.com

Korznikova Elena Aleksandrovna, Doctor of Sciences (Physics and Mathematics), Professor,
professor of Chair of Materials Science and Physics of Metals,
Head of Scientific Research Laboratory “Metals and Alloys under Extreme Impacts”.
Address: Ufa University of Science and Technology,
450076, Russia, Ufa, Zaki Validi Street, 32.
E-mail: elena.a.korznikova@gmail.com

Kukankov Leonid Sergeevich, student.
Address: Academician S.P. Korolev Samara National Research University,
443086, Russia, Samara, Moskovskoye Shosse, 34.
E-mail: kukankov02@gmail.com

Kuklina Aleksandra Aleksandrovna, PhD (Engineering),
assistant professor of Chair “Physics”,
Head of Scientific-Research and Testing Laboratory of Geocryology, Soil Physics and Materials,
engineer of Laboratory of Structural Methods of Analysis and Properties of Materials and Nanomaterials.
Address 1: Ural State Mining University,
620144, Russia, Yekaterinburg, Kuibyshev Street, 30.
Address 2: Ural Federal University named after the first President of Russia B.N. Yeltsin,
620002, Russia, Yekaterinburg, Mira Street, 19.
E-mail: kuklina@m.ursmu.ru

Maisuradze Mikhail Vasilyevich, PhD (Engineering), Associate Professor,
assistant professor of Chair “Heat Treatment and Physics of Metals”.
Address: Ural Federal University named after the first President of Russia B.N. Yeltsin,
620002, Russia, Yekaterinburg, Mira Street, 19.
E-mail: m.v.maisuradze@urfu.ru

Matveeva Nadezhda Sergeevna, postgraduate student.
Address: Togliatti State University,
445020, Russia, Togliatti, Belorusskaya Street, 14.
E-mail: nad.matveeva96@mail.ru

Medvedev Andrey Evgenyevich, PhD (Physics and Mathematics), junior researcher.
Address: Ufa University of Science and Technology,
450076, Russia, Ufa, Zaki Validi Street, 32.
E-mail: medvedevae@uust.ru

Murashkin Maxim Yurievich, PhD (Engineering), senior researcher.
Address: Ufa University of Science and Technology,
450076, Russia, Ufa, Zaki Validi Street, 32.

Muraviev Vitaly Vasilievich, Doctor of Sciences (Engineering), Professor,
professor of Chair “Instruments and Methods of Measurements, Testing, Diagnostics”.
Address 1: Kalashnikov Izhevsk State Technical University,
426069, Russia, Izhevsk, Studencheskaya Street, 7.
Address 2: Udmurt Federal Research Center of the Ural branch of the RAS,
426067, Russia, Izhevsk, Tatiana Baramzina Street, 34.
E-mail: vmuraviev@mail.ru

Muravieva Olga Vladimirovna, Doctor of Sciences (Engineering), Professor,
professor of Chair “Instruments and Methods of Measurements, Testing, Diagnostics”.
Address 1: Kalashnikov Izhevsk State Technical University,
426069, Russia, Izhevsk, Studencheskaya Street, 7.
Address 2: Udmurt Federal Research Center of the Ural branch of the RAS,
426067, Russia, Izhevsk, Tatiana Baramzina Street, 34.
E-mail: olgak166@mail.ru

Nafikov Ruslan Kamilovich, junior researcher
of Scientific Research Laboratory “Metals and Alloys under Extreme Impacts”.
Address: Ufa University of Science and Technology,
450076, Russia, Ufa, Zaki Validi Street, 32.
E-mail: nafickov.ruslan2011@yandex.ru

Nazarova Vera Vyacheslavovna, postgraduate student
of Chair “Heat Treatment and Physics of Metals”.
Address: Ural Federal University named after the first President of Russia B.N. Yeltsin,
620002, Russia, Yekaterinburg, Mira Street, 19.
E-mail: kamicure@yandex.ru

Polenok Milena Vladislavovna, student.
Address: Ufa University of Science and Technology,
450076, Russia, Ufa, Zaki Validi Street, 32.
E-mail: renaweiwei.179@mail.ru

Shaikhulova Aigul Fazirovna, PhD (Engineering), Associate Professor,
senior researcher.
Address: Ufa University of Science and Technology,
450076, Russia, Ufa, Zaki Validi Street, 32.

Shailesh Rao Agari, PhD, Professor,
Department of Mechanical Engineering.
Address: NITTE Meenkshi Institute of Technology,
560064, India, Bangalore, P.B. No. 6429.
E-mail: shailesh.rao@nmit.ac.in

Shchapov Gennady Valerievich, postgraduate student, junior researcher.
Address: M.N. Mikheev Institute of Metal Physics of the Ural Branch of RAS,
620108, Russia, Yekaterinburg, Sofya Kovalevskaya Street, 18.
E-mail: hg-1994@mail.ru

Tretyakov Vitaly Aleksandrovich, student.
Address: Academician S.P. Korolev Samara National Research University,
443086, Russia, Samara, Moskovskoye Shosse, 34.
E-mail: tretyakov.vitalick2015@yandex.ru

Vladykin Aleksey Leonidovich, postgraduate student.
Address: Kalashnikov Izhevsk State Technical University,
426069, Russia, Izhevsk, Studencheskaya Street, 7.
E-mail: pmkk@istu.ru

Volkova Lyudmila Vladimirovna, PhD (Engineering), Associate Professor,
assistant professor of Chair “Instruments and Methods of Measurements, Testing, Diagnostics”.
Address: Kalashnikov Izhevsk State Technical University,
426069, Russia, Izhevsk, Studencheskaya Street, 7.
E-mail: ludmila396@rambler.ru

Zhukova Olga Olegovna, postgraduate student.
Address: Ufa University of Science and Technology,
450076, Russia, Ufa, Zaki Validi Street, 32.
E-mail: olga.zhukova96@mail.ru

Zybin Igor Nikolaevich, PhD (Engineering), Associate Professor,
assistant professor of Chair “Technologies of Connection and Processing of Materials”.
Address: Kaluga Branch of Bauman Moscow State Technical University,
248000, Russia, Kaluga, Bazhenov Street, 2.
E-mail: igor.zybin@bmstu.ru

НАШИ АВТОРЫ

Абдрахманова Эльмира Дамировна, студент.
Адрес: Уфимский университет науки и технологий,
450076, Россия, г. Уфа, ул. Заки Валиди, 32.
E-mail: elmira.abdr2019@mail.ru

Белослудцев Константин Юрьевич, магистрант.
Адрес: Ижевский государственный технический университет
имени М.Т. Калашникова,
426069, Россия, г. Ижевск, ул. Студенческая, 7.
E-mail: kostya.belka99@yandex.ru

Бондарева Ольга Сергеевна, кандидат технических наук,
доцент кафедры технологии металлов и авиационного материаловедения.
Адрес: Самарский национальный исследовательский университет
имени академика С.П. Королева,
443086, Россия, г. Самара, Московское шоссе, 34.
E-mail: osbondareva@ssau.ru

Бражников Иван Сергеевич, инженер
Центра коллективного пользования «Технологии и Материалы НИУ "БелГУ"».
Адрес: Белгородский государственный национальный исследовательский университет,
308015, Россия, г. Белгород, ул. Победы, 85.
E-mail: 1216318@bsu.edu.ru

Бузырева Дарья Алексеевна, магистрант.
Адрес: Калужский филиал
Московского государственного технического университета
имени Н.Э. Баумана,
248000, Россия, г. Калуга, ул. Баженова, 2.
E-mail: dasha.buzyreva@bk.ru

Владыкин Алексей Леонидович, аспирант.
Адрес: Ижевский государственный технический университет
имени М.Т. Калашникова,
426069, Россия, г. Ижевск, ул. Студенческая, 7.
E-mail: pmkk@istu.ru

Волкова Людмила Владимировна, кандидат технических наук, доцент,
доцент кафедры «Приборы и методы измерений, контроля, диагностики».
Адрес: Ижевский государственный технический университет
имени М.Т. Калашникова,
426069, Россия, г. Ижевск, ул. Студенческая, 7.
E-mail: ludmila396@rambler.ru

Грызунова Наталья Николаевна, доктор физико-математических наук, доцент,
профессор кафедры «Нанотехнологии, материаловедение и механика».
Адрес: Тольяттинский государственный университет,
445020, Россия, г. Тольятти, ул. Белорусская, 14.
E-mail: gryzunova@tltsu.ru

Добычина Ольга Сергеевна, аспирант
кафедры технологии металлов и авиационного материаловедения.
Адрес: Самарский национальный исследовательский университет
имени академика С.П. Королева,
443086, Россия, г. Самара, Московское шоссе, 34.
E-mail: o.dobychina@zvpm.ru

Жукова Ольга Олеговна, аспирант.
Адрес: Уфимский университет науки и технологий,
450076, Россия, г. Уфа, ул. Заки Валиди, 32.
E-mail: olga.zhukova96@mail.ru

Зыбин Игорь Николаевич, кандидат технических наук, доцент,
доцент кафедры «Технологии соединения и обработки материалов».
Адрес: Калужский филиал
Московского государственного технического университета
имени Н.Э. Баумана,
248000, Россия, г. Калуга, ул. Баженова, 2.
E-mail: igor.zybin@bmstu.ru

Казанцева Наталия Васильевна, доктор физико-математических наук, доцент,
главный научный сотрудник.
Адрес: Институт физики металлов имени М.Н. Михеева Уральского отделения РАН,
620108, Россия, г. Екатеринбург, ул. Софьи Ковалевской, 18.
E-mail: kazantseva@imp.uran.ru

Корзникова Елена Александровна, доктор физико-математических наук, профессор,
профессор кафедры материаловедения и физики металлов,
заведующий научно-исследовательской лабораторией
«Металлы и сплавы при экстремальных воздействиях».
Адрес: Уфимский университет науки и технологий,
450076, Россия, г. Уфа, ул. Заки Валиди, 32.
E-mail: elena.a.korznikova@gmail.com

Короткова Юлия Николаевна, студент.
Адрес: Самарский национальный исследовательский университет
имени академика С.П. Королева,
443086, Россия, г. Самара, Московское шоссе, 34.
E-mail: korotkova.y.n@gmail.com

Куканков Леонид Сергеевич, студент.
Адрес: Самарский национальный исследовательский университет
имени академика С.П. Королева,
443086, Россия, г. Самара, Московское шоссе, 34.
E-mail: kukankov02@gmail.com

Куклина Александра Александровна, кандидат технических наук,
доцент кафедры «Физика»,
заведующий научно-исследовательской и испытательной лабораторией
геокриологии, физики грунтов и материалов,
инженер лаборатории структурных методов анализа и свойств материалов и наноматериалов.
Адрес 1: Уральский государственный горный университет,
620144, Россия, г. Екатеринбург, ул. Куйбышева, 30.
Адрес 2: Уральский федеральный университет
имени первого Президента России Б.Н. Ельцина,
620002, Россия, г. Екатеринбург, ул. Мира, 19.
E-mail: kuklina@m.ursmu.ru

Майсурадзе Михаил Васильевич, кандидат технических наук, доцент,
доцент кафедры «Термообработка и физика металлов».
Адрес: Уральский федеральный университет
имени первого Президента России Б.Н. Ельцина,
620002, Россия, г. Екатеринбург, ул. Мира, 19.
E-mail: m.v.maisuradze@urfu.ru

Матвеева Надежда Сергеевна, аспирант.
Адрес: Тольяттинский государственный университет,
445020, Россия, г. Тольятти, ул. Белорусская, 14.
E-mail: nad.matveeva96@mail.ru

Медведев Андрей Евгеньевич, кандидат физико-математических наук,
младший научный сотрудник.
Адрес: Уфимский университет науки и технологий,
450076, Россия, г. Уфа, ул. Заки Валиди, 32.
E-mail: medvedevae@uust.ru

Муравьев Виталий Васильевич, доктор технических наук, профессор,
профессор кафедры «Приборы и методы измерений, контроля, диагностики».
Адрес 1: Ижевский государственный технический университет
имени М.Т. Калашникова,
426069, Россия, г. Ижевск, ул. Студенческая, 7.
Адрес 2: Удмуртский федеральный исследовательский центр Уральского отделения РАН,
426067, Россия, г. Ижевск, ул. Татьяны Барамзиной, 34.
E-mail: vmuraviev@mail.ru

Муравьева Ольга Владимировна, доктор технических наук, профессор,
профессор кафедры «Приборы и методы измерений, контроля, диагностики».
Адрес 1: Ижевский государственный технический университет
имени М.Т. Калашникова,
426069, Россия, г. Ижевск, ул. Студенческая, 7.
Адрес 2: Удмуртский федеральный исследовательский центр Уральского отделения РАН,
426067, Россия, г. Ижевск, ул. Татьяны Барамзиной, 34.
E-mail: olgak166@mail.ru

Мурашкин Максим Юрьевич, кандидат технических наук, старший научный сотрудник.
Адрес: Уфимский университет науки и технологий,
450076, Россия, г. Уфа, ул. Заки Валиди, 32.
E-mail: maksim.murashkin.70@yandex.ru

Назарова Вера Вячеславовна, аспирант кафедры «Термообработка и физика металлов».
Адрес: Уральский федеральный университет
имени первого Президента России Б.Н. Ельцина,
620002, Россия, г. Екатеринбург, ул. Мира, 19.
E-mail: kamicure@yandex.ru

Нафиков Руслан Камилович, младший научный сотрудник
научно-исследовательской лаборатории «Металлы и сплавы при экстремальных воздействиях».
Адрес: Уфимский университет науки и технологий,
450076, Россия, г. Уфа, ул. Заки Валиди, 32.
E-mail: nafickov.ruslan2011@yandex.ru

Поленок Милена Владиславовна, студент.
Адрес: Уфимский университет науки и технологий,
450076, Россия, г. Уфа, ул. Заки Валиди, 32.
E-mail: renaweiwei.179@mail.ru

Третьяков Виталий Александрович, студент.
Адрес: Самарский национальный исследовательский университет
имени академика С.П. Королева,
443086, Россия, г. Самара, Московское шоссе, 34.
E-mail: tretyakov.vitalick2015@yandex.ru

Федосеева Александра Эдуардовна, кандидат технических наук,
старший научный сотрудник
лаборатории механических свойств наноструктурных и жаропрочных материалов.
Адрес: Белгородский государственный национальный исследовательский университет,
308015, Россия, г. Белгород, ул. Победы, 85.
E-mail: fedoseeva@bsu.edu.ru

Хафизова Эльвира Динифовна, кандидат технических наук,
доцент кафедры материаловедения и физики металлов,
старший научный сотрудник научно-исследовательской лаборатории
«Металлы и сплавы при экстремальных воздействиях».
Адрес: Уфимский университет науки и технологий,
450076, Россия, г. Уфа, ул. Заки Валиди, 32.
E-mail: KhafizovaED@uust.ru

Шайлеш Рао Агари, кандидат наук, профессор, кафедра машиностроения.
Адрес: Политехнический институт Нитте Минакши,
560064, Индия, г. Бангалор, п/я № 6429.
E-mail: shailesh.rao@nmit.ac.in

Шайхулова Айгуль Фазировна, кандидат технических наук, доцент,
старший научный сотрудник.
Адрес: Уфимский университет науки и технологий,
450076, Россия, г. Уфа, ул. Заки Валиди, 32.
E-mail: shaikhulova@inbox.ru

Щапов Геннадий Валерьевич, аспирант, младший научный сотрудник.
Адрес: Институт физики металлов имени М.Н. Михеева Уральского отделения РАН,
620108, Россия, г. Екатеринбург, ул. Софьи Ковалевской, 18.
E-mail: hg-1994@mail.ru

On the cover: SEM image of the surface of the initial sample of the Zn–1%Fe–5%Mg alloy after 56 days of corrosion tests (500x magnification). Author of the photo: E.D. Abdrakhmanova, student (Ufa University of Science and Technology, Ufa, Russia).

На обложке: РЭМ-изображение поверхности исходного образца сплава Zn–1%Fe–5%Mg спустя 56 дней коррозионных испытаний (увеличение 500 крат). Автор фото: Э.Д. Абдрахманова, студент (Уфимский университет науки и технологий, Уфа, Россия).